UNIVERSITY OF BIRMINGHAM

MICROMECHANICS OF COLLAPSE IN LOESS

by

ARYA ASSADI LANGROUDI

A thesis submitted to
the University of Birmingham
for the degree of
DOCTOR OF PHILOSOPHY

School of Civil Engineering
College of Engineering and Physical
Sciences University of Birmingham
August 2014

To

My parents

Leila & Homayoun

for when you sip your morning tea
and recall all that lifetime favours you did to me

&

To my wife

Armaghan

For your patience,
for trusting me,
and for your heart-warming words

L'idée est trop. Volonté est peu.
Ce qui importe c'est la volonté de
rendre l'idée en réalité.

(Ideas are great. Willingness is
little. What matters is a desire to
bring the idea into reality.)

From my father's letter dated
06.11.13

Acknowledgements

Special thanks are due to Prof. Ian Jefferson for his supervision and inspiration, for giving me soil and life lessons.

The author would also like to state his sincere thankfulness to:

- To Prof. Kenneth O'Hara-Dhand for helping me through the particle size analysis, co-authoring papers, and proofreading the thesis thrice
- To Prof. Chris Rogers and Dr. David Boardman for co-supervising the work
- To Prof. Martin Culshaw for reviewing Appendix A1-A3 and co-supervision
- To Prof. Andrew James Plater of Liverpool University for patiently editing the work on quartz crushability and fractal features
- To Dr. Gurmel Ghataora and Dr. David Chapman for their comments over three annual reviews, and for all the encouragements
- To Prof. Ian Smalley of Leicester University and Dr. Kevin Northmore of the BGS for the talks on quartz crushability and UK loess PTD model
- To Mr. Peter Gilbert and Dr. Imad Alobaidi of Atkins, for holding rounds of meetings to discuss Chapter 6 of this work
- To Prof. Kenneth Pye for useful talks on laser diffraction
- To Prof. Edward Derbyshire for sharing his medical research perspectives: trigger of my talk on the 19th Windy Day, Southampton
- To Dr. Sue McLaren and Prof. Zorica Svirčev for talks on loess stabilization by sticky polysaccharide exuded from cyanobacteria
- To Prof. Braja Das and Prof. Ian Moore for the talks on lab set-up.
- To Dr. Tom Dijkstra and Dr. Stephen Bentley for their encouragements on the INQUA Loess 2013.
- To Dr. James Kwong for the enjoyable talk over concerns with the current compaction practice in loess fills in Hawaii
- To Dr. Amirsoleymani, Birmingham University 1963 alumni for recommending me to the school to do the PhD on loess, a test material of his research
- To technical staff, Dr. J. Bowen, Dr. J. Deans, Mrs T. Morris, Ms. J. Harris and Ms. A. Mistry for their help with running the electron microscopy, light microscopy, laser spectroscopy and X-ray machines; and to Dr. A. Davenport for providing access to the petrological microscope

Abstract

Soil collapse is amongst one of the most significant ground related hazards to the built environment. A collapsible soil, in particular loess, typically has an open-structure of particles and collapse occurs when as a consequence of the addition of water and/or load the particles rearrange to form a more dense fabric, destroying much of inter-particle bonds. Collapse leads to a sudden reduction in the void space and volume of the soil and in turn, a suite of problems for buildings and infrastructures built on or in collapsing soil deposits. Treatment to mitigate collapse often involves in densification techniques. However, such approaches have been reported not always effective enough to fully combat the collapse problem (Wynne, 2007, Roohnavaz et al., 2011). This stems from a lack of in-depth understanding of soils' geochemistry and structure, the result of which is an oversimplification of the complex geotechnical and geological interactions. An important example of such limited knowledge is the increasing evidence of restoration of the collapsing structure upon wetting-drying cycles, which is widely ignored in the current compaction practice.

This research aims to first identifying collapse micro-mechanisms in fine-grained soils, examining the contribution of a handful of soil constituents in collapsibility, and finally developing a practical tool for ground engineers to evaluate the efficiency of the current compaction practice for systematically classified fine-grained soils, and to take modified/novel earthwork approaches where the current practice fails to fully remove the collapse risk. To do so, a framework for collapse mechanism is first developed by proposing a modified form of the principle of effective stress. The modified principle is formulated for a typical calcareous clayey collapsing soil through the real-time measurement of grain strength, grain-cement interaction, packing state and internal forces in the event of wetting. The framework is then used to examine the impact on collapsibility of many soil constituents (i.e. quartz silt, kaolinite, carbonate, silica amorphous, sulphate and chloride, cured under controlled climates), as individuals and pairs. Having examined the contribution of many soil constituents (and their

relative abundance) as well as internal forces in collapsibility, sub-63 µm soil is systematically classified into 11 main classes (41 sub-classes), each representing a certain combination of soil constituents, rendering a certain mechanical response upon wetting. A set of contour graphs are produced to estimate the maximum collapse/swell potential for each of the soil classes for given in-situ conditions. Contour graphs are re-produced for soils improved by the standard compaction practice. Where the risk of collapse remained after compaction, constraints to the compaction practice are identified and tentatively rectified through proposing modified/novel amelioration strategies.

Key words:

Loess, collapse, effective stress, mitigation

Table of Contents

List of Figures

List of Plates

List of Tables

List of Notations

$\mathbf{1}$	Kronecker delta tensor
a	Weibull modulus
$\dot{A}$	Angstrom
A_e	Effective stress
AV	Air volume
ae	Air entry value
BBM	Barcelona Basic Model
B_r	Relative breakage
CBR	California Bearing Ratio
C	Coordination number
C_v - $C_{v(i)}$	Coefficient of volume compressibility
C_{col}	Coefficient of collapsibility (collapse potential)
C_{con}	Coefficient of contraction (compressibility)
$Carb$	Calcium Carbonate
D	Pore width
DDL	Diffused Double Layer
dm	Decimeter
d_{pore}	Pore diameter
d_D	Dominan diameter
d_p	Particle diameter
d_{50}, D_{50}	Particle size corresponding to 50% passing
e	Void ratio
E	Energy
EC	Electrical conductivity
$ESEM$	Environmental Scanning Electron Microscopy
exp	exponential function
e_i, e_f	Initial void ratio
ex	Air expulsion value
$F_{N(Ske)}$	Skeletal force
$\overline{F_B}$ - B	Buoyant force
F_D - D	Drag force
F_{Cap}	Capillary force
g	gram
G_s	Specific gravity
$\dot{H}$	Water overhead
H_w	height of the water column in the oedometer chamber
$\overline{H_{w_i}}$	height to which water climbs within specimen at $t = t_i$
$\dot{H}_i$	height of the specimen at wetting time $t = t_i$
H_s	height of the solid column
H_{dr}	Maximum distance to the drain point
Hr	Hour

i	Hydraulic gradient
J	Joule
K - k_i	Coefficient of permeability
k_0	At rest earth condition
kV	Kilo Volt
keV	Kilo electron volt
LL	Liquid Limit
LD	Laser diffraction
Ln	Natural logarithm (logarithme népérien)
$M\ as\ in\ M-SO_4^{2-}$	Metal
mM	Millimole
$m_{v(i)}$	coefficient of volume compressibility
n - n_i	Porosity
N	Natural number
nm	Nanometre
$Norm.$	Normalized
$\boldsymbol{\rho}$	effective stress tensor
ρ_w	pore water pressure
ρ_a	pore air pressure
P_s	chance of grains to break
PP_i	% of grains finer than a given size in dry soil
PP_W	% of grains finer than a given size in wetted soil
PSD	Particle size distribution
PI	Plasticity Index
PL	Plasticity Limit
PTF	Pedo-Transfer Function
Q	Volumetric flow rate
r_1	external radius of the principal curvature
r_2	internal radius of the principal curvature
R	Grain radius
S_r - S_{r_i}	Saturation ratio
S_{r_T}	Threshold saturation ratio
S_r^e	effective saturation ratio
S_r^M	Saturation ratio at macro-pores
S_r^m	Saturation ratio at micro-pores
$S_{r\ Res}^{M}$	Residual saturation ratio at macro-pores
$S_{r\ Res}^{m}$	Residual saturation ratio at micro-pores
SOT	Single Oedometer test
$SWCC$	Soil Water Characteristic Curve
s	Second
$StDev.$	Standard deviation
T_s	Surface tension

t_b	Thickness of clay connector
t_{90}	Time by which consolidation reaches to 90%
Θ	contact angle of the contractile skin
U	Hydrostatic force
$\bar{u}_w^m$	Pore water pressure
${u_w}^M$	Water pressure at macro-pore level
${u_w}^m$	Water pressure at micro-pore level
u_a	Air pressure
μ	viscosity of water
µ	Mean value
γ_w	water density
γ_d	Dry unit weight
V	Voltage
V_s	Volume of soil's solid constituent
V_v^M	Macro-scale pores' volume
V_v^m	Micro-scale pores' volume
$vs.$	Versus
W	Weight force
W	Watt
W_{Pr}	Proctor compation work
ω_f	Funicular level water content
ω_p	Pendular level water content
ω_{sat}	Saturation water content
ω_{opt}	Optimum water content
ω_{comp}	Compaction (placement) water content
ω_n	Natural water content (in-service, in-situ)
Ψ	Matric suction
$\boldsymbol{\varepsilon}$	Volume Strain
XRD	X-ray Diffraction
χ	Effective stress parameter
λ	Wave length
σ'	Effective stress
$\overline{\sigma}$	Constitutive stress
σ_{net}, σ_v	Applied external net stress
δ_x	Error
.	Valence electron within the Lewis dot Structure
∋	For any
∈	element of

Chapter 1 INTRODUCTION

The most beautiful thing we can experience is the mysterious. It is the source of all true art and science

What I Believe. Albert Einstein 1879 - 1955

1.1 Thesis Overview

Loess soils are made up of quartz silt grains, which are connected together with cementing agents such as clay, capillary water, fine silt, salt or oxide. The grain-cement connection may however disappear in the event of loading/wetting, when connectors fail under shear stresses or migrate with the flowing water. This causes a sudden change in grains arrangement from an initial open state to a final closed state. Such change in the soil state is termed 'collapse'. Loess covers about 10-15% of earth's landmass (Jefferson and Rogers 2012). This area extends from Western Europe to China, and patchily covers North America, South America, central Africa, New Zealand and Australia. Loess may lose cementation and suddenly collapse upon loading and/or wetting. Collapse results in a range of hazards, ranging from ground subsidence in urban areas to differential settlements under atmospheric storage tanks (e.g. LPG – Liquid Petroleum Gas tank farms in the Gulf region), pipelines, roads and rail tracks. Damage to infrastructures (see Table 1.1) as a result of collapse, are widely reported in the literature (Plate 1.2). Loess geotechnical research generally aims to understand the controlling factors and mechanism of collapse, and to use this baseline information to mitigate the collapse or to re-use the poor quality site-won loess to construct fills beneath the planned developments. A correct choice of earthwork techniques however, can reduce the problem only to a limited extent. This is because:

(1) The current soil classification system fails to provide adequate boundaries, within which the viability of commonly practiced remedial

techniques is discussed. Similar soils may behave remarkably different due to the ignored bonding properties in classification (Smalley and Dijkstra, 1991).

(2) Wetting and ground improvement removes the collapsibility temporarily, since the collapsing soil structure may retrieve to limited degrees over time.

(3) Common practice occasionally appears not sustainable in removing and stockpiling the poor quality loess to build fills with imported materials.

Table 1.1 Examples of collapsing soils beneath structures posing geohazard

Structure	Example	Notes	In
Buildings	Nevada USA	18-inches sinkhole on 400 to 600 feet of pavement on Hacienda Street	McMurdo and Gomez (2005)
	Egypt	3-5 m deep, 10-20m in diameter sinkholes in Sabkha soil along the northern coast	Sakr et al. (2008)
	New Mexico	A $0.5 million damage to foundation of a commercial building due to differential settlement caused by watering the nearby landscapes	Houston et al. (2001)
Slopes	North West China	Over 1000 large landslides in the loess highlands of eastern Gansu, taking the life of 2000 people between 1965 and 1979.	Derbyshire et al. (2000)
Coastlines	Rissa, Norway: Lake Botnen	The Rissa land-slide taking place on 29 April 1978, covering an area of 330,000 m^2, killing one and destroying 7 farms and 5 family homes	NGI (1978) and Gregersen (1981)
Water conveyance structures irrigation channels	Tashkent, Tajikistan	1.5 to 2.5m of collapse in loess foundation of newly built canals	Rogers et al. (1994a)
Airport runways	Town of Gypsum, USA	200 feet in diameter sinkhole formed near the Eagle County Airport	CGS (2001)
	Heathrow, UK	Evidence provided for a calcareous aeolian loess layer (Langley silt) near the Heathrow airport	Rose et al. (2000) and Jefferson et al. (2003)
Earth-dams	Idaho, USA	Collapse of Teton Dam – see Plate 1.1	Smalley (1992)
Road embankments	North West China; Iowa, USA	Sinkholes formed in on the Galoanshan-Lanzhou road on 11 August 1990.	Derbyshire et al. (2000) Handy (1973)
Industrial installations	Kazakhstan	Occurrence of calcareous loess deposits in Northwest Kazakhstan, South of the River Ural, Karachaganak gas field	Roohnavaz et al. (2011)

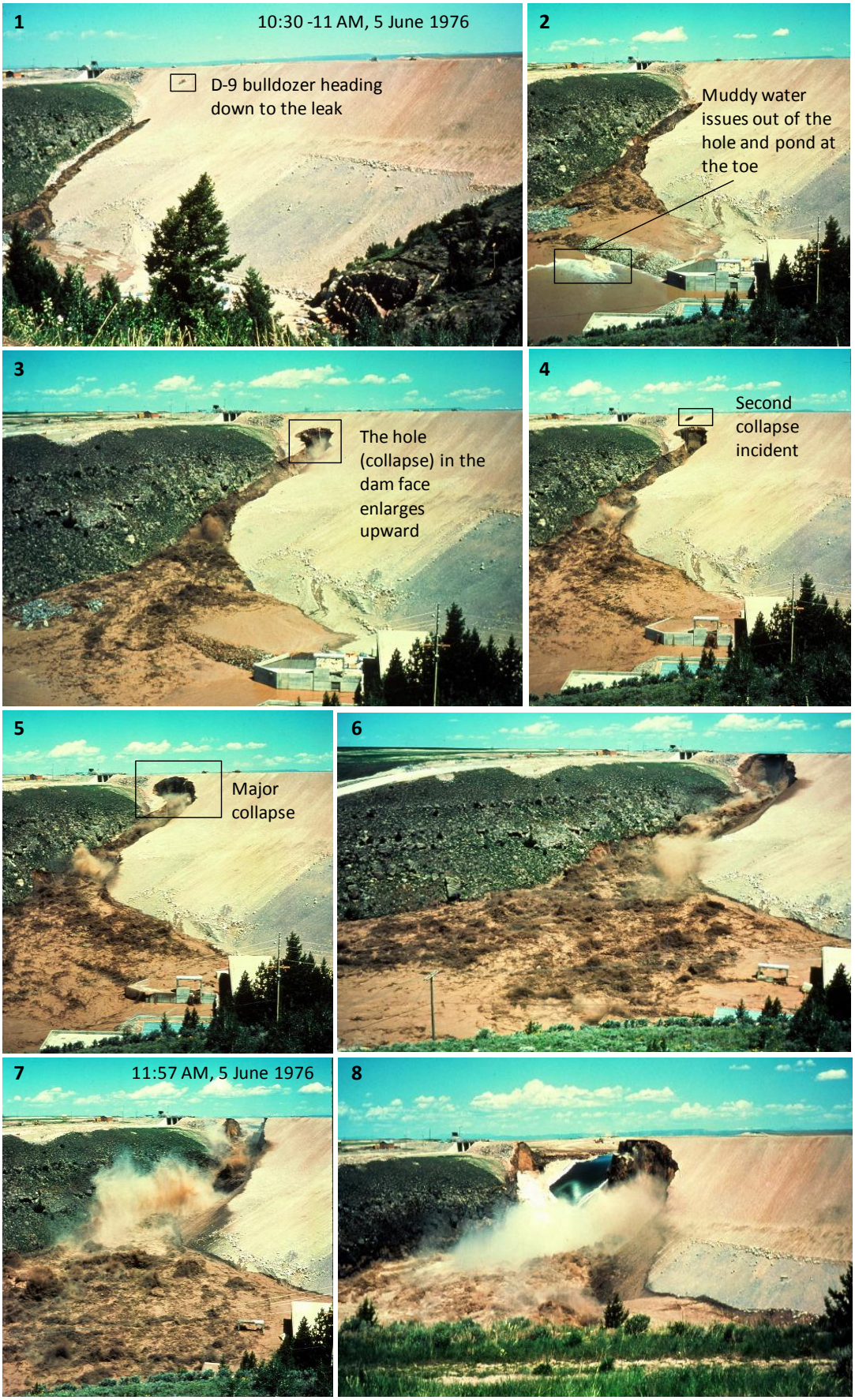

Plate 1.1 Teton Dam failure, pictures by Mrs. Eunice Olson in Arthur Gibbs Sylvester webpage, University of California: http://www.geol.ucsb.edu/faculty/sylvester/Teton_Dam

Plate 1.2 [1-2-3] Collapse of calcareous chalky silt soil (containing 10.8% chalk CaSO4.2H2O, 5.4% SO32- at the pH of 9.3 and calcite contents)beneath a rail-track (Assadi, 2007), [4-5] collapse in a chemical plant after dissolution of secondary crystals of Sodium Hydroxide connectors upon ingress of rain water (Assadi, 2009)

This thesis explores the mechanism of collapse throughout the pre-wetting, post-wetting, and wetting stress paths by means of integrated oedometer-microscopy experiments, as well as a range of spectrometry experiments. This work is presented in three levels:

Level I. Development of a framework for collapse mechanism modelling;

Level II. Development of a modified fine-grained soils classification system together with the collapse micro-mechanism models;

Level III. Development of contour graphs to estimate the value of collapse risk for fine-grained soils, identification of constraints to the compaction practice, and proposing tentative solutions to relax these constraints.

A number of identical artificial loess oedometer specimens (75 mm in diameter) were engineered by mixing and processing ground Leighton Buzzard Sand (70%), kaolinite (10%), and carbonate (20%). The constituents were initially prepared

and stored in sealed batches under cool dry state, and were processed through a novel step-wise method to build identical testing specimens (i.e. ideal loess). Identical specimens were used to examine the strength of silt, silt-cement interaction, and pore spaces and inter-particle forces under various wetting/drying conditions. Output was used to determine a collapse mechanism framework. To extend the framework, various combinations of ground sand, kaolinite, carbonate, silica and sulphate were used to engineer a wider range of loess specimens, as well as kaolinite specimens. Controlled contents of components were mixed together, processed, and cured to build the oedometer testing specimens. Based on the measured collapse potential, testing material (representing sub-63 μm soils) was systematically classified into 11 classes and 40 sub-classes. Specimens in each sub-class showed a reproducible trend of collapse potential against their bond (i.e. clay and carbonate) content. Collapse was modelled for soil classes using the initially developed framework. Collapse models were eventually used to examine the effectiveness of the current compaction practice in removing/reducing the risk of collapse. Limitations with the compaction practice are identified, and recommendations for improvement on a tentative level are presented.

1.2 Aim and Objectives

The principal aim of this thesis is to model the micro-mechanisms of collapse in loess in order to optimize common ground improvement practices.

The aim is fulfilled through:

1. Critical review of the collated loess literature since 1839 (D'Archiac, 1839) on formation mechanisms, physiochemical and mechanical properties, and remedial measures as well as the literature's interdisciplinary links to particle engineering, principle of effective stress, unsaturated soil mechanics, and micro-mechanics;
2. The study of interdisciplinary links (through novel test material synthesis and testing) to develop a modified form of the principle of effective stress by which the collapse mechanism is explained (Level I);
3. Modification of the <63 μm soils' classification system (Level II);

4. Modelling of the collapse for individual soil types using direct mechanical as well as micro-analytical examinations, using the framework developed in Level I (Level II);
5. Applying the models by producing collapse potential predictive graphs, examining the current compaction practice for any of the soils types, and proposing a set of modified/novel mitigation strategies (Level III)

1.3 Contribution to Knowledge

The debate on collapse mechanism and efficiency of classic/common mitigation practice has been a recurrent topic in ground engineering since its early introduction in 1820s (Smalley et al., 2001). In the last two decades, research was undertaken on undisturbed natural and artificial clayey silt soils, aerially deposited and wetted at a high void ratio. Contributions published in the 1990s and 2000s often explore the collapse behaviour throughout the stress-void ratio plane by means of a descriptive framework that incorporated packing, micro-textural, and micro-structural information. It could be inferred that examining the current state of development of loess research under a geotechnical theme would provide detailed information. This however, is only literally true, since loess spans a much wider range of components, and deserves a higher account of recognition of the role played by the clastic properties of the grains, the micro-morphology and chemical structure of the bonds, stress and hydraulic history and internal forces.

The genesis of 20-30 μm silt mode was examined through quartz crushing experiments, under controlled input energy (both in magnitude and in operation period) along with Petrological and Electron microscopy. The work evidenced the significance of internal crystalline controls and questioned an earlier clastic equation of McDowell and Bolton (2001), in which a greater chance of breakage was considered for finer grains. The synthesis of carbonate bonding materials (at controlled contents) in loess was practiced for the first time. Special emphasis was put into a better understanding of the association of soil's collapsing behaviour and carbonate's micro-morphology. Such an improved understanding was finally used to deliver a modified tentative ground improvement practice. The control of precipitated silica on collapsibility was

examined in loess soils containing varied contents of kaolinite and carbonate, in presence or absence of sulphate phases. This showed why the novel Russian silicatization technique (i.e. controlled injection of Sodium Silicate solution and Carbon Dioxide into the soil) could improve some but not all loess soils. To describe the collapse behaviour of loess, a new form of principle of effective stress was proposed, supported with a tailored oedometer test procedure. To do so, a novel test setup was designed and practiced to measure a handful of internal forces, real-time, on the wetting stress state surface. Having the principle in hand, and the produced collapse pressure database, a new classification system addressing fine-grained soils was proposed and detailed. For each of the soil classes, the collapse mechanism was systematically described. The current ground improvement practice was examined, and modifications were proposed at a tentative scale.

1.4 Impact

The improvements made in the principle of effective stress (Level I) brings an immediate impact on: (1) Explaining the collapse-rebound upon cyclic wetting-drying in young or aged quaternary soils. (2) Practicing the latest theoretical contributions including the double porosity concept and hydraulic hysteresis – microfabric interaction. The principle is conventionally a backbone of many constitutive models, and hence many finite elements and limit equilibrium modelling tools.

Collapse modelling described in the present work is based on a novel form of the principle of effective stress, as well as a novel collapse potential database corresponding to a wide range of fine soils, which are engineered for through new laboratory procedures. The practical output of such models, tentative modified ground improvement practice, looks into the problem of collapse differently, and hence can potentially be considered in forthcoming versions of codes of practice.

1.5 Thesis Organization

This work is organized in seven chapters, an overview of which is illustrated in Fig. 1.1.

Chapter 2 reviews the literature in the following five main areas: (1) the risk of collapse, (2) loess, a collapsing soil, (3) our current understanding of collapse, (4) our current understanding of collapse mechanism models, and (5) current solutions to mitigate the collapse.

Chapter 3 details the methods used to prepare and process a suite of primary materials to synthesis a range of testing specimens. A detailed account of background theories and testing set-ups used for modelling is given. Methodology is prepared in three levels, to satisfy the three levels of study.

Chapter 4 describes Level I testing outputs. Four micromechanical indices (i.e. grain strength, grain-cement interaction, and variation of internal forces and pore volumes under combinations of wetting-stressing paths) are examined for a representative collapsing loess testing specimen (i.e. ideal loess). Finally, the outputs are used to develop a final framework for the collapse modelling (i.e. a modified form of the effective stress principle).

Chapter 5 details the level II activities, through which a modified collapsing soils classification and collapse mechanism models are developed. Various combinations of silt, kaolinite, carbonate, sulphate, and silica are used to build a wide range of loess specimens, as well as kaolinite specimens. The collapse behaviour of specimens is examined by a series of integrated oedometer - micro-analytical tests. Putting specimens with similar collapse behaviour in individual groups, a novel classification system (specifically for the purpose of collapse behaviour studies) is proposed for sub-63 μm soils. The classification is suggested to be used when the risk of collapse is a matter of concern.

Chapter 6 addresses level III activities. A flowchart is suggested by which engineers can identify the type of a given fine-grained soil, estimate its maximum possible collapse/swell potential, measure the reliability of common compaction practice for specific soil types, and finally find a tailored tentative-level improvement practice which can fully and permanently remove the risk of collapse, should such risk apply.

Chapter 7 summarises the findings of this thesis and suggests future works.

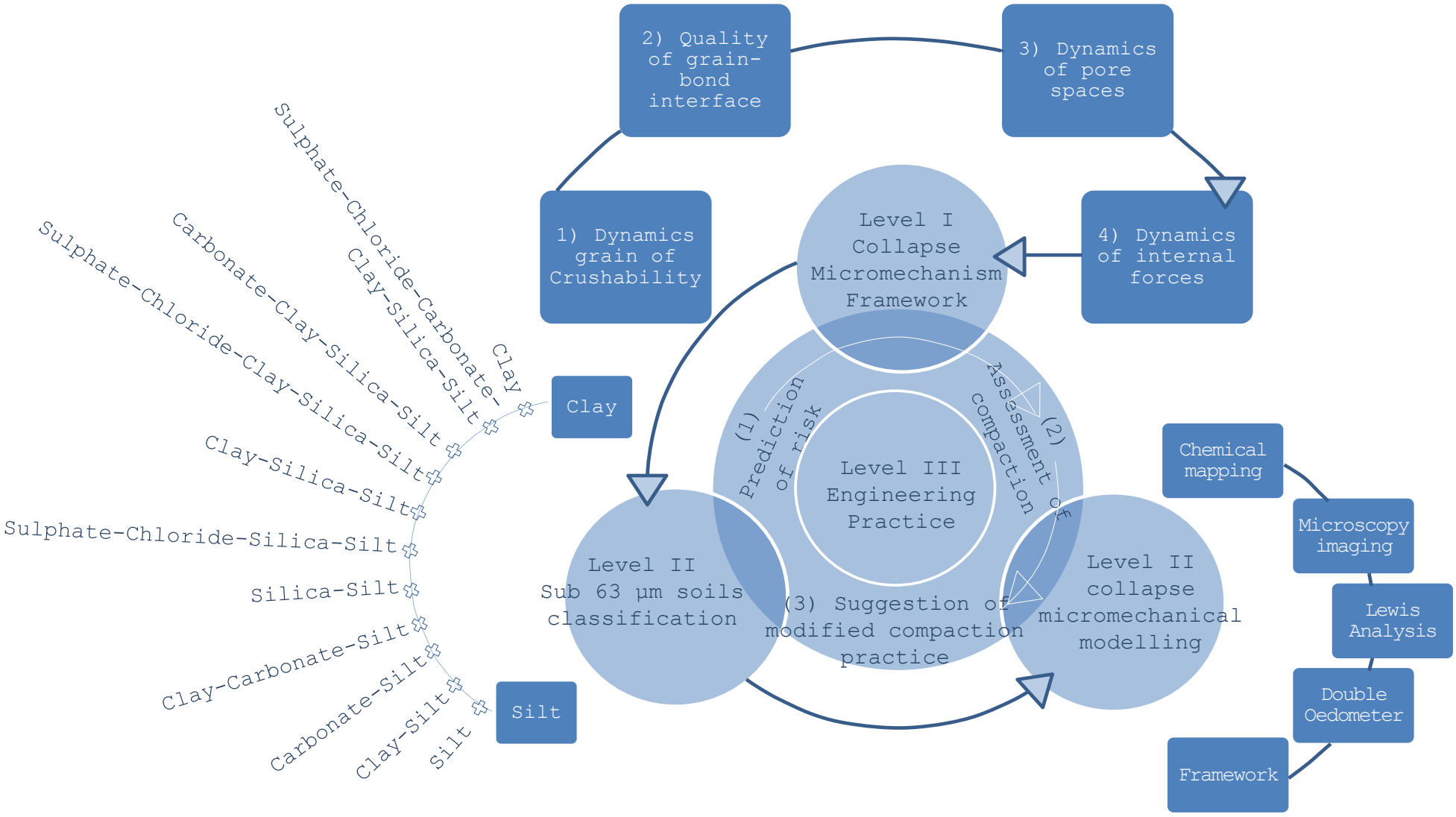

Fig 1.1 Map of the research

Chapter 2 LITERATURE REVIEW

2.1 Collapse in Soils: the Problem

Collapse is essentially a sudden change in soil structure from an initial open state to a final dense state when grain-to-grain connections fail in the event of wetting or loading. Collapse may trigger upon grain breakage under dynamic, transient, or prolonged static stresses, slippage of grains in the event of wetting or stress relief. Collapse may also trigger upon shear failure, migration of grain-to-grain connectors, and loss of capillary forces. For collapsing soils consisting of clay connectors, any decrease in clay's plasticity (and hence the water content at which clay connectors may fail upon shearing) changes the soils collapsing potential. Such changes in clay's plasticity can take place upon clay-salt-oxide interactions (weathering or reworking). Clay connectors may fail due to swelling (e.g. in active clays), heaving (upon anion exchange in clays or overgrowth of salt secondary crystals), dissolution (e.g. salty bonds), causing a trigger to the collapse volume change (Feda 1988, Osipov and Sokolov, 1995).

2.2 Loess: a Problematic Material

2.2.1 History and Definition

Loesch (also lȍsz in Jari and Badura (2013), loeβ in German, Schwemmlöss or löss in Pye (1995)) was introduced by countrymen from the Upper Rhine region (Southwest Germany) to describe the friable silt deposits along the Rhine Valley near Heidelberg. Although the term was literally introduced in 'Charakteristik der Felsarten' by Karl Caesar von Leonhard in 1824 (Smalley, 2013), it was only brought into the scientific literature in 1834 by Charles Lyell (Smalley et al., 2001). John Hardcastle introduced loess soil's association with past climates and environments as early as 1890. This was a base for the 1916 loessification hypothesis; a line of research, which still

is a matter of much dispute (Smalley and Marković, 2013). The first loess-specific soil classification system was introduced and elucidated in Jefferson and Smalley (1995), which considered the nominal particle size, as well as strength of inter-particle bonds and forces, microfabric and soil's tendency for problematic behaviour. In Britain, loess has been known as 'Brickearth' (d'Archiac, 1839, Prestwich, 1863, Fink, 1974). The brickearth was used in Roman[1] buildings (e.g. Roman London Amphitheatre and timber buildings discovered in Walbrook Valley – see Arkell and Tomkeieff (1953) and Lee et al. (1989)), and was described as homogeneous structure-less loam (Deakin, 1986).

Loess is a widespread water-sensitive soil with at-least one cycle of aeolian deposition (Rogers, 1995), and a possible history of post-depositional modifications (Smalley et al., 2006 a). The metastable aspect of loess is due to its air-fall sedimentation history (Rogers, 1995); while the post-depositional modifications are responsible for the collapsibility of the metastable structure (Smalley et al., 2006 a). Loess is composed of marked contents of 20-60μm sub-angular silts, which are mostly connected together by clay/salt bonds (Zourmpakis et al., 2005). In absence of bonds, grains interact with each other via their sharp asperities (Derbyshire and Mellors, 1988). An external force or hydraulic gradient affects the individual constituents through a network of internal forces (Bolton, 1999, Santamarina, 2003). Collapse occurs when internal forces exceed the bonds' shear strength, or bonds fail upon water ingress (Jehring, 2007). This shows the significance of internal forces in loess behaviour (Emeriault and Chang, 1997). The interaction between internal forces and soil components is generally termed as micromechanics (Gherbi et al., 1993).

2.2.2 Distribution

Loess soils cover 15% of the earth's landmass (Dibben, 1998), and particularly blankets significant areas of Eurasia between about 30-55° N from eastern China to the British Isles (Derbyshire and Mellors, 1988) and patchily

[1] The Roman occupation of Great Britain was between 43AD to 400AD: Early 19th century excavations in Walbrook channel (52-63 London Wall) revealed a large number of human skulls buried in brickearth, which could be the remnants of the AD60 massacre carried out by the rebellious Queen Boudicca.

distributes over North and South America, central Africa, New Zealand and Australia (Fig 2.1).

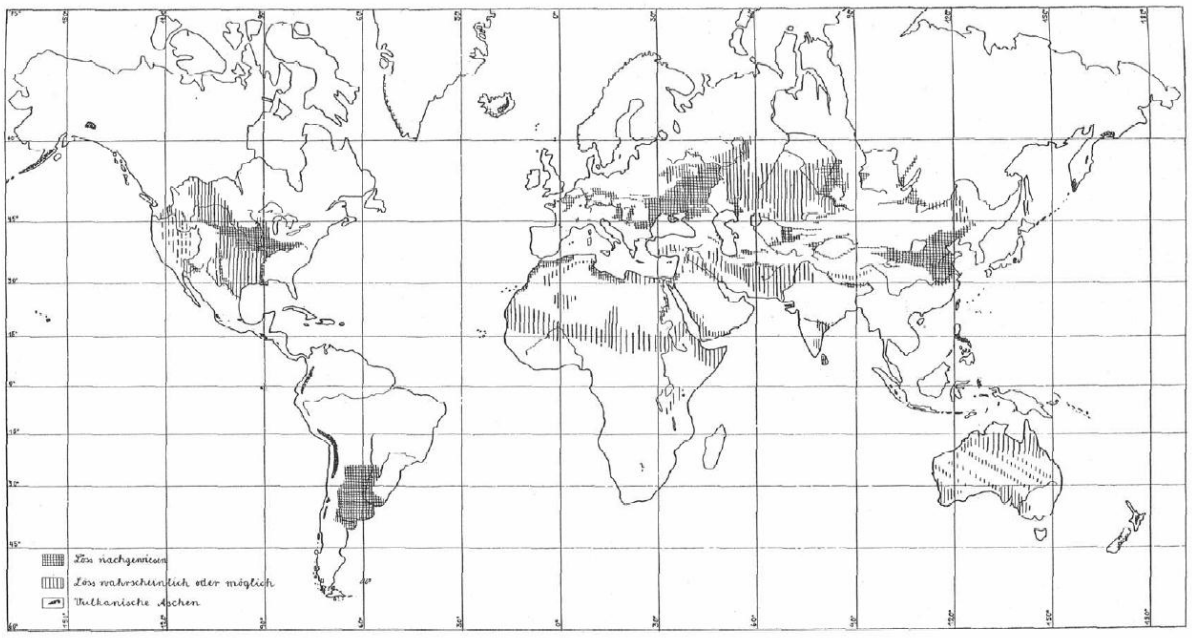

Abb. 5. Verbreitung des Lößes auf der Erde.

Fig. 2.1(a) Global distribution of loess soils after Scheidig 1934 (Der Loess und seine geotechnischen Eigenschaften), re-printed in Smalley and Jary (2005): Loess is devided into definite (nachgewiesen) deposits and possible/probable (wahrscheinlich oder moglich) deposits. This map became and remained the standard map of loess distribution (Smalley, 2013).

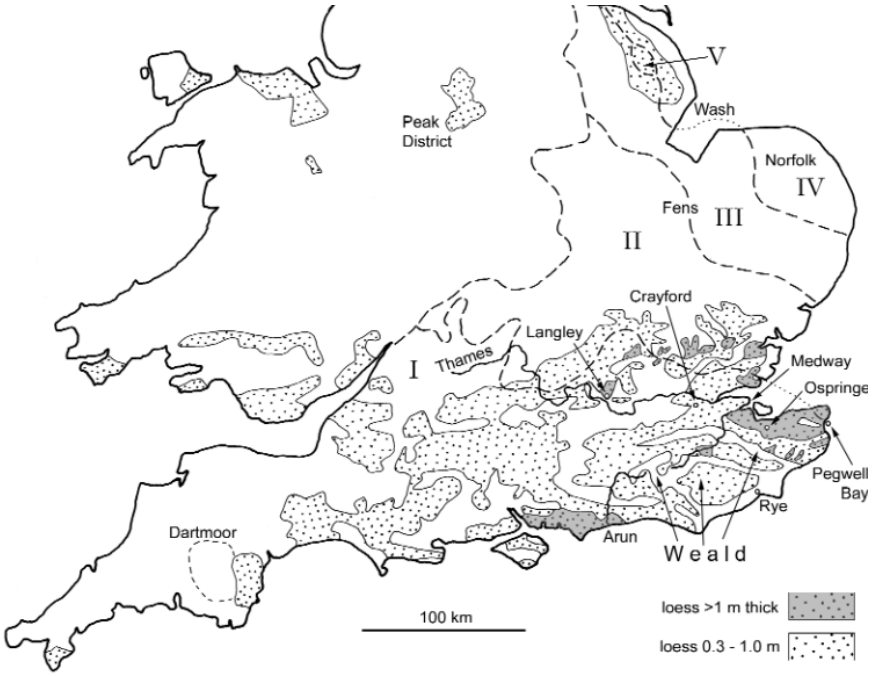

Fig. 2.1(b) The distribution of loess across midland and southern England: originally reported in Catt (1988) and Perrin et al (1974); zones I and V have mainly loess, zone III has mainly cover sand, while zones II and V contain both loess and the cover sand.

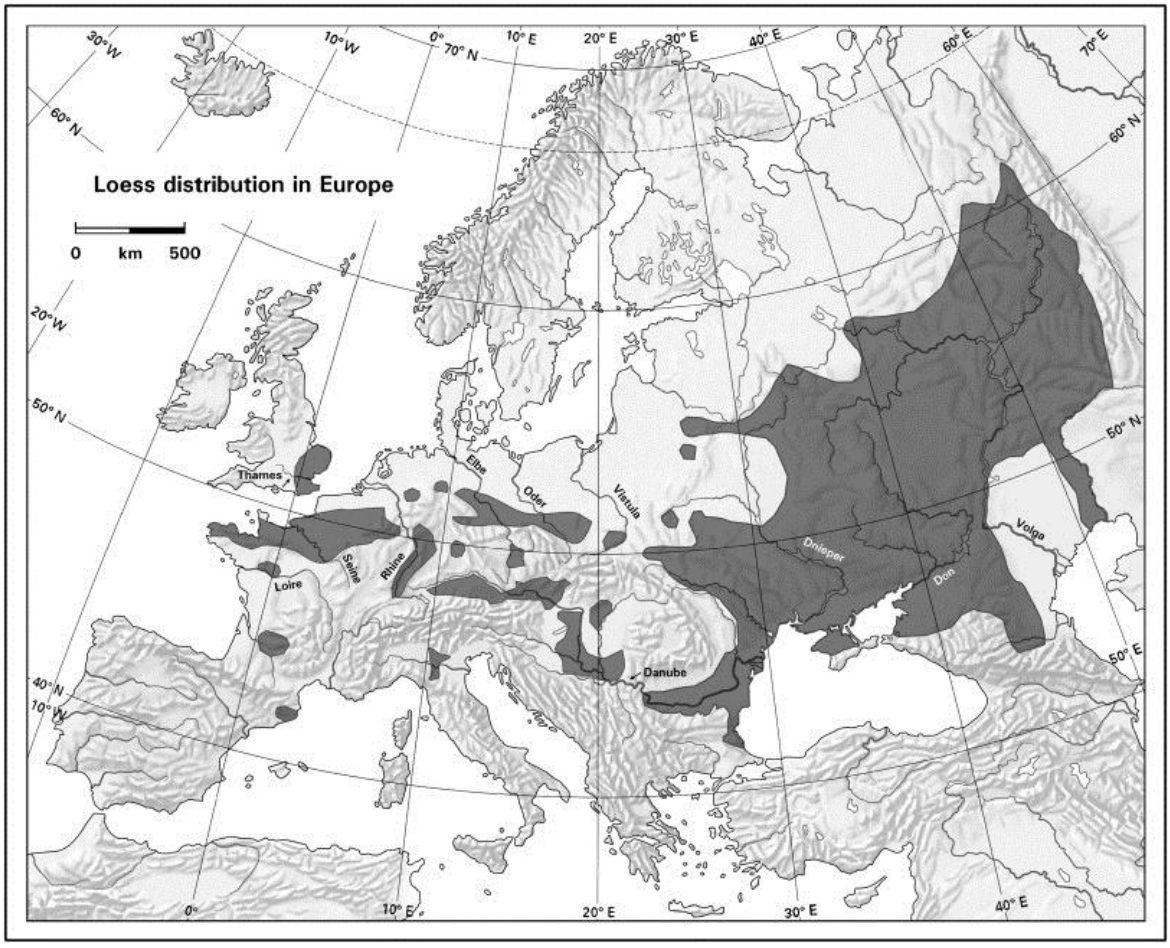

Fig. 2.1 (c) The distribution of loess across northern and western Europe (Smalley et al. 2009)

Brickearth occurs predominately as patches of >4 m thick in the South-East England (Boardman et al., 2001), patchily distributes over southern and midland England (Jefferson et al., 2003), eastern counties (e.g. Suffolk, Norfolk, Lincolnshire), West and South-West England (Catt, 1978). Fig. 2.1 shows the global distribution of loess soil. A detailed account on the distribution of brickearth in England is addressed in Appendix A1-A3.

2.2.3 Formation

The formation of loess represents a complex cycle within the sedimentary system, termed 'Loess cycle' (Smith et al., 2002).

2.2.3.1 Provenance Events

Loess for which silt is the main constituent is formed through cycles of Quaternary geologic (e.g. crystallization of magma), geomorphic (e.g.

solifluction or cryoturbation) and climatic (e.g. thermal or chemical weathering) processes (Smalley et al., 2006 b). Silt itself is formed mainly through reduction in quartz size. Jefferson et al. (1997) discussed a set of natural geochemical controls in quartz-bearing igneous and metamorphic rocks that assist with the formation of silts. These controls commenced with an initial transformation of 'high quartz (β-quartz)' into the more densely packed 'low quartz (α-quartz or ordinary quartz)' upon cooling to the hydrothermal temperatures in a granitic system. β-quartz forms after slow crystallization of siliceous (SiO_2-rich) magma. Sorby (1858) made a detailed study of quartz origin, and implicated the liquid inclusions in quartz to a history of slow crystallization of siliceous magma of granite at low heat (i.e. below 573 ˚C) but under great pressure. The quartz product is, in fact, a part of a coarse eutectic mixture of quartz and feldspar (Smalley, 1966). The eutectic reaction, which delivers two new phases from one original phase, leaves its footprints as is shown later herein (see Fig. 4.4 in Chapter 4). Magmas lose temperature to a degree below 573°C. Further temperature decrease allows the structure of high quartz to distort; such that 6-fold and 3-fold screw axes (60° and 120° inclination) change into 3-fold screw axes (60° inclination). Oxygen-Silicon bonds kink and bend, which provides a more densely packed assemblage. The transformation from 'high quartz' to 'low quartz' is displacive (i.e. no bond breakage occurs) but the angle between oxygen bonds' change. This causes contraction in the crystal. Contraction induces tensile stresses, normal to the c-axis (about which quartz contracts). These stresses fracture the crystal or induce a defect plane along the c-axis (Smalley, 1966). The defects lead to crushing, delivering 600 μm modal particles into the sedimentary system. There has been much emphasis, within a suite of sedimentological and geochemical works, on identification of the control of such defects on the quartz size reduction upon erosion and transportation. These works essentially examined the 600 μm to 10-20 μm quartz size reduction path in peridesert, perimountain, and perglacial environments (Smith et al., 2002). Peridesert silt is generated from chemical and salt weathering (Pye, 1995), temperature fluctuations (Smalley et al., 2001) and seasonal wetting/drying and heating/cooling (Smith et al., 2002). Perimountain silt is generated from cold weathering (Zourmpakis et al., 2003) and frost

shattering (Wright et al., 1998). Periglacial silt is produced from glacial grinding (Smalley et al., 2005) of granitic (or other rocks such as shale) beds (Sorby, 1858) of glaciers. Less appreciated disintegrating processes include: sub-aerial and fluvial transport actions (Smalley et al., 2006 a), loessification (i.e. in-situ dry weathering on carbonate rich parent material that originally was deposited as alluvium on flood plains during the Pleistocene – see Russell (1944) and Pecsi (1990)) and dry climate weathering (Assallay et al., 1996), desertification (Qiang et al., 2010), and volcanic actions (Pouclet et al., 1999). However, glacial grinding is widely accepted as the main source of present-day silt (Smalley et al., 2006 a).

Quartz size reduction is here explained further quantitatively, to show the discrete pattern of such natural erosion-transportation events. Blatt (1967) and Blatt (1970) averaged the diameter of quartz from disintegrated crystalline rocks in southern California and Arizona as of 600 to 670 µm (i.e. 720 µm for quartz in Gneisses and massive plutonic rocks and 440 µm for quartz in Schist). According to Blatt (1970), this 600 to 700 µm quartz was further crushed by 90%, bringing quartz of a pronounced mode (modal) size of 60 µm to the sedimentary environment. The role of quartz internal features in this 90% size reduction was later examined via a suite of abrasion experiments by Krinsley and Smalley (1973) and Moss and Green (1976). Similar abrasion experiments suggested that the 60 µm silt was further crushed into a pronounced mode size of 20 to 60 µm (Kumar et al., 2006) and then to 20 to 30 µm (Jefferson et al., 1997b). Such breakdown process suggested the existence of a control, which enables the quartz size reduction under moderate natural stresses (Jefferson et al., 1997a).

The mechanisms of quartz size reduction have been explained in a fractal framework (Mandelbrot, 1983, Hyslip and Vallejo, 1997). The use of fractal concept allows the simultaneous quantification of fragmentation and particle size distribution (Hyslip and Vallejo, 1997). Fragmentation (i.e. quartz size reduction) is a scale invariant natural process (Smalley et al., 2005), which is conventionally quantified by means of fractal concept (Turcotte, 1986). Fractal is basically a power law relation between number (particle population by mass) and size (particle diameter). Central to the fractal concept is the

fractal dimension, which is a measure of the fracture resistance properties of dispersed systems (Brown et al., 1996), such as crystalline defected quartz.

Lu et al. (2003) used the particle size distribution data to characterise the fractal properties of Leighton Buzzard Sand. They assumed a uniform shape of particles, which is arguable in loess soils according to Rogers and Smalley (1993) and Howarth (2010). They then used the Schuhmann's distribution (Fuerstenau, 2003) accompanied with Turcotte (1986) relation (between the fractal dimension and distribution index) and successfully described the fragmentation events. Fractal dimension however should be derived separately for clay and quartz minerals (Wang et al., 2008), due to the different origin of primary and clay minerals (Posadas et al., 2001). This however does not apply to the clean crushed Leighton Buzzard Sand, as this material contains no mineralogical gradient among its size scales.

2.2.3.2 Depositional Events

Dust deflates from outwash plains (Delage et al., 2006) and degraded lands (Qiang et al., 2010) with clay-constituent as low as 10% by-mass (Pye, 1995). Fine dust (sub-20μm) then travels by aeolian action over long distances to a suitable accumulation site. Examples of such dusts are the sub 3μm silts of Southern Nigeria (Smith et al., 2002), fine silts in Tajikistan (Karimi et al., 2009), silts which travelled from the margins of Weichselian glaciers to sites in East Yorkshire, East Lincolnshire, North Norfolk and Devon of Hampshire England (Lill and Smalley, 1978). Defilation triggered over periods of semi-aridity to aridity at a threshold mean wind velocity. Dust clouds are then carried with wind and deposited over water bodies, moist grounds, or vegetated surfaces, or upon a reduction in wind speed (Pye, 1987). Although the aeolian depositional rates are 2 to 20 times higher during glacial periods than that in interglacial periods (Qiang et al., 2010), soil erosion by wind and dust deposition is a continuous source of current-day silt. Favourable Mediterranean arid and windy climates through the coming decades encourage the on-going production of the modern silt (Costantini et al., 2009).

For South West, South, and South East England, Appendix A1-A3 fully describes quaternary processes involved in the production of current day loess. These are demonstrated in the framework of provenance-transportation-deposition (PTD) system for Thames and Southampton catchments.

2.2.3.3 Post-depositional Events

Geological events such as solifluction (Derbyshire and Mellors, 1988) and cryoturbation (Milodowski et al., In Press), ecological changes (e.g. erosion of Rhizolithic calcretes and formation of patchily distributed Calcium Carbonates), and seasonal wetting-drying cycles have a significant control on the degree of collapsibility (see Table 2.1 for some common natural bond formation mechanisms).

Table 2.1 Post-depositional events and formation of bonding agents

Bond Type	Post-depositional Events		In
Water-film	Retreatment of menisci upon drying Wet deposition of dust		Derbyshire and Mellors (1988) & Pye (1995)
Carbonates	Wetzel procedure		Fukue et al. (1999)
	Dissolution and re-precipitation	Rhizolithic calcretes Pedogenic carbonates	Milodowsky et al (In Press)& Asghari (2002)
	Bio-mineralisation (Calcite Carbonates)		Fukue et al. (1999) & Fukue et al. (2003)
	Bio-mineralisation (Argonite Carbonates)	Photosynthesi-s of Algae Bacterially-Induced via Ureolysis	Dipova and Doyuran (2006) & Chou et al. (2008)
	Weathering and deposition	Authigenic Calcites	Asghari (2002)
	Glacial uplift		Deynoux et al. (1994)
	Simple precipitation		IRCOLD (1999)
Clays	Migration to grains' contacts via suction		Boardman et al. (2001)
	Temperate weathering		Sivapullaiah and Manju (2006a)
	Chemical interaction	Kaolinization	Blyth and de Freitas (2006)
	Chemical interaction	Zeolitisation	Chandrasekhar et al.(1997)
	Precipitation	Dry Wet	Zourmpakis et al.(2003) Smalley et al.(2006 b)
Iron /Manganese oxides	Authigenic (dissolution - precipitation)		Fukue et al.(2003), Hue (1995)
	Bio-mineralisation (oxidation-reduction)		
Direct bonds	Cold welding		Grabowska-Olszewska (1989)
	Overgrowth of quartz		

For instance, following the post-depositional events occurred in the South East England (Smith et al., 2002), the upper non-calcareous strata exhibits negligible collapse; whilst the underlying calcareous low plasticity strata appears to be by far more collapsible. Examples can be made of the 6.3%, 16.9% and 9.4% coefficient of collapsibility for calcareous layer in Pegwell Bay, Sittingborne, and Starlane, respectively (Dibben, 1998). The varied mechanical response in different brickearth profiles signifies the contribution of post-depositional process. These are conventionally studied in the literature in the framework of loess cycle (Smith et al., 2002), or the multi-phase depositional PTD system (Jefferson et al., 2003).

A handful of factors control the collapsibility of loess deposits: Freezing and ice growth develops the abundance of pore spaces, aggregation of clays and therefore collapsibility. Thawing results in dispersion and alluvial migration of fines in depths and formation of loose clay bridges (Milodowski et al., In Press). Depending on the particle size and stress levels, wetting may either result in flocculation, softening and destruction of metastable fabrics, or leaching and decalcification. Drying may develop a negative pore water pressure, which draws clay fragments into the grains' contacts. Drying may also contribute in the precipitation of carbonates (Boardman et al., 2001, Milodowski et al., In Press), which increases the collapsibility. Solifluction is responsible for the formation of reworked loess. Solifluction may disrupt clay buttresses and cryogenic fabrics (Derbyshire and Mellors, 1988) and form more stable structures (Pye, 1995). Ecological changes may decrease the collapsibility by formation of nodular calcretes after erosion of roots (Joseph and Thrivikramaji, 2005, Milodowski et al., In Press), bio-mineralization (Lowenstam and Weiner, 1989), algae photosynthesis (Dipova and Doyuran, 2006), and bacterial Ureolysis (Chou et al., 2008). Collapsibility however may slightly increase through sulphate uptake by vegetation in wetlands. Temperature gradients may also slightly increase the collapsibility through chemical weathering and silica impregnation (Krauskope, 1956). Contamination slightly alters the collapsibility through oxidation-reduction (Fukue et al., 2003), protonation-deprotonation, and zeolition. In section 4.3 (Chapter 4), the contribution of hydraulic and stress factors is further investigated, since these accounts for most common conditions that occur

during fill service life. Major contributions in the quantitative interaction between stress and packing state are reported in some recent works (Nolan and Kavanagh, 1992, Miller, 2002). However, these are limited to clayey silt loess soils (e.g. significance of clay flake association in Mitchell (1976) and Mitchell and Soga (2005)), since few published works, if any, considers the contribution of carbonates. Suction-packing interaction also received much attention in literature within the framework of microfabric-associated effective stress models. Early attempts concerned the simplified single porosity concepts. Works of Terzaghi (1936) on a single fluid, Bishop (1959) on two immiscible fluids, and Matyas and Rahakrishna (1968) on two miscible fluids fall into this category. More recent works concern the double porosity concept, highlighting the interaction of collapse, microfabric, effective stress and suction (Khalili et al., 2005, Bagherieh et al., 2009, Alonso et al., 2010). However, the theoretical theme of these works lacks physical evidence for the multi-porosity features of loess. A better understanding of the interactions among micro-fabric, suction, and effective stress in loess allows one to estimate the air volume and hence the residual void space for further collapse. Such interaction is a factor of loess composition.

2.2.4 Loess Properties

Loess study, as in this work, requires a great deal of laboratory-scale reproduction of loess under controlled circumstances. This urges the need for a good understanding of loess composition and properties. This section briefly reviews such properties.

2.2.4.1 Physical and Mechanical Properties

Loess is a highly sensitive (Feda, 1966), slightly to highly plastic soil (Klukanova and Frankovska, 1995, Dibben, 1998, Al-Rawas, 2000, Miller, 2002), which falls into the range of 2.57 to 2.79 in specific gravity (Derbyshire and Mellors, 1988, Fall, 2003, Nouaouria et al., 2008), 1.61 to 0.53 in void ratio (Klukanova and Frankovska, 1995, Dibben, 1998, Miller, 2002), 1150 to 1750 Kg/m^3 in dry density (Assallay, 1998), 16 to 20 kN/m^2 in ultimate undrained cohesion, 17 to 25 kN/m^2 in residual undrained cohesion, 27° to 34° in peak drained internal friction angle, and 28° to 35° in residual drained internal friction angle (Fall, 2003), particularly in South England.

2.2.4.2 Chemical and Mineralogical Properties

Loess (Osipov and Sokolov, 1995) comprise a spectrum of primary minerals including quartz and more rarely feldspar (Klukanova and Frankovska, 1995), mica (including muscovite, biotite and illite), pyroxenes and hornblende (Assallay, 1998), gypsum (Osipov and Sokolov, 1995), primary detrital carbonates including chalk, foraminifera, and fragments in a micritic calcite matrix, plagioclase, and calcite (Milodowski et al., In Press), detrital dolomite, and volcanic glass shards (Pye, 1995). Bonding elements in loess include illite, montmorillonite, iron and manganese hydroxides, dispersed quartz, and calcite (Klukanova and Frankovska, 1995), hydro-mica, mixed-layered clays, kaolinite, chloride (Osipov and Sokolov, 1995), hematite, amphibole, rutile, halite (Feda, 1988), vermiculite, mixed layer illite-vermiculite (Mellors, 1995), mica, mixed-layer illite-smectite and pure smectite (Dibben, 1998). With the UK loess, a brief description of the geochemical and mineralogical account is given in Appendix A2.

2.2.5 Loess Components

2.2.5.1 Silt

Formation

Silt, as fully discussed in Section 2.2.3.1, is essentially a product of mechanical continuous size reduction in nature. However, not all quartz clasts split to finer grains, the reason of which has been the subject of much research: The significance of internal weakness in quartz was first scientifically described by Moss (1966). In line with earlier research work of Wright and Larsen (1909), Moss (1966) classified the quartz into mature (intact) and defected types. Mature quartz has a background of less post-solidification modifications and fracturing-healing cycles, contains more non-undulatory extinction features and is less structurally damaged. This background grants mature quartz a considerable resistance to weathering, high durability and hardness. With non-intact quartz, cracks form along the projected lines of internal defected planes, such as unopened healed fractures.

For non-intact type of quartz, Moss, in 1973, showed the contribution of transient loads in grain breakage. He emphasised that the magnitude of applying static load might not be high enough to trigger the breakage. The transient load of the same magnitude, however, could crush the grain. He differentiated the grain breakage under transient loading environments by using the 'fatigue fracturing' term. This can also be found in an earlier work, in which Moss (1966) showed that controlled-rate cyclic loads of low order can crush the granitic quartz, while static loads of the same value may fail to break a similar grain. He then simulated a fluvial transport system by subjecting the granitic quartz to rotation in a steel drum containing water. Quartz was weakened in the long-term in transient loading environment (i.e. waves and streams), highlighting the fatigue weakening of quartz grains[2]. This agreed with the suggestion of Sharp and Gomez (1986) that grains break through both fatigue and surface fracturing. The fatigue effect was also addressed in Rabinowicz (1976), where certain textural features were linked with splitting events as stresses apply and release. The idea of silt production through fatigue fracturing in fluvial systems however was questioned in the work of Wright and Smith (1993). Small amounts of 2 to 20 µm silts were produced by water-quartz abrasion, whereby significant amounts of 20 to 60 µm grains were generated when rigid ceramic spheres were used in the rotating drum. Wright and Smith (1993) then concluded a higher significance of impact-induced fracturing than fatigue fracturing. In a different attempt, air-abrasion was simulated in Smith et al. (1991), by subjecting 350 to 500 µm -sized Pannonian sand to air jet stream for 1 to 128 hours, generating remarkable contents of 20 µm grains in the first hour. Microscopic observations showed strong edge grinding (source of 20 µm fines) and appearance of fresh micro-fractures on large grains during the first hour. A secondary pronounced mode appeared after 16 hours at 20 to 40 µm, which then changed into 60 µm. Similar results were reported in Wright et al. (1998). The stepwise size reduction was in a good agreement with the fatigue fracturing concept.

[2] A rotational stress field (i.e. quartz rotating in a water-filled drum) allows grains to gently collide together while travelling the drum's perimeter. This can increase the smoothness of asperities (i.e. edge chipping) and develop micro-cracks along the crystalline imperfection lines. For an internally defected grain to break under a low applied stress (i.e. not high enough to split the grain), application of stress in a prolonged rotational fashion can eventually lead to the breakage.

To further examine the controversy within the experimental studies on the effectiveness of aerial/fluvial abrasion in silt production, Jefferson et al. (1997) discussed the significance of quartz internal controls in air-abrasion processes. They compared two similar wind tunnel experiments on two different sands (intact quartz in Kuenen (1960) and granitic quartz in Whalley et al. (1982)). Little silt was generated by crushing the crystallographically perfect quartz. After subjecting 250 to 500 µm ground Brazilian vein quartz (to simulate an identical stress history for entire grains according to Wright and Smith (1993)) to rotation under varying axial loads, Wright (1995) reported no evidence of fresh micro-cracks in grains. She then questioned the predominant role of grain breakage in silt production at glaciers' clast-bedrock interfaces. She referred to findings of Bond (1952) and Rittinger (1867) that acknowledged a relatively higher energy required for fine sand-to-silt size reduction. This, however, was argued in (Jefferson et al., 1997a, Kumar et al., 2006). These works showed significant contents of produced silt, after grinding 1 to 2 mm Leighton Buzzard quartz sand into Bromhead Ring Shear apparatus. They also showed two early and late periods of breakage at which easily breakable flawed and crystalline defected hard particles crushed, respectively. Kumar et al. (2006) also examined the earlier work of Wright (1995) by repeating the same testing procedure on un-weathered vein quartz and marine Leighton Buzzard sand. They concluded that the small amount of silt from un-weathered vein quartz is due to the absence of crystalline internal defects, and not a factor of the initial grain size. The outputs of experiments reported in Jefferson et al. (1997) were re-produced in Assallay (1998). Grinding the same test material used in the work of Jefferson et al. (1997) with an end-runner mill, Assallay (1998) reported that sand-size fragments were crushed by 70% in size to 10 to 50 µm silts by the end of 2-hour grinding period.

Mechanical Response

Moss (1973) developed one of the earliest quartz breakage models. He charged an unconfined compression test machine with 1.19-1.41 mm Gibraltar Creek granite quartz. Moss (1973) then attributed the edge grinding to concentration of stresses at grains' asperity tips, which provides a greater chance for

grains to split. Generated fine fragments fill the void spaces and overflow thereafter around survived larger particles. He postulated a higher chance of breakage in coarse granitic quartz (in agreement with Sharp and Gomez (1986)), since these possess higher degrees of internal imperfections. Recently, McDowell and Bolton (2001) and Bolton (1999) employed 2D numerical simulations to study the micromechanics of crushable grains. Models were supported with the 'compression between parallel platens' experiments conducted on 1 to 3 mm in diameter Leighton Buzzard Sand in the Cambridge University 1992 PhD thesis of Lee. Results indicated a decreasing trend of tensile strength with increasing grain size. Bolton (1999) drew the attention particularly to the higher tendency of smaller particles to split (in contrast with the view in Moss (1973)), while correlating grain's resistance to contact constraint conditions, particle size, and level of applied internal stresses. Small grains get trapped between neighbouring larger grains and attain the maximum chance of splitting in presence of two point contacts. Relatively finer grains carry the same force over a smaller surface area (Santamarina, 2003, Mitchell and Soga, 2005) and therefore are subjected to higher levels of internal stresses. Coop and Altuhafi (2011) agreed with Bolton (1999), and emphasised that well sorted grains break more readily. This was ascribed to the increased number of grain contacts, which favours the edge grinding and fine crushing. To recap, there are clearly questions of the quartz size reduction – a question of breakability of sand and silt and a question of controls on the size and population of the silt output.

2.2.5.2 Clay (Supporting Element)

Wetted-collapse is likely to occur in soils containing 5% to 40% kaolinite clays. This is evident in the box plot produced from the broad literature review undertaken in Assallay (1998). The box plot (Fig. 2.2) also demonstrates the mead minimum and maximum clay content between which a soil is most vulnerable to collapse upon wetting (i.e. 11% to 24%). The greatest chance of collapse is reported at 8% to 15% clay content. The latter, however, is regardless of soil's packing state. Unlike the views discussed in (Assallay, 1998), with particular reference to the collapsible loess deposits across the central regions of North America, active clay minerals can also contribute in collapse (Russell, 1944, Handy, 1973, Lattman, 1973, Parsons et

al., 2009). Considering the work of Feda (1988), collapse may take place at stresses higher than the swelling pressure and at water contents less than a threshold. Fig. 2.3 shows the micro-morphological setting of clay in loess.

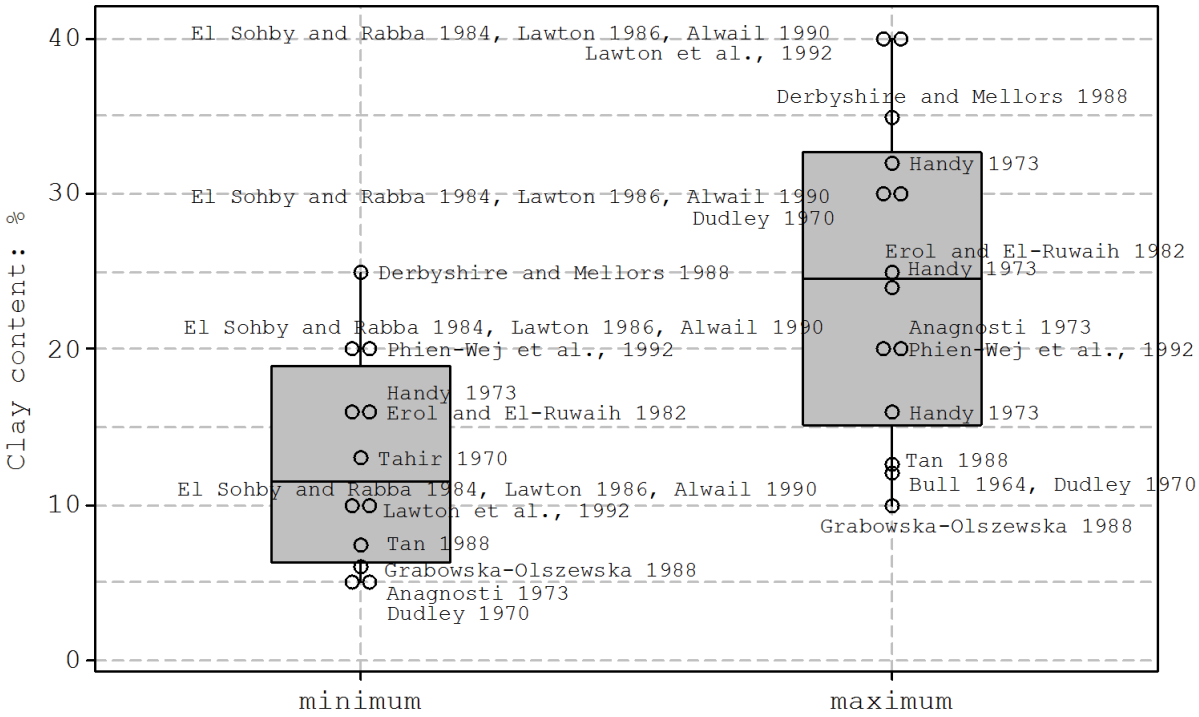

Fig. 2.2 (a) Correlation between the collapse potential and collapsing soil clay content (box plot presentation)

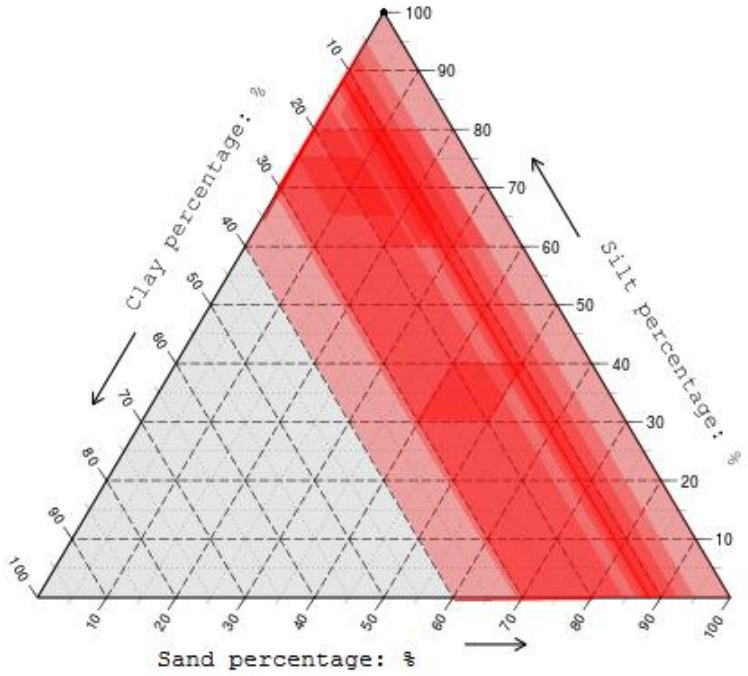

Fig. 2.2 (b) Correlation between the collapse potential and collapsing soil constituent proportions, according to some key research works on natural loess deposits as reported in Assallay 1998 (ternary diagram presentation: red colour indicates the intensity of collapsibility)

Fig. 2.3 Clay connectors under the ESEM microscope

(a) Bridge in UK loess from Kent, in Derbyshire and Mellors (1988)

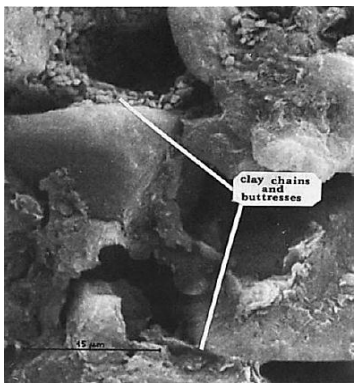

Fig. 2.3 (b)

Clay buttress in young polish loess in Grabowska-Olszweska (1989)

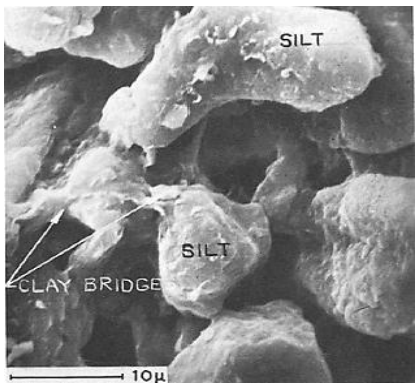

Fig. 2.3 (c)

Clay bridge in brickearth deposits, Ford, Kent, in (Barden et al., 1973)

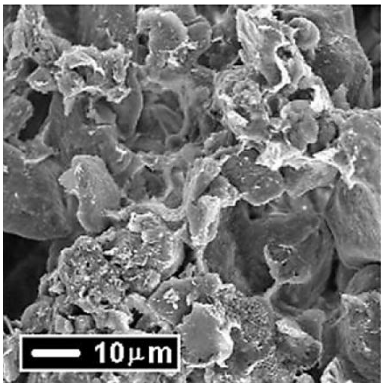

Fig. 2.3 (d) Loess at 140km North of Paris, in (Delage et al., 2006)

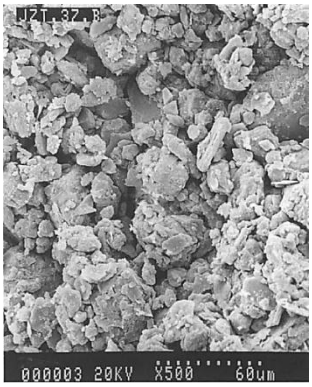

Fig. 2.3 (e) Lishi China, overgrowth of clay coats into bridge in (Dijkstra et al., 1994)

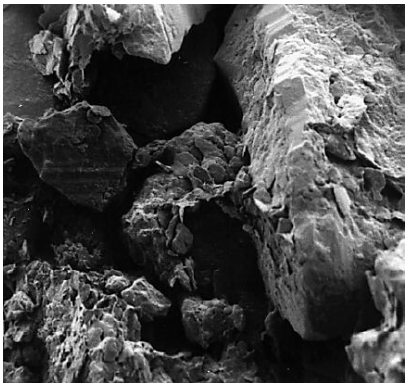

Fig. 2.3 (f) Allington UK, overgrowth of clay coats into bridges in (Bell et al., 2003)

2.2.5.3 Calcium Carbonate (Supporting Element)

Formation and Morphology

Carbonates appear in six major morphologies (Fig. 2.4). Scaffolding, encrusting, reinforcing, linings to rootlet holes, inter-particle meniscus and nodular cementing (Derbyshire and Mellors, 1988, Grabowska-Olszewska, 1989). Carbonate bonds can also emerge in combination with other types of non-clayey bonds, resulting in a change in plasticity and thus the resistance against polar fluids. For instance, free amorphous oxides (e.g. goethite, haematite and colloidal ferric oxides, aluminium and magnesium ions) reportedly imply stronger water resistivity, less compressibility, and higher liquid limits. Poly-mineral combinations may decrease the rate of solubility (Boardman et al. (2001).

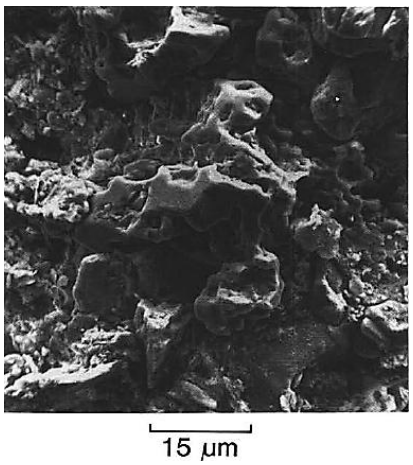

Fig. 2.4 Carbonate connectors under the ESEM microscope

(a) Authigenic[3] calcite, China in Derbyshire and Mellors (1988)

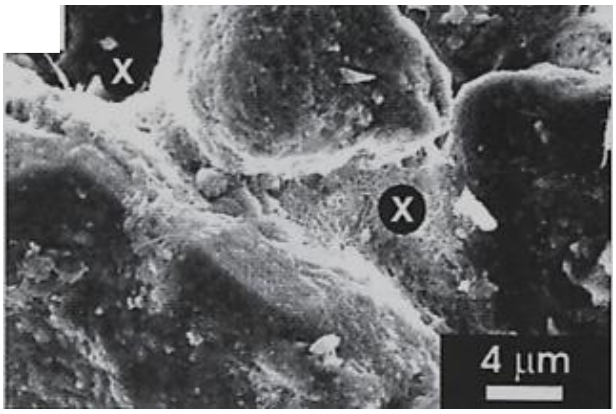

Fig. 2.4 (b) Fine needle calcites forming a meniscus film bridging between adjacent silt grains - Calcareous Brickearth, Ospringe, England, in Milodowski et al. (In Press)

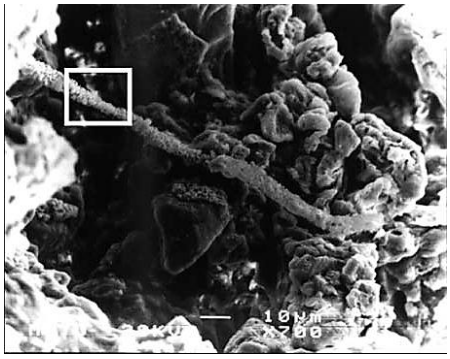

Fig. 2.4 (c) Biological Clacite tube in Tufa deposits of Antalya, Turkey, in Dipova and Doyuran (2006)

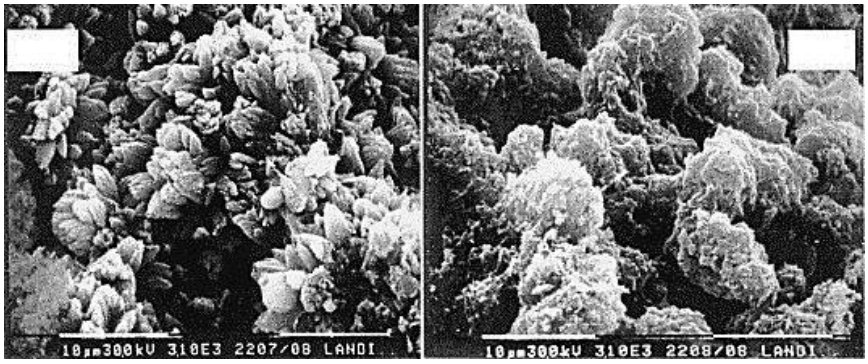

Fig. 2.4 (d) Pedogenic[4] Carbonates in Saskatchewan soils, Canada in Landi et al. (2003)

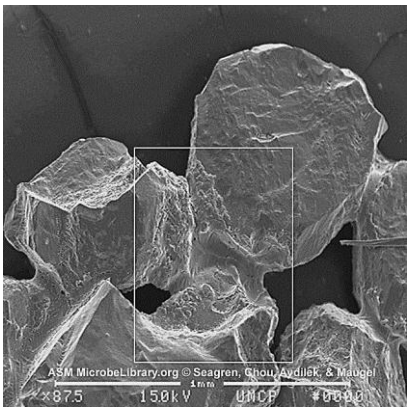

Fig. 2.4 (e) Sporosarcina pasteurii (formerly Bacillus pasteurii) induced Calcium Carbonate in Chou et al. (2008)

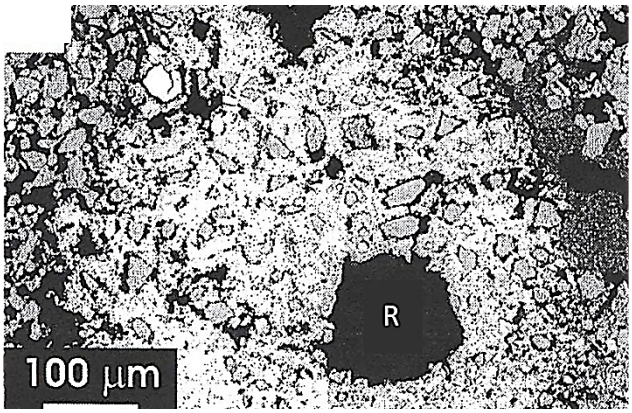

Fig. 2.4 (f) Meshwork of fine needle calcites sorrounding silt particles around an open root hair channel - Calcareous Brickearth, Ospringe, England (Milodowski et al., In Press)

[3] Authigenic Calcite: Calcium Carbonates, which precipitate in soil over, time (Lal et al., 2000).

[4] Pedogenic Carbonate: same as Authigenic (secondary) carbonates, which precipitate in soil over time (Lal et al., 2000).

Any of the carbonate formation mechanisms is associated with a particular crystal carbonate shape (e.g. needle shaped carbonates in Rhizolithic Calcrete of high Ca^{++} component in Fig. 2.4 (b) and 2.4 (f) and nodular shaped carbonates in secondary Authigenic calcites in Fig. 2.4 (a)). The shape of carbonate elements may affect their mechanical response to wetting. As such, seven common natural processes that supply Calcium Carbonate in soil together with the shape of carbonate cement produced by each of the processes are briefly discussed in this section.

Fukue et al.(1999) addressed the Wetzel (1989) process in which carbonate rich sediments at the bottom of oceans (originated from the accumulation of coccolith and foraminifer[5] remnants in deposited dusts from land) petrifies through self-weight consolidation (also see Grine and Glendinning (2007)).

Brown (2008) put forward the formation of Rhizolithic Calcretes[6] via a dissolution and precipitation process. Rhizoliths are 'organo-sedimentary' structures formed in plant roots (Write, 1994), exhibiting features of arid/semi-arid (Goudie, 1983), to sub-humid (Milodowski et al., In Press) climates. Combination of water and humic acids[7] form light calcrete sheaths around the living roots, and promotes the precipitation of calcites between the surrounding soil particles. Calcrete thickens after the decay of the root and fills the hollow space (Brown, 2008).

The dissolution of lithogenic carbonates[8] with carbon di-oxide (originated from root and rhizo-microbial respiration within the soil-air) liberates calcium cations. Subsequent re-crystallization forms pedogenic (i.e. secondary) carbonates (Gocke et al., 2010a, Gocke et al., 2010b). Loess in Germany (Gocke et al., 2010a), and the southern United States and the Russian steppe (Gocke

---

[5] Coccolith and Foraminifera: Marine microorganisms with $CaCO_3$ shell. Foraminifera are sub-1mm in size, while Coccolith appear in a diameter of up to 20 mm. Carbonates tend to attract and cement soil particles (condensation effect). When seabed upheaves, the resulting calcareous deposit appears. In particular, Coccoliths are the main constituent of chalk deposits such as the white cliffs of Dover (Braby, 2001).

[6] Rhizolithic Calcrete: Rhizoliths are tubular root systems formed through the interaction between Ca^{++} and HCO_3^- due to weathering, re-precipitation. Rhizoliths can form calcareous sediments of high Ca^{++} constituent.

[7] Humic acid: The principal organic constituent of soil, which forms by biodegradation of organic matters, such as decayed roots.

[8] Lithogenic Carbonate: Calcium Carbonate supplied by parent materials in soil. Also named detrital (Kraimer et al., 2005)

et al., 2010b) contain pedogenic carbonates. Sfriso et al.(2008) suggested eight stages for diagenesis of pedogenic carbonate bonds in loess: wind-blown silt deposition under calm water, deposition of amorphous silica and volcanic ash in heterogeneous concentrations, sea-level reduction and consolidation, droughts and desiccation forming heavily over-consolidated deposits, precipitation of carbonates and magnesium oxides during drying process, development of fissures in arid climate, and accumulation of calcium carbonate precipitates in fissures after rain-water infiltration.

Calcites may form via bio-mineralization through dissolution of Coccolith, Foraminifera, and Arthropoda organisms (condensation effect). The subsequent re-precipitation of soluble limestone forms secondary carbonate nodules and carbonate rich tuff layers (Fukue et al., 1999, Fukue et al., 2003). Grabowska-Olszewska (1989) and Assadi and Yasrobi (2010) showed electron microscopy images of calcite nodules in Poland and Iran, respectively.

Calcites may form via a biogenic re-precipitation. Crystals are formed as single fibres hanging off algae, following the daylight photosynthesis of algae and the net removal or partial pressure decrease of carbon di-oxide of water. This results in sparry calcite[9] and thin meniscus cements at the soil grain contacts (Dipova and Doyuran, 2006).

Chou et al. (2008) described the bacterially-induced Calcium Carbonate (and bicarbonate) bonds in sand. Precipitation takes place in a favourable alkaline environment, induced by Sporosarcina Pasteurii bacteria after releasing inorganic carbon and ammonium. Homogeneous and heterogeneous nucleation takes place in the absence and existence of calcium ions, respectively.

Acidic environments (after interaction of carbon di-oxide and water) allow the weathering of Plagioclase, Hornblende and Augite minerals. Calcium cations liberate, which then leads to the formation of authigenic calcites (Derbyshire and Mellors, 1988).

[9] Sparry Calcite: spar is non-metallic, readily cleavable, transparent light-coloured mineral such as feldspar

Abundance and Mechanical Response

There has been much controversy in the literature on the effectiveness of non-clayey bonds and in particular, Calcium Carbonate. Osipov and Sokolov (1995) referred to carbonates and calcites as medium and low soluble salts, respectively. They estimated a time course of several hours to several months for dissolution of low soluble salt bonds. This conforms to the work of Mansour et al.(2008), who suggested a descending trend of solubility from Calcium Chloride to Sodium Chloride, Sodium Carbonate, Sodium Sulphate, and Calcium Carbonate (also see Ouhadi and Goudarzi (2007)). The idea however has been challenged by many including Assallay (1998) and Zourmpakis et al.(2005). They hypothesised the predominant contribution of clay bonds in collapse. With particular reference to loess, Mellors (1995) in a study on Pegwell Bay Brickearth, questioned the effect of Calcium Carbonate bonds. In contrast, in Milodowski et al.(In Press), the role of calcites in enhancing the structural stiffness in Pegwell Bay was emphasised. Calcium Carbonate content is key to its contribution in collapse behaviour. This has been widely studied for: (1) specific soil types, and (2) specific geographical regions. With the first theme, Penck (1931) reported a range of 0% to 40% as for loess carbonate constituent. Grabowska-Olszewska (1988) narrowed down the range to 6% to 12% in un-weathered silty loess with random texture, 0% to 1% in weathered silty loam loess with random texture, 5% to 18% in un-weathered loess with banded-random texture and 4% to 6% in weathered loess with banded-random texture. Within the second theme, for British loess, Lill (1976) reported a very weak to moderate accumulation of calcites in Pegwell Bay Brickearth, South East England. Such calcareous loess soils are also reported in Funton, Cherry Orchard Lane, Star Lane and Allington (at a mean depth of 1.5 m), and also in South East Hampshire, Halling and Pegwell Bay, south of River Roach except Eastwood centred at the Great Wakering, south east Stambridge to River Roach, Ospringe, and South Essex. Calcareous layers are generally agreed to have greater tendency to collapse (Northmore et al., 2008). To the east, collapsible calcareous loess is reported in Poland in Grabowska-Olszewska (1988). Trofimov (1990) reported 7 to 8% carbonate content and about 10% water-soluble salt content in Atel loess of the Lower Volga region in Russia. Further to the east, 9 to 15% Calcium Carbonate was reported in Lanzhou loess,

either as silt-size crystals or secondary coats (Meng, 1998). Derbyshire et al.(2000) reported pore linings, encrustations, concretions, and inter-granular cements of Calcium Carbonates in Chinese loess.

There has been much controversy in literature on the contribution of carbonates in collapsibility. Calcites may dissolve in water over a short time from several hours to months. Calcium carbonate dissolves quicker than calcites, but slower than Sodium Carbonate, Sulphates, and Chlorides (Ouhadi and Goudarzi (2007) and Mansour et al. (2008)). Despite the proven records of Calcium Carbonate solubility, carbonates' marked role in collapsibility was subjectively challenged by many including Assallay (1998) and Zournpakis et al. (2005). In a study on Pegwell-Bay Brickearth, Mellors (1995) suggested a little contribution of carbonates in the collapse risk. Same deposit was systematically observed under scanning electron microscope recently by Milodowski et al. (in press), showing a suite of carbonate inter-particle connectors which can potentially induce collapsibility. Reading the literature suggests the possible control of carbonate content on collapsibility. Penck (1931) reported a range of 0% to 40% as for loess carbonate constitute. Grabowska-Olszewska (1988) narrowed down the range to 6% to 12% in un-weathered silty loess with random texture, 0% to 1% in weathered silty loam loess with random texture, 5% to 18% in un-weathered loess with banded-random texture and 4% to 6% in weathered loess with banded-random texture.

2.2.5.4 Amorphous Silica (Supporting Element)

Formation and Morphology

The shape of amorphous silica in soil was firstly discussed in the work of (Krinsley and Doornkamp, 1973). They showed microscopic images of quartz grains covered with smooth onionskin silica and ascribed it to a quick precipitation history. They then showed images of upturned plates on the surface of quartz grains and bridge connector units; and attributed them to a more moderate rate of precipitation background (also in Grabowska-Olszewska (1989) – and Fig. 2.5).

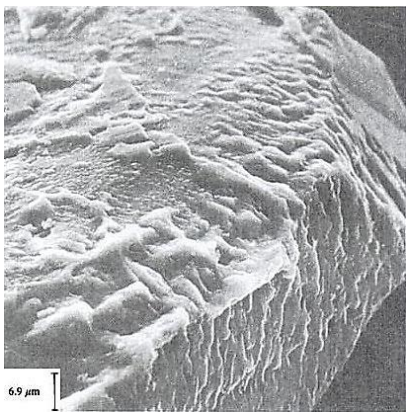

Fig. 2.5 Amorphous silica under the ESEM microscope
Silica precipitates in Glen Rosa granite, Isle of Arran, Scotland in Krinsley and Doornkamp (1973)

Fig. 2.5
Smooth precipitated silica in palaeosol[10], Lanzhou, China in Derbyshire and Mellors (1988)

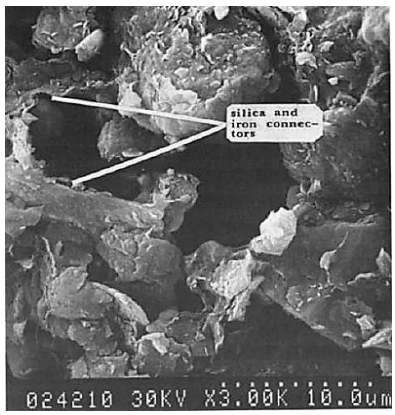

Fig. 2.5
Precipitated silica (upturned flake) in Grabowska-Olszewska (1989)

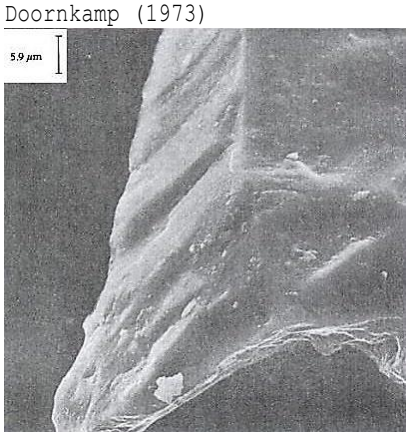

Fig. 2.5
Precipitated silica on the edge of a quartz grain in Krinsley and Doornkamp (1973)

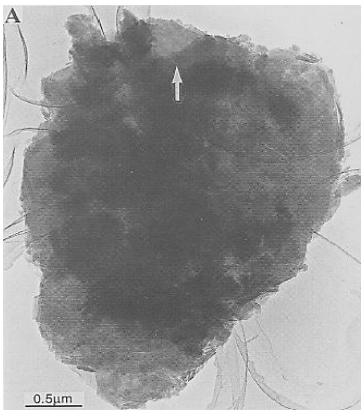

Fig. 2.5
Amorphous silica adhering the surface of kaolinite crustal in Singh and Gilkes (1993)

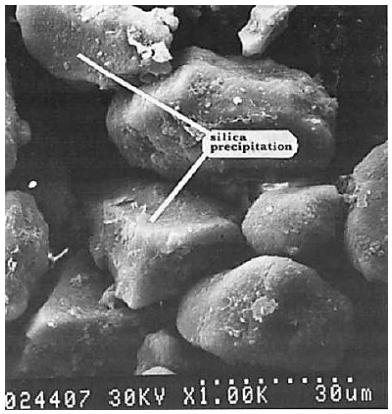

Fig. 2.5
Smooth precipitated silica in Grabowska-Olszewska (1989)

However, the significance of the precipitation regime had been investigated about 20 years earlier, in the 1955 work of Iler (see Krauskope (1956)). Iler showed that anhydrous SiO_2 (silica) deposits on a solid surface in 'a continuous dense layer', under a slow evaporation condition. For higher rates of evaporation, silica probably polymerizes in the soil solution and thus deposits as a hydrated gel. The disagreement between the 1950s and 1980s works is examined in the present work (Chapter 5), where it will be shown that silica, in the absence of clay and carbonates, crystallizes in form of coagulated structures (i.e. 'hydrated' units). At lower temperatures however, evaporation is shown to form continuous smooth coats of silica (i.e. 'anhydrous' units). Findings were consistent with the work of Iler (1955). The

[10] Palaeosol: former soil preserved by the upper loess layer. Palaeosol can have no sign of the present day chemical signatures.

quick precipitation may occur in presence of ferric oxides as discussed in Krauskope (1956) or simply at elevated temperatures.

Other less-occurring forms of silica precipitates are also reported, for which examples can be made of chemically weathered induced silica globules, silica flower, and silica pellicle (Fig. 2.6 - see Madhavaraju et al.(2009)).

According to Pye (1987), the origin of amorphous silica is chemical and thermal weathering through a dissolution re-precipitation process.

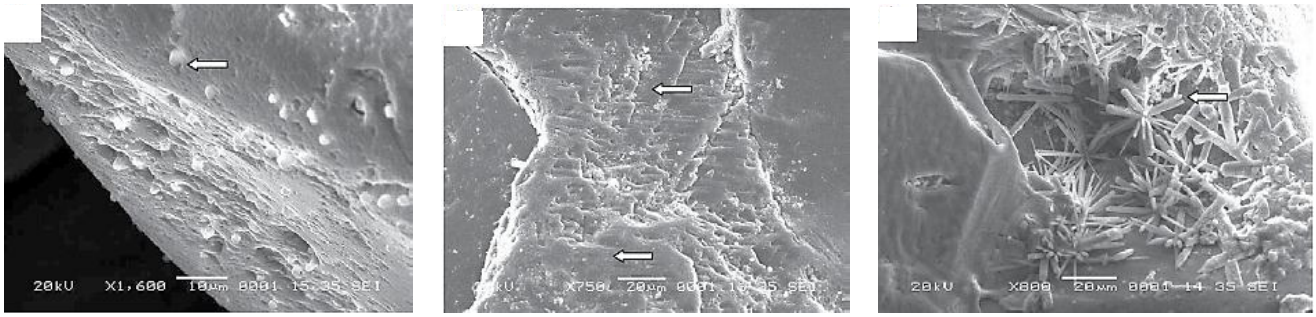

Fig. 2.6 (left to right) Silica globule, silica pellicle, silica flower

Abundance and Mechanical Response

Despite the significance of the research on amorphorous silica, its control on the mechanical properties of loess has been less well investigated (e.g. in Grabowska-Olszewska (1989)). This is due to a perception that silica has a minor control on the collapse process; However, whether to choose silicatization (Askalonov, 1949) to stabilize loess or not requires a better insight into the interaction of amorphous silica with other soil components.

Amorphous silica can act as an inter-particle bonding agent in loess. From a geotechnical perspective, silica was used in the former Soviet Union to stabilize loess through silicatization and gaseous silicatization. Depending on the chemical composition of loess, amorphous silica was deemed capable to strengthen the loess via formation of CAH cements (Calcium Aluminate cements), polymerization (i.e. precipitation of silica), and sediment-air replacement at the void spaces (Askalonov (1949), Sokolovich (1965), Sokolovich and Gubkin (1970), Sokolovich and Ibragimov (1971) and Isaev et al. (1979)). From a geomorphological perspective, electron microscopy images of amorphous silica in loess were first presented in Derbyshire and Mellors (1988) for the Chinese

Lanzhou aged loess. A year later, the bonding role of silica was highlighted in Grabowska-Olszewska (1989) for weathered horizons of Polish Loess. She deemed the weathering and quartz dissolution responsible for formation of amorphous silica. The high critical pressure[11] and the soil's resistance to water was attributed to the role of the silica component. However, she ignored the effect of the approximate 20% by-mass authigenic Calcium Carbonate in the soil, and implied that the carbonates' nodular non-continuous micro-morphology does not allow the carbonates' contribution in the bonding mechanism. Since 1989, this short comment has never been viewed as a possible revolutionary finding. This will be shown in the present work that collapsibility tightly ties in with the micro-morphology of bonds, while the shape is a factor of the chemical elemental properties of the bond. The role of amorphous silica at the presence of metal-based oxides has also been the matter of discussion. The low degree of solubility of silica connectors may be due to the role of certain free oxides stacked to the amorphous silica agents forming poly-mineral bonds. Krauskope (1956) pointed to the role of aluminium and magnesium ions in decreasing the rate of solubility of amorphous silica due to formation of protective poly-mineral coats of either Aluminium or Magnesium Silicates.

Reading the literature on the amorphous silica offers a great opportunity for close study of the interaction between silica amorphous and rest of the loess components.

2.3 Loess Modelling: Our Understanding of the Problem

Trofimov (1990) ascribed the genesis of collapsibility to two subsequent loess formation stages. With dust accumulation, he referred the collapsibility as 'syngenetic'. With progressive lithogenesis, dissolution and re-precipitation process, he referred the collapsibility as 'epigenetic'. In other words, with free-fall clayey/salty silt deposition, pre-consolidation, and clay/salt-bond mobilization, collapsible loess of 'syngenetic' properties appear. With secondary carbonates' diagenesis, weathering, fine migration and meteoric cycles, collapsible loess of 'epigenetic' properties appear. The latter was appreciated as most of the present-day calcareous collapsible deposits.

[11] Threshold stress at which soil may collapse in the absence of water

2.3.1 Simulation of Naturally Occurring Quartz Silt

Jefferson et al. (1997) produced significant contents of silt by grinding batches of 1-2 mm Leighton Buzzard sand in a high-energy disc mill. To produce descent contents of 2-20 µm, 20-30 µm, 30-40 µm, 40-50 µm, 50-63 µm, and 63 µm to 0.2 mm grains, Jefferson and colleagues realized the need for grinding the sand for a maximum of 150, 150, 150, 120, 60, and 60 s, respectively. They also showed two early and late stages of crushing at which easily breakable flawed and crystalline defected hard particles broke, respectively.

Assallay (1998) showed that more than 70% of the crushed Leighton Buzzard sand falls in the silt range of 10-50 µm after 2 hours of grinding (using a range of high energy mills). Obtaining two grading patterns, the 'typical grading' encompassed less than 2% sub-2 µm, 62% sub-20 µm, 84% sub-30 µm, 90% sub-40 µm and nearly 100% sub-50 µm particles; whilst the 'coarse grading' included negligible clay-size grains, 15% sub-20 µm, 44% sub-30 µm, 85% sub-40 µm, and nearly 100% sub-50 µm particles.

2.3.2 Synthesis of Artificial Loess with Clayey Bonds

Mulilis et al. (1975) suggested the earliest technique for simulation of air-fall deposition. Clean uniform sub-rounded dry sand was allowed to fall freely into a test cylinder from a glass tube held at a constant height, while travelling the sample's cross section. They postulated a good reproducibility of bulk density, supplied by the technique. Density was controlled by the diameter of the glass tube or nozzle, height of free fall, and the rate at which the glass tube's end was moved. In a different attempt, Kolomitsev 1985 (in Trofimov (1990)) mixed 10-50 µm coarse silt and 50-100 µm fine sand with carbonates of 7.5% by-mass and added a further 10% by-mass of other soluble salts. The mixed material was then air-dried and pulverised by means of a rubber pestle, and simply poured into a standard 100 mm oedometer ring. To mobilize the bonds, Kolomitsev tried three methods:

(1) capillary rise from the lower drain,

(2) wetting from the upper drain,

(3) simultaneous water spray and deposition.

Samples were eventually air-dried at 18-20°C. A year later, Korolev and Eremina 1986 (in Assallay (1998)) suggested two alternative approaches: Laterally confined specimens were placed on top of small masses of wet sand as a moisture-holding medium. The assemblage was kept inside a desiccator for two weeks to air-dry the specimens. In the second attempt, hydration-dehydration cycles were simulated in a climate chamber. Specimens were kept inside a 'Feitron' climate chamber for one month during which 25 wetting-drying cycles took place. Wetting was simulated at the relative humidity of 99-100% and the temperature of 20°C, while drying was simulated at the relative humidity of 20-30%. A year later, Galai (1987) highlighted the significance of wind intensity in deposition quality (in Assallay (1998)). He sieved pulverized air-dried particles through a 0.5 mm mesh into an oedometer ring to imitate certain wind intensity. Galai then wetted the deposited dust (up to the Liquid Limit) by putting a moist filter paper on the upper surface. After four cycles of wetting-drying, specimens were air-dried to in-situ water content (value not reported). To simulate the field's natural stress state, specimens were loaded to 50 kPa pressure (roughly 2.5 m overburden). Shrinkage was restricted to the first cycle of wetting-drying, showing the early activation of bonds.

More recently, Dibben (1998) used controlled contents of crushed dry sand together with varying contents of kaolinite to synthesis loess at certain bulk densities. Dibben (1998) obtained a spectrum of voids' ratio ranging from 1.25 for the pure crushed sand to 1.03 at 40% clay content. She passed the disaggregated material through a 63 μm sieve at a vertical distance of 400 mm to the oedometer ring, incrementally. She gently tapped the surface of freshly deposited layers prior to any forthcoming deposition action. She used varied compaction effort to reach to target density in soils made up of different clay contents. A drawback to Dibben's method is the varied compaction effort for which the naturally occurring void ratio was disturbed. Due to the vertical heterogeneity of applied effort, 3 circumstances may appear:

(1) solids may exceed the ring's volume which then shall be compressed further to fit into the ring. This results in higher densities at upper layers,

(2) solids may naturally fit into the ring's volume,

(3) solids may not fill the ring's volume, indicating densely packed layers at the bottom and loosely packed layers at upper profile.

To mobilize the bonds, four methods were adopted:

(1) spraying distilled water over the surface of deposited layers,

(2) subjecting the specimen to the capillary water rise,

(3) combined capillary rise and fine spraying, and

(4) exposing the specimen to water vapour in a steam chamber.

Treated specimens were oven-dried and then subjected to a second round of steaming (also in Miller (2002)). Dibben, however, acknowledged the uncertainty over even moisture distribution.

Assallay (1998) generated artificial loess samples at controlled void ratio. Clean ground sand was mixed with clay through two different approaches. It was inferred that crumbling silt-clay slurry at liquid limit water content, followed by drying and sieving provides a more even distribution of clay, in comparison with simple dry-mixing. Varying masses of dry clay-silt materials were screened through 63 μm sieve into the standard 75 mm oedometer ring from the height of 200 mm. The early unstable structure (e=1.35) was then compressed to a metastable state (e=0.9) with a steel piston. To mobilize the bonds, fine water spraying, capillary water rise, treatment under controlled humid environment, and wetting by wrapped humid cloths methods were attempted.

Miller (2002) criticized the use of larger efforts for compaction of silts containing higher clay contents to imitate either a certain dry unit weight or void ratio. She wetted the dry-mixed clayey silt up to certain preparation water content and lightly compacted the wet paste into the standard 75 mm oedometer ring by a wooden pole. The samples were then subjected to a certain constant axial pressure mirroring a certain pre-consolidation pressure (5 kPa). Subsequent drying mobilized the clayey connectors. To reproduce the target initial water content, she then attained a steaming approach.

Zourmpakis et al. (2003) passed the oven-dried ground silica through a 63 μm sieve before mixing it with 5% to 25% kaolinite in a mechanical mixer at a low

rate for 60 minutes. The mixed material was then pulverised by a pestle for 20 minutes followed by the second phase of oven-drying lasting for 24 hours. Dry mixed material was then gently pluviated into a 120 mm ring at 1-2 mm height intervals. The surface of each layer was wetted by spraying water droplets. Samples were then oven-dried at 50°C for 48 hours in an attempt to imitate the arid climates. Using the 120 mm ring avoided post-drying side shrinkage induced defects in the 75 mm diameter core specimens. Specimens were subjected to 9 kPa axial pressure (stress history). This however may be argued as the consequent unsaturated-consolidation was supposed to be countered by backfilling, which could induce vertical heterogeneity. To avoid this heterogeneity, the oedometer ring should be placed inside a standard compacted mould resting on a layer of pluviated soil. The deposition-spraying sequences should be continued until the top surface of the ring was covered with a column of deposited soil. A piston should be used to statically compress the assembly in a CBR loading frame or an automated hydraulic jack, before extracting the embedded ring (see Assadi and Yasrobi (2007)).

Zourmpakis et al. (2003) introduced another approach which was claimed to provide a maximum number of clay bonds. They postulated this relatively best performance for identical specimens of similar stress history. They also suggested that higher values of void ratio were generated through fine spraying than capillary rise and steaming methods. This is due to the absorption of water packets by freshly deposited dust from the wet layers beneath. Clay bonds were deemed capable to support the metastable structure even in the absence of meniscus water. Zourmpakis and colleagues however under-reported the possible vertical heterogeneity of pore spaces. Relatively higher volumes of pores may form at the interface between each two subsequent layers. This allows the infiltration of water front via preferred pathways, forming a non-uniform moisture profile (Assadi and Yasrobi, 2012).

Static compression at optimum water content is a rarely attempted alternative approach. This was recently reported in Medero et al.(2005), where mixed residual soil with proportions of Portland cement, water, and expanded polystyrene particles were compacted into open-packed specimens.

2.3.3 Synthesis of Artificial Soils with Carbonate Bonds

Akili and Torrance (1981) simulated the cement formation process by chemical precipitation of Calcium Carbonate and Calcium Sulphate in a pluviated sand. Experiments were conducted in an attempt to replicate the Sabkha deposits of the Persian Gulf coasts. Sabkha was defined as an assemblage of predominant windblown to sub-aqueous silty sands together with varying contents of cements, including Calcium Carbonate (Aragonite) and Calcium Sulphate (gypsum and anhydrite). Sabkha shows high resistance under dry condition and appears feeble upon wetting (similar to the behaviour of collapsible loess). To re-produce Sabkha at lab-scale, they attained the 'solution approach'. A carbonate bearing fluid was passed through the host soil. Given the low solubility of Calcium Carbonate in water, the bypass of oversaturated fluid via gravity or capillary forces gave negligible contents of calcite precipitates. However, the bypass/prolonged standing of an over-saturated fluid through/in the network of pores, generated precipitated carbonates at pore spaces (but not the contact points). Through the second attempt, Akili and Torrance (1981) flushed Calcium Chloride solution into a pluviated sand-powdered Sodium Sulphate/Sodium Carbonate medium. The fluid passed a sand filter at the bottom, and then climbed slowly up through the column, flowed for one week, and evaporated (drying) thereafter.

Kucharski et al. (1996) developed a non-particulate, water-based, pH-neutral and non-toxic aqueous solution of low viscosity, containing two chemical ingredients. They also synthesised a set of dry-of-optimum compacted laterally-confined cylindrical specimens (38 to 63 mm diameter, 300 to 425 mm length) of uniformly-graded fine to coarse marine calcareous sand. To generate bonds, the solution was flushed from the lower drain at 50 to 210 kPa pressure for a minimum duration of 10-minutes. Solution displaced the pore water up to two-time the initial pore's volume. Solution then was retained in specimen for 7 days before further flushing. Eight rounds of flushing-standing were conducted. Grains were coated with a 5-10 µm thick calcite cement layer. Calcite then crystallized within the pores. Post-treatment increase in mechanical strength and slight decrease in porosity were reported. Ismail et al. (2002) compared two alternative techniques to generate artificial calcite

bond. They evidenced greater degrees of crystallization by flushing the solution through the soil than mixing the dry soil with the solution. They also postulated higher degrees of calcite precipitation and lower bond strength for more angular host grains. Host soils composed of relatively finer grains, allowed calcites to crystallize at the many inter-grain contact points. The Fine-grained matrix appeared as a filter, which trapped calcite particles. Nonetheless, despite the higher number of potential cementation sites, a denser initial packing (lower initial void ratio) appeared in the fine-grained host soil, which provided less space for calcites to precipitate. Ismail et al. (2002) also emphasized on adherence between calcite units along the successive solution flushes. This resulted fewer nucleating sites, larger size of calcite crystals and thus higher overall structural stiffness.

Ouhadi and Goudarzi (2007) synthesised artificially cemented silty sands to simulate karst sinkholes. Sodium Sulphate, Sodium Carbonate, and Calcium Carbonate of 2.5 to 15% by-mass were mixed with silty sand (containing 90% sand, 5% clay, and 5% silt) in a dry state. Mixed soils were then wetted and dried, crumbled and statically compacted into a standard oedometer ring. The preparation might be criticized as it was not consistent with the soil's diagenesis. They observed significant increase in collapsibility of soils in presence of salt-constituents. Collapsibility however varied as a factor of salts' solubility. Soils with Sodium Sulphate and Sodium Carbonate exhibited greater void ratio loss upon wetting than soils containing Calcium Carbonate. Calcium-base salts including chalk, calcium hydro-carbonate, and Calcium Carbonate was postulated to have a negligible impact on collapsibility. This however contradicts the findings of (Akili and Torrance, 1981).

Lab-scale generation of Calcium Carbonate was also attempted in many out-of-discipline works. Zhao et al. (2009) synthesized carbonate nanoparticles in aqueous solutions via a bubbling method. They digested 10gr of Calcium Oxide in 100 ml distilled water and formed a Calcium Hydroxide slurry. After 12 hours standing time, pre-mixed Carbon Dioxide and nitrogen were bubbled into the filtered slurry at a certain flow rate and temperature. Calcium Carbonate nanoparticles formed as soon as suspension's pH dropped to 7. More recently, Kedra-Krolik and Gierycz (2010) modelled the precipitation of Calcium

Carbonate in a rotating disk reactor by flushing Carbon Dioxide into $Ca(OH)_2$ lime slurry. To prepare 23 and 56mM Calcium Hydroxide (molar mass of 74.093 g/mol) solution, 4.15 and 7g of $Ca(OH)_2$ powder was dispersed into distilled deionized water in a 1-litre volumetric flask. The mixture was thoroughly stirred. After 2 days standing time, the thermostatic solution (at 26°C) was treated in ultrasonic bath for 15 minutes. The solution was mixed with Carbon Dioxide at 2 dm^3 min^{-1} inflow rate while discs stirred the mixture at 30 to 120rpm revolution speed, until the pH reached to 7.5. Gocke et al. (2010a) also highlighted the key role of carbon Dioxide in precipitation and re-crystallization of Ca^{2+} ions from soil resulting in formation of pedogenic carbonates in soil. They implemented the origin of Carbon Dioxide of soil to the root and rhizo-microbial respiration, and acknowledged hundreds of years are required for the similar re-Calcium Carbonate crystallization in the absence of CO_2.

2.3.4 Synthesis of Artificial Soils with Amorphous Silica Precipitates

Apart from a handful of out-of-discipline works, engineering of silica bonds in artificial soils has never been attempted. According to Krauskope (1956) and Kato and Kitano (1968), silica gel can dissolve in distilled water at 105 to 160ppm concentration under 22 to 27°C after few weeks of standing time. Equilibrium takes place between dissolved silica and colloidal silica. Higher rates of dissolution applies in artificial sea water instead of distilled water (Krauskope, 1956, Kato and Kitano, 1968). With supersaturated solutions however, the reverse reaction occurs, in which silica re-precipitates in the form of colloidal particles. This is the philosophy behind the silicatization technique, which was reportedly employed to limited extents to stabilize loess deposits in former USSR and China.

2.4 Collapse Modelling: Our Understanding of the Problem

2.4.1 Collapse Mechanism

Given the limitations with the principle of effective stress in unsaturated collapsible soils, the collapse mechanism has been conventionally explained in the framework of structural mechanics (Feda, 1988). This includes the verbal description of bond modification, and the more advanced micromechanical

descriptions of modifying bonding forces and granular media. Structural mechanics, however, fails to provide an input for constitutive models.

2.4.1.1 The Effective Stress Viewpoint

Effective stress is a fundamental well-established concept in the mechanics of fully saturated soils (Terzaghi, 1936, Skempton, 1960). The earliest form of the principle was developed for single dominant porosity conveying one fluid (Terzaghi, 1936). Other forms were later developed for pores conveying two immiscible fluids (Bishop, 1959), and two miscible fluids (Matyas and Rahakrishna, 1968). Numerous efforts have been made to extend this concept to unsaturated soils since the late 1950's (Croney et al., 1958, Bishop, 1959, Aitchison, 1960, Jennings, 1960, Jennings and Burland, 1962, Fredlund and Rahardjo, 1993). Bishop (1959) derived the effective stress equation for unsaturated soils (Eq. 2.1 - Fig. 2.7), based on two stress states (net stress and matric suction) and a soil property (χ).

$$\boldsymbol{\rho} = \boldsymbol{\sigma}^{tot} + \rho_a \mathbf{1} - \chi(\rho_a - \rho_w)\mathbf{1} \qquad Eq.\ 2.1$$

Where $\boldsymbol{\rho}$ is the effective stress tensor, $\boldsymbol{\sigma}^{tot}$ is the net stress tensor, ρ_a is the pore air pressure, ρ_w is the pore water pressure, $\mathbf{1}$ is the Kronecker delta tensor, and χ is a soil property. The Bishop expression (Eq. 2.1) has been widely practiced in constitutive modelling (Gallipoli et al., 2003, Wheeler et al., 2003, Borja, 2004). Where the soil is idealised as a four-phasic material (with or without phase interfaces), other less frequently practiced expressions have been developed (Fredlund and Rahardjo, 1993, Sharma, 1998, Delage et al., 2006, Rust et al., 2005, Zeghal and Medina, 2008). Much research has been done to develop a proper function for the χ parameter; state-of-the-art reviews of these can be found in Coussy (2007) and Gens (2010). The choice of the χ parameter equal to the saturation ratio (Houlsby, 1997, Hutter et al., 1999, Borja, 2006, Borja and Koliki, 2009) has been argued for soils containing clay, where the residual saturation ratio exceeds zero and thus $\chi(\rho_a - \rho_w) \longrightarrow \infty$ when $(\rho_a - \rho_w) \longrightarrow \infty$ (Tarantino and Tombolato, 2005, Pereira and Alonso, 2009, Alonso et al., 2010, Vlahinic et al., 2011). Particularly for unsaturated collapsing soils, Jennings and Burland (1962) argued that Bishop's equation can provide an adequate relation between volume change and effective stress. A decrease in suction reduces the effective stress and thus, in

accordance with the tenets of Bishop's equation, increases the volume. This, however, contradicts the collapse behaviour. To ensure that $\chi(\rho_a - \rho_w)$ never diverges, a suite of approaches have been proposed in the literature, such as assuming zero residual saturation ratio, idealisation of water phase as two distinguished free and residual water phases (Fuentes and Triantafyllidis, 2013) or idealisation of pore phase (including air, water, or a combination of the two) as micro- and macro-pore spaces and setting the χ parameter equal to the effective saturation ratio (Khalili et al., 2005, Bagherieh et al., 2009, Alonso et al., 2010). A theoretical zero value for the χ-parameter was considered along the saturation of micro-pores (clay fragments of clayey silt soils), which resulted a constant effective stress equal to $\sigma - u_a$. Despite the fact that formulations describe the collapse, these fail to describe the early rebound volume change happening under low external net stresses. This has remained an open question, which needs addressing. Furthermore, soil's hysteresis effect (along seasonal wetting and drying) cannot be explained with current formulations. These drawbacks have challenged the use of the principle in unsaturated soils.

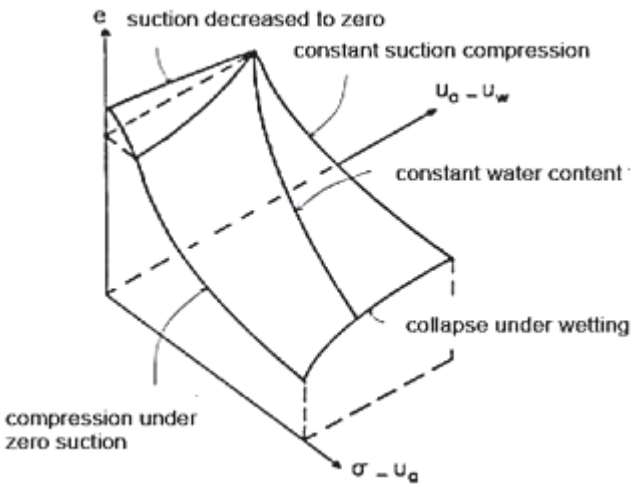

Fig. 2.7 The stress state surface e vs. $(\sigma - u_w)$ vs. $(u_a - u_w)$ in Delage et al. (2006)

2.4.1.2 The Micromechanical Viewpoint

'Micromechanics' explains the contribution of structural components, particle arrangements, and internal stress in the soil's deformation. Micromechanical relations are conventionally formulated with discontinuous numerical techniques (e.g. discrete elements), and are occasionally used (Meier et al., 2008) to describe the discrete failure phenomena of collapsing soils.

Triggering Mechanisms

Wetting, stressing or liquefaction can trigger the collapse. Casagrande (1932) showed the consolidation of fines between pairs of sand/silt grains under the in-situ overburden pressure. Upon wetting, and beyond a threshold water content, shearing of fines led to the collapse of the soil's structure. This was later acknowledged in Mellors (1995) work. Mellors addressed Lamb's equation (1960) to describe the grain arrangement and contact modification on the wetting surface. On this basis, wetting leads to the rehydration of clay bonds and the expansion of Diffused Double Layer, decrease in attraction forces (A), increase in repulsion forces (R), and ultimate bonds' disaggregation. For constant external net stress (σ), Mellors reported a decrease in the effective stress (σ': $\sigma = \sigma' + u + R - A$) and consequently the inter-particle shear resistance (τ) of clayey connectors. He, however, underreported the contribution of pore water pressure variations. He also ignored the contribution of the bonds' microfabric (higher shear strengths for flocculated configuration), geochemistry and of shear plane's orientation. Rogers (1995) noted that wetting reduces the negative pore water pressure, increases the positive pore water pressure and thus reduces the effective stress, and therefore bonds' shear resistance (Fig. 2.8). Both works (Mellors (1995) and Rogers (1995)) viewed the effective stress as a shear strength component of bonding soil elements. This is a meso-level viewpoint, which is not the sole approach in the literature. Effective stress is alternatively regarded as skeletal inter-particle stress (Santamarina, 2003) at micro-scale.

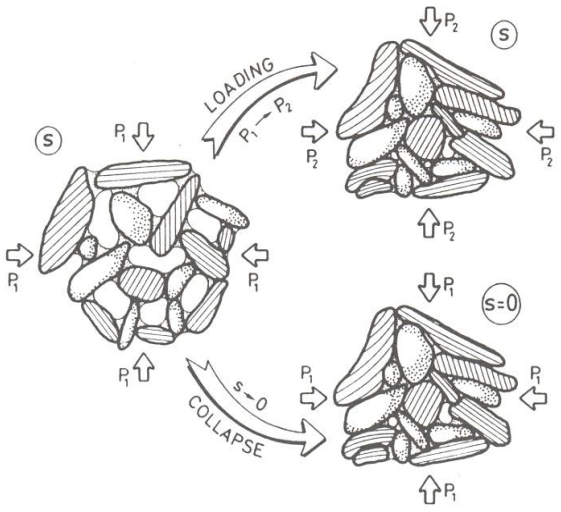

Fig. 2.8 Collapse due to stressing or wetting: crossed referenced in Rogers (1995)

Proceeding Mechanisms

A series of particle-level events leads the soil state to a collapse triggering threshold. Despite the many works undertaken on the reconnaissance of these events, few works, if any, could quantify how significant the contribution of each event in the collapse is (Boardman et al., 2001).

Klukanova and Frankovska (1995) described the wetted collapse in Slovak Carpathians loess in six stages:

(1) disintegration of clay coating units, connectors, and aggregates,

(2) dissolution and migration of carbonates within the pore network,

(3) migration of clay

(4) reduction in carbonate content,

(5) further compression of soil,

(6) formation of new microfabric of novel basic relations, in which clay aggregates and matrix units replace the coating and connector units.

Osipov and Sokolov (1995) broke down the collapse process into seven stages:

(1) formation of hydrated films of adsorbed water and subsequent increase in inter-particle distance,

(2) destruction of less water-resistant aggregates,

(3) destruction of most tubular micro-pores (small to medium),

(4) disappearance of capillary forces,

(5) structural collapse,

(6) consolidation,

(7) formation of new contacts.

Milodowski et al. (In Press) in a work on British calcareous clayey loess outlined the collapse sequences in clay, silt, and clay-silt ped units. Wetting firstly targets the clay connectors. Clay platelets attain a dispersive association, which encourages the slippage and therefore failure of connectors. Silt matrix units compress swiftly due to the lubricating role of water. After disintegration of connectors, skeletal stresses divert into clay-

silt ped structures. Clays lubricate the grains (Derbyshire et al., 1995), leading shear failure under applying pressures and disaggregation.

2.4.2 Controlling Factors

2.4.2.1 Dynamics of Grain Crush

Bolton (1999) in a work on Dog's Bay carbonate sand (e=1.1~1.6) showed that grains crush in a stepwise manner under stress levels as low as of 170 kPa, which may either be lower or higher than the collapse critical pressure (i.e. the pressure which triggers the collapse). A grain between two larger and harder grains may split by extending its equator. Assuming 'C' as the coordination number (also see Rogers et al.(1994b)), Bolton (1999) showed that C=2 supplies the maximum chance of grain to crush (P_s). He then formulated P_s as a factor of $(C-1)^{-a}$, where 'a' is the Weibull modulus, a modelling parameter. Similarly, he formulated P_s as a factor of $\left(\frac{d_0}{d}\right)^{A}$, where '$d_0$' is the diameter of the largest enamouring grains. The chance of grains to crush therefore is:

$$P_s = exp\left[-\left(\frac{d}{d_0}\right)^2 . \left(\frac{\sigma}{\sigma_0}\right)^m . (C-1)^{-a}\right] \qquad Eq.\ 2.2$$

Where σ_0 is the grain's resistance, 'd' is the grain's diameter.

Instantly after fracturing/splitting of grains, an excess pore water pressure forms in the neighbouring pore spaces, which are supported by the grain. Pore fluid expels to counter the rise in the pore water pressure. In the absence of hydrostatic water pressure, the vacant air-filled void appears susceptible to collapse. Under undrained conditions, the excess pore water pressure radiates and decreases the effective stress. This encourages the elastic rebound at the grains' contacts. For grains (crushed and intact) smaller than the pore space, solids migrate into the pore space to counter the excess pressure. For grains larger than the pore space, solids take up the excess pressure as skeletal forces, which may lead to more splitting events.

2.4.2.2 Dynamics of Bonding Elements

Bonding elements in loess (see also Section 2.2.5) include capillary water films, clay connectors, quartz connectors, and chemical connectors (including salts, sesquioxides, and amorphous oxides).

Water film binds grains together within a range of saturation ratios (S_r). For $S_r < 0.15$, loess is susceptible to water due to the formation of a tightly bound adsorbed water film at grains' contacts (Sharma, 1998, Wheeler, 1996, Saarenketo, 1998). The formation of water film reduces the molecular and ion-electrostatic forces. For $0.15 < S_r < 0.80$, a relatively lower rate of collapse but of potentially greater magnitude applies. This is due to the contribution of capillary forces in enhancing the soil's stiffness. A relatively far less structural strength was reported at $S_r > 0.8$ (also often cited as $S_r > 0.9$-0.95), indicating the disappearance of capillary forces (Osipov and Sokolov, 1995, Mellors, 1995).

Rogers et al. (1994a) suggested four ideal stress shearing systems including two short range and long-range clay bonds. Short-range clay bonds represent the accumulation of small contents of clay flakes, which exhibit high strength, but fail suddenly on wetting. Long-range clay bonds represent the accumulation of large contents of clay flakes, which exhibit moderate strength and fail with a plastic deformation.

The internal stability of grains aligned in chains is a factor of 'rotational frustration'[12] (Santamarina, 2003), and 'capillary forces' (Barden et al., 1973). Higher coordination numbers and higher degrees of anisotropy restrict the possible axis of rotation and thus arrest the rotational freedom of grains. Rotational frustration changes as a factor of:

- The relative size of grain pairs

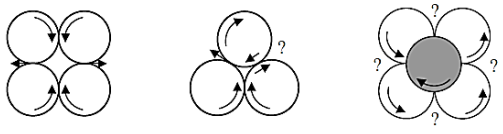

12 Lower rotational degree of freedom (i.e. better rotational frustration) when the number of contacts per grain (i.e. coordination number) increases after Santamarina (2003)

- Coefficient of uniformity
- Particle shape and texture
- Water content

Chemical bonds are categorized into three classes of easily, moderately, and hardly soluble (Osipov and Sokolov, 1995). Salts and sesquioxides of iron and aluminium provide chemical forces (10^{-7} to 10^{-8}N per individual contact), which form the strongest cement bridges. Amorphous oxides may contribute as individual bonds or as a shield in a poly-mineral grain coat (Xia and Han, 2009). These include gypsum $CaSO_4$ and hydrous iron oxides Fe.O.OH (Zourmpakis et al., 2003), silica oxides SiO_2 (Grabowska-Olszewska, 1989), ferric oxides Fe_2O_3 (Krauskope, 1956), goethite, haematite and colloidal ferric oxides (Xia and Han, 2009). These are characterised with high degrees of water resistance.

According to Rogers et al. (1994a), carbonates generally exhibit short-range brittle behaviour. Higher contents of carbonates provide higher degrees of strength and a more pronounced brittle behaviour. Carbonates may appear as bonding elements in six micro-morphologies (Fig. 2.4): scaffolding, encrusting, reinforcing bridges, linings to rootlet holes, inter-particle meniscus and nodular cements (i.e. primary clastic crystals). Scaffolds facilitate the deposition of illuviating clays, while encrusting reinforce the clay bonds (Milodowski et al., In Press). Delicate fibres of secondary calcites may either accommodate on the surface of clay-coated silts, or directly contribute in bonding as bridge structures (Jefferson et al., 2003).

2.4.2.3 Dynamics of Bonding Forces

Few attempts have been put into the measurement of interparticle forces in the event of wetting and stressing. Smalley (1970) developed a mathematical model to estimate the average bond strength in a dry soil. He presumed that soil comprises of randomly packed spheres of equal diameter with silty inter-particle units. Smalley suggested that bond strength is proportional to the tensile strength (i.e. equalling external forces, applying to a given contact) and cube of silt diameter, and is inversely proportional to the fractional packing density (i.e. the relative proportion of solids and voids), coordination number, and thickness of the failure zone (i.e. the zone within

which the failure takes place). Jones and Hodges (2004) reported the use of Atomic Force Microscopy (AFM) to probe inter- and intra-molecular forces between substances, surface adhesive forces, friction forces and elastic properties of soil materials. Hence, no record of real-time measurement of bonding forces could be traced in the loess literature.

2.5 Collapse Mitigation: Our Solutions to the Problem

2.5.1 Ground Improvement Techniques in Common Practice

Ground improvement techniques generally fit into six main categories of mechanical, physical, hydraulic, chemical, biological and soil reinforcing. Following a critical review of the classic literature, common practice is here described within the framework of the six categories.

In the mechanical (also known as densification) category (Burland et al., 2012), common techniques include preloading and the use of vertical drains[13], test-fills[14], water treatment, vacuum isotropic consolidation, shallow compaction, use of mixed material and re-compression, dynamic compaction[15], vibroflotation[16], blasting, compaction grouting and the installation of densification piles[17] (lime, cement, lime-fly ash, stone).

Loess soils containing relatively high contents of clay cannot practically be treated by densification piles, through vibroflotation, and dynamic compaction (Charles and Watts, 2001). This is genuinely due to the low permeability of

[13] The use of water tanks or fills (3-8 m high) accompanied with drain columns. Total load scales from 1.3 times the construction load for more than 6 months in embankments to 2.5 times the construction load for 2 to 6 months for more sensitive structures.
[14] Test fills: 4-6 compaction passes for 25 cm lifts at 15 ton-force effort or 8-10 compaction passes for 50 cm lifts with at 20 ton-force effort.
[15] 10 to 15 blows with 10 to 30-ton square concrete tamper (2-3 m in diameter) from a height of 10 to 20 m, in a pattern of 3, 8, or 12 m^2 (1.5 to 2.5 times tamper diameter) at the dry season.
[16] 30 cm-to-30 cm passes, each throughout a time-scale of 25 to 30 s in a triangular pattern, from bottom to surface, in 2-3 m spacing, at 30-100 horse power. Replacement material is clean sub-rounded 2-20 µm quartz.
[17] Up to 7-15 m long columns, each 50-60 cm in diameter at about 3 m centre-to-centre distances. Auger mechanical mixing at 10-bar grouting pressure or jet grouting technology at 150-200 bar pressure is conventionally used. For lime-cement columns, a combination of 5-12% lime and 1-3% type II Portland cement is conventionally used.

soil at higher clay contents. Shallow compaction in loess involves serious limitations, a detailed account of which is discussed in Chapter 6.

Physical techniques deal with modification of the grading curve, mostly by adding sub-rounded grains. The holistic perspective follows the simple target of decreasing plasticity and coefficient of volume compressibility (m_v). However, the role of clastic properties of soils' core elements (crushability) is under-reported in the literature.

Hydraulic techniques concern the control of groundwater flow, or extraction of water from hazardous zones. Techniques include the application of sump pumps, well points, deep wells, ejector wells (Preene, 2011), geo-membranes and electro-osmosis. Efficiency of water extraction scenarios depends on the soil's permeability, which itself is a factor of natural water content, density and therefore void ratio (Gibbs and Holland, 1960). Young desiccated clayey silt loess or reworked calcareous loess may exhibit high degrees of permeability due to the shrinkage induced cracks or rhizoliths (root-like macro-pore spaces). On the other hand, dense and heavily reworked loess deposits exhibit far less degrees of permeability. Water outflow may remove 2 to 20 μm quartz filling grains and thus decrease the lateral support of pore spaces, dissolve the chemical connectors and drive primary clays into the residual macro-pore spaces. These can significantly reduce the collapsibility.

Chemical mitigation techniques fit into three main categories of chemical stabilization (grouting, deep mixing), and more novel approaches such as soil gassing and electro-kinetic. Chemical stabilization concerns the use of calcium-base reactants including lime (Glassey, 1986), soil-cement, cement, fly ash and appropriate pozzolans such as plastic deprotonated clay[18].

Biological strategies account for natural lithification processes, through which the pore water chemistry is changed and therefore cementing agents precipitate within the granular medium. Van Paassen (2009) cited series of

[18] With slightly calcareous, very clayey silts, addition of fly ash might be effective if pH of the soil solution records less than 12. Lime content by mass is roughly about 2-10% in clayey soils and 2-5% in clayey silts.
Lime stabilization is inefficient in loess deposits of low clay contents. Stabilization with Portland cement is in efficient in loess deposits of moderate to high clay contents. Addition of fly-ash to cement may however increase the stabilization efficiency.

works since 1995 on the microbial induced calcite cement. The technique briefly includes the injection of Calcium Chloride (calcium source) and 0.5 to 5 μm Sporosarcina Pasteurii bacteria ($CO(NH_2)_2$ source) into the wet host soil (Eq. 2.3-2.4)

$$CO(NH_2)_2 + 2H_2O \xrightarrow{yields} 2NH_4{}^+ + CO_3{}^{2-} \qquad Eq.\ 2.3$$

$$Ca^{2+} + CO_3{}^{2-} \xrightarrow{yields} CaCO_{3(s)} \qquad Eq.\ 2.4$$

2.5.2 Novel Ground Improvement Techniques

2.5.2.1 Electro-Kinetics (EK)

As an alternative to hydraulic flush of stabilising chemicals into soft soils, Electro-Kinetics (EK) is a less common recently developed practice (Tajudin, 2012). EK counteracts the negligible hydraulic flow in fine soils (the drawback to hydraulic improvement techniques) by providing an independent, 10^{-6} to 10^{-7} m/sec flow rate in any type of soil. For problematic soils, the technique reportedly has been used to mitigate swelling in active clays through ion movement, cation exchange and plasticity reduction (Jones et al., 2008). It is also used to strengthen the soft clays through dewatering and consolidation (Rogers et al., 2002). Abdullah et al.(1997) studied the effect of exchangeable ion properties on the compressibility of clays (also see Mitchell and Soga (2005)). They showed relatively higher dry densities at lower optimum water contents in Ca^{2+}/K^+-enriched clays than in Na^+-enriched clays. Depressed diffused double layer (DDL) in the absence of Na^+ ions led to coagulation, increased the abundance of compressible macro-pores, and improved the densification. In other words, clay-to-clay adhesion improved with increasing exchangeable ion charge (Saejiew et al., 2004). On a different perspective, Lal (2005) discussed overlapping or repelling of cation clouds after pairs of clay flakes approached each other (Waxman and Smits, 1968). The overlapping occurred when electric conductivity (EC) increased due to an increase in electrolyte concentration (Waxman and Smits, 1968) or replacement of a mono-valent cation with a divalent cation e.g. the ingress of Ca^{2+}-enriched water into Na^+-enriched soil solution. The reduction in the cloud thickness gave rise to attraction forces. At a critical EC, at which the Van

der Waals attraction forces overcome the repulsive forces (Van Olphen, 1977), rapid coagulation took place. More recently, Abdullah et al. (1997) acknowledged high degrees of pre-consolidation pressure and low degrees of compression/swelling index in K^+-enriched soils.

2.5.2.2 Soil Gassing

Application of soil gassing for stabilization fits into four main categories: (1) compressed air flush in tunnels for balancing the ground water level, (2) artificial ground freezing by liquid Nitrogen and the release of Nitrogen gas to atmosphere, (3) dissolution-re-precipitation of carbonates and (4) silicatisation.

Dissolution re-precipitation can stabilizes the loess through a chemical reaction between some soil elements (e.g. Calcium hydroxide, Calcium Carbonate, Calcic Plagioclase Anorthite) and carbon dioxide, and formation of secondary carbonates. Silicatization can stabilize the loess through C-A-H cementation, or polymerization and sediment-air replacement at the void spaces. A detailed account of these two techniques is discussed in the present section.

The mechanism of natural diagenesis of secondary carbonates (Gocke et al., 2010a, Gocke et al., 2010b) laid the foundation for the carbonation 'bubbling' stabilization. Enrichment of the parent soil with alkaline calcium hydroxide slurry (Eq. 2.5) and gassing the soil with carbon dioxide to reduce the pH from 12 to 7 (Kedra-Krolik and Gierycz, 2010, Molenaar and Venmans, 1993) triggered the nucleation of Calcium Carbonate.

$$Ca(OH)_2 + H_2O \xrightarrow{yields} Ca^{2+} + 2OH^- + H_2O$$

$$CO_{2(g)} \xrightarrow{yields} CO_{2(l)}, \quad CO_{2(g)} + OH^- \xrightarrow{yields} HCO_3^-, \quad HCO_3^- + OH^- \xrightarrow{yields} CO_3^{2-} + H_2O$$

$$Ca^{2+} + CO_3^{2-} \xrightarrow{yields} CaCO_{3(s)} \qquad Eq.\ 2.5$$

To overcome the spontaneous nucleation (technique's drawback according to Wiechers et al. (1975)), Molenaar and Venmans (1993) suggested the use of magnesium and calcium oxides. Calcium/Magnesium Hydroxide slurry was formed after hydration of metal-based oxides. The process was claimed to inhibit the early nucleation of calcites. Molenaar and Venmans (1993) also explained a

continuous flow model through which the concentration of Calcium Carbonate was controlled by a control on the pressure of carbon dioxide (Eq. 2.6). Sequences of CO_2 and air flush provided a desirable environment of pH 7.3 to 7.4 for precipitation of calcites, as solution encountered suitable nucleation sites. Higher pH values formed aragonite cements of higher solubility.

$$CaCO_{3(s)} + 2H_2O_{(l)} + CO_{2(g)} \xrightarrow{yields} Ca^{2+}{}_{aq} + 2HCO^-_{3(aq)} \xrightarrow{yields} Ca(HCO_3)_2$$

$$Ca(HCO_3)_{2(aq)} \xrightarrow{yields} CO_{2(g)} + H_2O_{(l)} + CaCO_{3(s)} \qquad Eq.\ 2.6$$

The interaction of Calcic Plagioclase Anorthite ($CaAl_2Si_2O_8$) and acidic water Casey et al. (1991) can also result in re-precipitation of Calcium Carbonate, although this has never been attempted (Eq. 2.7).

$$H_2O + CO_2 \xrightarrow{yields} H_2CO_3 \xrightarrow{yields} H^+ + HCO_3^-$$

$$Ca(Al_2Si_2O_8) + H^+ + H_2O \xrightarrow{yields} Ca^{2+} + SiO_2 + Al_2Si_2O_5(OH)_4$$

$$Ca^{2+} + 2(HCO_3)^- \xrightarrow{yields} Ca(HCO_3)_2 \xrightarrow{yields} CO_{2(g)} + H_2O_{(l)} + CaCO_{3(s)} \qquad Eq.\ 2.7$$

Unlike the very few attempts on stabilization via dissolution-re-precipitation of carbonates, the use of silicatization at both lab and field scales is widely reported in the literature. With the CAH cementation approach, Tu (1986) made a major contribution. Tu (1986) described the unpressurized injection of boiling Sodium Hydroxide dilute solution into the foundation bed through boreholes (a 20 mm steel grouting pipe surrounded by 2-5 cm in diameter crushed gravel filter material). He aimed to release Calcium ions via cation exchange, and to leave the Calcium Hydroxide precipitates and sodium ions behind (Eq. 2.8).

$$2Na(OH) + CaCO_3 + Al_2Si_2O_5(OH)_4 \xrightarrow{yields} 2Na^+ + Ca(OH)_2 + (CO_3)^{2-} + Al_2Si_2O_5(OH)_4 \qquad Eq.\ 2.8$$

Tu (1986), however, did not discuss the probable effects of readily soluble hydrated sodium carbonate precipitates and soluble secondary crystals of Sodium Hydroxide, as treatment's by-products. The degree to which hardly soluble Calcium Carbonates donate calcium was not addressed either. Given the three underreported issues, some degrees of post-stabilization collapsibility could be expected.

Tu (1986) then referred to the reaction of Sodium Hydroxide with aluminosilicates, producing $Na_2O.nSiO_2$ and $Na_2O.mAl_2O_3$. Assadi and Yasrobi (2007) showed that sodium hydroxide does not react with the clay crystal, but instead causes a stepwise hydration. Sodium ions flow into the intra-lattice space after an ionic gradient, and form discrete chains of water molecules – sodium ions, resulting in the expansion of the diffused double layer. This may cause swelling at grains contact points (i.e. where clay normally crystallize), and consequently the collapse of pore network. This might be a pathway to void ratio loss and thus stabilization, but not a method to preserve the void spaces during the stabilization.

Tu (1986) also referred to a "complex compound of the silicate of calcium and aluminium", which cements the soil against water. He might be referring to the formation of C-A-H Calcium Aluminium Cements (deemed in Eq. 2.9-2.10), where the $Ca(OH)_2$ component gives rise to the pH of the soil solution. Alkaline environment encourages de-protonation, where an H^+ atom releases from the hydroxyl tail of the clay crystal. Ca^{2+} replaces with H^+, supplying a net positive charge to the clay system (Eq. 2.8). This is a pozzolanic reaction responsible for soil cementation. Fig. 2.9 shows the effect of some common compounds on soil solution's pH. The dilute aqueous Sodium Hydroxide can provide an alkaline environment, a favourable condition for de-protonation.

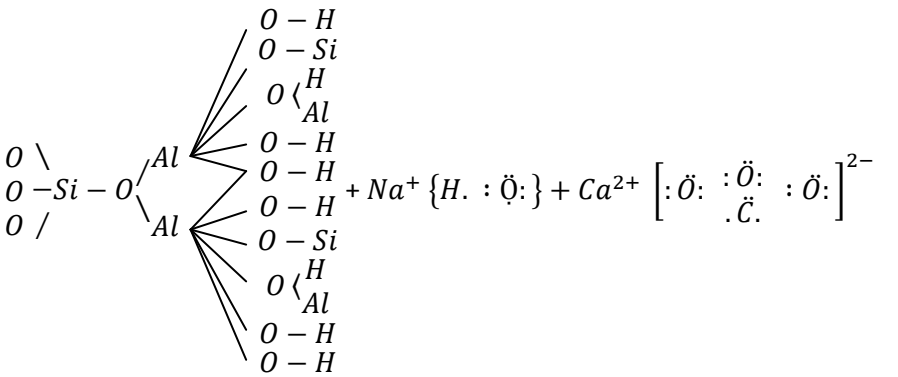

$$+ Na^+ \{H. : \ddot{O}:\} + Ca^{2+} \left[:\ddot{O}: \; :\ddot{O}: \; :\ddot{O}: \right]^{2-} \qquad Eq.\ 2.9$$

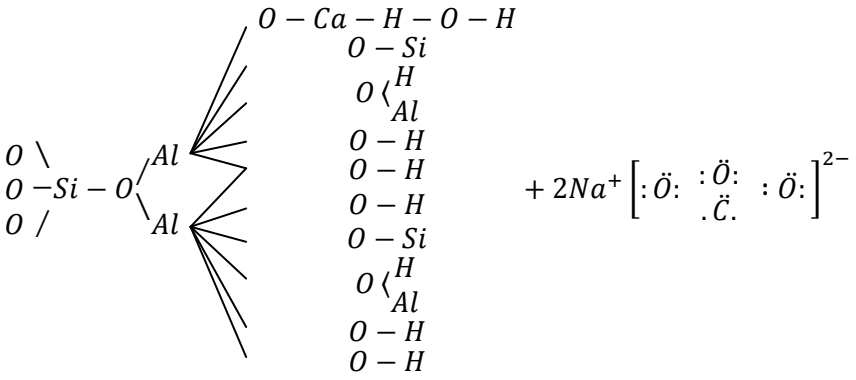

$$+ 2Na^{+}\left[:\ddot{O}: \ :\ddot{O}: \ :\ddot{O}: \right]^{2-} \qquad Eq.\ 2.10$$

To guarantee a sufficient amount of $Ca(OH)_2$ product, Tu (1986) suggested a 'double-fluid' process, by which the $CaCl_2$ solution was injected into the soil, after the injection of NaOH. With the 'double-fluid' process, he assumed a minimum content of Calcium Carbonate in the parent soil. The reaction is deemed as in Eq. 2.11.

$$Na_2O.nSiO_2.mAl_2O_3.xH_2O + CaCl_2 \xrightarrow{yields} CaO.nSiO_2.mAl_2O_3.xH_2O + 2NaCl \qquad Eq.\ 2.11$$

With the second approach, major contributions follow the works of Askalonov 1949 in Sokolovich (1965), Sokolovich and Gubkin (1970), Sokolovich and Ibragimov (1971), Isaev et al.(1979).

Sokolovich (1965) brought the 'Silicatization' term to the literature, which was earlier coined by Askalonov in 1949. Sokolovich referred to the published work of Zakharchenko over the practical use of the method in 1962. It was suggested that the aqueous solution of Na_2SiO_3 can release Ca^{2+} ions and replace them with Na^{+} ions, leaving behind an insoluble solid phase of $Ca(OH)_2.SiO_2$ (Eq. 2.12).

$$AC\begin{pmatrix} Ca \\ Ca \\ Ca \end{pmatrix} + 3Na_2SiO_3 + 3H_2O \xrightarrow{yields} AC\begin{pmatrix} Na \\ Na \\ Na \\ Na \\ Na \\ Na \end{pmatrix} + Ca(OH)_2.SiO_2 \qquad Eq.\ 2.12$$

However, Sokolovich's hypothesis does not conform to the classic work of (Kolhoff and Stenger, 1933). They evidenced the formation of an insoluble film of Calcium Silicate (Ca_2SiO_4) on the surface of silica nuclei's, upon a fast reaction between Calcium Hydroxide and silica. This later halts the chemical reaction. Therefore, the $Ca(OH)_2.SiO_2$ compound is actually SiO_2 nuclei's

covered with a thin film of $2CaO.SiO_2$ in $Ca(OH)_2$ aqueous solution. This suggests that the reaction in (Eq. 2.12) takes place only at limited levels.

In an attempt to tackle the 30% to 50% rate of Sodium Silicate solidification, heterogeneous distribution of solution in the pore network and extraction of the 50% to 70% unreacted remnant by subsurface waters, Sokolovich and Gubkin (1970) suggested the use of soil gassing. The lush of carbon dioxide improved the setting rate up to 1.5 to 2.0 times and extended the influence radius up to 2.0 times by facilitating mobilization of silicate (Eq. 2.13)

$$Na_2SiO_3 + 2CO_2 + m\,H_2O \xrightarrow{yields} SiO_2.nH_2O + 2NaHCO_3 \qquad Eq.\ 2.13$$

The 50% to 70% aqueous un-reacted Sodium Silicate was reported to react with CO_2, producing a secondary precipitate of silica amorphous.

Sokolovich and Gubkin (1970) reported 'few months' time' water inundation experiments, which indicated a better water resistance of treated Russian loess via silicatization.

Although the technique developers manoeuvred on the filling role of silica at macro-pore level, our findings (Chapter 5) showed the chemical interaction of clay and carbonate with silica. The technique however fails to preserve the initial porosity of the soil and thus is not suitable for the foundation soils underlying structures. Furthermore, in a geochemical theme, sodium bicarbonate by-product is a readily soluble bonding material. This results in some degrees of post-stabilization collapsibility in the carbonated silicatized loess.

Sokolovich and Ibragimov (1971) described the silicatization as rapid solidification of the silica gel (28 days according to Sokolovich and Gubkin (1970)), which wraps and coats sand grains and forms an impermeable shield. With calcareous non-clayey deposits, they pointed to the formation of calcium bicarbonate coat on Calcium Carbonate nodules (Eq. 2.6), assisting the adhesion of amorphous silica to the Calcium Carbonate and the grains. The interaction is deemed as Fig. 2.9.

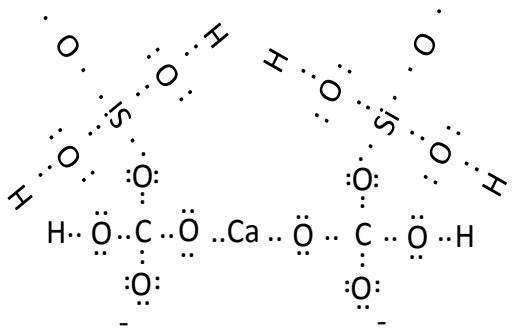

Fig. 2.9 The Lewis structure of the potential interaction of calcium bicarbonate grain coats with amorphous silica

With non-calcareous non-clayey deposits, Sokolovich and Ibragimov (1971) emphasised that solidification occurs easier in acidic environments. This can be formed by flushing carbon dioxide into the soil and thus driving the bulk water out of the pore network. CO_2 enriched micro-pores then homogeneously host the silicate liquid. They reported an increase in the slightly calcareous silty soil's uniaxial strength after both the pre-activation (early flush of CO_2) and gaseous silicatization.

Sokolovich (1976) discussed the mechanism of silicatization in non-calcareous clayey silts. In absence of evidence, he suggested the release of Aluminium of Aluminosilicate after injection of Sodium Silicate. Aluminium ions and silicic acid were assumed to form a cement gel, stabilizing the soil. This mechanism however does not conform to present work (see Chapter 5). Sokolovich (1976) concluded that silicatization is more effective in calcareous soils than in non-calcareous soils. Isaev et al.(1979) reported the satisfying application of gaseous silicatization in stabilization of a clayey loam soils with 30% clay content, 10 to 15% Calcium Carbonate, and 60 to 55% quartz silt and sand.

2.6 Missing Elements in the Current Body of Knowledge

Silt makes loess via aeolian processes; it is of consequence as a grain (discrete nature among particles in texture, crystal, shape, and size), as an arrangement (open packing), and as an assemblage (linked together through bonding forces and binding solids). Table 2.2 reviews the variation of key parameters in globally distributed loess.

Table 2.2 Variation of key parameters in globally distributed loess

	America	Europe					Africa		Asia	
	N	UK			C,N	E	C	N	E	C.S
		SE [1]	S [2]	SW [3]						
Clay	5-20	5-30	16-34	13-42	15-20	6-10	16-25	5-20	7-35	10-40
Silt	2-60	58-88	>40	>50	>60 [4]	63-88	30	51-77	60	60-90
Sand	4-23	7-22	5-35	5-60	<15	20	40-50	10-40	9-10	1-15
Carb	3-30	0-15 [5]	-	-	10-15	0-20	20-50	20-50	9-15	20
PI	4	7-45		LL: 25-35	12-19	4-6	9-13	3-6	10-17	10-13
										5-22
G_s	2.57-2.79	2.68-2.70	2.59-2.70	-	2.65-2.70	2.66-2.71	2.68-2.73	2.60-2.73	2.65-2.75	-
Y_d	1.06-1.66	1.48-1.73	1.57-1.71		1.3-1.7	1.46-1.73	1.42-1.43	1.30-1.80	1.40-1.46	1.24-2.13
e	0.62-1.42	0.55-0.90			0.75-0.95	0.97-1.14	0.89-0.91	0.8-1.0	0.81-1.08	0.42-0.88

N=North; S=South; C=Central; E=East; SW=South West; SE=South East; Carb=Carbonate; [1] Wealden, [2] Hampshire Basin, [3] Devon and Dorset; [4] silt content increases to 70% towards south; [5] see Appendix A1 and A2.

Miller (2002)	Klukanova & Frankovska (1995)	Fall (2003)	Assallay (1998)
FAO	Goudie and Middleton (2001)		IRCOLD (1999)
Delage et al. (2005)	Munoz Castelblanco et al. (2012)	Cattell (1997)	Meng (1998)
Smalley (1987)	Jefferson et al. (2001)	Jehring (2007)	
Bettis et al. (2003)	Assallay et al. (1996)	Derbyshire & Mellors (1988)	
	Nouaouria et al. (2008)	Grabowska-Olzewska (1988)	

Loess may collapse upon wetting and/or stressing, the significance of which is a factor of strength (of solids including silt and connectors), stress history (internal stored versus released stresses), hydraulic history (internal effective stresses and hence the state of pore spaces), and evolution environment (thermal and pH variations). Loess therefore shall be understood and explained in relation to these controls, much have received little attention. Key questions remained to be discussed are:

(1) How would minerals contribute in the soil stiffness and hence collapsibility either as discrete or as combined matters?

(2) Why may the collapse recur with thermal-chemical-hydraulic proceedings? How would the dynamics of pore spaces be explained with the widely appreciated principle of effective stress?

(3) Could chemical cementation have a control on collapsibility? Can the contribution of bonding mechanisms including capillary water, kaolinite-associated ion-electrostatic forces, and chemical cementation in collapsibility be compared in loess in the event of wetting?

(4) Why common compaction practice is reportedly not good enough to fully remove the collapse risk? Can stress-wetting history play a role in this failure?

(5) Can micro-mechanics (i.e. a perspective that views soil as an assemblage of genuinely discrete constituents) be any helpful in modifying the current compaction practice?

Chapter 3 METHODOLOGY

3.1 Introduction

This chapter presents details of experimental procedures as well as theoretical modelling procedures used to: (Level I) develop a framework for modelling the collapse; (Level II) develop collapse mechanism models for systematically classified sub 63μm collapsing soils; (Level III) develop a practical tool for engineers to estimate the risk of collapse, evaluate the effectiveness of compaction in removing the risk of collapse, and use a suite of tentative, tailored, and novel techniques for a full and permanent removal of collapse.

Level I procedures used a combination of in-house test set-ups, limited modelling, and standard mechanical, microscopic, and micro-analytical experiments. This then allows the real-time measurement of the indexes below. These are to be used to develop a collapse micromechanics framework:

- *Grain strength* under load
- *Pore volume* upon loading and wetting: through different combinations of loading and hydraulic paths
- *Grain – bond interface quality* upon loading and wetting
- *Internal forces* upon wetting

Level II studies included:

- Developing artificial specimen preparation techniques to mimic the mechanisms responsible for the formation of Quaternary aeolian loess as well as kaolinite
- Conducting single oedometer tests to examine the collapse potential of synthesised soils

- Conducting ESEM-EDS (environmental scanning electron microscopy – Energy dispersive X-ray spectroscopy) experiments to study the microfabric changes during the collapse process

Level III studies included:

- The use of a collapse potential database produced in Level II to draw predictive contours of collapse potential for each of the soil classes
- Producing complementary collapse potential database addressing kaolinite soils at varied compaction states
- The use of evidence produced in Level II to review the efficiency of the current ground improvement practice
- Producing complementary coupled standard proctor compaction – single oedometer tests on clayey silt soils to review the efficiency of the current ground improvement practice
- Outlining the philosophy behind the designed modified ground improvement practice

Level I, II and III meet the requirements set within objectives 2, 3-4, and 5, respectively (see Section 1.3 in Chapter 1).

3.2 Overview

3.2.1 Testing Specimens

A series of oedometer specimens of 75 mm in diameter and 20 mm in height were used as testing materials throughout the thesis. Combinations of key loess constituents, including quartz silt, clay (throughout the thesis, clay should be read as kaolinite clay, unless stated otherwise), salt (carbonate, sulphate) and oxides (silica), were used to build the testing specimens. To build the collapse models (Level I and Level II), specimens were artificially synthesized to a high initial void ratio and dry state (at the hygroscopic water content unless stated otherwise). Tailored specimen preparation techniques were used to mirror the natural soil formation processes. To examine the efficiency of compaction practice (Level III), a final series of

oedometer specimens were prepared by static compression as well as standard proctor compaction (where required).

To meet the objectives set in Level I of this study, micro-mechanical indices were measured on an 'ideal loess' specimen, containing 70% silt, 20% carbonate, and 10% kaolinite. Such a combination was observed to provide the maximum degree of collapsibility, and hence was deemed suitable to be used for developing the collapse mechanism framework.

To meet the objectives set in Level II of this study, various combinations of quarts silt, kaolinite, and carbonate were used, in the presence and the absence of silica-, and sulphate-phases. Collapse behaviour was examined on 11 classes of fine-grained potentially collapsing soils.

To meet the objectives set in Level III of this study, a suite of clayey silt specimens were remoulded via static compression and compaction.

3.2.2 Testing Specimen Components

The oedometer specimens were made up of varied contents of silt-sized ground Leighton Buzzard Sand, kaolinite, carbonate, amorphous silica, and sulphates. A brief account of these constituents is discussed in this section.

3.2.2.1 Leighton Buzzard Sand

Leighton Buzzard Sand is a 1.15 mm in size (with a pronounced mode size on 0.5-0.6 mm), rounded to sub-rounded, natural, uncrushed silica sand, that is almost free from silt, clay or organic matter (see also Kingston et al. (2008)). Unlike vein quartz, the Leighton Buzzard Sand has proven records of crushability into silt (Dibben, 1998, Miller, 2002). As such, the material was conveniently ground by a disc mill, and graded through sieving and gravity sedimentation to produce sufficient amounts of silt, which was the base component of the entire specimens used in the present study. The silt batch was fully produced in the beginning of the study and stocked in sealed and close buckets throughout the work. The use of the stocked silt prevented unwanted errors in specimen preparation, which might be caused through poor reproducibility of grinding-grading process over time (due to the probable changes to the efficiency of the milling machine and room humidity as well as

human errors). Fig. 3.1 shows the particle size and mode size distribution of the Leighton Buzzard Sand.

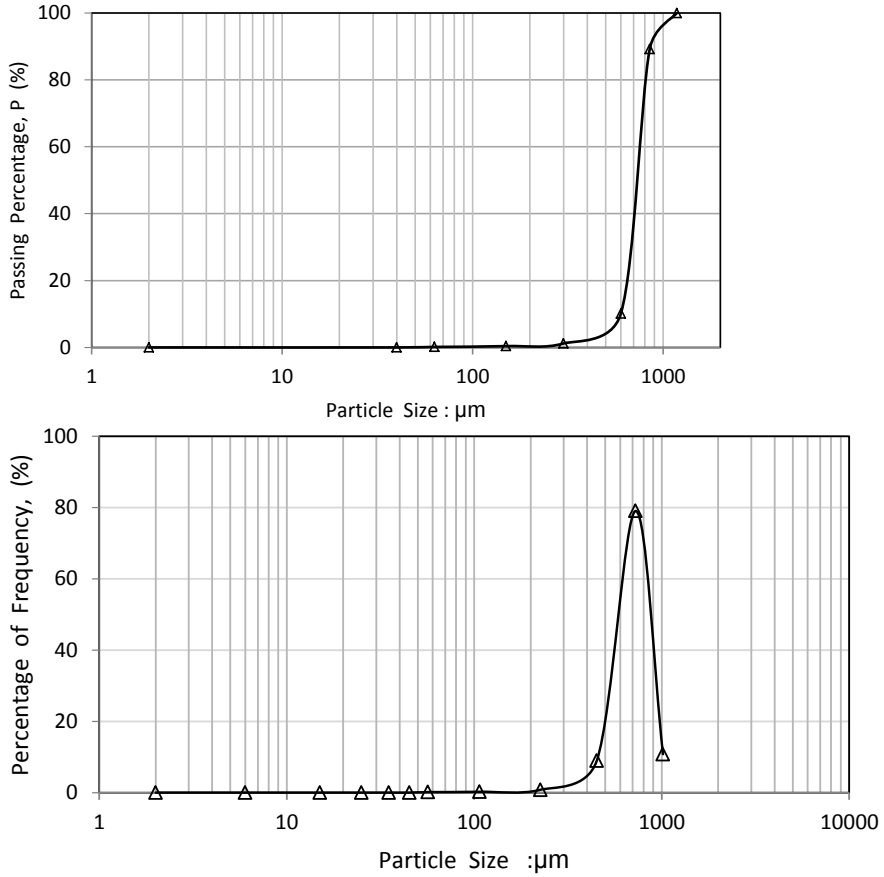

Fig. 3.1 Particle and mode size distribution of the Leighton Buzzard Sand

3.2.2.2 Kaolinite

Collapsible loess may contain active clay minerals of up to 13% (e.g. in north America according to Erol and El-Ruwaih (1982)). The clay content in loess however may be significantly greater than that of active minerals (e.g. montmorillonite) where total clay content varies from 0 for unsaturated dune sand to more than 50% for well-reworked loess. The choice of kaolinite (with limited activity) allowed the examination of rebound and collapse volume changes, while the swelling volume changes were kept to a minimum in the event of wetting. PolWhite-E English China Clay (refined clay) was used as the kaolinite material. The mineralogy (according to the supplier's data in IMERY (2008)) and chemical composition (Royal et al., 2011) of PolWhite-E is given in Table 3.1. The particle size distribution of the PolWhite-E is shown in Fig. 3.2.

Table 3.1 Mineralogical-chemical composition of kaolinite

Mineral	Population: %-by weight	Element	Population: %-by weight
Kaolin	74-80	Carbon	25
Feldspar	5-12	Oxygen	50
Quartz	1-2	Aluminium	10
Mica	5-15	Silica	15
Montmorillonite	2-3		

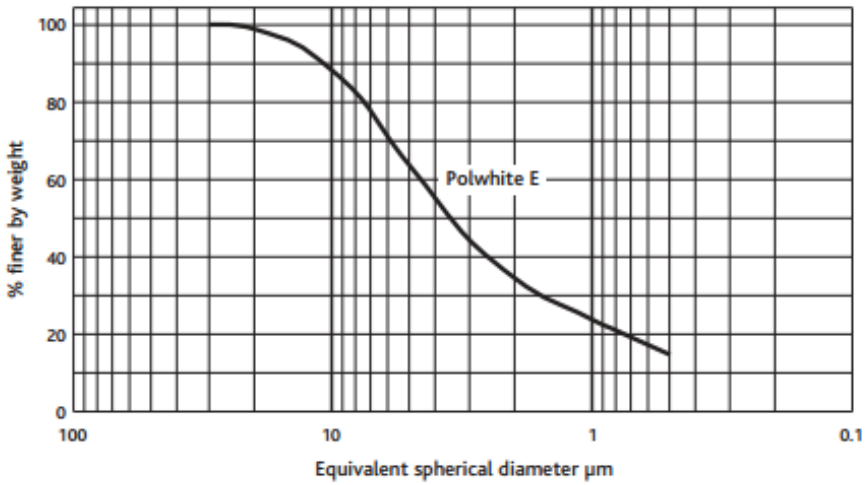

Fig. 3.2 Particle size distribution of kaolinite (IMERY, 2008)

3.2.2.3 Calcium Carbonate

Carbonate is a tangible cementing component of loess, which largely contributes to soil's dry-state stiffness and wetted collapsibility. A detailed account of carbonate's role in collapsibility was discussed in Chapter 2. Through a novel approach, Calcium Carbonate was engineered in testing specimens by processing Anhydrous Sodium Carbonate with dilute Calcium Chloride solution. X-ray Diffractometry was used to examine the successful formation of Calcium Carbonate. The control of sodium and calcium content on carbonate shape was examined by ESEM-EDS observations. The control of carbonate's shape on collapsibility was examined by oedometer testing.

3.2.2.4 Amorphous Silica

Warm periods in inter-glacial eras are a prime source of the amorphous silica precipitates. Such oxides are abundant in the West European loess, while lesser accounts of these have occurred in the British loess. A detailed

account of silica's role in collapsibility was presented in Chapter 2. Through a novel approach, silisic acid was introduced to testing specimens. Silicic acid was once introduced in water solution and once in artificial seawater solution to allow a control on sulphate-phases. Precipitation of silica was undertaken under varied temperatures to control the deposition rate.

3.3 Level 1: Fundamental Modelling

An illustrative workflow is displayed in Fig. 3.3, showing the links between micromechanical indexes, and their association with the fundamental collapse mechanism model, to be developed.

3.3.1 Dynamics of Crushability

3.3.1.1 Significance

As outlined in Section 2.6 of Chapter 2 (gaps in the literature), fracturing of quartz grains in loess disturbs the equilibrium in the pore water pressure. This encourages the pores to collapse under drained and undrained conditions. However, there is little knowledge on the maximum point at which a grain can break. As such, it is of prime importance to look into the factors, which affect quartz grain strength.

3.3.1.2 Sand Crushing Experiments

Washed oven-dried Leighton Buzzard Lower Greensand quartz from Bedfordshire was mechanically ground in a high-energy Siebtechnik agate disc mill (see Fig. 3.4 and Table 3.1). The disc mill consisted of a barrel, which accommodates a ring and a tungsten carbide pestle. By means of predominantly horizontal vibrations, the material was ground by impact and friction. Analogous conditions to glacial abrasion are provided in the disc mill (Jefferson et al., 1997a) due to the combined abrasion between grain asperity tips, and also between grains and rotating smooth tungsten carbide pestle.

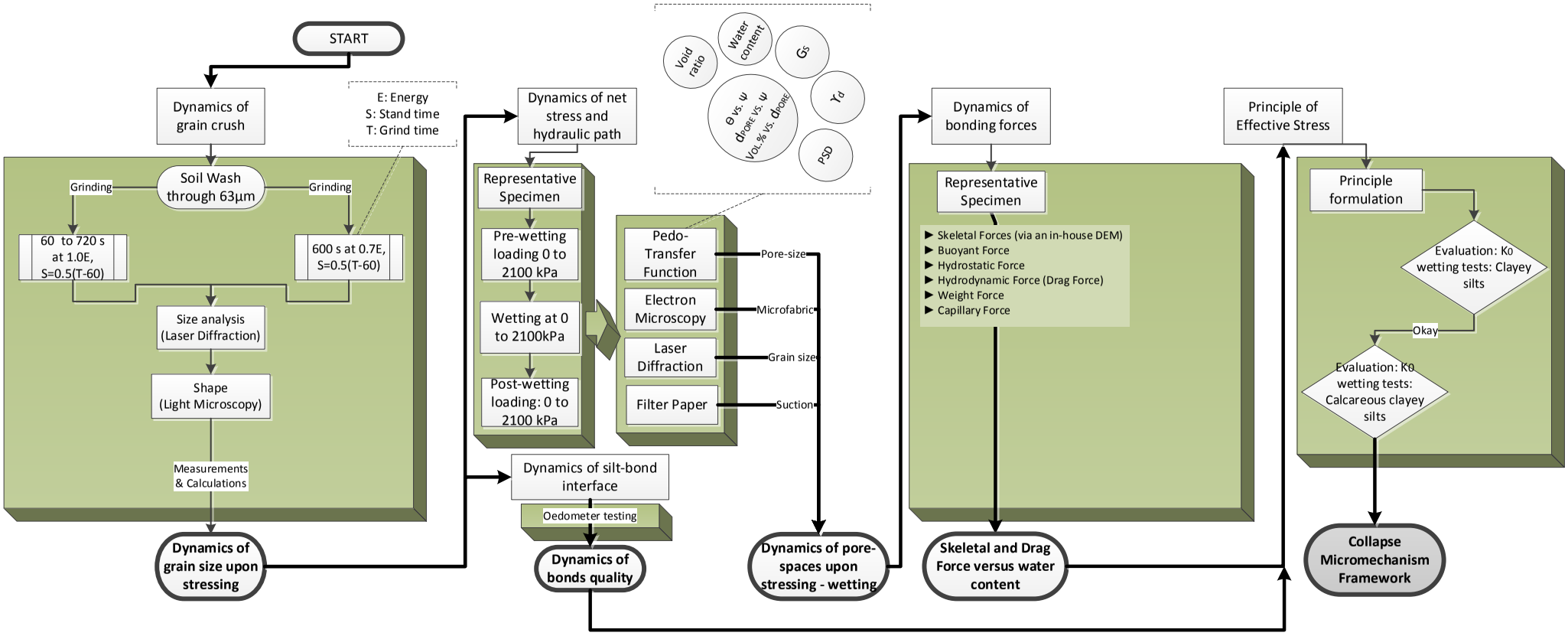

Fig. 3.3 An illustrative workflow for the fundamental modelling (Level I)

Table 3.2 Grinding scenarios used to crush the washed Leighton Buzzard sand

Path	Energy[19]	Grind time length: s	Stand time length: s
1	E	60	0
2	E	120	30
3	E	180	60
4	E	240	90
5	E	300	120
6	E	360	150
7	E	600	270
8	E	720	330
9	0.7E	600	270
10	E	360	120

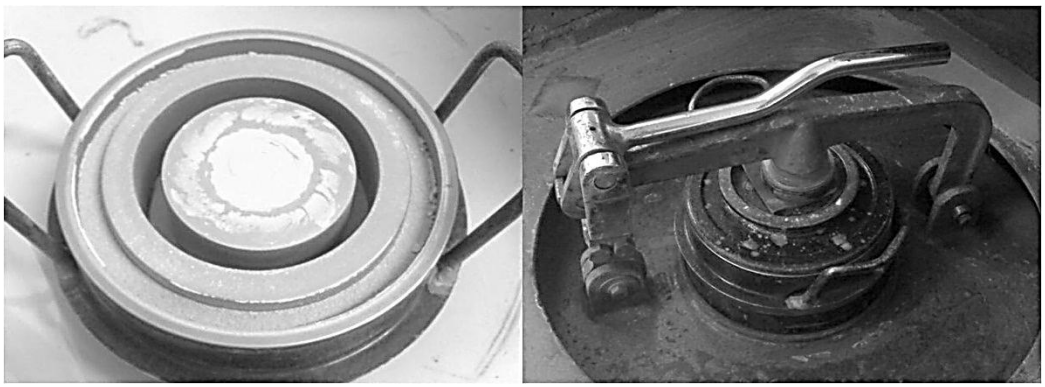

Fig. 3.4 (Left) Crushed sand after grinding, (Right) General setup of the disc mill

The sand was initially washed with tap water (standard process of wet sieving) and then Calgon through a 63 μm sieve to remove the silt- and clay-sized fragments (quartz and clay minerals) before operating the grinding experiments (BS 1377-2, 1990). This allowed an accurate control on the mass of 'silt' product for a given energy input. At a constant energy input, sand was milled through a series of timed events with each grind time (up to 60 s) followed by a 30 s cooling period to prevent overheating[20]. The discontinuous grinding

[19] For a constant mean force (supplied by the vibratory disc unit – Siebtechnik 800W TS1000 machine), which applies to soil grains in the barrel, any control on the feed mass affects the mean travel distance of grains between the ring and the barrel wall, and consequently the work (i.e. energy). The reduced work of '0.7E' in value was associated with 360g of dry sand feed, as a resolution throughout the grinding process.

[20] The entire ground material from a previous grind phase was used for subsequent grind phases. This allowed the fatigue stresses to gradually build up. However, since there was a need for recording the shape and size of crushed particles by the end of each grinding phase, several identical original sand samples instead of one sample were used. Each batch was ground to a certain total grind time, analyzed, and eventually disposed.

(frequent stress application and release) controlled the internal fatigue stresses. In addition to the grinding duration, the magnitude of the energy input has a significant control on the silt output. A control on the feed mass (mass of the original sand inside the barrel) was utilised to imitate two input energies. The barrel could hold up to 360 g of sand, the full capacity of which were used initially. The sand mass was then reduced by 30%. This was felt to give greater impact energy as particles were allowed to move back and forth more easily, in a given grinding timescale. After grinding, crushed material was carefully placed in sealed and labelled plastic bags to determine the particle size distribution (PSD) through the laser diffraction (LD) spectroscopy technique (detailed in Section 3.2.2.4).

Using the disc mill allowed a control on the length of grinding and cooling periods. The discontinuity of grinding controlled the fatigue stresses, affecting the integrity of crystalline discontinuities (Jefferson et al., 1997a). The Disc mill however does not exactly imitate the governing conditions under glaciers (Kumar et al., 2006).

3.3.1.3 Light Microscopy

Six to eight-gram samples taken after each set of grinding were viewed under microscope (Leica DM LM optical and light transmission Zeiss Axioplan 2 petrological microscopes). Light microscopy allowed the observation of crystalline features by transmitting the light through the grains. Drawbacks with light microscopy included: poor magnification and low resolution. In addition, real-time observation of grain modification was not possible. However, according to Footnote 20 and as the sand fraction was completely crushed after 180 s of grinding, the observed surface imperfections in crushed grains were deemed to differ from textural features of grains at their initial stage.

3.3.2 Dynamics of Stress and Hydraulic Path

3.3.2.1 Significance

As outlined in Section 2.6 (Chapter 2 Gaps in the literature), the loss in the void spaces on wetting is a factor of the stored skeletal forces in the grain network before the infiltrating water washes (either dissolves or carries as

suspended matters) the connectors. However, the current standard for measuring the collapse potential and consolidation coefficient (BS1377-4, 1999), advises a self-weight flooding process and hence ignores a potentially more critical scenario of flooding under skeletal stresses. This stems from a lack of in-depth understanding of the soils' geochemistry and structure, the result of which is an oversimplification of the complex geotechnical and geological interactions. As such, the relevance of the soil's packing state with loading environment is examined in the present section by looking into the dynamics of void spaces on controlled stress and hydraulic state surfaces.

3.3.2.2 Overview

The dynamics of pore spaces upon wetting/loading is tested for 20 identical 'ideal loess' specimens, as fully described earlier in Section 3.2.1. Each specimen was subjected to a particular pattern of loading/wetting, as detailed in Table 3.3: The first batch of specimens (path 1 to 3) was saturated with distilled water through the lower drain under K_0 conditions via the capillary rise. By the end of the wetted-induced subsidence (when three subsequent specimens' height reading gave similar value over a 60 minutes period as a resolution), specimens were incrementally loaded under K_0 conditions through the standard pattern suggested in BS 1377-5: 1990. At target stress values, specimens were removed from the oedometer ring, air-dried, and used for producing scanning electron microscopy images, as well as particle and pore size distribution curves. Sections 3.3.3.5 and 3.3.3.7 detail the microscopy and particle size analysis methods. Section 3.3.2.6 describes the technique by which the pore size distribution was derived. The second batch of specimens (path 4 to 12) was incrementally loaded under dry conditions to target stresses. The third batch of specimens was incrementally loaded to certain stress values, wetted via the capillary rise, and incrementally stressed to a maximum of 2100 kPa. Similar to the first batch of specimens, for both second and third batches of specimens, SEM images, pore and particle size distribution curves were produced by the end of the wetting/stressing process.

The measured particle and pore size distribution curves, micro-fabric arrangements, and void ratio were synchronized to build the packing state of the specimens. Packing state is defined as the spatial relative arrangement of

solids and void in a soil domain. This is analogous to the definition provided in 1984 by Basumallick from an earth science perspective (Rogers et al., 1994b) and is used in this section to examine the loess under varying patterns of stressing-wetting.

3.3.2.3 Oedometer Tests

Oedometer tests were conducted in three phases (see Table 3.3). The packing state indices were recorded on the stress state surfaces. Under the dry state, each loading increment was retained for a minimum of one hour. Under the wet state, this minimum time was increased to four hours to satisfy the primary consolidation (deemed upon pilot testing).

Table 3.3 Simulated stress-hydraulic paths on which the ideal loess specimen (containing 20% carbonate, 10% clay, and 70% quartz silt) was examined via its packing state parameters

Path	Flooding stress: kPa	Stress: kPa	State surface
1	0.01	0	Wet
2	0.01	200	Wet
3	0.01	2100	Wet
4	-	12.5	Dry
5	-	25	Dry
6	-	50	Dry
7	-	100	Dry
8	-	200	Dry
9	-	400	Dry
10	-	800	Dry
11	-	1600	Dry
12	-	2100	Dry
13	25	2100	Wetting - Wet
14	50	2100	Wetting - Wet
15	100	2100	Wetting - Wet
16	200	2100	Wetting - Wet
17	400	2100	Wetting - Wet
18	800	2100	Wetting - Wet
19	1600	2100	Wetting - Wet
20	2100	2100	Wetting - Wet

3.3.2.4 Filter Paper Test

To investigate the suction-packing interaction, a standard filter paper test (ASTM, 2003) was conducted on cubic specimens of 20 mm and 10 mm width and 20

mm height. The target water contents were set to increase in a step-wise fashion of 5-7% increments, starting from soil's hygroscopic water content (0.4%) up to 30.5% in six stages. Wetting was continued until water content tended to the saturation state (ω_{sat}=39%). An equilibrium time of eight days was considered adequate for each stage (Munoz-Castelblanco et al., 2012).

3.3.2.5 Laser Diffraction Spectroscopy

The Laser Diffraction (LD) analysis was applied over the 0.4 µm to 2 mm size range (i.e. the Sympatec QICPIC & GRADIS/L range), at 1.544 refractive index (IR factor for quartz in Eshel et al. (2004)). For the micronization process, 4 g of grains (crumbled with a plastic pestle) were fed into the vibrating channel with 0.5 mm free-fall distance. Grains were then passed through the jet milling channel at four bar gas pressure. The machine provides cumulative distribution using the third quartile (Q3) of a normal distribution (at 99.73% degree of confidence). Laser diffraction appeared to slightly under-estimate the size of the sub-angular coarse grains (when comparing the LD outputs with that of the back-scatter electron microscopy – see O'Hara-Dhand et al. 2013). Such a limitation is due to the fact that the LD machine assumes all grains as perfect spheres (see Pye and Blott (2004)). It also appeared that the Laser Diffraction method under-estimates the population of sub-rounded <2.5 µm grains (when comparing the LD outputs with that of the standard gravity sedimentation – see O'Hara-Dhand et al. 2013). The source of such an uncertainty is deemed to be the coagulation of sub-rounded <2.5 µm grains into larger aggregates on the LD vibrating channel, before the testing material enters the laser chamber. Despite the discussed limitations, Laser Diffraction was chosen to take particle size measurements in this study because of the high reproducibility of the measurement outputs. Random measurements were repeated and PSD outputs were compared (Appendix A4).

3.3.2.6 Pedo-Transfer Function

The Arya-Paris model (Arya and Paris, 1981, Arya and Paris, 1982, Haverkamp and Parlange, 1982, Arya et al., 1999) was used to measure the pore size distribution. The consistency of the model with loess was examined earlier in the work of Mingbin et al. (2009) on Chinese Loess Plateau deposits. Mingbin et al. (2009) showed that the method must be applied cautiously to soils of

high clay content, high sand content, or to soils of bimodal grading. Since the synthesised specimens used contained 10% kaolinite, 20% silt-sized carbonates, and 70% silt arranged with a single pronounced mode size at 20 μm, the Arya-Paris model was concluded suitable for the present study. To derive the pore size distribution curve, cumulative particle size distribution curve (see Fig. 4.32 in Chapter 4) was divided into 14 fractions, with boundaries at 2, 3, 4, 5, 6, 7, 8, 9, 10, 20, 30, 40, 50, 60 and 63 μm grain diameters. Void ratio, specific gravity, and water content values were recorded against wetting time. Applying the function, for any given void ratio, a suite of parameters were plotted against grain size, including pore volume, volumetric water content, mean pore radius and matric suction. An example of such graphs for 'path 16' (see Table 3.3) is demonstrated in Fig. 3.5.

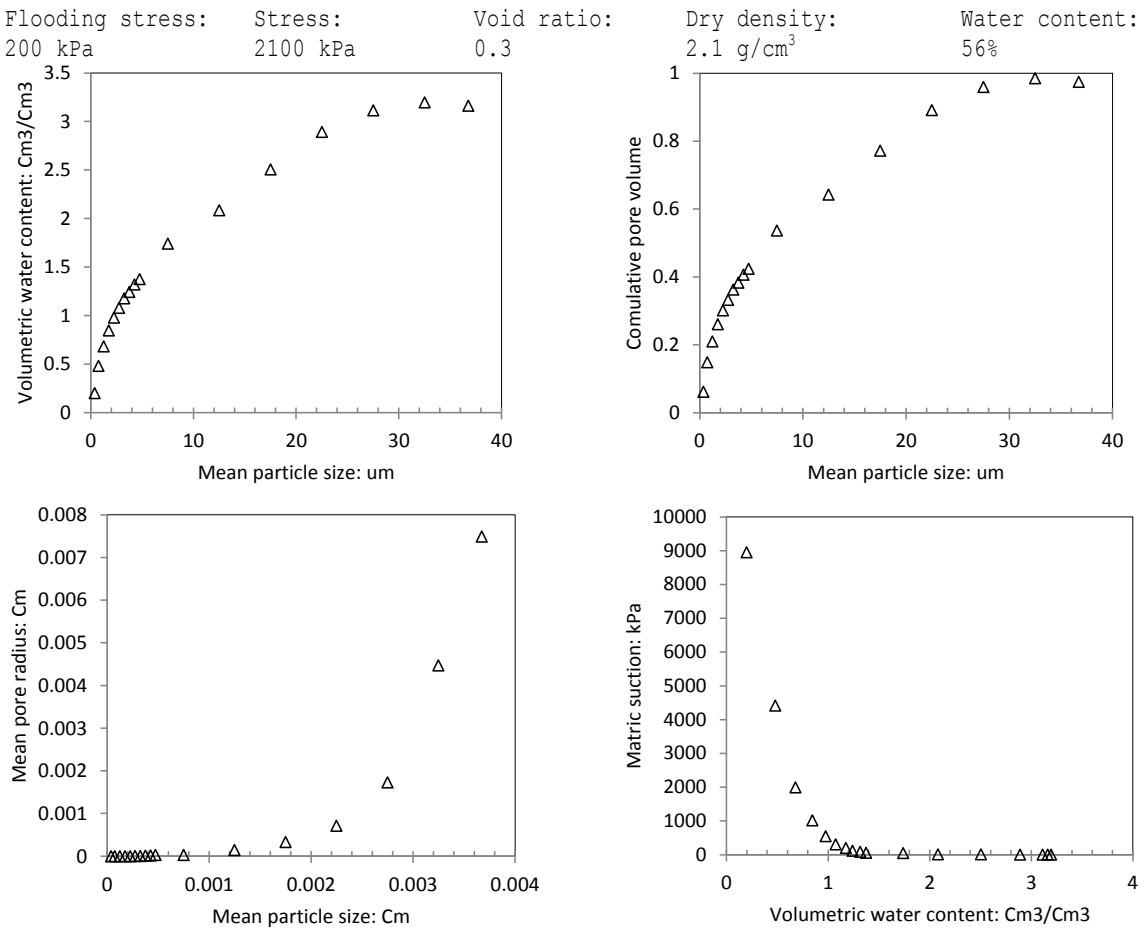

Fig. 3.5 An example of the Arya-Paris output data for stress path 16

A scaling parameter was selected in accordance with the 'texture dependent' method of 'logistic growth curve in Arya et al. (1999), which was the latest modifying update of model, presented by the function developers. Fig. 3.6

shows the model output for 'ideal loess' testing specimen. Concepts and forculation together with a working example of the model is explained in Appendix A5 (A5.1). Since the model converts the the particle size distribution data to pore size distribution data, the use of the conventional semi-logarythmic presentation of the grading curves poses a limitation, which is fully explained in Appendix A5 (A5.2). The impact of such limitation in the present study is remote, the reasons of which are fully explained in Appendix A5 (A5.3).

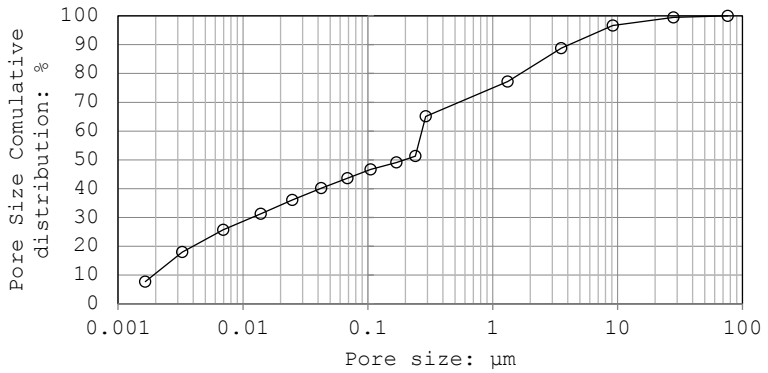

Fig. 3.6 Pore size distribution – 'ideal loess' testing specimen (containing 70% quartz silt, 20% carbonate, 10% kaolinite)

3.3.2.7 Environmental Electron Microscopy

Vertical aligned cubic samples were viewed under a Philips XL-30 LaB6 (General purpose 50x50 millimeter stage SEM) in conjunction with an Oxford INCA EDS system with NordlysS camera of 1344x1024 pixels resolution. Conventional drying methods were discussed by a number of authors (Sides and Barden, 1971, Collins, 1978, Smart and Tovey, 1982, Al-Rawas and McGown, 1999, Pusch and Schomburg, 1999). However, the choice of sample drying technique is still a matter of much debate (Al-Rawas and McGown, 1999). Cryofixation in liquid nitrogen (i.e. sample's pre-cooling and complete immersion in liquid nitrogen or any other cryogenic liquid), may disturb the fabric due to the rapid freezing (Marashi et al., 2005) or contaminate the soil (Tan, 2005). Freeze-drying can be applied on wet test samples only. Water constituent can disturb sensitive loess samples. With hot mounting, brittle soft materials (such as loess) may not stand up to working pressure. Therefore, a simple slow-drying process was undertaken in the present work. Samples were dried under a

relatively constant 23°C temperature over three to four weeks (i.e. air drying). Samples were then fractured by applying a combined bending and pulling actions (i.e. by hand). The obtained semi-circular samples were fractured once more and trimmed to prepare specimens of maximum size 7 mm and sector in shape. Given the brittle nature of loess specimens, no air-jet, cellar-tape peeling, or similar destructive actions were taken to clear the surface from remnant dust. The specimens instead were glued to the stubs with hardener and resin. Surface dust was allowed to fall by turning the stub upside-down, several times. Conductance to ground was insured by bridging the top of the coated specimen and the stub by means of a quick drying silver stripe. Specimens were than vacuumed to 0.15torrs to properly remove the pore-water. Specimens were then vacuum-coated with a few angstroms layer of Platinum. Microfabric was studied at visual level (X40) magnification to clay-sized level (X6500).

3.3.3 Dynamics of Grain-Bond Interface

3.3.3.1 Significance

Quartz continuously fractures under a given loading environment and therefore changes the sorting and textural properties of loess silt-constituent (Section 3.3.1 and Chapter 4). Carbonates and clay migrate, and re-crystallize in loess upon wetting-drying cycles (Section 3.3.2 and Chapter 4). The quality of restored bonds and therefore the degree to which reworked loess can collapse is a factor of grain-bond interface properties. The present section describes the method-of-statement used here to examine the contribution of interface properties in restored collapsibility.

3.3.3.2 Overview

Crushed Leighton Buzzard sand was used to engineer repeatable loess specimens of the same silt and bond content, depositional, post-depositional and stress history. Details of specimen synthesis are outlined in Section 3.4.1. Uniformly graded sand (Fig. 3.7), was crushed in a disc mill for 600 s in ten stages, each lasting 60 s together with nine cooling stages (each lasting 30s). The product (containing a mixture of sand, silt and clay-sized quartz, Fig. 3.7) was graded to silt-sized range (20-63 μm) by sedimentation: 150 g of

crushed sand was thoroughly mixed with a dilute Calgon solution (any 1-litre containing 33 g Sodium Hexametaphosphate, 7 g Sodium Carbonate, and distilled water). The suspension was then retained in a water bath at 25°C. The isothermal suspension was agitated and placed in the water bath. Stokes' law was applied to measure the settling velocity of particles of varying sizes (Lamb, 1994) and hence determine travel time for 63 μm and 2 μm grains to fully settle. Fig. 3.7 (c) shows the particle size distribution by the end of sedimentation.

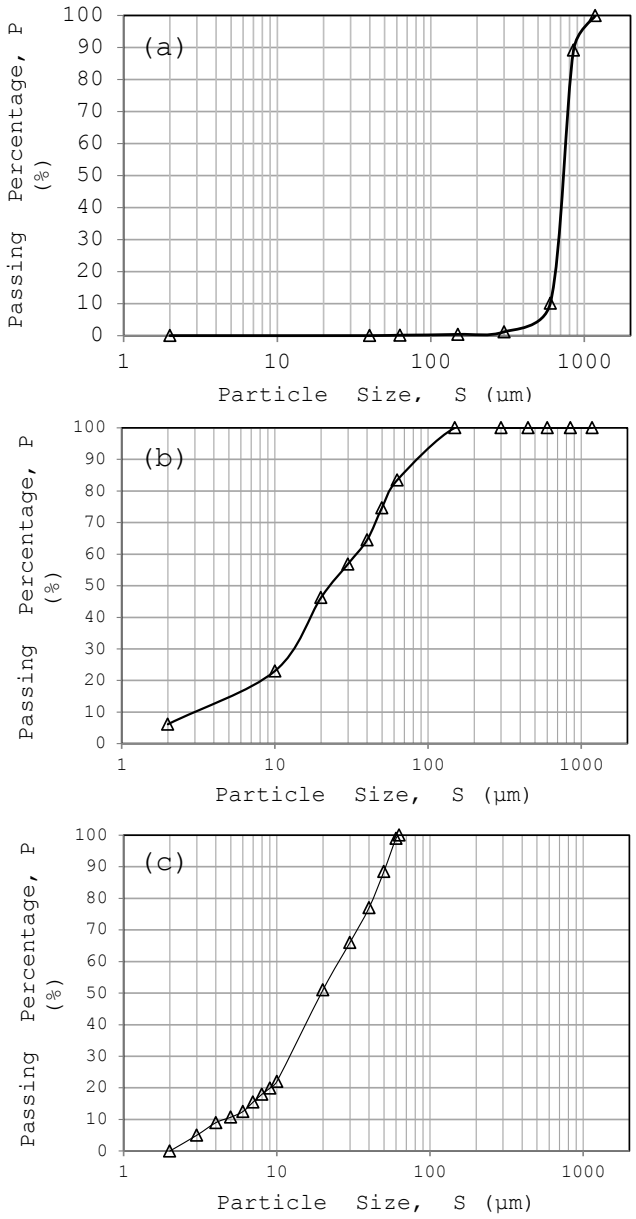

Fig. 3.7 Particle size distribution (a) the Leighton Buzzard Sand, (b) Ground Leighton Buzzard Sand, (c) Ground and graded Leighton Buzzard Sand (silt)

In a second attempt, by controlling travel times, a range of graded silt grains (>2 μm, 2-10 μm, 10-20 μm, 20-30 μm, 30-40 μm, 40-50 μm, 50-63 μm) were produced, dried, and mixed together to build the material detailed in Fig. 3.8. Fig. 3.9 shows the grading curve of the silt output (i.e. first attempt) together with the grading curves of ground and graded Leighton Buzzard Sand, produced and reported in Dibben (1998), Assallay (1998), and Zourmpakis (2005). The PSD of the ground silt has a marked population of 10 to 20μm, not untypically of many loessic soils (Assallay et al., 1998).

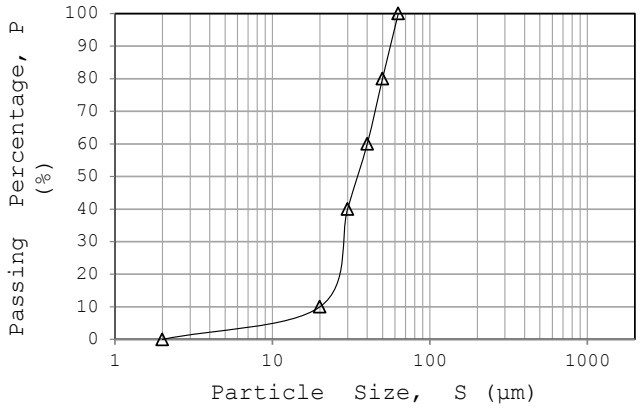

Fig. 3.8 Particle size distribution of ground and uniformly graded Leighton Buzzard Sand

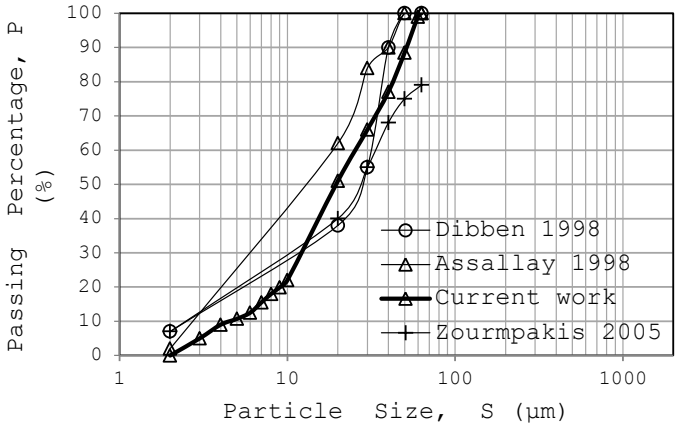

Fig. 3.9 Grading curve of the silt constituent of artificial loess (current study & previous studies)

A series of silt-kaolinite-sodium carbonate mixtures were then prepared under a dry state. At 10% kaolinite content, the carbonate content was varied from 0 to 30% (90-60% silt). The mixtures were then processed to engineer loess specimens (fully detailed in Section 3.4.1). Silt component of both grading patterns were used to engineer identical specimen pairs. The mechanical

response of specimen pairs was eventually examined through single oedometer test, which is detailed in Section 3.4.2.

3.3.4 Dynamics of Internal Forces

3.3.4.1 Significance

As outlined in Section 2.6 of Chapter 2 (gaps in the literature), there is still no form of the effective stress principle, which can interpret the dynamics of pore spaces in collapsing soils. Earlier in Section 3.3.2, a series of tests was described, which enable the study of the pore space volume change on varied stress state surfaces. As detailed in Chapter 4, test outputs suggested the existence of three separate pore space phases (of particular size ranges), which function individually along the course of wetting. To consider such discrete behaviour in the principle of effective stress, a method is detailed in the present section, which enables the estimation of internal stresses along the wetting course in a representative loess specimen of similar properties with that outlined in Section 3.3.2.

3.3.4.2 Overview

A semi-empirical technique was established to probe the inter-particle forces on the wetting stress-state surface. Capillary forces were estimated via the use of a pedo-transfer function (PTF) in conjunction with a water content controlled oedometer test. A filter paper test was used to check the PTF. Drag forces were formulated as a factor of unsaturated and saturated coefficients of permeability. Unsaturated permeability was roughly measured by conducting a coupled water content and constant head permeability test (Darcy's law – see BS 1377-5: 1990), while a Terzaghi Consolidation test provided the saturated coefficient of permeability. Skeletal forces were measured as a factor of void ratio in a simple discrete elements framework. Buoyant, hydrostatic and weight forces were measured under oedometer wetting tests with a controlled hydraulic head applied.

3.3.4.3 Model Rationale

The test material (discussed in Section 3.3.2) consisted of 'particles' of quartz silts. Particles were assumed to be mono-dispersed in size ($d=d_{50}$), spherical in shape, incompressible and non-crushable. Forces are applied to

particle-to-particle contact points (i.e. grain or bonding agent), 'c', at the mid-height of soil specimens. This can be shown with c=(p,q), where 'p' and 'q' are a pair of particles linked together at point 'c'. Particles were sorted in columnar structures and were aligned into load-carrying paths to carry the applied boundary stresses. The load-carrying paths (direction of the principal stresses) however were liable to change. Although the wetting regime (capillary flow and flow under a controlled constant head) could result in a non-uniform moisture profile (Ogawa et al., 1999, Gerke et al., 2010), the water content was assumed to be homogeneously distributed. In the light of the small contribution of tangential forces to the skeletal stress (average stress is largely borne by the normal forces after Cundall and Strack (1979)), the contribution of tangential skeletal forces and contact moments in the equilibrium equations were therefore neglected. The damping of forces was presumed negligible in the light of the high degree of particles' angularity and interlocking (Fratta and Santamarina, 2005).

3.3.4.4 Model Formulation

The balance between active (i.e. forces which tend to detach grains from each other) and passive (i.e. forces which tend to pull grains together) internal forces controls the volume change of a soil. The active forces include: skeletal, weight, buoyant, hydrostatic, and drag[21] (Santamarina, 2003). The passive forces include: balanced attractive Van der Waals (i.e. ion-electrostatic), capillary, chemical/cementation (Osipov and Sokolov, 1995) and interlocking (Bolton, 1999). Skeletal forces have been often written as a factor of three variables: external effective stress, particle diameter, and void ratio (Fratta and Santamarina, 2005). On this basis, Santamarina (2003) proposed a semi-empirical formulation for the skeletal forces (Eq. 3.6), which was valid for a random packing of spheres at void ratios ranging from 0.4 to 1.0. However, for void ratio between 0.4 to 1.0, this is valid only for net stress values between 12.5 and 400 kPa (see Chapter 5 – 70% silt, 10% kaolinite, 20% carbonate) on the wet stress-state surface. Therefore, a void-ratio-independent formulation needs to be developed. Such a formulation is derived in the present section using a framework of a simple discrete element

[21] Drag forces act as temporary load conductors, transferring the load from the pore fluid to the particles.

model. In developing a formulation for the skeletal forces, it was assumed that net stress applies uniformly on the surface of a half hemisphere spherical grain. The modelling also assumed the soil as an isotropic medium. Any random domain was modelled as an elementary prism containing d-size cubic solids aligned in perpendicular columns. Chains of solids were aligned along three Cartesian axes, each surrounded by same-size columns of voids. Void columns represented the macro-pores. Where a proportion of void columns were occupied with solid cubes of <d in size, or where a proportion of solid columns were occupied with void cubes of <d in size, void represented a micro-pore. The effective area (A_e) was defined as the minimum area (of available solids) to characterise stress distribution in a 2d-sized square space (i.e. area of available solids to bear the applied load). In Table 3.4 and Fig. 3.10(a) the model outputs are shown for varied void ratio. The 'cubic expression' was then written in an equivalent 'spherical expression'. Eq. 3.1 describes the uniform pressure distribution on the surface of a hemisphere and a cube of identical dimensions (Fig. 3.10(b))

Table 3.4 Stress distribution results

Void ratio	Effective area (cubic expression) – A_e	Effective area (spherical expression) – A_e	Mean normal contact force
0.000	4 d^2	$(\pi/2)$ 4d^2	$(\pi/2)\sigma'$ 4d^2
0.286	2.67 d^2	$(\pi/2)$ 2.67 d^2	$(\pi/2)\sigma'$ 2.67 d^2
0.330	3 d^2	$(\pi/2)$ 3 d^2	$(\pi/2)\sigma'$ 3 d^2
0.385	2.44 d^2	$(\pi/2)$ 2.44 d^2	$(\pi/2)\sigma'$ 2.44 d^2
0.600	2.5 d^2	$(\pi/2)$ 2.5 d^2	$(\pi/2)\sigma'$ 2.5 d^2
0.800	2.22 d^2	$(\pi/2)$ 2.22 d^2	$(\pi/2)\sigma'$ 2.22 d^2
1.000	2 d^2	$(\pi/2)$ 2 d^2	$(\pi/2)\sigma'$ 2 d^2
1.250	1.67 d^2	$(\pi/2)$ 1.67 d^2	$(\pi/2)\sigma'$ 1.67 d^2
1.286	1.625 d^2	$(\pi/2)$ 1.625 d^2	$(\pi/2)\sigma'$ 1.625 d^2
1.670	1.5 d^2	$(\pi/2)$ 1.5 d^2	$(\pi/2)\sigma'$ 1.5 d^2
2.200	1.25 d^2	$(\pi/2)$ 1.25 d^2	$(\pi/2)\sigma'$ 1.25 d^2
2.600	1.11 d^2	$(\pi/2)$ 1.11 d^2	$(\pi/2)\sigma'$ 1.11 d^2
3.000	1 d^2	$(\pi/2)$ 1 d^2	$(\pi/2)\sigma'$ 1 d^2
>3.000	1 d^2	$(\pi/2)$ 1 d^2	$(\pi/2)\sigma'$ 1 d^2

$$d_{squ.}{}^2 = \frac{1}{2} 4\pi \left(\frac{d_{sph.}}{2}\right)^2 \Rightarrow d_{squ.} = d_{sph.}\sqrt{\frac{\pi}{2}} \qquad Eq.\ 3.1$$

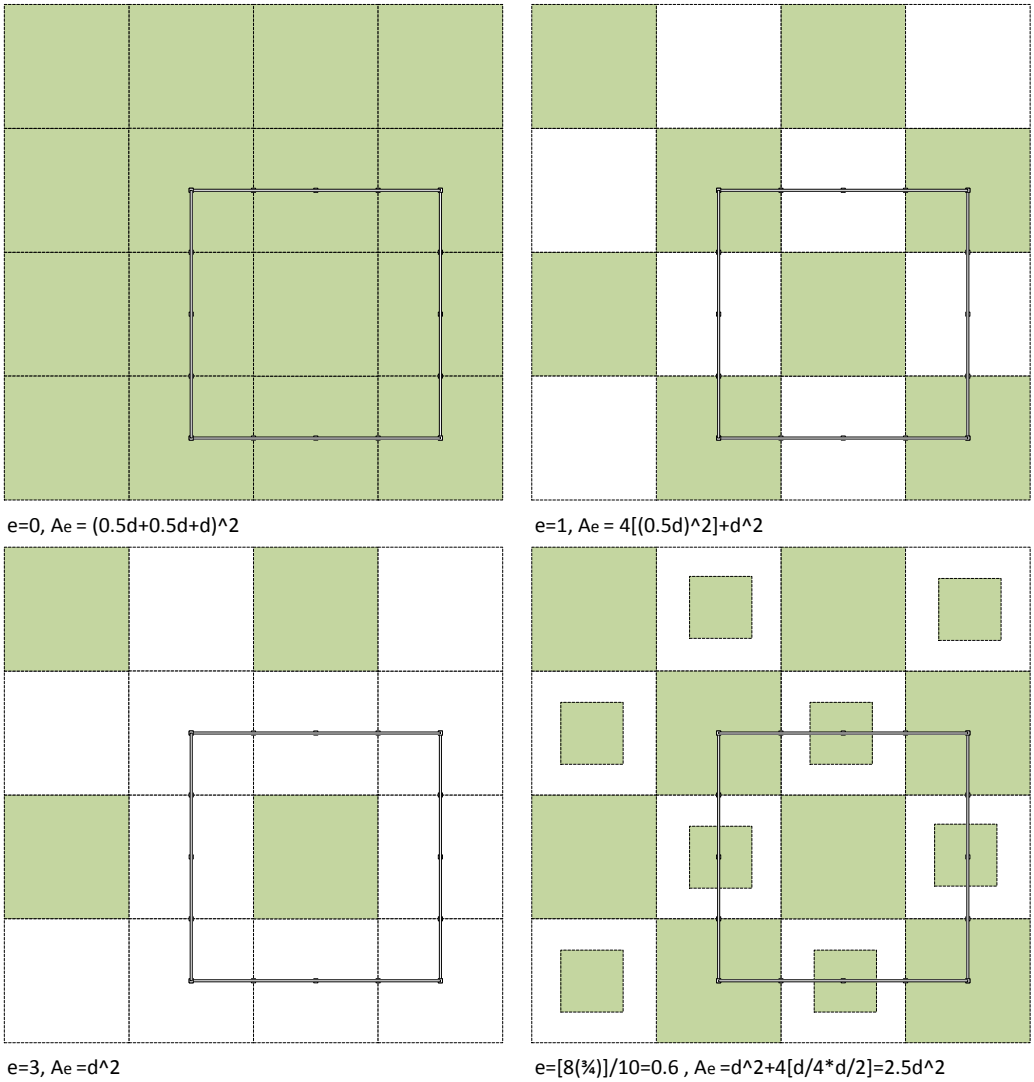

Fig. 3.10(a) DEM outputs for e=0, e=0.6, e=1.0, and e=3.0

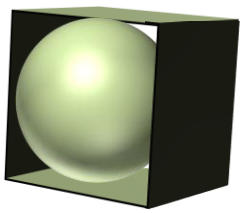

Fig. 3.10(b) Cube of d_{squ} in width, which surrounds a sphere of d_{sph} in diameter

For a two-dimensional stress distribution, the mean normal contact force is:

$$F_{(N)ske} = \sigma'.f\{e,d\} \qquad Eq.\ 3.2$$

where $f\{e,d\}$ is a function of void ratio and particle mean diameter, and can be expressed in an exponential form using a non-linear regression using the Levenberg-Marquardt algorithm (Pereira da Silva and Pereira da Silva, 2011):

$$f\{e,d\} = \frac{\pi}{2} d^2 . A . exp\left(B . e + C\sqrt{e}\right) \qquad Eq.\ 3.3$$

Where A, B, and C are equation constants and are obtained as detailed in Table 3.5. $A . exp\left(B . e + C\sqrt{e}\right)$, is plotted against the void ratio in Fig. 3.11.

Table 3.5 Equation constants

Equation constant	Value	Standard Deviation
A	0.399686E+01	0.134100
B	-0.1431937E0	0.691641E-01
C	-0.5718751E0	0.997244E-01

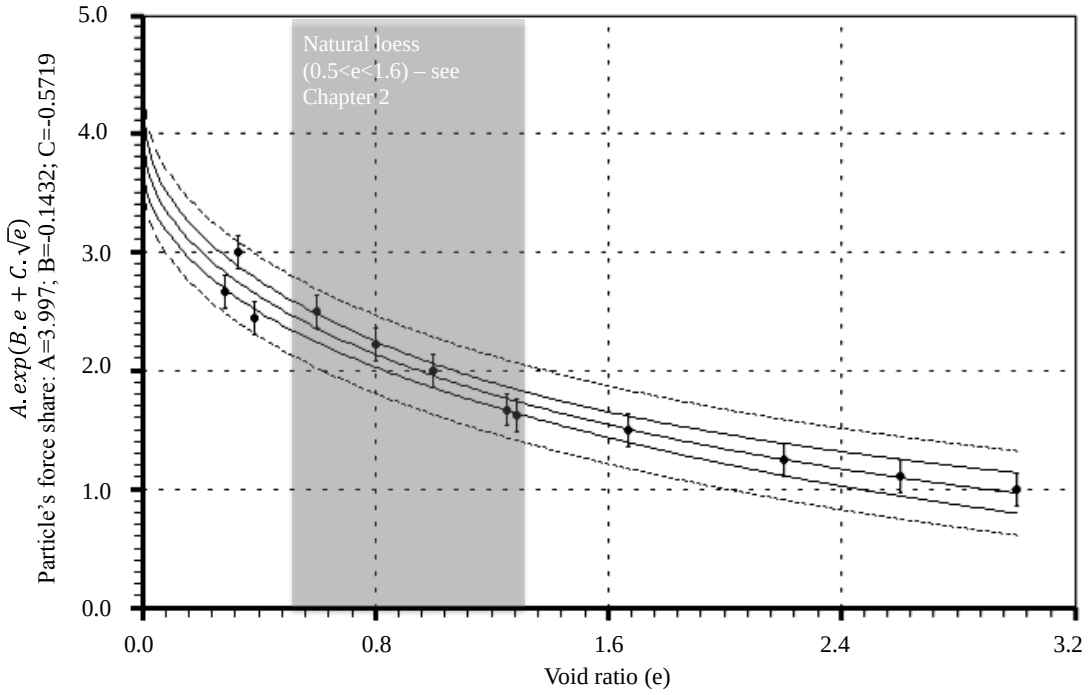

Fig. 3.11 Share of a particle's boundary-level force versus void ratio

Along the course of wetting, the buoyant, hydro-static and drag forces rely on the extent of which the waterfront travels in the soil column. It was here assumed that the travel distance of the waterfront via capillary rise was linearly and directly proportional to the wetting time. The drag force is a factor of the hydraulic gradient, which is derived at demarcated time intervals as detailed in Section 3.3.5.3. The formulation of active internal forces is described in Eq. 3.4-3.9, and Eq. 3.12-3.13.

$$F_{(N)ske} = (\sigma - u_a)_0 \times d^2 \times \left(\frac{\pi.(1+e^2)}{12}\right)$$
$$= \sigma_{ext} \times D_{50}^2 \times \frac{\pi}{12} \times \left[1 + \left(\frac{\dot{H}_i - H_s}{H_s}\right)^2\right] \qquad (After\ Santamarina\ 2003 - Eq.3.4)$$

$$F_{(N)ske} = \sigma'.f\{e,d\} = \sigma'.\frac{\pi}{2}d^2.A.exp\left(B.e + C\sqrt{e}\right) \qquad (After\ Assadi\ model - Eq.3.5)$$

$$F_{Drag} = 3\pi \times \mu \times V \times d = 3\pi \times 10^{-3} \times D_{50} \times \frac{K_i \times i_i}{n_i} \qquad Eq.\ 3.6$$

$$F_B = Vol._{solid} \times \gamma_w = \frac{1}{6} \times \pi \times \gamma_w \times D_{50}^3 \qquad for\ t > {}^{t_1}/_2$$

$$F_B = 0 \qquad for\ t \leq {}^{t_1}/_2 \qquad Eq.\ 3.7$$

$$U = 0.5\left(\frac{\dot{H}_i}{2} + \dot{H}\right).\rho_w.4\pi.\left(\frac{D_{50}}{2}\right)^2 \qquad for\ t \geq t_1 \qquad Eq.\ 3.8$$

$$W = \sum W_j = \frac{\dot{H}_i}{2D_{50}} \times \frac{1}{6} \times \pi \times \gamma_w \times G_s \times D_{50}^3 \qquad Eq.\ 3.9$$

Where $F_{(N)ske}$ is the mean normal skeletal force for a random packing of spheres at the contact point (Fratta and Santamarina, 2005), 'U' is the hydrostatic force (i.e. integral of the fluid pressure, which applies to the chain of particles), 'F_B' is the buoyant force and 'W' is the weight force. σ_{ext} is the applied net stress, $\dot{H}_i$ is the specimen height at each increment, H_s is the height of the solid column within the specimen, and $\dot{H}$ is water overhead. Drag force was estimated via Stoke's equation at low Reynolds numbers (Bear, 1972, Graf, 1984, Santamarina, 2003). 'i' is the hydraulic gradient, 'n_i' is the porosity, 'μ' is the viscosity of water (0.001 N.S/m^2 at 20°C), and K_i is the coefficient of permeability, which can be derived at the saturated state through a Terzaghi consolidation test setup (Fig. 3.12(a) and Eq. 3.10). The initially excess pore water pressure formed immediately after loading was assumed to be constant throughout the height of the specimen (a common simplifying assumption in Terzaghi's theory).

$$m_{v(i)} = \frac{H_{i-1} - H_i}{H_{i-1}} \times \frac{1000}{\Delta\sigma_i - \Delta\sigma_{i-1}};\ C_{v(i)} = \frac{0.0848 \times {H_{dr}}^2}{4t_{90}} = \frac{0.3392 \times {H_i}^2}{4t_{90}};$$

$$k_i = C_v \times \gamma_w \times m_v \qquad Eq.\ 3.10$$

Where $m_{v(i)}$ stands for the coefficient of volume compressibility at increment 'i', $C_{v(i)}$ is the coefficient of consolidation at increment 'i', and 'K_i'

represents the coefficient of permeability at loading increment 'i'. the obtained permeability values agree with much of the reported values in similar soils (e.g. 0.25-0.35 m/d in Bulgarian silty loess reported in Evstatiev (1995)). The unsaturated coefficient of permeability was derived through Eq. 3.25 and was plotted against wetting time in Fig. 3.12(b).

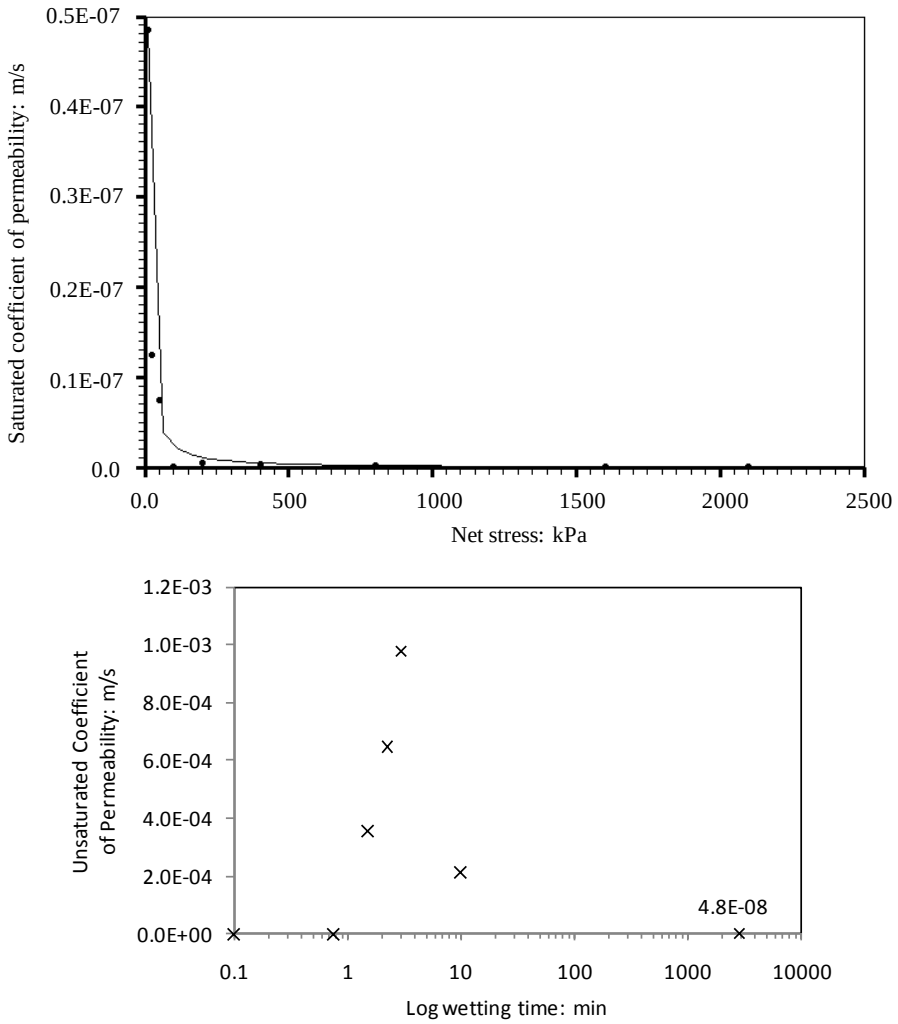

Fig. 3.12(a) Plot of saturated coefficient of permeability against net stress, (b) plot of unsaturated coefficient of permeability against the wetting time

The weight force was assumed compressive and aligned with the gravity direction. The buoyant force was assumed tensile, reducing either the normal skeletal or weight forces. Any decrease in specimen's height led to a decrease in water head and thus a decrease in the hydrostatic force.

Capillary force is a factor of the shape of the meniscus formed at the particle contact points. It can be funicular (i.e. analogous to buttress connectors) or pendular (i.e. analogous to bridge connectors) in shape at high (ω_f) and low (ω_p) water contents, respectively. The pendular state of a water

film is associated with high matric suction values and occurs at very low moisture contents, where disconnected water remains in the form of menisci at the interparticle contact. The funicular state of water film is associated with low matric suction values and occurs at high moisture contents, where the fluid phase remains continuous (Santamarina, 2001). Fig. 3.13 shows the progressive development of meniscus at the interparticle contacts for a pair of micro-size silica spheres (Lourenco et al., 2012).

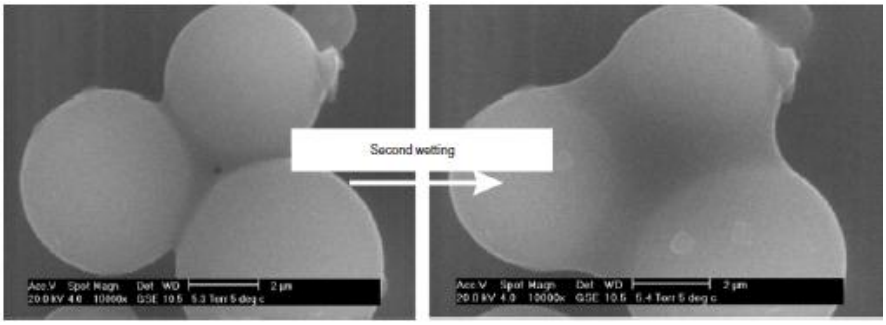

Fig. 3.13 ESEM images of wetted silica spheres; (left) water film in pendular state; (right) water film in funicular state (Lourenco et al., 2012)

The funicular state capillary force is conventionally estimated by solving the Laplace's differential equation for unique curvature radii (Eq. 3.11 (Santamarina, 2003)).

$$F_{cap} = \frac{T_s}{d_{pore}} \times 0.5 \times \left[4\pi \left(\frac{D_{50}}{2}\right)^2\right] = \frac{\pi \times D_{50}^2 \times T_s}{2d_{pore}} \qquad Eq.\ 3.11$$

where d_{pore} denotes the mean pore size (i.e. corresponding with the D_{50} and void ratio at $\omega = \omega_f$ and derived here from the Arya-Paris pedo-transfer function) and T_s is the surface tension for water-air interface at room temperature (Fredlund and Rahardjo, 1993).

The pendular state capillary force is reportedly approximated by solving the Laplace differential equation for different principle curvature radii values (Soulie et al., 2006). A good deal of research has focused on the formulation of the pendular water film. The early formulations concerned the capillary force of a buttress water film, supported with two spherical particles in direct contact. However these lacked accuracy in restricting the capillary water to form between pairs of same-size grains, which are linked directly

together. This inaccuracy can be discussed in light of the early work of Haines (1925). Haines (1925) plotted the apparent cohesion (capillary forces) against the increasing water content for uniform rigid spherical particles. At low water contents, for a pair of spheres ('a' in radius) in direct contact, Haines reported the formation of a water film with curvature radii of 'r_1' and 'r_2' (in two perpendicular principal directions). The total pull force between the spheres was formulated (see Eq. 3.12), where T is the surface tension and 2θ is $Arctan\ \frac{r_1+r_2}{a}$. Haines (1925) then formulated the apparent cohesion as $\sum_{i=2}^{n} \Pi_i$, where 'n' was the number of particles in the soil and Π was the pull force over unit cross section area for any given contact. To calculate the unit cross section area, Haines (1925) inspected two extreme packing states: open and closed packing. For the closed state, grains received support from 12 points around their perimeter[22]. For the open state, the number of contact points per grain reduced to six. He scaled down the numbers to four and two for a planar condition and on the main load-bearing axis, respectively. On this basis, the calculated cross section areas of $2\sqrt{3}a^2$ and $4a^2$ for close and open states of packing rendered the pull forces of $4 \times 2\pi aT.\frac{1-2\tan\theta}{1+tan\theta}\frac{1}{2\sqrt{3}a^2}$ for the close packing and $2 \times 2\pi aT\frac{1-2\tan\theta}{1+\tan\theta}\frac{1}{4a^2}$ for the open packing. The validity of these values, however, could be questioned; the argument generally concerning the predominance of in-direct connectors between grains. The water film can appear at the void space or alternatively as a coat to the inter-particle connectors.

$$P = 2\pi a.T.\frac{1-2\tan\theta}{1+\tan\theta} \qquad Eq.3.12$$

To resolve this limitation, the Laplace differential equation (Soulie et al., 2006) was written by deriving the volume of the liquid bridge. The internal

[22] Coordination number of twelve, made up of 6 contact points on the plane x-y surface, and 3 contact points on top, together with 3 contacts points on bottom along the z-surface (normal to the x-y surface):

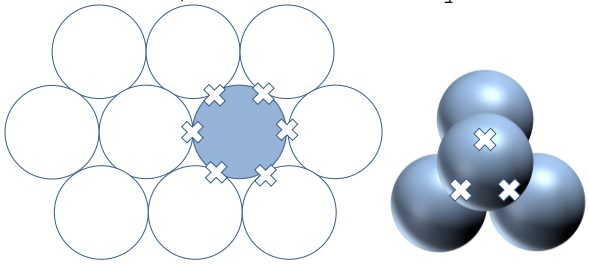

radii of the principle curvature of water film at pendular level was assumed equal to the mean radius of the inter-particle pore space (Hillel, 1998). The mean pore size was associated with the mass-mean-diameter (D_{50}), which was indirectly approximated by using an appropriate pedo-transfer function (i.e. Arya-Paris model explained in (Arya and Paris, 1981, Arya and Paris, 1982, Haverkamp and Parlange, 1982, Arya et al., 1999). Fig. 3.14 shows a schematic of the geometric representation of a water film (bridge) between two particles of unequal sizes. This leads to:

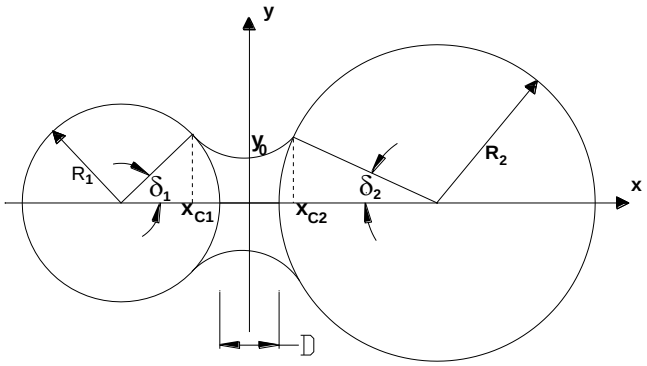

Fig. 3.14 Liquid bridge geometry between two particles

$$F_{cap} = \pi \times T_s \times \sqrt{R_1 \times R_2}.\left[c + exp\left(a\frac{D}{R_2} + b\right)\right]$$
$$= \pi.T_s.\sqrt{\left(\frac{D_{50}}{2}\right)^2}.\left[c + exp\left(a \times d_{pore} \times \frac{2}{D_{50}} + b\right)\right] \quad Eq.\ 3.13$$

Where

$$a = -1.1 \times \left(\frac{V}{R_2^3}\right)^{-0.53} = -1.1 \times \left(V \div \left(\frac{D_{50}}{2}\right)^3\right)^{-0.53} \quad Eq.\ 3.14$$

$$b = \left(-0.148Ln\left(\frac{V}{R_2^3}\right) - 0.96\right)\Theta^2 - 0.0082\mathrm{Ln}\left(\frac{V}{R_2^3}\right) + 0.48$$
$$= \left(-0.148Ln\left(V \div \frac{D_{50}{}^3}{2}\right) - 0.96\right) \times \Theta^2 - 0.0082\mathrm{Ln}\left(V \div \frac{D_{50}{}^3}{2}\right) + 0.48 \quad Eq.\ 3.15$$

$$c = 0.0018Ln\left(\frac{V}{R_2^3}\right) + 0.078 = 0.0018Ln\left(V \div \frac{D_{50}{}^3}{2}\right) + 0.078 \quad Eq.\ 3.16$$

$$V = 2R\left(\int_{x_{c1}}^{x_{c2}} y^2\,(x)dx - 2s\right)$$

$$= 2R \times \left\{\left[2\int_{-\left(R+\frac{D}{2}-\frac{(r_1+r_2)Rcos\delta}{R+\frac{D}{2}}\right)}^{\left(R+\frac{D}{2}-\frac{(r_1+r_2)Rcos\delta}{R+\frac{D}{2}}\right)}\int_0^{R.sin\delta}(x^2+y^2+A^2-2Ay-{r_1}^2)^2 dydx\right] - 2s\right\} \qquad Eq.\ 3.17$$

Where:

$$s = \frac{\pi.R^2}{360}\times 2\delta - \frac{R^2}{2}.Sin2\delta \qquad Eq.\ 3.18$$

$$A = (R + r_1).Sin\delta \qquad Eq.\ 3.19$$

$$\delta = ArcCos\left(\frac{R+\frac{D}{2}}{R+r_1}\right) \qquad Eq.\ 3.20$$

Where Θ is the contact angle between the contractile skin (i.e. zero for pure water and glass after Fredlund and Rahardjo (1993) and between clean quartz grains), r_2 is the internal radius of the principal curvature and r_1 is the external radius, which can be estimated from the Laplace equation as follows:

$$(U_a - U_w)_p = T_s \times \left(\frac{1}{r_1} - \frac{1}{r_2}\right) \qquad Eq.\ 3.21$$

The matric suction at the pendular state can be estimated from the Soil Water Characteristic Curve (SWCC), which is here derived from the Arya-Paris pedo-transfer function. Matric suction values were derived for a given void ratio and volumetric water content. The super-imposed active and passive forces are summarized as follows (Fig. 3.15):

$$Active: \quad W + U + \underline{F_{(N)ske}} - F_B - F_{Drag}$$

$$Passive: \quad Att - Rep + F_{cap} + T \qquad Eq.\ 3.22$$

Where 'Att' is the electrostatic attraction force, 'Rep' is the repulsive force and 'T' stands for the maximum tensile force (i.e. cementation). The ratio of passive to active forces of Eq. 3.22 seems analogous to in 'R' parameter in the R/size diagram devised in Smalley and Dijkstra (1991) and later in Dijkstra et al.(1994) and Jefferson and Smalley (1995).

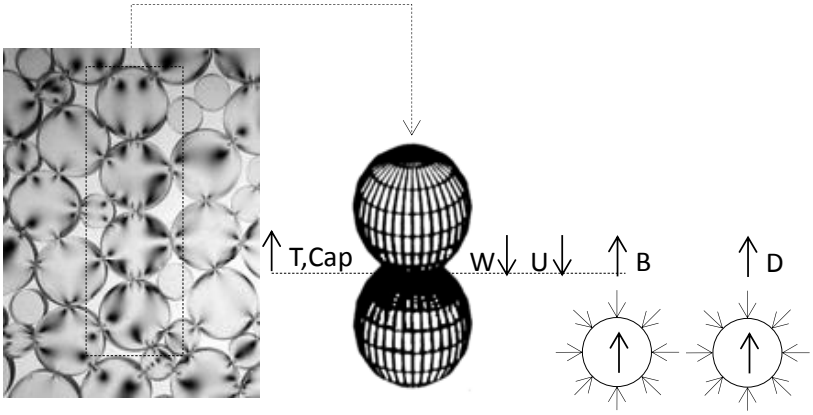

Fig. 3.15 Super-imposed internal forces operating on a grain-to-grain contact point

3.3.4.5 Model Scenarios

Having identified and formulated the internal forces in the previous section, these were attempted to be measured on identical 'ideal loess' testing specimens. At an initial trial phase, different combinations of loading and wetting patterns were implemented, making up four scenarios (i.e. modes), as explained in Table 3.6. The third and fourth wetting-loading regime (modes 3 and 4) were concluded appropriate for the purpose of internal force measurement. The mode 3 was eventually selected as the most appropriate set-up and was used in the final testing process. The four testing scenarios and their evaluation are explained throughout this section.

Table 3.6 Physical properties of the synthesised specimens (see Section 3.4 for the detailed account of specimen preparation process)

Mode	Gs	Depositional phase				Post-depositional phase		
		ω (%)	γ_m (kN/m3)	e	S_r (%)	ω (%)	e	γ_m (kN/m3)
1	2.85	5.98	8.13	2.64	6.46	0.60	1.19	12.1
2	2.85	10.08	8.45	2.64	10.88	0.60	1.08	12.7
3	2.85	6.33	8.20	2.62	6.87	0.60	1.41	11.01
4	2.85	8.67	9.95	2.05	12.04	0.60	1.32	11.43

In mode 1, a net stress greater than the swelling pressure (at the hygroscopic water content) was applied. Wetting under such pressure led to self-weight compression followed by self-weight unsaturated consolidation (Fig. 3.16). In mode 2, a net stress lower than the swelling pressure (at the hygroscopic

water content) was applied. Wetting under such stress led to swelling (Fig. 3.16).

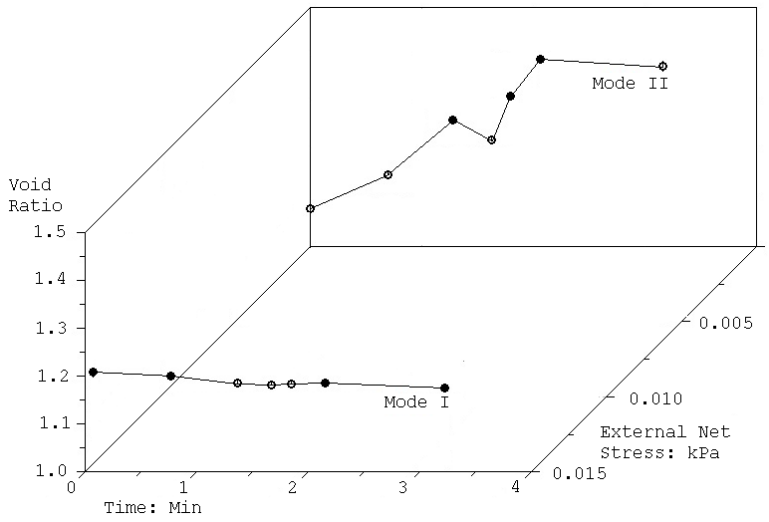

Fig. 3.16 Volume change through suction decrease – modes 1 and 2

None of the two first modes (described above) were found suitable for the purpose of measuring the internal stresses. This was due to the need for a combined swelling-collapse volume changes to measure the internal forces (drag force in particular) in a general context. This was satisfied in modes 3 and 4 (Fig. 3.17), through which a net stress slightly lower than the swelling pressure (at the hygroscopic water content) was applied to the soil (0.015kPa).

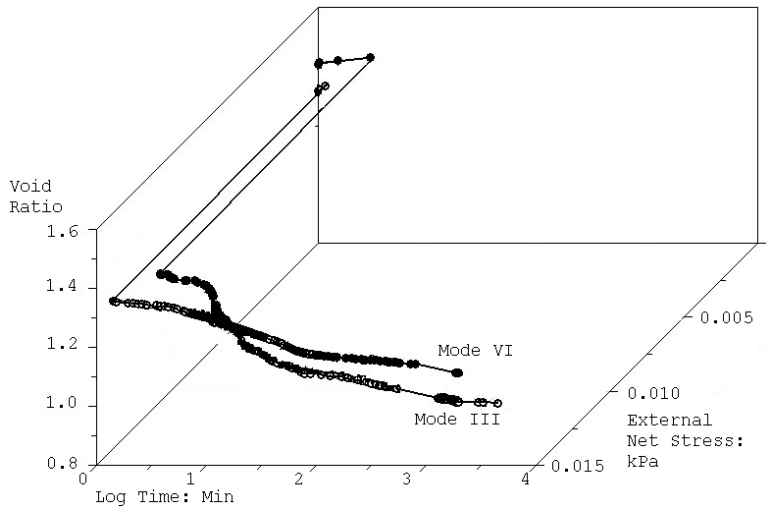

Fig. 3.17 Void ratio change along suction decease – modes 3 and 4 (mode 3 to be fully commented and analysed in Chapter 4)

Modes 3 and 4 differ from each other in the wetting regime. In mode 3, the soil was wetted through an initial steady state flow for 70 minutes through the lower porous disc (i.e. under a constant head of water column) followed by a period of standing water (phreatic condition). This imitated the inflow of ground water followed by a non-flowing phreatic condition. In mode 4, the soil was wetted through capillary rise for 90 hours through the lower porous disc, followed by a period of standing water (phreatic condition). This simulated the capillary-rise of ground water followed by a non-flowing phreatic condition. A dry laterally confined 75 mm in diameter oedometer specimen was placed on a Whatman No.40 filter paper overlying a boiled, oven-dried, and cooled porous disc. The assemblage was placed in a graduated Perspex cylinder. A 75 mm in diameter non-porous transparent cap was placed on top of the specimen to supply a seating pressure of 0.015 kPa. Distilled water was poured into the cylinder to the lowest surface of oedometer ring. Water was allowed to penetrate into the specimen, while the height of specimen was measured in a timed manner by means of three 0.002 mm compression dial gauges set on the top cap, at 120° angle (i.e angle between any two dial gauge tips on the surface of top cap). Average values of dial gauge recordings were used to determine the void ratio. In Fig. 3.11, the soil specimen in mode 3 slightly swelled after the introduction of the net stress and then collapsed sharply. Hence, mode 3 was deemed the most informative wetting scenario and is studied in Chapter 4.

3.3.5 Dynamics of Effective Stress (Collapse Micro-mechanism Framework)

3.3.5.1 Significance

Constitutive stresses, $\bar{\boldsymbol{\sigma}}$, are used in constitutive models to predict the solid deformation (volume change), $\boldsymbol{\varepsilon}$. The effective stress, σ', is a constitutive stress commonly used to simulate the behaviour of earth structures in dry and wet conditions. With unsaturated collapsing soils, Jennings and Burland (1962) criticized that Bishop's equation (most frequently practiced form of the effective stress principle) can provide an adequate relation between volume change and effective stress (see Section 2.6, Chapter 2). As a closing to the Level I studies, the evidences obtained on the multi-porosity nature of collapsing soils (in Section 3.3.2 and Chapter 4) and the role of drag forces

in bypassing the water through such a multi-porous network (in Section 3.3.4 and Chapter 4), were read together to explain the collapse through a modified form of the principle of effective stress.

3.3.5.2 Overview

The general philosophy behind the proposed modified formulation is the recent contributions made to the principle (Bagherieh et al., 2009, Alonso et al., 2010, Khalili et al., 2005, D'onza et al., 2011), which considered two distinct void spaces (i.e. micro- and macro- pores) in the formulation of the χ parameter (i.e. weighing factor). Although the problem of collapse can be partially explained via these contributions, the principle still fails to explain the initial swelling volume changes upon wetting at net stresses lower than the swelling pressure and also the change in the pattern of volume changes between the first and the proceeding cycles of seasonal drying-wetting (all fully detailed in Chapter 4, Section 4.6.2).

The modified principle is written for a soil domain consisting of solids surrounding two levels of macro-void spaces (i.e. trans- and macro-pores), which are bound together by a transitional void space (micro-pore). This arrangement corresponds well with the double porosity concept that considers distinct pore spaces, which, periodically and sequentially, accommodate migrated fines, air or water. Among these pore spaces, drag stress will be shown operating temporarily on micro-pores, to deliver the positive excess pore water pressure from the fluid to the solid phase. The stress is successfully attempted as a third stress variable (operating on a unit-side square domain), and is introduced to the general form of the principle. Finally, the modified form of the principle is verified for drying-wetting cycles on an artificial clayey silt loess sample.

3.3.5.3 Materials and Methods

The ‘ideal loess’ laterally confined testing specimen was wetted under the mode 3 condition. Void ratio was measured throughout the wetting process in a timed pattern. Likewise, thirteen identical ‘ideal loess’ testing specimens were wetted under the mode 3 condition over a 0.75, 1.5, 2, 2.25, 3, 5, 7, 10, 80, 160, 320, 720, and 1527 minutes period. Water contents were measured by the end of the wetting periods. The void ratio and the water content data were

coupled with the outputs of a standard filter paper test, conducted on the 'ideal loess' specimen, to correlate the water content (and saturation ratio), void ratio, matric suction, and wetting time. Permeability was estimated for varied wetting time by conducting a coupled constant head oedometer (mode 3) wetting – water content test. Bulk fluid temperature was constantly measured to estimate the viscosity of water (Fredlund and Rahardjo, 1993). For 'ideal loess', the mean particle and pore size were extracted from the particle and pore size distribution curves. Having the water viscosity, the mean particle size, the permeability, the void ratio, and the hydraulic gradient, drag force was computed using Stoke's equation at low Reynolds numbers (Bear, 1972, Graf, 1984, Santamarina, 2003) as a factor of the distance that waterfront travels through the soil column (Santamarina, 2003). Considering a domain of unity in size, and having the timed variation of void ratio, matric suction, drag force, and net stress; a modified form for the principle of effective stress was formulated and qualitatively assessed through the wetting and drying cycles. In addition to the ideal loess specimen, the wetting-drying outputs on clayey silt specimens of varied kaolinite content were also used to qualitatively verify the proposed form. Methods to conduct above test procedures were developed in previous sections, except with the drag force development, which is detailed in this section.

An oven-dried 'ideal loess' oedometer specimen (75 mm in diameter) was assembled in a graduated Perspex oedometer chamber. The specimen was directly put on top of a boiled, oven-dried, and cooled porous disc and Whatman No 40 filter paper of a cumulative thickness of t_{SL}. To measure and control the water head in oedometer chamber (H_w), a graduated (at 0.02 ml increments) glass pipette was vertically passed through the flanged top disc to the bottom of the chamber. A syringe was used to refill the water chamber throughout the wetting process. The volume of chamber was carefully measured by an electronic micrometre, allowing the estimation of the volume of water travelling into the porous disc and specimen. The pore volume of the disc was estimated by weighting the porous disc at 20°C under both oven-dried and fully saturated states. The specimen was flooded through the lower drain point. Three compressive gauges were set on a transparent top cap (overlaying the specimen) at 120° angle. The specimen's height was recorded against the wetting time

upwards from 0 second at intervals of ten seconds. A constant head flow condition was followed throughout. According to the Stoke's law:

$$F_{Drag} = 3\pi \times \mu \times V \times d = 3\pi \times 10^{-3} \times D_{50} \times \frac{K_i \times i_i}{n_i} \qquad Eq.\ 3.23$$

Where unsaturated coefficient of permeability (K_i) was estimated at $t = t_i$, porosity (n_i) was measured at $t = t_i$, mean particle size (D_{50}) was assumed constant under an applied low net stress (Sections 4.2 and 4.3), and i_i was written (see Eq. 3.24 below) for three equal time fractions of $0 \le t < {t_1}/{2}$, ${t_1}/{2} \le t < t_1$, $t \ge t_1$, where t_1 was the time elapsed between the arival of the water at the top of the sample and the beginning of the percolation at its base. It was assumed that the capillary water travels to the half-height of the specimen's column by $t = t_1$. Thus:

$$\forall\ 0 \le t < {t_1}/{2} \Rightarrow\ i = 0$$

$$\forall\ t = {t_1}/{2} \ \Rightarrow\ i = \frac{\Delta H}{H} = \frac{H_w - (t_{SL} + \frac{H_i}{2})}{{H_i}/{2}}$$

$$\forall\ {t_1}/{2} < t < t_1 \Rightarrow\ \ i = \frac{\Delta H}{H} = \frac{H_w - (t_{SL} + {3}/{4}\,H'_i)}{{3}/{4}\,H'_i}$$

$$\forall\ t = t_1 \Rightarrow\ \ i = \frac{\Delta H}{H} = \frac{H_w - (t_{SL} + H''_i)}{H''_i}$$

$$\forall\ t > t_1\ \Rightarrow i = \frac{\Delta H}{H} = \frac{H_w - (t_{SL} + \overline{H_{T_i}})}{\overline{H_{T_i}}} \qquad Eq.\ 3.24$$

where $\overline{H_{T_i}}$ was the height of the specimen at $t = t_i$, t_{SL} was the thickness of the lower porous stone in oedometer set, H''_i was the height of the specimen at $t = t_1$, H'_i was the height of the specimen at $t = {3t_1}/{4}$, and H_w was the height of the water column in the oedometer chamber.

The unsaturated coefficient of permeability was obtained by conducting a coupled constant head oedometer wetting - water content controlled oedometer test. Thus:

$$\forall\ t = t_i \Rightarrow K_i = \frac{Q_i}{i_i \times A} = \frac{\frac{V_{w_i} - V_{w_{i-1}}}{t_i}}{i_i \times A},\ \ whereby,$$

$$V_{w_i} = S_{r_i} \times \frac{\overline{H_{w_i}}}{\overline{H_{T_i}}} \times e_i \times V_s \qquad Eq.\ 3.25$$

Where $\overline{H_{w_i}}$ was the height to which water climbs within the specimen at $t = t_i$. Applying Eq. 3.23-3.25, the drag force operating on the test domain was plotted against wetting time (and saturation ratio). To bring the obtained trend of drag force into the effective stress expression, the drag force was formulated for four ranges of saturation ratio at the clay level, between zero and one, and among the air entry and air expulsion values. Any of these four ranges are tightly associated to a specific repeatable pore space. To examine the variation of drag force within the four phases of saturation ratio, a Soil Water Characteristic Curve (SWCC) was first produced (Section 3.3.2.4). To assign specific pore sizes to each of these four phases of saturation ratio, pore size distribution curves were produced (Section 3.3.2.6).

A range of limitations applies to the new form of the effective stress principle, including:

(1) The new form of the principle is neither valid for clay (i.e. active or non-active) nor the clean silt/sand soils. The presence of a multi-porous medium is the backbone of the computations. The modified form is however valid for loess, in which silt is a predominant component.

(2) The new form of the principle is capable of explaining the early rebound volume change, collapse, and following rebound volume changes upon seasonal wetting and drying. Nonetheless, the capability of the principle to provide the exact value of the effective stress at a given wetting time is left to be researched. The present conceptual form of the modified principle satisfies the Level I objective (i.e. determining the collapse mechanism framework).

A suite of assumptions applies to the formulation of the principle, including:

(1) The soil is isotropic and homogeneous. The soil properties are independent of the soil domain size.

(2) Grains are mono-dispersed in size and spherical in shape.

(3) Grain crushing and thus the chance of any change in mass mean diameter is assumed slim.

It is also assumed that:

A suite of assumptions was set to develop the modified form of the principle of effective stress:

(1) The solid constituent is assumed incompressible. However, if the formulation is to be used for an undrained system (applying to any soil immediately after the load application), under a net stress greater than fragmentation load (i.e. average load causing breakage in grains), grains split and an excess pore water pressure builds up. This decreases the effective stress (see Section 2.4.2.1). The modified form of the principle appreciates this decrease by a third new stress variable (see Chapter 4). As explained in Chapter 4, the drag force delivers the energy of the excess pore water pressure to the grains at the expense of a temporary decrease in the effective stress.

(2) The fluid distribution is discontinuous.

(3) In Section 4.3 it is shown that independent pore subspaces (inter- and intra-assemblage) enclose domains of solids and fluids. Individual pore spaces respond to stressing as individual entities (Borja and Koliji, (2009)).

3.4 Level II: Fine Soils Classification and Collapse Modelling

Many combinations of silt, kaolinite clay, carbonate, amorphous silica, sulphates, and climate are used in Level II to engineer a range of fine-grained soils. These soils are then systematically classified and examined to identify the specific modes of collapse involved in each specific class. Collapse mechanism is explained within the framework developed in Level I.

3.4.1 Specimen Preparation: Aeolian Soils (Loess)

The engineering of artificial loess involves the simulation of provenance (silt formation), depositional, self-weight loading, and post-depositional events. The latter includes seasonal wetting-drying, high di-electric ground water flow (i.e. leaching salty upper soil layers) and chemical (thermal) weathering. Primary clay and secondary crystals of salt were formed through

the depositional events. A change of packing from the initial unstable state to metastable state took place through self-weight loading. Secondary clayey bonds, medium-soluble carbonate bonds as well as reinforced clayey and calcareous bonds with silica and metal-based sulphates formed by the end of the post-depositional events (Fig. 3.18).

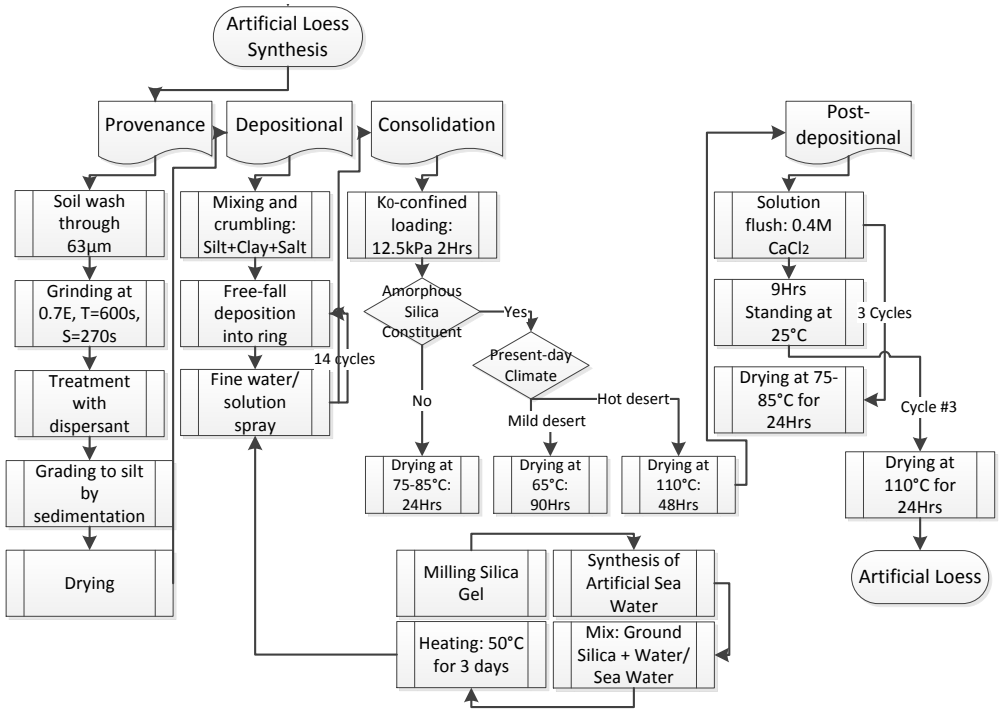

Fig. 3.18 The work flow diagram showing the synthesis of artificial loess specimens (see details discussed in 3.4.1.1 to 3.4.1.5)

3.4.1.1 Provenance Events

To produce the desired silt fraction, Leighton Buzzard Sand was initially washed with tap water (and then Calgon) through a 63 μm sieve to remove the silt- and clay-sized fragments. The oven-dried sand was then milled in a Siebtechnik disc mill for ten 60 s long grinding intervals, each followed by a 30 s cooling period (to prevent overheating). Standard sedimentation (i.e. the use of Stoke's law) were undertaken to extxract the 2 to 63 μm silt fraction. The produced silt had a marked mode size of 10-20 μm, not untypical of many loessic soils (Assallay et al. 1998). Fig. 3.3 in Section 3.3.3.2 shows the particle size distribution of sand, crushed sand, and graded crushed sand.

3.4.1.2 Depositional Events

Predetermined contents of oven-dried ground and graded Leighton Buzzard Sand, kaolinite, and anhydrous Sodium Carbonate were crumbled and mixed thoroughly in a beaker. An example of the particle size distribution of the mixed material is shown in Fig. 4.37 (Chapter 4). The process is shown in Plate 3.1 (1-4).

The mix was pluviated into a standard 75 mm oedometer ring from a constant height of 400 mm via a nozzle. Distilled water was finely sprayed on the top surface of each freshly deposited layer (of 2 mm in thickness) from a distance of 500 mm. This simulated the deposition of dry dust passing across a wet-land. The sequences were continued to form a deposited column of 27.5 mm high.

With silica-indurate soils, a super-saturated silica solution (instead of water) was sprayed on the pluviated dry soil layers, which consisted of varied contents of ground sand, clay, and Anhydrous Sodium Carbonate. Spraying allowed the structure-less silica to distribute evenly on the solids as well as in the pore network. To produce silica solution (i.e. poly-silicic acid), 4g (i.e. 10 times the solubility to provide the super-saturation condition) of finely ground silica (i.e. powder prepared by milling silica gel) was poured into a Pyrex beaker containing one litre of either artificial sea water (for soil with metal-based sulphates) or distilled water. The method used to produce the artificial seawater follows the approach developed by Kato and Kitao (1968), by dissolving 24 g of Calcium Chloride $CaCl_2$, 11.5 g Sodium Sulphate Decahydrate $Na_2SO_4.10H_2O$, and 10.5 g Magnesium Chloride Hexahydrate $MgCl_2.6H_2O$ in distilled water to a volume of 1 litre. The silica solution was well stirred and heated to 50°C in closed glass containers for three days[23] [24].

Samples were then loaded to 12.5 kPa under K_0-condition. Consolidation simulated the solifluction/erosion of surface layers or the retreat of the ice during the early interglacial era. The pressure was maintained for two hours

[23] Solubility of silica gel in water (pH: 2-9) is 105-120 ppm at 22-27°C after few weeks time. Curing of silica solution at 50°C increased the rate of silica-water interaction (Krauskope, 1956).

[24] The use of seawater significantly increases the rate of silica dissolution (Krauskope, 1956). It also allows the homogeneous formation of sulphate bonds (i.e. through spraying) in loess specimens.

(Plate 3.1 (6)). The lightly over-consolidated moist samples were then gently dried at the temperature of 75 to 85℃ for more than 24 hours, to mobilize the clayey connectors and salt crystals and to imitate a semi-arid climate.

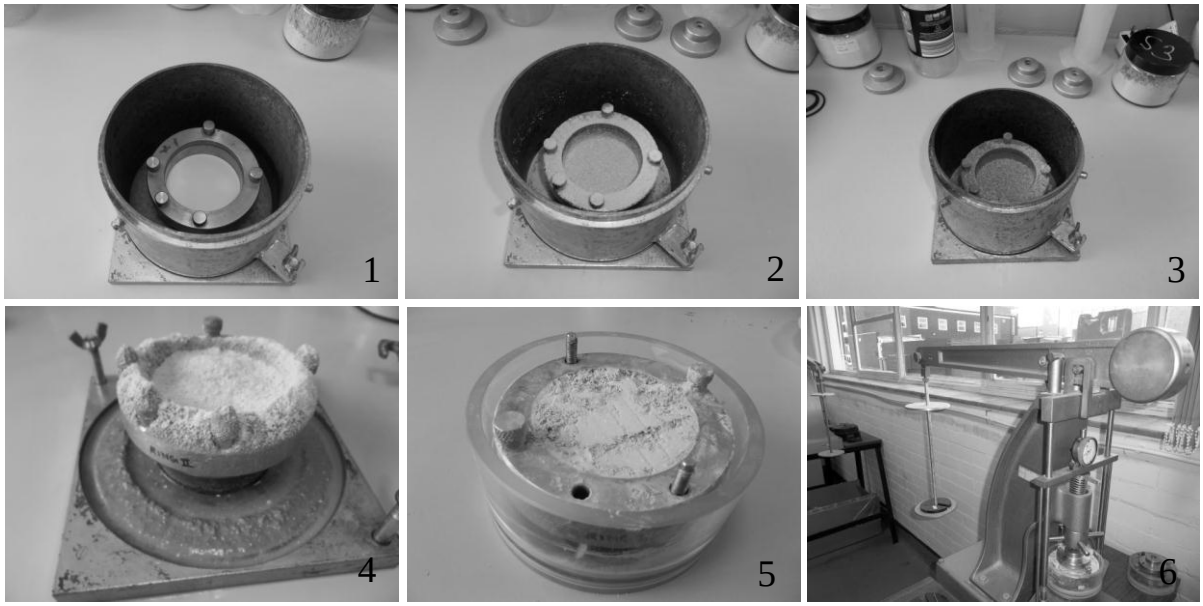

Plate 3.1 Air-fall deposition, wetting and pre-consolidation

With silica-indurate soils, both re-precipitation of silica from the super-saturated solution and evaporation of silica-contained water occurred in loess specimens. Capillary forces drove the re-precipitated silica fragments to the contact points of finest silt grains (i.e. which surround pore spaces of minimum diameter). Evaporation was achieved using two different temperatures to control the quality of precipitated silica, notably fast and slow rates of silica precipitation. As such, impregnated specimens were dried once at 110˚C for 48 hours and once at 65˚C for 90 hours. The benchmark 110˚C at 48 hours was chosen to ensure the drying of soil to water contents less than the hygroscopic water content according to BS:1377-2 (2002).

3.4.1.3 Post-depositional Events

A series of wetting and drying cycles were undertaken on oven-dried specimens with the aim of transforming the Anhydrous Sodium Carbonate units to Calcium Carbonates, by percolation of a Calcium Chloride solution through the loess. The 0.4 M $CaCl_2$ aqueous solution (pH=8.0-9.0) was introduced through capillary action over a 9 hour period at 25℃, follow the approach used by Akili and Torrance (1981). This imitated the inflow of high dielectric melt-water into

the soil in a mild climate. Treated samples were then dried at 75 to 85°C for 24 hours. A lower temperature than the advised 110°C of BS1377-2: 1990 was applied to supply enough time for the Calcium Chloride to interact with the sodium carbonates and form carbonates crystals. In all, three wetting-drying cycles were implemented. Test specimens were finally oven-dried at 110°C for 24 hours (BS1377-2, 1990). To investigate whether, and to what extent, the specimen preparation process is representative of natural loess, a selected sample containing 25% carbonate and 10% kaolinite was viewed in a scanning electron microscope (SEM), coupled with an electron dispersive X-ray (EDX) unit. X-ray diffraction (XRD) diffractogram ascertained the formation of Calcium Carbonate units. Any 1-litre reactant aqueous solution was prepared by dispersing 44.4 g of ground anhydrous $CaCl_2$ in 1-litre of distilled water (110.98 g/mol molar mass). The suspension was vigorously stirred with a glass rod to obtain a clear solution. Plates 3.2 and 3.3 show common morphological signatures of natural loess and engineered specimens.

Plate 3.2 [1], [2]: First and second wetting phases along the chemical treatment, [3] Kharg Island, the Gulf: the biogenic Calcium Carbonate (coral reef) and the underlying ML calcareous sand (Nasrollahi and Assadi, 2007, Van Paassen, 2009) which was mirrored in engineered specimens as a chloride-carbonate fragile skeleton

Plate 3.3 Natural lithification of Calcium Carbonate: [1] and [2] Lab-scale synthesis; [3] Combination of dissolution-re-precipitation of Calcium Carbonate close to plant roots at Nambung National Park, Australia (Van Paassen, 2009)

3.4.1.4 X-Ray Diffraction

To qualitatively study the changes in minerals after chemical treatment, X-ray Diffraction (XRD) was operated on randomly selected bulk samples. Due to the presence of high amounts of soluble salts (i.e. bi-product NaCl and Na_2CO_3 remnants); XRD (Bruker D5005) was coupled with Energy-dispersive X-ray spectroscopy (EDS). As recommended in (Ulery and Drees, 2008), high-energy short-wavelength radiations were applied to decrease the attenuation. The consequent lower resolution of peak maximal was felt to have negligible effect, as minerals with small d-spacing were of interest. The target d-spacing ranged over 1.31 to 7.17 Å for kaolinite, 1.83 to 3.58 Å for carbonates, and 1.38 to 4.26 Å for quartz. Particularly, the re-emitted intensities corresponding with d-spacing values of 3.40, 1.98, and 3.27 Å for Aragonite Carbonates, 3.03, 1.87, and 3.85 Å for Calcite Carbonates, 7.17 and 3.58 Å for kaolinite, and 3.34, 4.26, and 1.82 Å for quartz were measured. In addition to the Eva Software, Bragg's law was used to interpret the graphs (n=1, λ=0.0061 nm, V=40 kV). XRD, however, fails to properly identify the amorphous phases due to their poor crystal quality (Bentley and Roberts, 1995).

3.4.1.5 Technique Limitations

The engineering process is open to some uncertainties, listed below, and thereby is a tentative simulation of natural global loess:

(1) The specimens did not contain quartz sand and flint constituents.

(2) The preparation set-up did not allow a controlled rate of deposition. However, the rate was manually kept unchanged.

(3) 20-60 µm silt represented a certain wind regime.

(4) Fine spraying could not provide accurate target preparation water content.

(5) The capillary rise of Calcium Chloride solution led to accumulation of secondary crystals on top of specimens.

(6) The fine spraying led to the formation of Sodium Carbonate monohydrate by-product. This, however, had no effect on the synthesis of Calcium Carbonate (Eq. 3.26).

$$Na_2CO_3.H_2O + CaCl_2 \rightarrow CaCO_3 + H_2O + NaCl \quad \text{Eq. 3.26}$$

3.4.2 Specimen Preparation: Kaolinite Clay

With clay (kaolinite) specimens, preparation was undertaken by static compression (replicating the consolidation history) at varied placement water content, placement energy input, and service (i.e. in-situ) water content. Static compression allowed a control on the energy input and therefore net stress. Specimens made up by this technique were deemed highly reproducible (Sivakumar, 1993, Sharma, 1998, Cui and Delage, 1996, Jotisankasa, 2005). The technique was first introduced to the literature about 40 years ago (Lambe and Whitman, 1969), among three laboratory-scale compaction methods including dynamic compaction (i.e. standard and modified Proctor), kneading and static compaction (i.e. compression). Table 3.7 summarizes the properties of kaolinite test specimens.

Table 3.7 Physical properties of synthesised specimens

Specimen	ω_k:[1] %	ω_c:[2]%	e_c[2]	ω_n:[3]%	σ_v:kPa	E_{eq}[4]
1	2.0	1.2	2.05	1.2	200	30%
2	2.0	2.0	1.86	2.0	200	30%
3	10.0	9.6	1.67	9.6	200	30%
4	10.0	9.6	1.63	9.6	200	30%
5	20.0	20.6	1.56	20.6	200	30%
6	20.0	20.6	1.61	20.6	200	30%
7	30.0	29.8	1.43	29.8	200	30%
8	30.0	29.8	1.39	29.8	200	30%
9	40.0	37.3	1.04	37.3	200	30%
10	50.0	42.0	1.17	42.0	200	30%
11	50.0	42.3	1.17	42.3	200	30%
12	50.0	42.3	1.24	42.3	200	30%
13	2.0	1.7	1.91	0.0	200	30%
14	2.0	2.0	1.89	0.0	200	30%
15	10.0	9.7	1.69	0.0	200	30%
16	10.0	9.6	1.71	0.0	200	30%
17	20.0	20.6	1.59	0.0	200	30%
18	30.0	30.0	1.27	0.0	200	30%
19	40.0	37.3	1.02	0.0	200	30%
20	40.0	37.3	0.90	0.0	200	30%
21	50.0	42.3	1.10	0.0	200	30%
22	50.0	42.3	1.01	0.0	200	30%
23	2.0	2.6	1.61	2.6	400	60%
24	10.0	9.2	1.47	9.2	400	60%
25	10.0	9.2	1.48	9.2	400	60%
26	20.0	19.1	1.29	19.1	400	60%

Table 3.7 (Cont.) Physical properties of synthesised specimens

Specimen	ω_k:[1] %	ω_c:[2]%	e_c[2]	ω_n:[3]%	σ_v:kPa	E_{eq}[4]
27	40.0	37.5	1.05	37.5	400	60%
28	40.0	34.3	0.998	34.3	400	60%
29	40.0	34.3	0.92	34.3	400	60%
30	50.0	38.3	1.07	38.3	400	60%
31	2.0	2.0	1.62	0.0	400	60%
32	10.0	10.6	1.52	0.0	400	60%
33	20.0	20.0	1.08	0.0	400	60%
34	30.0	30.2	1.13	0.0	400	60%
35	30.0	29.3	1.16	0.0	400	60%
36	40.0	36.0	0.86	0.0	400	60%
37	40.0	34.3	1.05	0.0	400	60%
38	40.0	34.3	0.81	0.0	400	60%
39	50.0	38.3	0.94	0.0	400	60%
40	50.0	38.9	0.93	0.0	400	60%
41	2.0	3.0	1.45	3.0	600	90%
42	10.0	10.2	1.32	10.2	600	90%
43	20.0	20.0	1.23	20.0	600	90%
44	30.0	27.8	1.01	27.8	600	90%
45	30.0	30.0	1.03	30.0	600	90%
46	40.0	35.5	0.98	35.5	600	90%
47	40.0	33.3	0.96	33.3	600	90%
48	50.0	45.4	1.16	45.4	600	90%
49	2.0	1.9	1.52	0.0	600	90%
50	10.0	10.3	1.36	0.0	600	90%
51	20.0	20.5	1.22	0.0	600	90%
52	30.0	30.1	1.07	0.0	600	90%
53	40.0	35.5	0.84	0.0	600	90%
54	50.0	40.5	0.49	0.0	600	90%
55	50.0	37.5	0.91	0.0	600	90%

[1] $_K$: Kneaded
[2] $_C$: Compacted (after consolidation)
[3] $_n$: Natural (in-situ, test water content)
[4] E_{eq}: Static-equivalent energy for 25 blows of standard proctor

Kaolinite specimens were statically compressed in 3-inch (75 mm) oedometer rings (attached to a top flanged disc). The soil was spooned and lightly tapped into the ring and base and then retained under 200, 400, and 600 kPa for 60 minutes. Following an unloading stage, specimens were eventually trimmed to the ring size. The state of kaolinite soil for varied combinations of compression pressure and placement water content is shown in Fig. 3.19 on a dry density – water content space. As a reference surface, seven kaolinite specimens were compressed under 618 kpa, representing the static standard proctor energy surface. The state of a final six additional specimens, compressed under the elevated 1000 kPa pressure is also displayed, which refers to the pseudo-static standard proctor energy. The 1000 kPa energy level was found analogous to the dynamic Proctor energy level as shown in Fig. 3.20. Properties of reference specimens are outlined in Table 3.8.

Table 3.8 Physical properties of clay specimens[25]

Specimen	ω_k:[26] %	ω_c:[27]%	γ_d: kN/m^3	σ_v:kPa	E_{eq}:%	Attempt
1	10.0	10.4	11.13	618	100	1
2	20.0	20.4	11.48	618	100	1
3	25.0	21.6	11.82	618	100	1
4	30.0	30.4	12.78	618	100	1
5	35.0	31.7	13.40	618	100	1
6	40.0	34.9	13.19	618	100	1
7	50.0	38.7	12.70	618	100	1
8	2.0	1.9	9.68	1000	160	1
9	10.0	9.8	11.84	1000	160	1
10	20.0	19.4	12.48	1000	160	1
11	30.0	29.4	13.31	1000	160	1
12	40.0	34.9	13.35	1000	160	1
13	50.0	36.3	13.20	1000	160	1

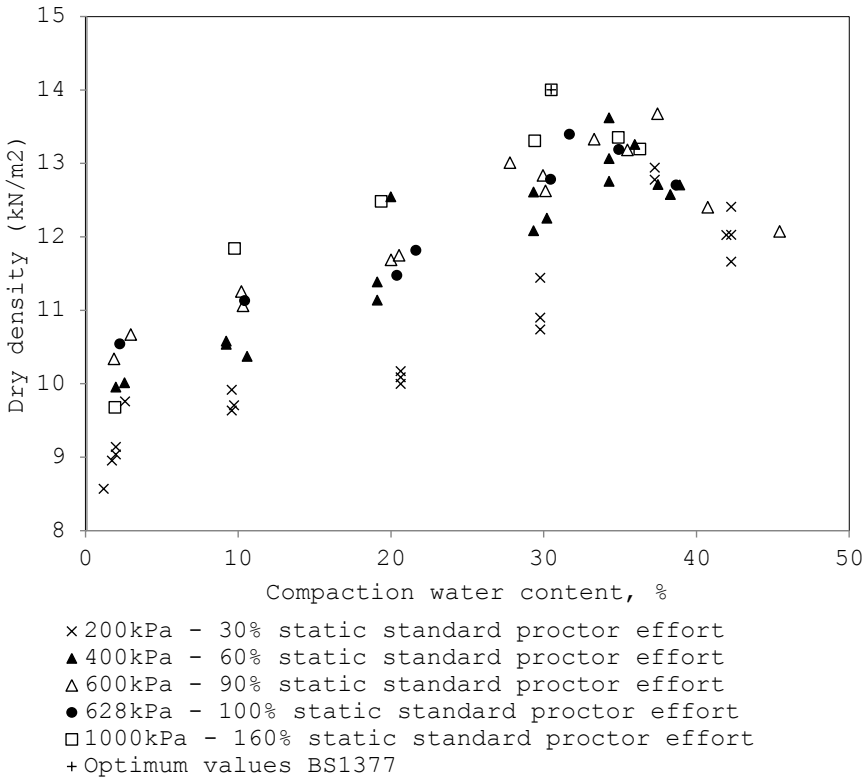

Fig. 3.19 The state of clay testing specimens on dry density – water content space

[25] According to Raghavan and Oho (1985), an static pressure of 618 KPa corresponds to the equivalent standard proctor blow number of 25. This is roughly the same compaction effort of 600 kN-m/m^3 in 101.6 mm diameter mould stated in EN13286-2 (2010) and ASTM: D698-12 (2012). The effort can be estimated through calculating the Proctor compaction work per unit volume of a given soil block. For rammer mass of 2.5 kg, falling height of 30.5 cm, and 25 blows in 3 lifts along the 11.6 cm height of compaction mould, the Proctor compaction work is $W_{Pr} = 2.5 \times 9.81 \times 25 \times 3 \times 0.305 = 561.0094\ N-m\ (J)$.
The work per unit volume is $561.0094 \div (0.1016^2 \times \pi \times 0.25 \times 0.116) = 596533.49\ N.m/m^3 = 596.5\ kN.m/m^3$. This agrees with the 618 kPa and 600 kPa values discussed above.

[26] $_K$: Kneaded

[27] $_C$: Compacted (after consolidation)

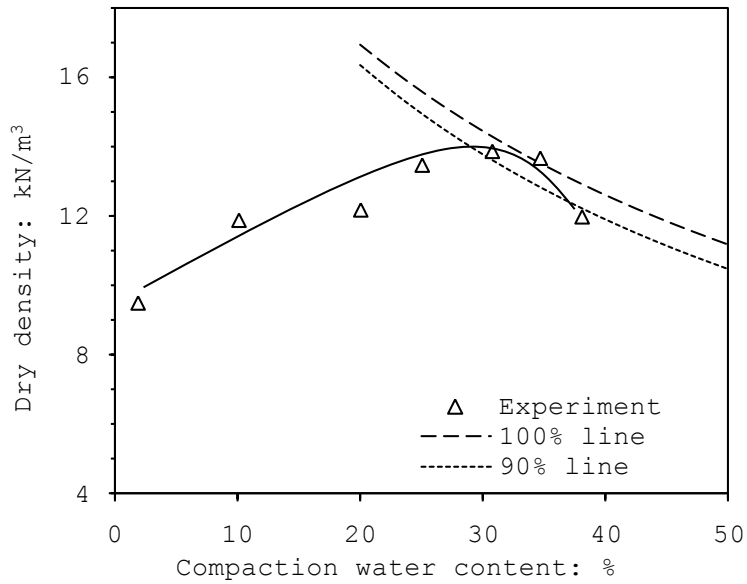

Fig. 3.20 Standard proctor compaction curve

3.4.3 Single Oedometer Test

Testing specimens were prepared in 75 mm standard oedometer rings via the process detailed in the workflow diagram (Fig. 3.18). Standard step-loading (SL) single oedometer tests (SOT) were practiced, increasing the external net stress from 12.5 kPa at doubled stress intervals each time to 200 kPa on the dry-surface (pre-wetting). Contraction took place following the escape of entrapped air packets out of the pore network. Specimens were then allowed access to water, replicating the transition from the dry-surface to the wet-surface at 200 kPa (standard collapse pressure in oedometer tests according to Houston et al., 2001). To do so, the oedometer chamber was filled with distilled water up to the lowest-surface of the specimen, allowing the specimen to take up the water from the lower drain point through the capillary rise. This pattern of wetting allows the soil air to extract from the upper drain point. The same incremental loading was taken on the wet-surface (post-wetting) up to 2100 kPa. Further stressing was undertaken when three subsequent readings showed the same values of settlement. With the dry-state, each pressure was retained for at-least one hour. This rest time was increased to the minimum four hours on the wet-surface. Pilot testing guaranteed that these durations satisfied the unsaturated compression and saturated consolidation, respectively. The wetting time was maintained at one hour in all tests as a resolution. According to the pilot test results, the stepwise

collapse events never lasted longer than an hour in any specimen before changing into consolidation. A simple relation exists between the measured voids ratio and risk potential, defined as:

$$C_{con} = \left(\frac{H_{i+1} - H_i}{H_i}\right) \times 100 = \left(\frac{e_{i+1} - e_i}{1 + e_i}\right) \times 100 \quad | \quad Norm\, C_{con} = \frac{\left(\frac{e_{i+1} - e_i}{1 + e_i}\right)}{e_0} \times 100 \qquad Eq.\ 3.27$$

where e is the void ratio, C is coefficient (i.e. potential of risk), H is the specimen height and Norm represents a normalized value. The subscript con indicates dry-state contraction. The subscript i indicates a loading increment and the subscript 0 the initial condition of an oven-dried specimen. The collapse potential (generally for a wetting pressure of 200 kN m^{-2}) is associated to the void ration change, where e_{i+1} is the void ratio at 200 kN m^{-2} after saturation, and e_i is the void ratio at 200 kN m^{-2} before saturation.

3.4.4 Energy-dispersive X-Ray Spectroscopy (EDX/EDS)

EDX/EDS is typically used as a stand-alone system (Yurugi, 2001) combined with environmental electron microscopy. The system was used to map the distribution of chemical elements and to match this distribution with microfabric features. The choice of coating agent was of prime importance as this affects the quality of the images and may interfere with some elements during EDS mapping. Although Carbon coating provides the best quality EDS data, where charging is potentially more of a problem, micrographs may not have the contrast and resolution of metal-coated samples. Gold (Au) coating induces X-ray peaks at 2.1-2.2 KeV and 9.7 KeV, which interfere with P K_α, S K_α, and Zn K_β during the EDS mapping (Ulery and Drees, 2008). Platinum interferes with the same elements as gold, while palladium interferes with chlorine and potassium (which is the key to identification of micas and feldspars). For these reasons, gold coating was concluded as the best choice.

3.4.5 Classification

Five main classes were initially considered as core groups: basic silt, basic clay, clayey silt, calcareous silt, and calcareous clayey silt. (i.e. five combinations of silt, clay and carbonates in silt-predominant loess soils). In the absence of clay, carbonate was varied from 0% to 40%. Swapping the bond type, in the absence of carbonates, clay was varied from 0% to 40%. Then clay

and carbonate were both used in silty specimens and carbonate was varied from 0% to 30% at 10%, and 15% clay contents. Sub-classes were defined on the basis of the measured collapse potential for controlled clay/carbonate contents: slightly clayey, clayey, very clayey, slightly calcareous, calcareous, and very calcareous. To refine the sub-class boundaries, clay was varied from 0% to 30% at 5%, 20% and 30% carbonate contents. The list of synthesised specimens is outlined in Table 3.9.

Further to these five classes, the sixth to eighth classes were defined to replicate the weathered (silicatization) silt, clayey silt, and calcareous clayey silt. Specimens were engineered under mild and hot weathering conditions. Moreover, traces of metal-based sulphates and chlorides were added to the weathered specimens, resulting in the three last main classes. Sub-classes were associated with a certain combination of main components (silt, carbonate, clay), within which the collapse potential varied with the clay/carbonate content in a repeatable trend (Table 3.10).

Table 3.9 Physical properties of synthesised specimens

No.	Silt: %	Clay: %	Salt: %	Prep. water content: %	Testing water content: %	void ratio[28]	Moist density: kN/m^3	No.	Silt: %	Clay: %	Salt: %	Prep. water content: %	Testing water content: %	void ratio	Moist density: kN/m^3
1	90	10	0	5.0	<0.6%	1.64	10.03	23	55	25	20	6.5	<0.6%	2.22	7.73
2	90	10	0	11.3	<0.6%	1.37	10.15	24	50	30	20	6.2	<0.6%	2.24	8.90
3	85	10	5	7.5	<0.6%	1.36	10.21	25	95	0	5	6.4	<0.6%	1.55	10.30
4	80	10	10	-	<0.6%	2.24	-	26	90	5	5	6.7	<0.6%	1.37	11.16
5	75	10	15	13.6	<0.6%	1.83	9.37	27	75	20	5	5.7	<0.6%	1.66	9.97
6	70	10	20	13.3	<0.6%	1.55	10.38	28	70	25	5	10.9	<0.6%	1.66	9.97
7	65	10	25	11.5	<0.6%	1.71	9.76	29	65	30	5	10.2	<0.6%	1.62	10.12
8	60	10	30	13.6	<0.6%	1.88	9.21	30	70	0	30	10.8	<0.6%	2.13	8.47
9	75	10	15	25.6	<0.6%	1.11	12.56	31	65	5	30	12.5	<0.6%	1.69	9.85
10	85	15	0	3.4	<0.6%	1.69	13.02	32	55	15	30	11.8	<0.6%	1.43	10.89
11	80	15	5	3.0	<0.6%	1.79	8.40	33	50	20	30	6.4	<0.6%	2.16	8.37
12	75	15	10	6.3	<0.6%	1.82	8.99	34	45	25	30	20.3	<0.6%	1.77	9.57
13	70	15	15	4.5	<0.6%	1.71	8.28	35	40	30	30	7.0	<0.6%	1.72	9.73
14	65	15	20	4.3	<0.6%	1.79	8.92	36	100	0	0	4.2	<0.6%	1.72	10.10
15	60	15	25	4.5	<0.6%	1.69	9.36	37	95	5	0	8.3	<0.6%	1.52	10.49
16	60	15	25	6.8	<0.6%	2.05	8.08	38	80	20	0	12.5	<0.6%	1.84	9.34
17	55	15	30	9.1	<0.6%	2.19	8.04	39	60	40	0	4.0	<0.6%	2.19	8.31
18	80	0	20	4.8	<0.6%	1.50	9.51	40	90	0	10	6.5	<0.6%	1.48	10.67
19	75	5	20	4.5	<0.6%	1.84	8.85	41	70	30	0	6.4	<0.6%	2.29	8.05
20	70	10	20	N/A	<0.6%	1.55	10.38	42	85	0	15	7.2	<0.6%	1.57	10.32
21	65	15	20	4.3	<0.6%	1.79	8.92	43	60	0	40	10.1	<0.6%	2.06	8.65
22	60	20	20	6.3	<0.6%	1.93	8.02		-	-	-	-	-	-	-

[28] mean 'e' by the end of the post-depositional preparation stage: Fig. 3.18

Table 3.10 Physical properties of synthesised specimens

Specimen	Sulphate phases		Weathering		Specification: %			Mechanical Response	
	with	without	Mild	Hot	Silt	Clay	Salt	e_i	γ_d (kN/m^3)
1					100	0	0	1.72	10.10
2	X		X		100	0	0	1.51	10.57
3	X			X	100	0	0	1.55	10.21
4		X	X		100	0	0	1.64	10.21
5		X		X	100	0	0	1.43	10.55
6					90	10	0	1.64	10.03
7	X		X		90	10	0	1.77	9.36
8	X			X	90	10	0	1.78	10.04
9		X	X		90	10	0	1.73	10.24
10		X		X	90	10	0	1.68	10.43
11					80	20	0	1.84	9.34
12	X		X		80	20	0	1.95	8.99
13	X			X	80	20	0	1.98	8.88
14		X	X		80	20	0	2.07	8.68
15		X		X	80	20	0	1.99	8.87
16					60	40	0	2.19	8.31
17	X		X		60	40	0	1.91	9.10
18	X			X	60	40	0	2.05	8.68
19		X	X		60	40	0	1.71	9.78
20		X		X	60	40	0	2.52	7.52
21					50	50	0	0.78	14.74
22	X		X		50	50	0	2.05	8.68
23	X			X	50	50	0	2.05	8.69
24		X	X		50	50	0	2.56	7.44
25		X		X	50	50	0	2.39	7.81
26					85	10	5	1.67	9.91
27	X		X		85	10	5	1.69	9.83
28	X			X	85	10	5	1.76	9.61
29		X	X		85	10	5	1.45	10.79
30		X		X	85	10	5	1.48	10.68
31					70	10	20	1.55	10.38
32	X		X		70	10	20	1.62	10.11
33	X			X	70	10	20	1.97	8.90
34		X	X		70	10	20	2.20	8.29
35		X		X	70	10	20	1.72	9.74
36					60	10	30	1.88	9.21
37	X		X		60	10	30	1.99	8.87
38	X			X	60	10	30	2.02	8.77
39		X	X		60	10	30	1.41	10.97
40		X		X	60	10	30	1.89	9.15

3.5 Level III: Engineering Practice - Earthwork Design

The collapsing fine-grained soils (including Loess) were systematically classified into eleven main classes in Level II. The proposed classification improves the current soil classification system, which labels the <63 μm particles as silt and clay. Many modes of collapse volume change were then identified for each soil class and explained in the light of a general collapse mechanism framework developed earlier in Level I. Having the collapse mechanisms for specific soil combinations, Level III provides a predictive tool to estimate the collapse volume change, and then examines the

effectiveness of the current ground improvement practice in each class. Ultimately, modifications to the current practice are proposed by using the mechanisms developed in Level II as well as the micromechanical controls detailed in Level I.

3.5.1 Evaluation of the Collapse/Swell Risk

The empirical estimation of collapse potential has long been investigated incorporating grading and plasticity properties of soil, but the key issue concerning the significance of chemical and environmental controls remains a contentious topic. In the present work, for loess specimens, collapse/swell potential is plotted against kaolinite and carbonate content. For kaolinite specimens, placement stress and water content are set as parameters against which volume change is plotted, for testing water contents once equal to the placement water content and once the hygroscopic water content.

The Akima's polynominal interpolation for 5-8 contour levels was used (Rottinger, 1999). This method uses the data from the adjacent points to draw the coefficients of the interpolation function and therefore does not result in wiggles in the final curve (Rottinger, 1999).

3.5.2 Evaluation of the Compaction Practice

3.5.2.1 Overview

Section 3.3 detailed the testing programme aiming to examine important micromechanical indices, such as the grains' clastic properties (grain strength), the dynamics of pore spaces on varied stress and hydraulic paths, the interplay of pores and the hydraulic hysteresis, the interplay of size and shape of grains and cements, and the dynamics of internal forces on wetting. It was shown that all these indices have a part to play in the dynamics of the effective stress, which serves as a solid framework for the collapse mechanism. In Section 3.4, the chemical, the micro-morphological and the packing indices were added to the size criteria to re-classify the <63 μm soils. Methods to examine the many collapse modes corresponding to each soil class were then detailed in Section 3.4. These mechanisms together with the existing body of knowledge are discussed further in Level III of this thesis to re-examine the effectiveness of compaction practice.

3.5.2.2 Specimen Preparation and Test Set-up

To verify the narrative, a supplementary test set-up was designed and implemented into clayey silt specimens. Forty-one clayey silt specimens were engineered by standard Proctor compaction at optimum, wet-of-optimum, and dry-of-optimum water contents, in 75-mm oedometer rings, which were embedded in 101-mm standard compaction moulds. Varied clay (kaolinite) contents, notably 10%, 15%, 25%, 35%, and 45% by dry weight, were used to build the specimens. To examine the effect of compaction on the collapse behaviour, compacted specimens were examined by a series of single oedometer tests under wet and dry initial states. Table 3.11 shows the placement and initial properties of testing specimens. Fig. 3.21 shows some of the standard Proctor compaction curves, associated to the testing specimens.

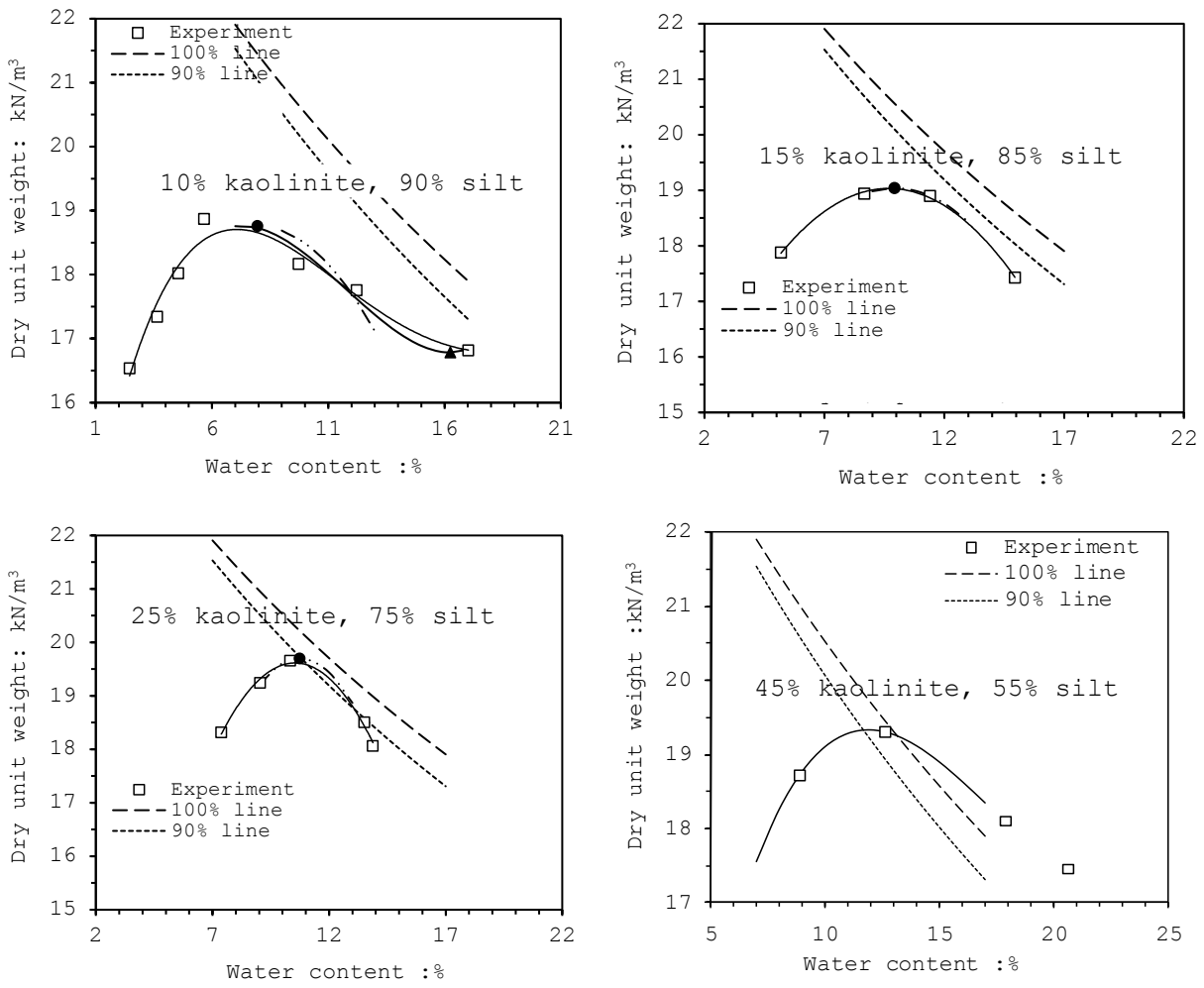

Fig. 3.21 Compaction curves at 10% to 35% clay content (Hatched and dotted lines represent air volume lines)

Table 3.11 Properties of non-calcareous compacted specimens

Specimen	$\omega_{comp}/\omega_{opt}$	ω_n:%	Clay: %	Specimen	$\omega_{comp}/\omega_{opt}$	ω_n:%	Clay: %
1	0.47	0.0	10	21	0.12	0.0	25
2	0.66	0.0	10	22	1.24	0.0	25
3	0.25	0.0	10	23	0.12	0.0	25
4	2.05	0.0	10	24	0.72	7.7	25
5	1.03	0.0	10	25	0.39	4.2	25
6	0.52	4.1	10	26	1.24	13.3	25
7	0.66	5.2	10	27	0.12	1.3	25
8	1.04	8.3	10	28	0.56	0.0	35
9	1.03	8.2	10	29	0.79	0.0	35
10	0.85	0.0	15	30	1.12	0.0	35
11	0.54	0.0	15	31	1.29	0.0	35
12	1.57	0.0	15	32	0.56	8.9	35
13	1.09	0.0	15	33	0.79	12.6	35
14	1.58	0.0	15	34	1.12	17.9	35
15	0.07	0.7	15	35	1.29	20.6	35
16	0.26	2.6	15	36	0.86	0.0	45
17	0.54	5.4	15	37	1.07	0.0	45
18	0.85	8.4	15	38	1.36	0.0	45
19	1.09	10.8	15	39	0.86	17.4	45
20	1.24	0.0	25	40	1.07	21.6	45
-	-	-	-	41	1.36	27.5	45

3.5.3 Improvement of the Compaction Practice

The discussions within the last section of this thesis are genuinely proposals and, as such, some are inevitably tentative. Nevertheless, the section serves as a good basis of a new perspective in the collapsing ground improvement technology specific.

A modified compaction practice as well as a suite of more novel mitigation techniques is discussed for five key soil classes: (1) silt, (2) clayey silt, (3) silty clay and clay (kaolinite), (4) calcareous silt, and (5) calcareous clayey silt. This section explains how the Level I to Level III experimental outputs of this work are synchronized to develop improved mitigation techniques, which are capable of minimizing or removing the risk of collapse.

3.5.3.1 Target soils: silt and clayey silt

The collapse mechanism model outputs (i.e. certain combinations of wetting and loading paths which result in the maximum densification - Chapter 5) together with the outputs of the collapse mechanism framework (Chapter 4) were used to design a modified improvement technique through which the following requirements are fully satisfied: (1) maximal grain breakage and minimal wetted/loading-induced coagulation, (2) maximal skeletal stresses and minimal

void ratio loss on the dry stress-state surface. The modified practice is supplemented with a follow-up treatment. The latter is designed by considering the role of stress-relief, which is detailed in Section 3.4.3.4. The supplementary practice ensures the integrity of compacted fills in transient loading environments.

Where a mechanical approach appears to be feasible, the findings of Lewis Structure analyses (Chapter 5) and microscopy evidences on the cation nucleation (EDS mapping) were used to develop an alternative chemical practice.

3.5.3.2 Target soils: Clay, Silty Clay

The outputs of the wetting oedometer tests on compacted kaolinite specimens were used to develop an improved densification practice to remove the risk of collapse/swell.

3.5.3.3 Target soils: Calcareous Silt, Calcareous Clayey Silt

For soils containing low to moderate carbonate contents, the findings of the stress-hydraulic path study (Chapter 4) were used to design pre-loading-wetting strategies which maximized soils' densification. In section 3.4.1, an impact coefficient was derived which allowed the conversion of static compression energy to the standard proctor compaction energy. The coefficient was used to derive the equivalent dynamic compaction energy required and hence, the appropriate field work arrangements.

3.5.3.4 Supplementary Examinations (Transient Loads effect)

Three aeolian clayey silt specimens made up of 5, 20, and 40% kaolinite, were examined by the standard single oedometer (BS1377-4, 1990). These specimens represented kaolinite clay (clay>60%), and clay-silt composite (5%<clay≤ 60%). Specimens were flooded under 200 kPa and retained under load over an hour period, before further loading at intervals of four hours to 400, 800, 1600 and 2100 kPa. Load was then incrementally reduced to 200 kPa. Two more cycles of incremental loading and unloading between 200 kPa and 2100 kPa pressures were implemented. The output data was converted into the Barcelona Basic Model (BBM) 'k' parameter (a representation of soil stiffness). As such, the role of soils' clay content as well as stress history was investigated on stiffness.

To interpret the results, the recent concept of double porosity (Alonso et al., 2010), and fine migration (Chapter 4) were employed.

3.6 Validity and Reproducibility

This section examines the efficiency of the designed and implemented specimen preparation techniques.

With aeolian soils, the quality of frame elements (i.e. silt grains) as well as bonding elements (i.e. engineered carbonates) is studied. Since the lab-scale synthesis of carbonates has never been attempted, shape and chemistry of engineered bonds are compared with those of naturally occurring loess in Kent, UK. The reproducibility of specimens is then examined by error analysis (coefficient of contraction in identical slightly clayey, calcareous specimen pairs).

With kaolinite soils, since the standard preparation technique is attained, the reproducibility of engineered specimens are examined and reported only. A statistical population of 10% was randomly chosen and the mean standard deviation was measured along the oedometer wetting tests.

3.6.1 Validity of Engineered Specimens

3.6.1.1 Specimen Preparation: Provenance Phase

The silt production simulation dates back to the work of Griffith 1920 (in (Moss, 1973)). With Leighton Buzzard Sand (i.e. the present testing material), key grain-crushing simulations include Jefferson et al., (1997), Dibben (1998), Assallay (1998), and Zourmpakis (2005). Despite the variations in crushing apparatus and regimes, the grading curve of the specimens' silt constituent is compared with grading curves of silt-constituent of engineered loess in the above works.

3.6.1.2 Specimen Preparation: Depositional Phase

Synthesis of artificial loess dates back to the work of (Mulilis et al., 1975). Works using Leighton Buzzard Sand to reproduce quaternary loess date back to early 90's (Assallay, 1998, Dibben, 1998, Miller, 2002, Zourmpakis, 2005). The preparation techniques have been continuously improved, although the bond type was restricted to primary clays. The latest technique detailed

in (Zourmpakis et al., 2005) were used in the current work after slight modification. To examine the accuracy of the preparation technique, the properties and mechanical response of three specimen pairs, made by Zourmpakis in 2005 and the author are compared in Tables 3.12 and 3.13. The outputs of single oedometer tests, conducted in the three specimen pairs, are detailed in Fig. 3.22.

Table 3.12 Physical properties

	Sample Silt:Clay:Carbonate		G_s	Depositional				Consolidated post-depositional		
				ω:%	γ_m:kN/m^3	e	S_r:%	ω:%	e	γ_m:kN/m^3
Zourmpakis (2005)	100:0:0	0-d-fs-2	2.64	-	N/A	1.99	-	-	1.35	N/A
	90:10:0	10-d-fs-48	2.64	-	N/A	2.74	-	-	2.64	N/A
	85:15:0	15-d-fs-63	2.64	-	N/A	3.02	-	-	2.65	N/A
current Research	100:0:0		2.65	4.2	-	-	-	0.0	1.72	10.10
	90:10:0		2.68	5.0	9.88	1.76	7.6	0.0	1.64	10.03
	90:10:0(R)		2.66	11.3	11.37	1.54	19.5	0.0	1.37	10.15
	85:15:0		-	3.4	-	-	-	0.0	1.69	13.02

R: Repeated: identical specimen under higher preparation water content. Values are actual.
fs: abbreviation used in Zourmpakis (2005), denoting 'fine spraying'

Table 3.13 Coefficient of contraction (pre-wetting loading path)

kPa	0 2	2 12.5	12.5 25	25 50	50 100	100 200	0 200
Silt:Clay:Car[1]. C_{con}%							
100:0:0	21.94	0.90	2.72	2.78	2.86	1.93	30.30
90:10:0	3.07	11.50	9.07	10.01	7.92	6.91	39.84
85:15:0	8.78	13.64	7.89	7.16	7.68	5.00	40.92
100:0:0	N/A	13.92	9.32	5.41	4.07	3.40	31.58
90:10:0	N/A	12.68	4.83	4.59	4.44	4.07	27.33
90:10:0 (R)	N/A	3.94	6.59	5.73	4.64	2.82	21.61
85:15:0	N/A	2.98	4.82	8.08	6.37	5.74	25.08
kPa	0 2	2 12.5	12.5 25	25 50	50 100	100 200	0 200
Silt:Clay:Car. Norm. C_{con}%							
100:0:0	11.03	0.45	1.37	1.40	1.44	0.97	15.23
90:10:0	1.12	4.20	3.31	3.65	2.89	2.52	14.54
85:15:0	2.91	4.51	2.61	2.37	2.54	1.66	13.55
100:0:0	N/A	8.07	5.40	3.14	2.36	1.97	18.30
90:10:0	N/A	7.72	2.94	2.80	2.71	2.48	17.69
90:10:0 (R)	N/A	2.88	4.81	4.18	3.38	2.05	15.76
85:15:0	N/A	1.76	2.84	4.76	3.75	3.38	14.78

[1]: Calcium Carbonate

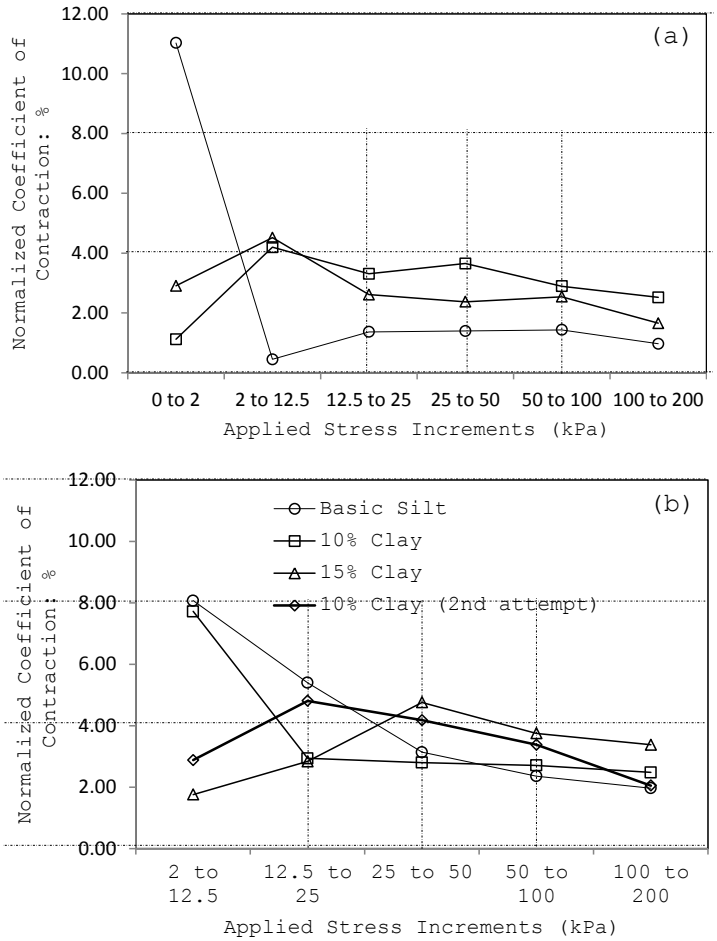

Fig. 3.22 Normalized C_{con} (%)[29] for identical specimens under (almost) identical stress path (a) work of Zourmpakis (2005), (b) the present work

3.6.1.3 Specimen Preparation: Post-depositional Phase

The microfabric of a representative clayey calcareous specimen and an undisturbed clayey calcareous brickearth specimen from Kent are compared in Fig. 3.23. The specimen from Pegwell Bay, Kent, comprised 66% quartz, 5% K-feldspar, 14% calcite, 2% dolomite, 3% Mica, 3% kaolinite and 1% smectite (McKervey and Kemp, 2001). For the same sampling location and depth, (Milodowski et al., In Press) reported 0% calcite, 2% dolomite, and 11% Mica. An artificial loess specimen containing 72-75% silt, 4-5% clay, and 20% carbonate was deemed a true representation of the natural loess specimen.

[29] for loading increment 'i', normalized C_{con} is $(e_i-e_{i-1}/1+e_{i-1})/e_0$

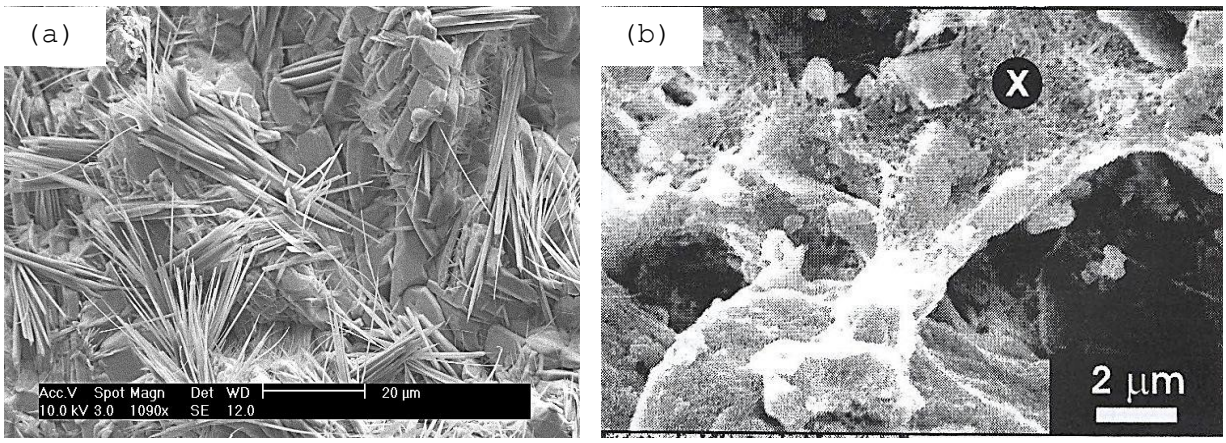

Fig. 3.23 (a) engineered carbonates at intermediate fabric level, (b) meshwork of fine needle calcite – Lower Calcareous Brickearth, Kent (Milodowski et al., In Press).

Needle-shape Carbonates were observed in both images. X-Ray Diffraction micrograph of the engineered loess soil conformed (Fig 5.22-5.12) the engineered carbonates were made up of burbankite (Anhydrous Carbonate), vaterite (Calcium Carbonate), Calcium Carbonate Hydrate, aragonite, Calcium Chloride, Calcium Carbide, defernite and Sodium Chloride.

3.6.2 Reproducibility of Engineered Specimens

The standard deviation and error (δx) was measured (Taylor, 1982, Cox and Hinkley, 1974) for the Normalized C(con) on calcareous clayey (D2) specimens, loaded on pre- and post-wetting surfaces.

Up to 18 data points (xi = Normalized C(con)) were averaged (μ=mean value) and the error (δx) was computed as $\{\text{average } \{(x_1-\mu)^2, (x_2-\mu)^2, (x_3-\mu)^2, \ldots\}\}^{0.5}$. 95% of the available data points were used in the above statistical computations. This can be seen as the 95% confidence intervals on the illustrated bar charts. For the dry stress-state surface, 95% of repeating oedometer test outputs fit within a range of ±2.04% the mean normalized coefficient of contraction. For the wet stress-state surface, 95% of repeating oedometer test outputs fit within a range of ±1.95% the mean normalized coefficient of contraction. Below bar charts illustrate the outputs of the statistical computations.

0.0 to 12.5kPa on dry-surface: 2.3033 ± 1.3667% with 95% confidence (StDev 1.7780)

12.5 to 25.0kPa on dry-surface: 1.4767 ± 1.362% with 95% confidence (StDev 1.7719)

25.0 to 50.0kPa on dry-surface: 2.0888 ± 1.439% with 95% confidence (StDev 1.7220)

50.0 to 100.0kPa on dry-surface: 2.4586 ± 1.0408% with 95% confidence (StDev 1.1254)

100.0 to 200.0kPa on dry-surface: 5.5183 ± 2.3023% with 95% confidence (StDev 2.1938)

200.0 to 400.0kPa on dry-surface: 7.1300 ± 4.003% with 95% confidence (StDev 3.2239)

400.0 to 800.0kPa on dry-surface: 6.5050 ± 1.9567% with 95% confidence (StDev 1.2297)

800.0 to 1600.0kPa on dry-surface: 5.6933 ± 2.847% with 95% confidence (StDev 1.1461)

Any stress increment on dry Stress-State surface: $\boldsymbol{\delta_x = \pm 2.040\%}$.

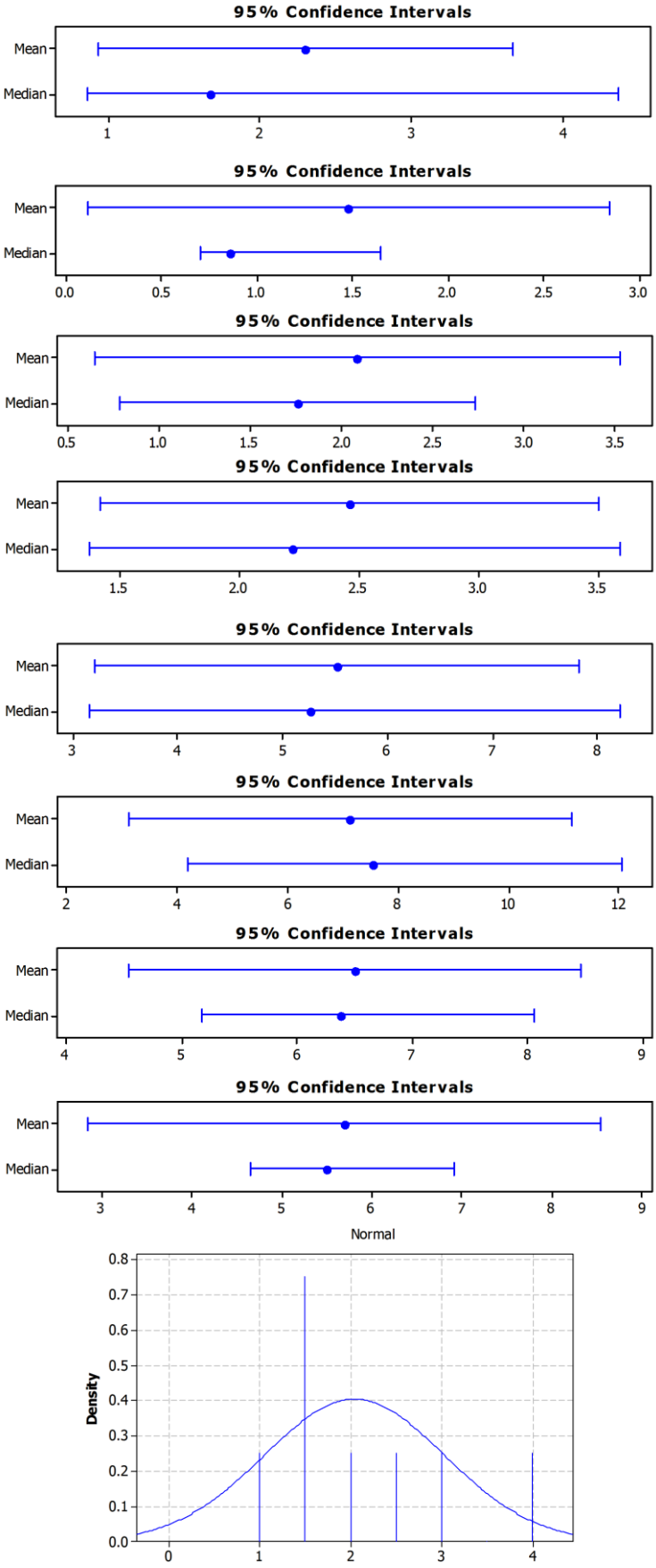

100.0 to 200.0kPa on Wet-surface: 6.660 ± 1.6808% with 95% confidence (StDev 1.0563)

200.0 to 400.0kPa on Wet-surface: 6.6320 ± 1.9216% with 95% confidence (StDev 1.5476)

400.0 to 800.0kPa on Wet-surface: 6.0500 ± 2.0238% with 95% confidence (StDev 1.9258)

800.0 to 1600.0kPa on Wet-surface: 4.9171 ± 2.3184% with 95% confidence (StDev 2.5067)

1600.0 to 2100.0kPa on Wet-surface: 2.7550 ± 1.8231% with 95% confidence (StDev 2.1806)

Any stress increment on wet Stress-State surface: $\boldsymbol{\delta_x = \pm 1.954\%}$.

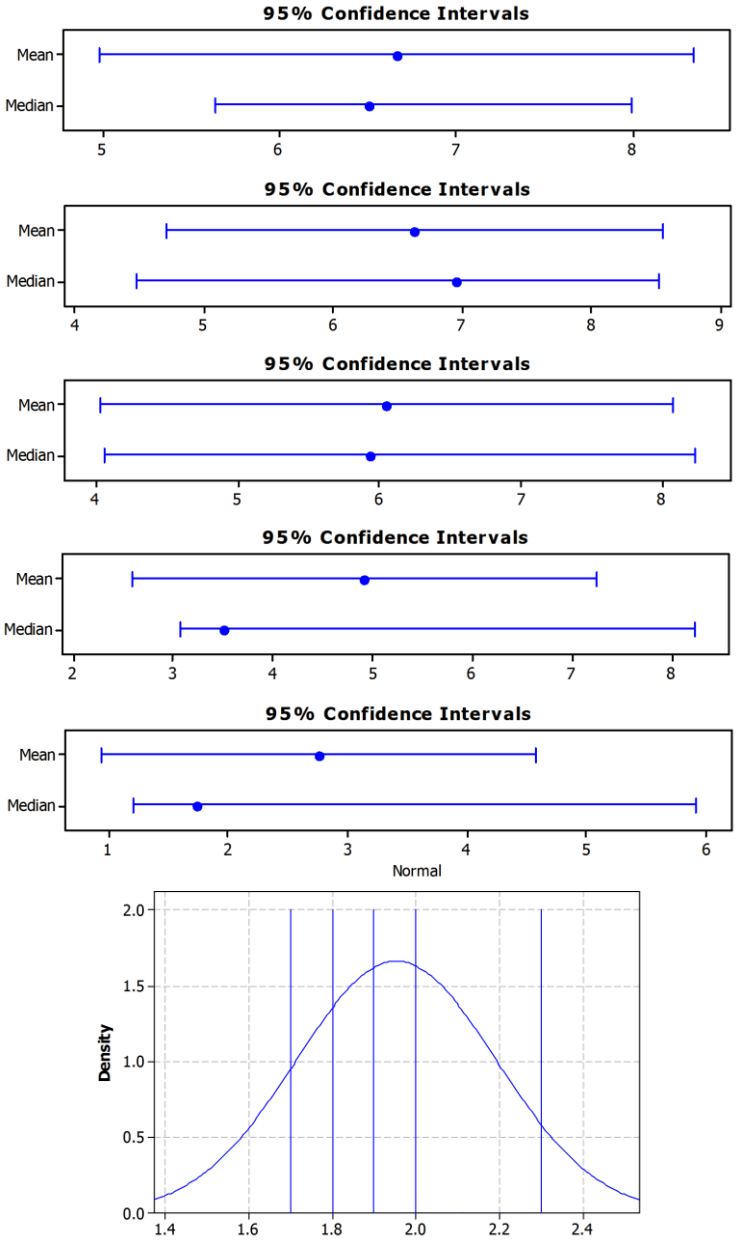

Ten percent (in number) of kaolinite specimens were randomly selected for reproducibility checks. Free oedometer tests were repeated on selected identical specimens. A mean standard deviation of 3.6% was recorded for the collapse/swelling potential values. The choice of collapse/swelling potential for such statistical analysis allowed the consideration of the entire uncertainties with specimen constituents, specimen preparation, testing procedures and human errors.

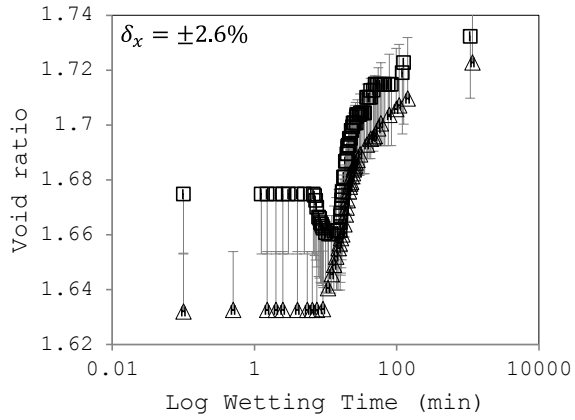

□Wn=Wi=10%, 30% Stand. Energy, Kaolin

△Wn=Wi=10%, 30% Stand. Energy, Kaolin - Attemp 2

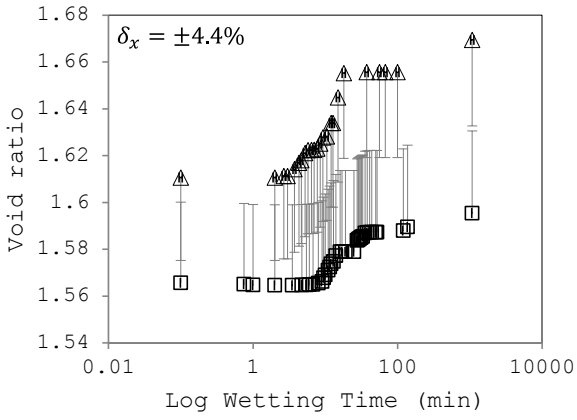

□Wn=Wi=20%, 30% Stand. Energy, Kaolin

△Wn=Wi=20%, 30% Stand. Energy, Kaolin - Attemp 2

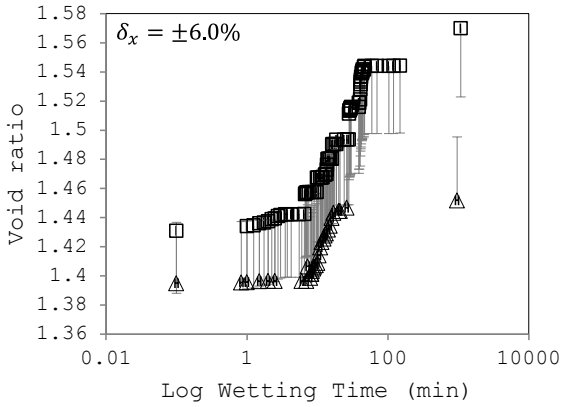

□Wn=Wi=30%, 30% Stand. Energy, Kaolin

△Wn=Wi=30%, 30% Stand. Energy, Kaolin - Attemp 2

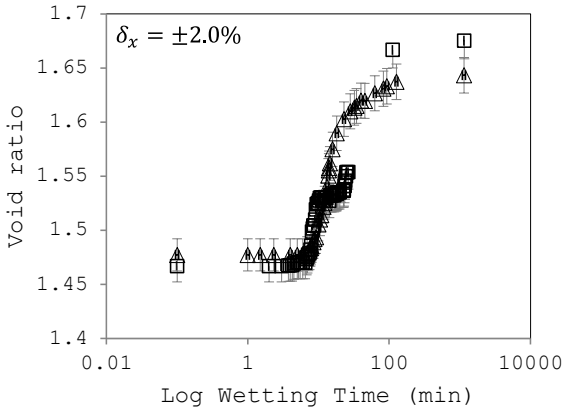

□Wn=Wi=10%, 60% Stand. Energy, Kaolin

△Wn=Wi=10%, 60% Stand. Energy, Kaolin - Attemp 2

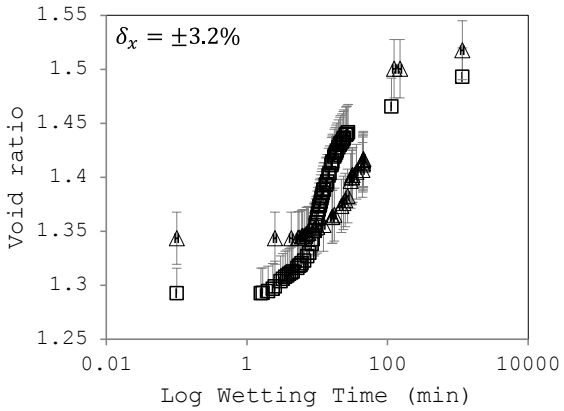

□Wn=Wi=20%, 60% Stand. Energy, Kaolin

△Wn=Wi=20%, 60% Stand. Energy, Kaolin - Attemp 2

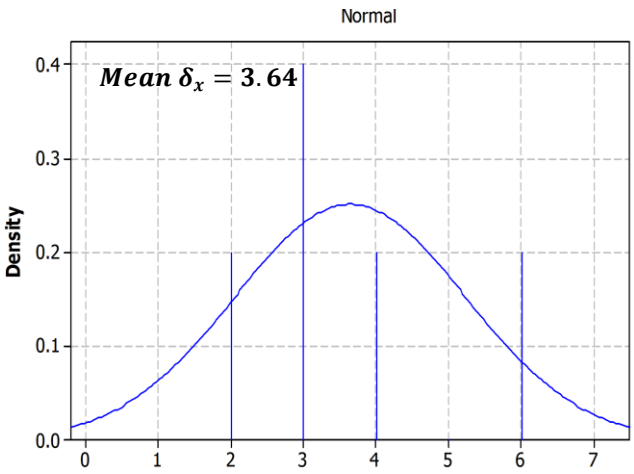

Fig. 3.24 The mean standard deviation of 3.6% for the collapse/swelling potential values

3.7 Summary

This chapter described the methods used to examine the quartz grains' crushability (its fractal and micromechanical properties), the pore space dynamics associated with various stress and hydraulic paths, the bonding force dynamics associated with two main hydraulic paths and the grain-bond interface dynamics. These, together with a series of wetting experiments, were used to develop a modified form of principle of effective stress, which served as a framework for collapse mechanism. The chapter then described the methodology used for the development of a new classification system for fine soils, and the collapse mechanisms developed for each of the classes using the framework worked earlier. The methodology by which findings were used to contribute in the engineering practice was lastly detailed in three phases. The results and discussion are detailed in Chapters 4 and 5.

Chapter 4 | LEVEL I: FRAMEWORK OF COLLAPSE MICRO-MECHANISM

4.1 Introduction

The present chapter examines four micromechanical indices, and their use to develop a final constitutive model: a modified form of the principle of effective stress, and a framework for collapse mechanism modelling. This framework will be used in Chapter 5 to diagnose the various modes of collapsibility in different fine-grained soils directly related to their composition.

This chapter is organized to describe four micromechanical indices:

(1) Dynamics of grain crushability (Section 4.2),

(2) Dynamics of pore space under varied stress/hydraulic paths (Section 4.3),

(3) Bond-grain interface properties (Section 4.4), and

(4) Dynamics of internal forces on wetting stress path (Section 4.5).

From these, the theoretical basis of the framework and the test programme used in its development are derived and fully detailed. This will then allow assessment of collapsibility and its application to be developed in later chapters.

4.2 Dynamics of Crushability (Clastic Properties)

4.2.1 Fundamental Concepts

As outlined in Section 2.4.2.1 Chapter 2, fracturing of quartz grains in loess disturbs the equilibrium of pore water pressure. Pores may collapse under drained conditions when water flows out of the voids. Under undrained conditions contacts could modify and grains migrate or split further, leading

to collapse. To examine this, it is first necessary to assess the micromechanics of the sand-to-silt size reduction. This will elucidate the nature of grains/primary building blocks that make up many collapsible soils. Key questions to be answered are:

(1) Should quartz possess fractal features, could grain breakage take place at entire silt- and sand-sized ranges?

(2) Do quartz grains tend to break to a certain pronounced mode size and hence, form a certain pronounced pore size?

(3) What controls can limit/stop the particle breakage?

(4) Is breakage a factor of stresses operating on grains, or the grains' crystalline properties?

To answer the above questions, a time-line for quartz sand-to-silt size reduction is produced through a series of grinding experiments conducted on Leighton Buzzard sand using a disc mill. To build the time-line, a range of indices are measured the real-time, while a batch of quartz sand is exposed to a controlled stress environment, namely: fractal dimension, relative breakage index, maximum grain size, pronounced mode size, sorting and particle shape.

4.2.2 Fractal[30] Features of Breakdown Timeline

The Hardin equation for relative breakage, B_r (Hardin, 1985) was used to describe the size-reduction in quantitative terms. According to Hardin (1985) 'Breakage potential', B_p, is the area above the initial grading curve up to the '100% passing' line, confined between the lower-bound 63 μm and the upper-bound maximum grain diameter (as for sand-size index) or the 2 μm lower and 63 μm upper bounds (as for silt-size index). The 'Total breakage', B_t, underlines the amount of crushing that the granular assembly has undergone and is represented by the area between the particle size distribution (PSD) curve

[30] A fractal dimension is a ratio providing a statistical index of complexity comparing how detail in a pattern (strictly speaking, a fractal pattern) changes with the scale at which it is measured. It has also been characterized as a measure of the space-filling capacity of a pattern that tells how a fractal scales differently than the space it is embedded in; a fractal dimension does not have to be an integer (O'Hara-Dhand, 2013)

pair of the initial and post-crushed state, while confined in the latter span of B_p. The relative breakage is defined as the ratio of B_t over B_p. To derive the associated areas, the fitted functions of each grading curve were integrated along the particle size axis. Fig. 4.1 shows the relative breakage for silt-sized and sand-sized scales against grinding time.

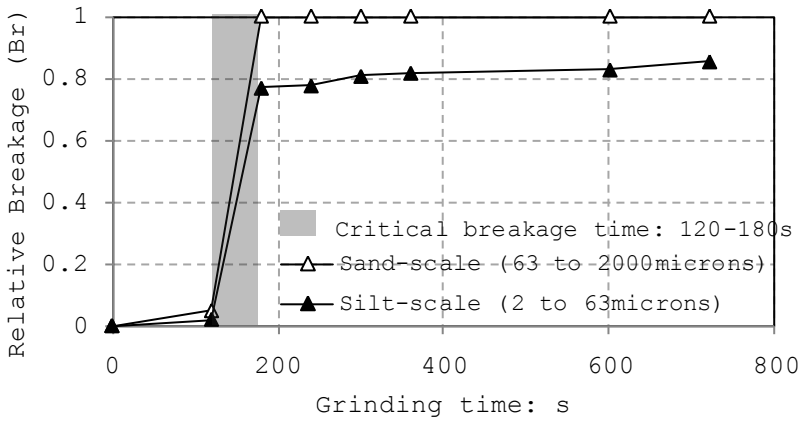

Fig. 4.1 The Hardin's relative breakage (i.e. how far the grains are crushed in the scale of 0 to 1) against grinding time for silt-sized and sand-sized grains

At a sand-sized scale, there was a gradual rise in the relative breakage over a 0-120 s timescale from zero to just under 5%. The B_r then steeply increased by 95% to a peak of 100% over the 120-180 s timescale. In other words, sand fragments were entirely crushed to silt-sized grains by 180 s of grinding. Examining the relative breakage at silt-sized scale however showed that size reduction gradually continuous for increasing grinding time. At a silt-sized scale, B_r slightly increased over 0-120 s timescale to just above 2%. It then sharply increased by 75% in the 120-180 s timescale, before flattening out in the 180-240 s timescale. The B_r improved thereafter at a decelerated rate, levelled off, and finally recovered in the subsequent timescales. At 720 s of grinding, the B_r hit the course high of 86%. The early sharp increase in B_r (120-180 s timescale), agrees with the activation of surface imperfections and existing micro-fractures (see Fig. 4.2-4.3).

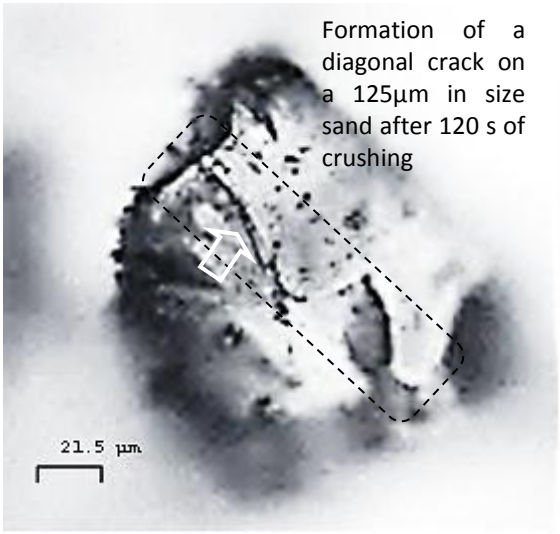

Fig. 4.2 Petrological microscopy image of a silt grain with surficial evidence of a fracture: a possible un-opened healed micro-crack

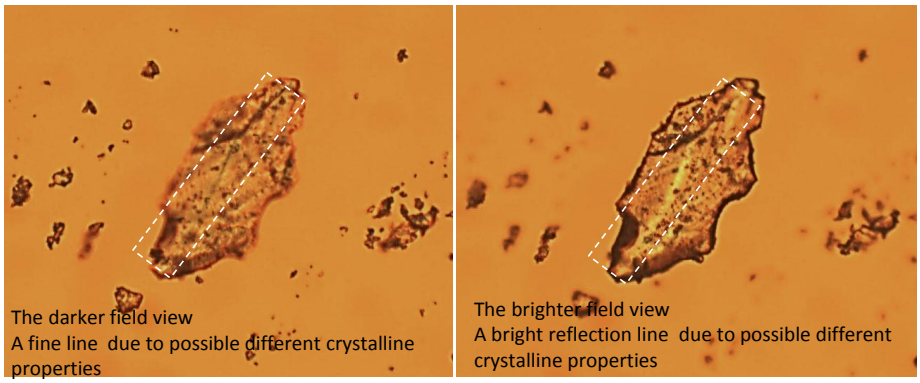

Fig. 4.3 Transmission light microscopy image of a sub-angular platy crushed quartz grain with surficial evidence of an internally crystalline defect plane: an inclined cleavage plane inside the grain

In Fig. 4.4, signs of crystalline gradients were spotted on the original sand grains. These may either indicate a history of fracturing-healing through the post-solidification period, or conditions under which quartz crystallized. Irregular V-shaped pits on the grain's surface are potential lines of weakness through which splitting occurred after 180 s of grinding.

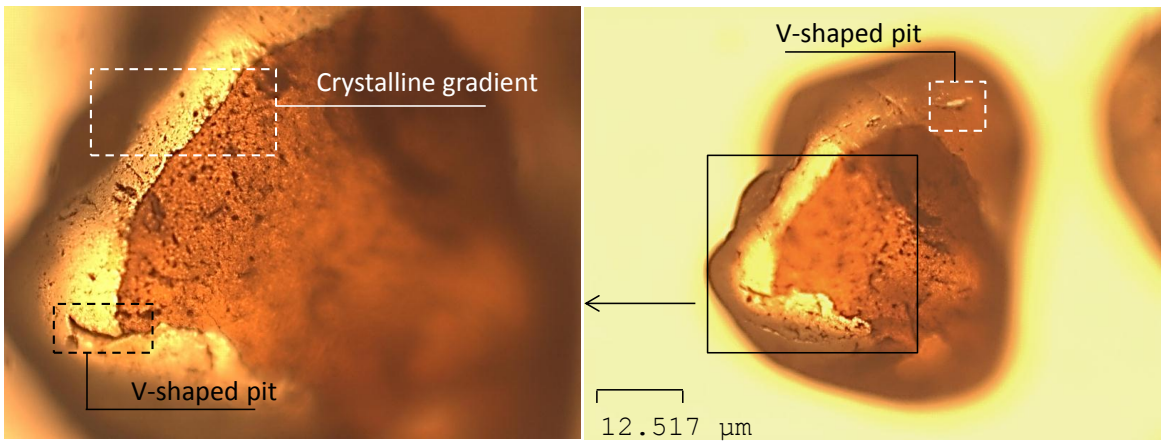

Fig. 4.4 Crystalline gradients and surface imperfections under transmitted light for randomly selected silt before grinding

According to the PSD curve shown in Fig. 4.5, the early breakage improved the degree of uniformity by eliminating the sand-size fragments. Jefferson et al. (1997) ascribed the early gap between the PSD curves to the "simple breakage of the original flawed sand grains". Fig. 4.2 illustrates a flaw in a silt grain after <180 s of grinding.

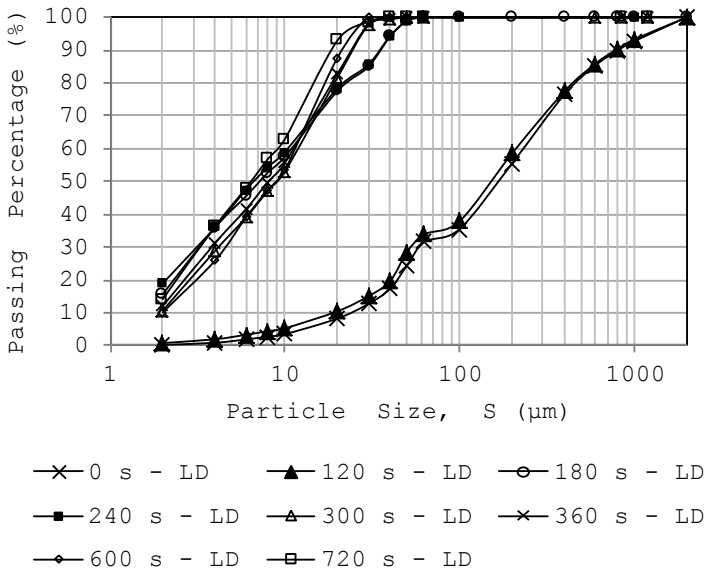

Fig. 4.5 Particle size distribution curves of original sand material as well as ground materials (i.e. crushed for 120s to 720 s)

Fig. 4.6 shows the progression of PSD curves with grinding time from 240 s to 720 s. The phi-scale divisions are added to the grading plots to address the silt sub-divisions more easily. For an increase in grinding time from 240 s to

300 s, a positively skewed gap appeared between the PSD curves at 4-5Ø, which was then proceeded with a negatively skewed gap at 5-6Ø. These gaps represented crushing events in very coarse to coarse silts. Almost the entire volume of very coarse silts was crushed at the 240-300 s grinding timescale.

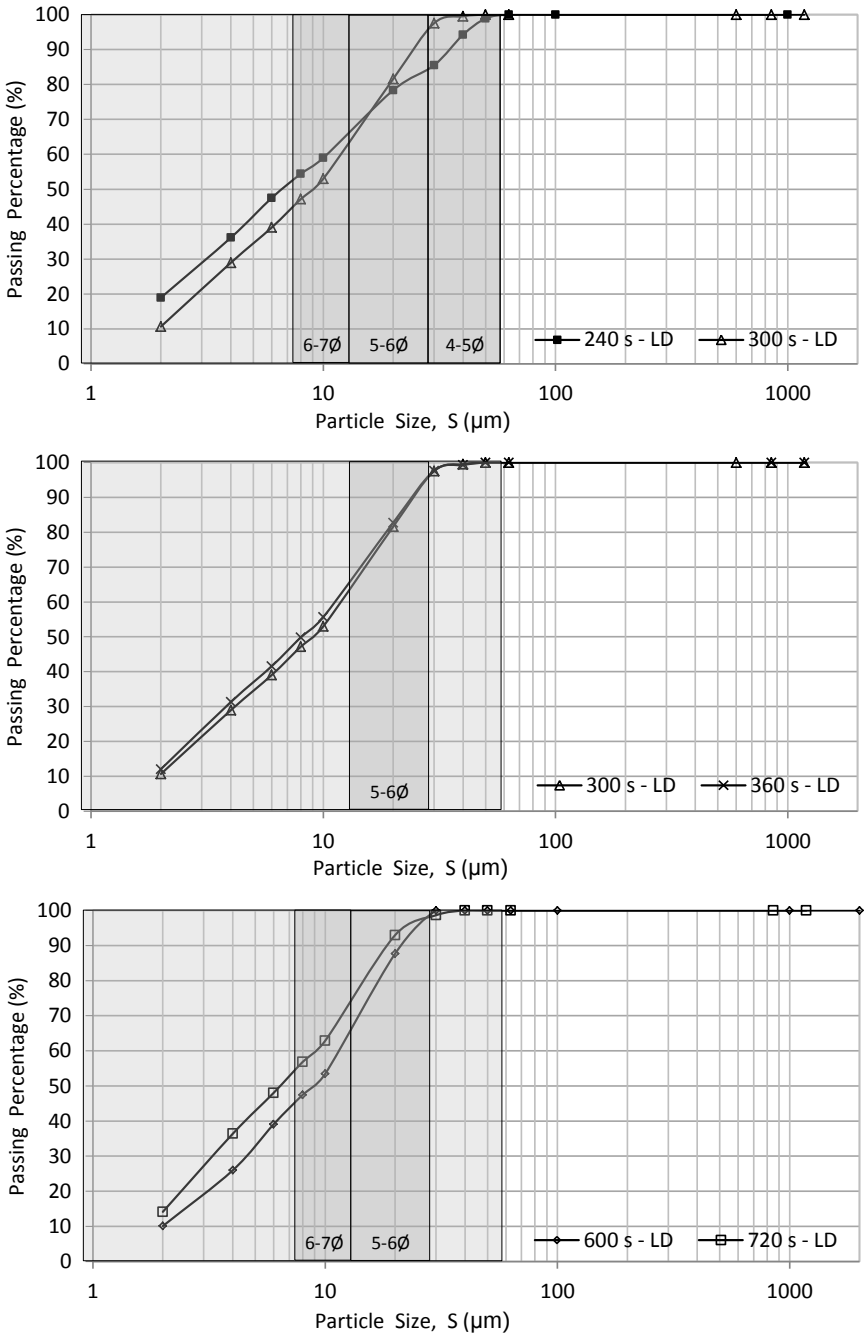

Fig. 4.6 Particle size distribution curves of ground quartz material: crushed for 240 s, 300 s, 360 s, and 720 s

Further increases in grinding time from 300 s to 360 s produced very little breakage and therefore led to a negligible gap between PSD curves at 5-6Ø.

Coarse silt grains were resistant against the impact energy, while crushing events in finer fragments continued at limited levels.

Over the 600-720 s grinding timescale, the rate of breakdown surged at the 5-6Ø (coarse silts). The positively skewed gap between PSD curves suggested higher degrees of particle breakage in finer fragments.

A possible reason for lack of significant abrasion[31] over the 300-360 s timescale may be associated with the mature state of material after 300 s of crushing. However, sets of fresh micro-fractures formed within the crystal of mature grains. Formation of such fresh imperfections may be a physical signature of fatigue fracturing under relatively moderate impact energies. The randomly selected grains at 300-360 s timescale show signatures of fresh (sharp) parallel ridges on surfaces.

The higher degree of breakage in finer fragments over 240-300 s (6-7Ø) and at 600-720 s timescales reveals the tendency of silt-sized particles for continuous breakage.

The results presented above showed that size reduction in quartz is a fractal phenomenon, consisting of periods of breakage followed by periods of fatigue fracturing. The experiments also showed that both survived and broken grains continue to break and re-arrange along the period of impact energy application. A given impact energy level might not be sufficient enough to trigger breakage, but the prolonged application of the energy can potentially induce fresh surface imperfections along the internal crystalline defect planes. These highlight that neither sand nor silt is the end-product of abrasion at a given energy level. The experimental work also showed that high energy earth-surface processes such as the glacial abrasion generates significant amounts of silt-sized particles (early gap between the PSD curves at 5-7Ø, the pronounced mode size of loess, the main constituent of which is silt). However, further size reduction continues under less efficient input energies (i.e. damping, to be discussed in 4.3) but prolonged duration.

[31] The phrase 'abrasion' is used throughout to describe the act of glacier-bed rock movement against each other

4.2.3 Fractal Dimension on Breakdown Timeline

In Fig 4.7, grinding time is plotted against K_{100} (i.e. maximum particle size). The lowest size at which the PSD curve intersects the 100% line was defined as K_{100} for a given grind time. The plot shows fractal features, in which plateau trend intervals are followed by decreasing trends. Maximum particle size, however, decreased at a lower rate as grinding time progressed.

The largest particles survived within the first 120 s of grinding. The maximum diameter then plummeted at 180 s grinding time. Microscopic inspections suggested that this probably occurred due to the breakage of defected sand particles along lines of weakness (Fig. 4.2, 4.3, 4.4). The second period of resistance (little breakage) appeared at 180-240 s before the second breakage event at 240-300 s. This was then followed by the third period of resistance and the third breakage event.

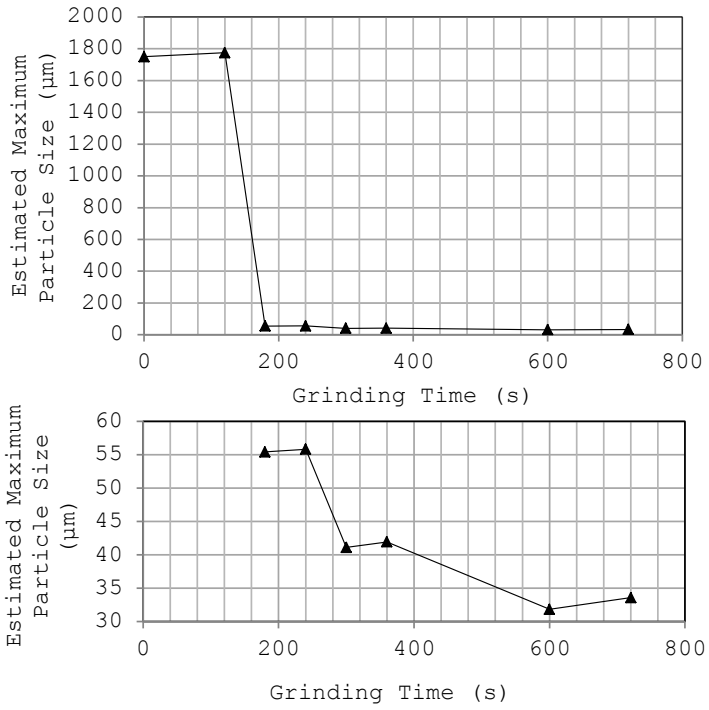

Fig. 4.7 (upper) The significance of the drop in maximum particle size (K_{100}) with an increase in the grinding time from 120 s to 240 s (Lower) The fractal pattern of decreasing K_{100} with the impact energy input.

At 120-180 s timescale, sand-sized scale breakage index reached 100% (Fig. 4.5), indicating the transition of entire sand-fraction into silt (Fig. 4.1)

material. The significance of this transition appeared in the markedly decreased 'maximum grain size' by 96.8% (Fig. 4.7 – in agreement with Blatt (1970)). Breakdown in larger grains was more pronounced than in finer grains (Fig. 4.5). Microscopic examinations revealed chevron-shaped cracks on the surface of randomly selected fine sand, after 120 s of grinding (Fig. 4.8 – in agreement with Smith et al. (1991) and also with Krinsley and Doornkamp (1973) images 55 and 56). As the sand-fraction faded by an increase in grinding time to 180 s; splitting possibly occurred by exploitation of existing micro-fractions (consistent with Cheng (2004)). The next grinding timescale (180-240 s) could be regarded as a period of the grains' resistance against the applying energy. This probably occurred due to the establishment of an elevated number of contact points between grains (55 µm) and several edge-grinded finer particles (Fig. 4.5). The enhanced lateral confinement for grains allowed a better resistance against the applying energy. A further increase to the grinding time (to 300 s), however, led to the breakdown of very coarse to coarse silt grains (4-6Ø – see Fig. 4.6) and the second major drop in the maximum grain size (Fig. 4.7).

Fig. 4.8 Chevron-shaped cracks on the surface of a fine sand (120 s grinding)

K_{100} flattened out thereafter at 300-360 s, and marginally fell at 360-600 s timescale. The sequences of decreasing-plateau trends revealed the fractal feature of K_{100}. The sequences also revealed the continuous breakage of large grains, although these grains survived splitting at certain previous grinding timescales due to the increasing number of lateral support from finer grains.

The step-wise particle breakage can be explained via the fractal dimension. This is drawn here from the power law exponent of Schuhmann distribution (Eq. 4.1).

$$P = \left(\frac{S}{K_{100}}\right)^{n_s} \qquad \text{Eq. 4.1}$$

where 'P' is the passing percent (by mass) through sieve size 'S'. The 'index of uniformity', n_s, can be demonstrated by the slope of PSD fitting line on a double logarithmic plot of cumulative passing percentage versus normalized nominal diameter (i.e. diameter divided by K_{100}). The fractal dimension is then derived from the index through Eq. 4.2 (Lu et al., 2003).

$$D = 3 - n_s \qquad \text{Eq. 4.2}$$

In the fractal dimension versus grinding time plot (Fig. 4.9) a steep rise in fractal dimension (i.e. poor sorting, well-developed graded) over 0-180 s timescale from 1.7 to a peak of 2.6 is evident. Fractal dimension then remained constant throughout the 180-720 s timescale, with slight variation between 2.3 and 2.6. The plateau trend was probably due to the loss of energy efficiency through the grinding time. The declining trend of energy efficiency is due to the constant energy input through the experiment and the rising trend of the fines population.

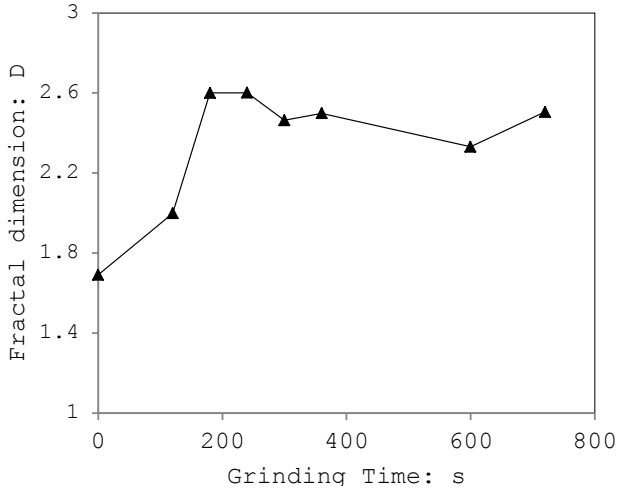

Fig. 4.9 Sharp change in the fractal dimension through the early (i.e. under relatively low energy input) sand-to-silt transition and the significance of loss of impact energy efficiency due to the marked increase in population of crushed fine particles.

As discussed earlier, fines provide lateral supports to relatively coarser grains and therefore damp the energy. Damping also improves by the formation of platy crushed grains, and through enhanced degrees of lateral support to survived grains.

4.2.4 Mode-size Distribution on Breakdown Timeline

The Leighton Buzzard Sand possesses a pronounced mode at around 100-400 µm (Fig. 4.10a) and a secondary pronounced mode at around 40-60 µm. This corresponds very well to the quartz sand modal distribution in Assallay et al. (1998). By the end of the initial grinding for 120 s, the original modes slightly shifted to the left. This increased the population of grains at silt-scale mode size. Further grinding to 180 s led to the disappearance of sand-scale mode size at the expense of an increased population of grains at silt-scale mode sizes (Fig. 4.10c). An increase in the grinding time to 300 s removed the first pronounced silt-scale mode size (4-5 Ø or 31-62 µm Fig. 4.10d). This can be viewed in conjunction with increasing breakage index and decreasing K_{100} over 240-300 s timescale (Fig. 4.1 and 4.7).

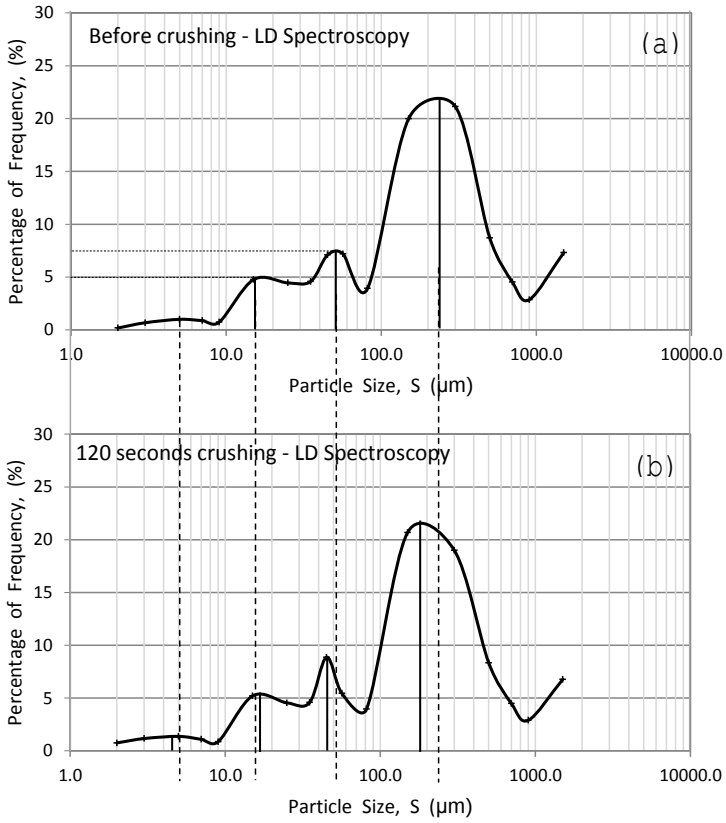

Fig. 4.10 Mode size distribution: original & ground sand (a) primary pronounced modes in the original sand (b) initial grinding and change in the population of the grains of pronounced mode sizes

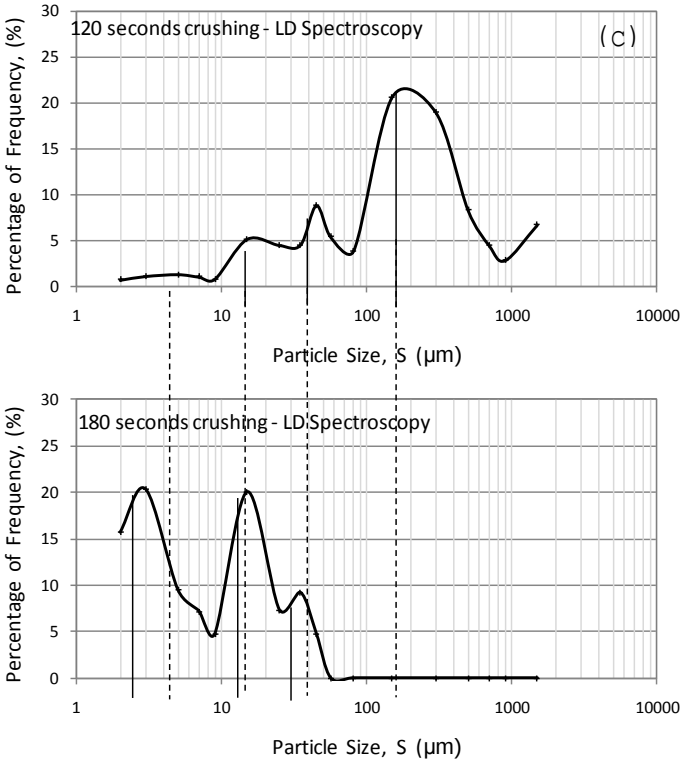

Fig. 4.10 (c) the fully sand-to-silt transition after an increase in grinding time

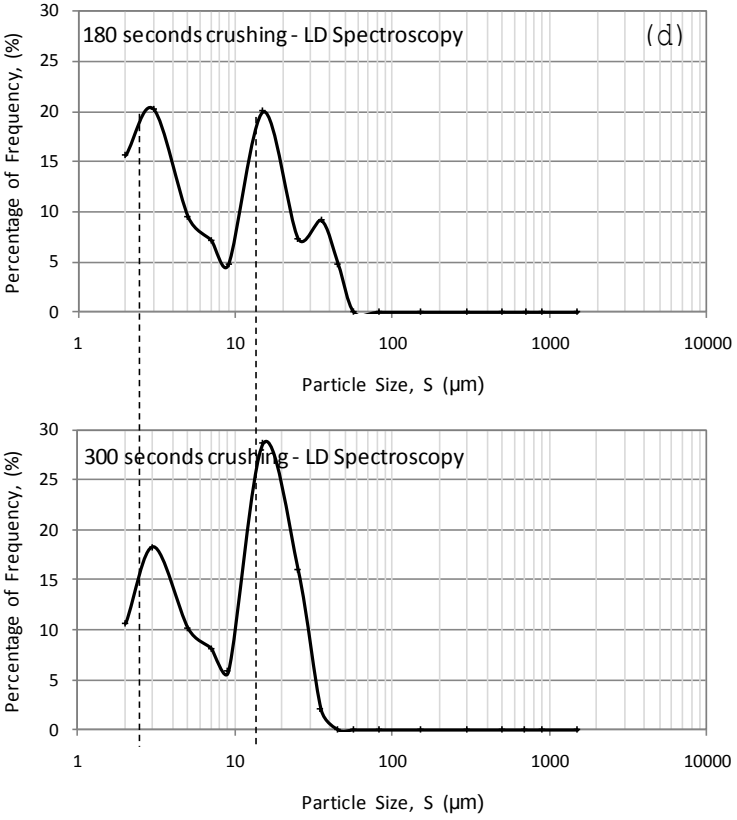

Fig. 4.10 (d) the crushing of coarse silt into fine silt after a further increase in grinding time

The results showed that all mode sizes at both sand- and silt-sized scales were shifted or removed, except the 10-20 µm mode size, which was preserved through the entire grinding time. The 10-20 µm mode appeared as an intrinsic characteristic of the quartz, which was reproducible at varied grinding durations.

4.2.5 Energy Input on Breakdown Timeline

The input energy was varied by putting a control on the mass of sand batch in the mill's barrel. For ten 60 s long discontinuous grinding intervals, the disk barrel's feed mass was reduced by 30%. Increased input energy led to a poorly sorted silt output (Fig. 4.11a), maximal crushing of middle-sized grains and minimal crushing of relatively finer and coarser grains, and increases in populations of 10-20 µm and 3 µm sized grains (Fig. 4.11b).

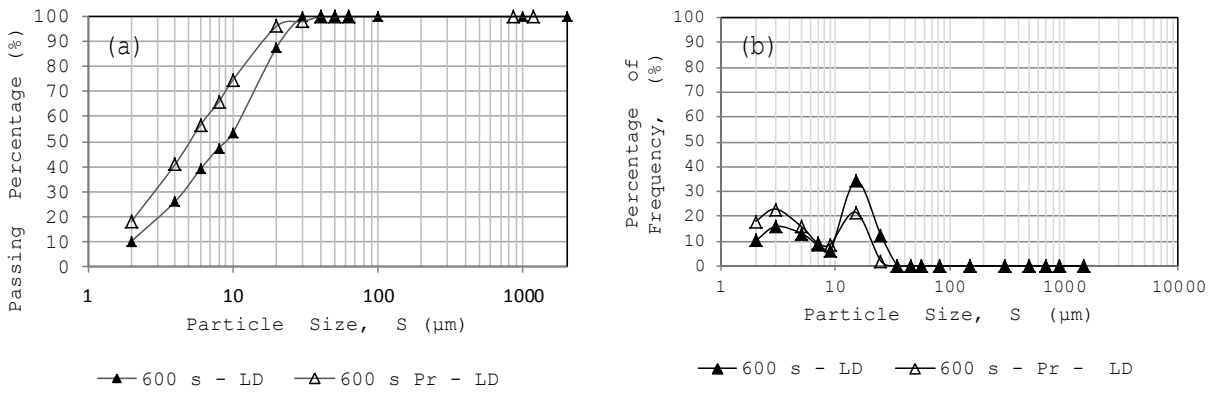

Fig. 4.11 Loss in middle-sized silt grains and survival of fine and coarse sized silt grains upon an increase in the impact energy

The maximum grain size changed marginally with increasing energy input. This was probably due to the insufficient increase in prompted energy to break the 32 µm silts, or due to the enhanced population of edge-grinded materials, which in turn improved the confinement (or damping) around the 32 µm grains.

4.2.6 Discussion

The sand-to-silt approach in Leighton Buzzard Sand was examined. To enable an objective assessment of the micromechanics of size reduction, measurements of particle and mode size distribution, fractal indices and micromorphological signatures were made. The crushing approach was probed through varied grinding time at a constant energy input, as well as varied energy input at constant

grinding time. The close inspection of sorting, mode sizes, grain population at mode sizes, fatigue stresses, and energy efficiency would suggest that:

(1) The sand-to-silt size reduction pathway in quartz possesses fractal properties (in sorting, maximum particle size, fractal dimension, and mode size distribution). Light transmission microscopy examination of sand- and silt-sized quartz samples before crushing revealed evidence of surface imperfections and internal planes of varied taxonomy. As these were observed in grains after crushing, the surface and internal defects appears to be fractal features. This, however, defers slightly from the findings of Moss (1973) and Sharp and Gomez (1986). Therefore, the breakdown process explained here will also represent the size reduction mechanisms in coarser particles of debris at the base of glaciers.

(2) Sand and silt are not final resistant products of the glacial comminution. Also, they are not the products of two mechanisms. These are in contrast with some earlier works (Rogers et al., 1963, Haldorsen, 1981, Wright, 1995), but in agreement with another line of works (Jefferson et al., 1997a, Cheng, 2004, Kumar et al., 2006). This is because of the differences between crystallographically pure quartz and that with internal defects.

(3) The results showed that there needs to be a prolonged application of moderate and declining energy (or alternatively application of a sudden but considerable energy) to crush a quartz fine sand or coarse silt to finer fragments. In other words, grain breakdown is not necessarily an energy-dependent process. The results also demonstrated that fatigue fracturing may occur either through prolonged stressing or transient stressing in a relatively shorter period. This agrees with the earlier works of Moss (1966) and Rabinowics (1976) but argues the findings by Rittinger (1867) and Bond (1952) reported in Wright (1995).

(4) The results showed an intrinsic pronounced mode size of 10-20 μm in crushed material at varied grinding timescales. It is most probable that the internal crystalline defects have some control on the size of the silt output.

(5) The sand-to-silt approach affects the relatively larger grains more. Further crushing of the silt fragment via increased energy input re-

distributed grains' population evenly without changing the maximum grains size. Further crushing mostly affected the middle-sized grains.

4.2.7 Concluding Remarks

To look into the collapse mechanism at the quartz grain scale, a grain breakage timeline was produced by coupling the real-time variation of six fractal indices and the grains' shape. Since these grains are the skeletal structures, which make up the collapsing soils (in particular loess), and due to the interaction between the pore size and the particle size in a given stress environment, the breakage timeline was chosen as the first step in development of the framework for collapse modelling.

Experiments showed that quartz breakdown is a fractal phenomenon. Sand and silt are not the products of two mechanisms, even though certain controls brought the sand into the sedimentary system. This is generally in agreement with the early idea of Wentworth (1933). However, this research suggests that sand and silt are not final resistant products of abrasion. Sand can break to silt-size, while silt (i.e. broken sand) can experience continuous size reduction under a prolonged and transient application of stress. Damping of stress does not impede the breakage in grains indicating the contribution of fatigue effect in crushability. The internally defected sand and silt are inherently breakable. Experiments affirmed that a control exists which delivers significant contents of particles in the 10-20 μm size. This control is independent from energy input, energy duration, and the grains' starting size.

4.3 Dynamics of Stress and Hydraulic History

4.3.1 Fundamental Concepts

Among the many factors that control collapse, stress and hydraulic history are the most significant as certain combinations of these can alter the packing state to great extents. However, published works on stress path-packing state interaction are limited to clayey silts, underreporting the contribution of carbonates. Studies on the control of hydraulic path lack physical evidences for pore distribution, leading to considerable dispute over the variation of

air-volume over time and hence soil long-term behaviour. In this section, the control of stress and hydraulic path in ideal loess (containing 20% carbonates, 10% kaolinite, and 20% silt) on pore space is investigated. Within the next three sub-sections, pore and particle size distribution and microfabric are probed on the pre-wetting, wet-, and post-wetting surfaces.

4.3.2 Wetting Stress-State Surface

4.3.2.1 Wetting under Zero External Net Stress

A pronounced reduction in the mass of 5-20 µm grains upon wetting was recorded in sizing data (Fig. 4.12). This suggested that a remarkable quota of <20 µm grains were coagulated into larger assemblages on wetting. In other words, the tendency for aggregation reduced in >20 µm particles.

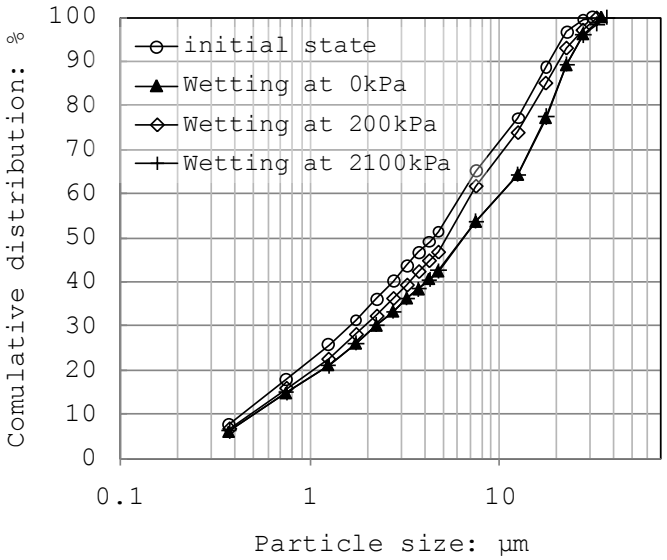

Fig. 4.12 Particle size distribution on suction decrease surface

The $(PP_i-PP_W)/PP_i$ ratio is plotted against particle size in Fig. 4.13, where: PP_i is the passing percent of grains through a given mesh opening size before wetting, and PP_W is the passing percent of grains through a given mesh opening size after wetting. Higher $(PP_i-PP_W)/PP_i$ indicates stronger aggregation. In Fig. 4.13, the signature of constant but strong aggregation is showen in <5 µm grains. The aggregation slightly decreased for 5-20 µm grains. A sharp reduction in aggregation took place with increasing grain size from 20 µm to 87 µm. The plot highlights the significance of <20 µm particle loss on wetting. The change in the particles' population is commented on Table 4.1 after reading Fig. 4.12 in conjunction with Fig. 4.13.

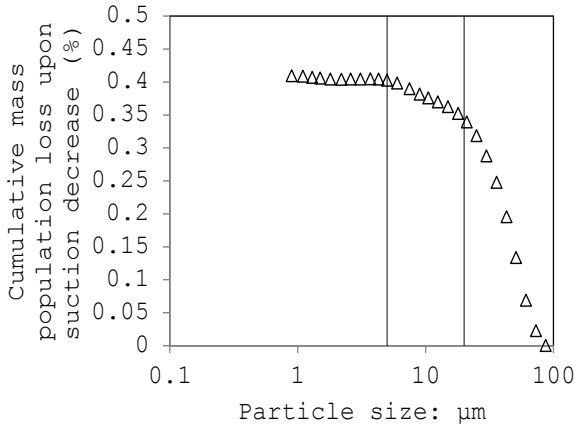

Fig. 4.13 Cumulative population loss upon suction decrease at zero net stress

Table 4.1 Population loss in % in distinct grain size intervals[32] as a result of Self-weight wetting induced

Particle size: µm	Population (mass):%
0.35	Loss of 40%
0.35 to 5	Loss of 40%
5	Loss of 40%
5 to 20	Loss of 40% to 34%
20 to 87	Loss of 34% to 0%

Fig. 4.14 (commented on Table 4.2) shows the dynamics of pore size distribution on wetting for varied wetting stresses (i.e. hydraulic history).

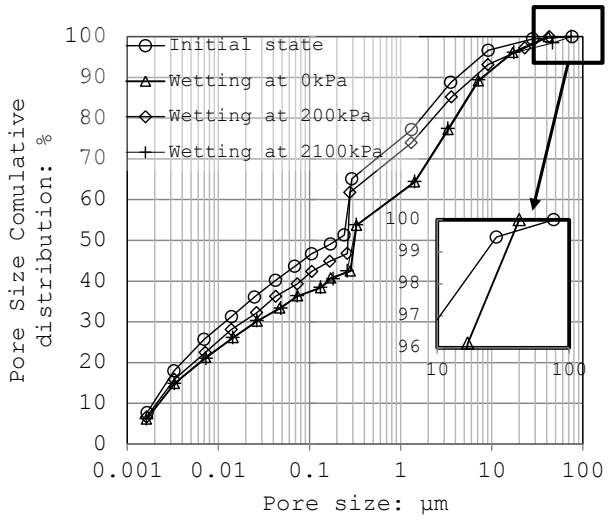

Fig. 4.14 Pore size distribution on wetting surface

[32] Population change percent is a factor of the PSD. In chapter 3, the reproducibility of ideal loess preparation, loading and wetting was examined. Studying the results of 95% of up to 18 repeated oedometer tests on ideal loess revealed a standard error of ±2.04%. Furthermore, Laser Diffraction experiments were conducted twice to assure the trend as well as the marked mode size is reproducible. An example of such repeated graphs is reported in an appendix to this thesis.

Table 4.2 Contribution of wetting in changing the volume of pore spaces with certain size

Pore size: µm	Population (volume)
0.001	Minimum loss
0.001 to 0.25	Degree of loss improving at slow rate
0.25 to 0.3	No change
0.3 to 1.5	Some high degree of loss, lesser at 1.5µm
1.5 to 8	Sharp reduction in loss (lowest at 8µm)
8 to 19	Some high degree of loss, lesser at 19µm
19 to >19	Sharp reduction in loss (negligible at >19µm)

The maximum pore size dropped from 76 to 42 µm on wetting (Fig 4.14). Reduced pore size gave rise to the curvature radii's and thus decreased the suction. This agrees with the hysteresis effect (Fig. 4.15).

Hydraulic hysteresis is linked to the association of micro-fabric and the soils' affinity for water. Therefore, any change to particle/pore arrangements allows the hydraulic hysteresis to take place. On this basis, 5-20 µm gains, and 0.001-0.25 µm as well as 0.3-1.5 µm in diameter pores were deemed responsible for the hydraulic hysteresis. This agrees with the work of (Munoz-Castelblanco et al., 2012) on French calcareous loess, consisting of 80-85% silt (of 20 µm mode) and 15% Calcium Carbonate, which showed matrix clusters of relatively low pore size and population were most sensitive to the water content changes.

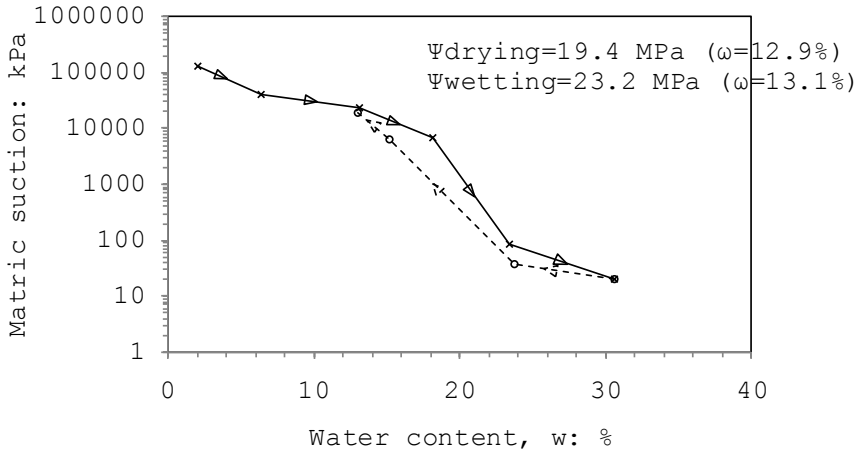

Fig. 4.15 SWCC curve derived after filter paper test

In section 4.6, shrinkage has been recorded upon drying in identical artificial loess specimens of 10 to 30% carbonate content. Strong aggregation and considerable loss of <20µm particles led to the development of trans-

assemblage pore spaces. Pellet structures at the saturated state were surrounded with the water phase. The loss of the water upon drying left behind air surrounding grains, which is a proper space for aggregates to approach their contact points. This implements the drying-induced contraction, or the commonly used 'shrinkage' term.

4.3.2.2 Wetting under Varying External Net Stress

In the presence of an external net stress, which was high enough to maximize the skeletal forces, but low enough to sustain the pores, wetting led to the maximum collapse (Fig. 4.16). The coefficient of collapsibility in Fig. 4.16 was determined for varying flooding stresses and is given by $C_{col} = \Delta e/(1+e_1)$, where Δe is the wetting-induced decrease in void ratio; and e_1 is pre-wetting void ratio. C_{col} is normalized against the initial void ratio (before stressing and/or wetting), to allow the comparison between identical specimens.

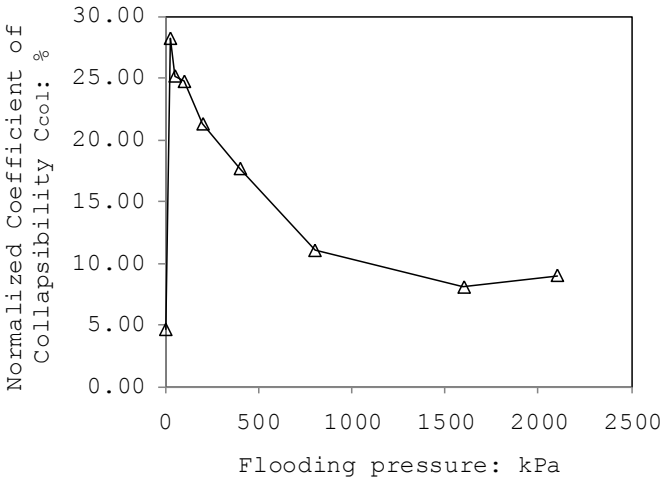

Fig. 4.16 Plot of normalized coefficient of collapsibility (collapse potential) against flooding pressure (e.g. for the flooding pressure of 50 kPa: $(e_{50kPa\ dry} - e_{50kPa\ wet}\ /1+e_{50kPa\ dry})/e_0$ vs. flooding pressure

20% carbonates appeared as poor macro-pore bracing units (Fig. 4.17) and strong inter-silt bridge connectors (Fig. 4.17), while the relatively minor 10% clay appeared as clayey coats for silt, beneath the external carbonate shield (Fig. 4.17) and aggregates at the macro-pore space (Fig. 4.18). The clay therefore had a relatively minor contribution to the collapse mechanism.

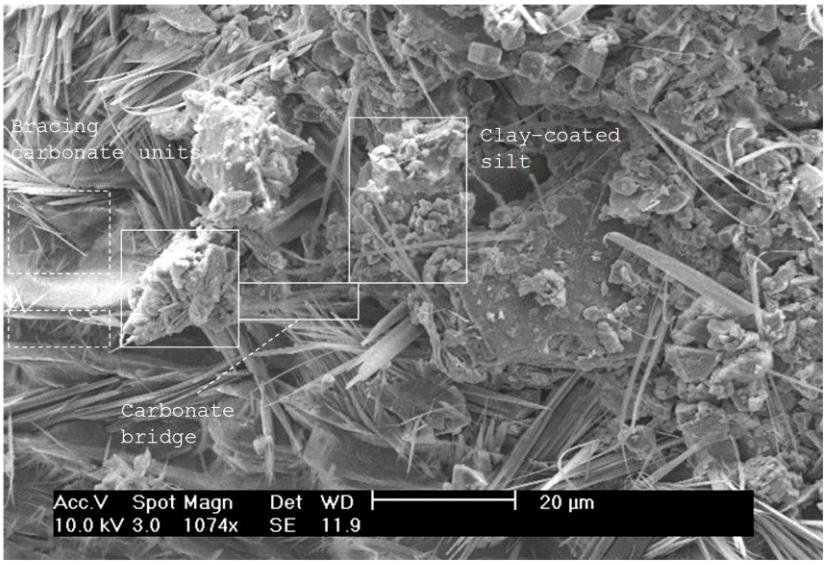

Fig. 4.17 Shape of carbonate units at 20% carbonate content

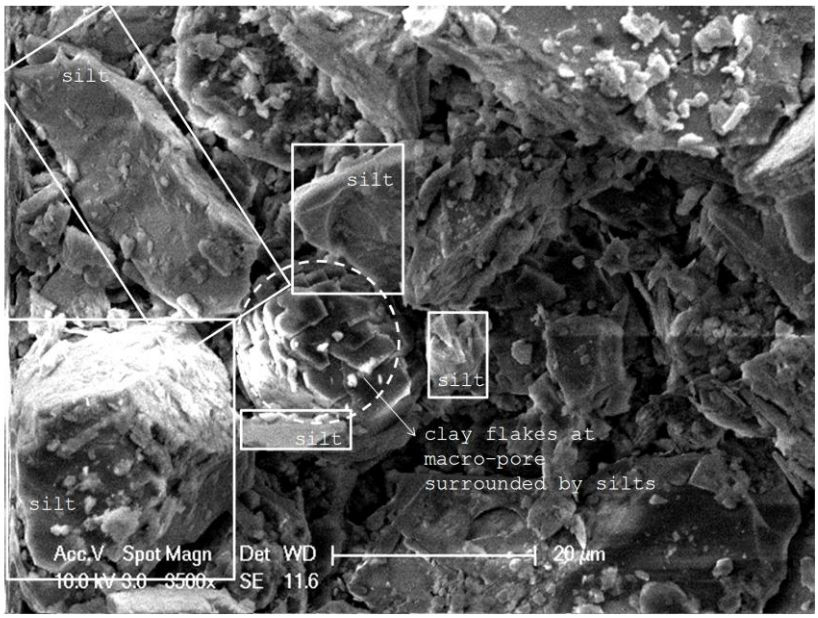

Fig. 4.18 migration of clay flakes to macro-pore spaces

Wetting released the inter-particle connectors (through physical washing and mechanical shearing). The particles approached to contact points (asperities) by the driving force of gravity and stored skeletal forces. Higher skeletal forces induce higher grain-to-grain impact forces and thus more crushed grains (Fig. 4.19). The reduction in skeletal force with increasing flooding stress allowed the coagulation to develop. This countered the size reduction effect at stress levels as high as 1600 kPa (Fig. 4.16).

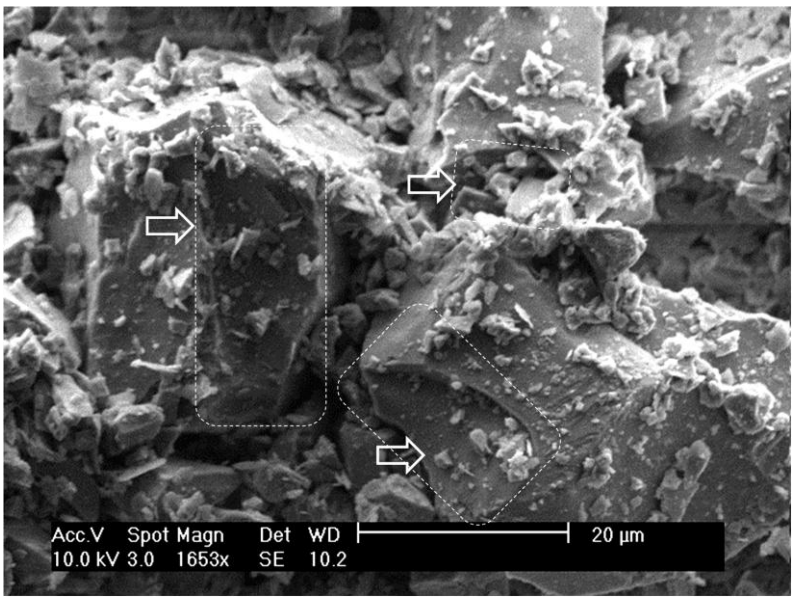

Fig. 4.19 Three adjacent silt grains with sharp, concave features of edge chipping

To examine what range of particle sizes were most affected by coagulation, the $(PP_i-PP_w)/PP_i$ ratio (i.e. PP is the passing percent on PSD curve, 'i' and 'w' refer to 'initial' and '2100 kPa wetting pressure' states on Fig. 4.12, respectively) was plotted against particle size in Fig. 4.20 for the flooding stress of 2100 kPa. In Fig. 4.20, coagulation took place at both clay-size (<1µm) and silt-size (20-30 µm).

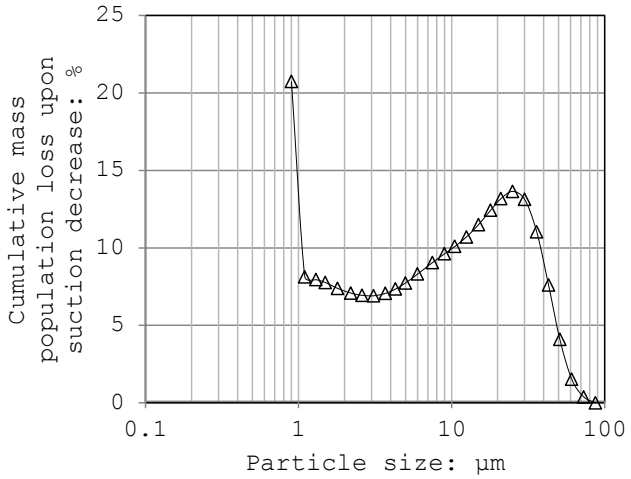

Fig. 4.20 Cumulative particles' population loss upon wetting at 2100 kPa net stress

Reading the loss of 1 µm particles in conjunction with microscopic images (Fig. 4.18) revealed the migration of clay from contact points to the macro-pores. Silt- and clay-size crushed quartz also migrated with clay/carbonates into the macro-pores.

From a different perspective, some tubular carbonates re-precipitated in a scaffolding framework and formed re-stored bridges (Fig. 4.21). This induced a residual post-wetting collapsibility.

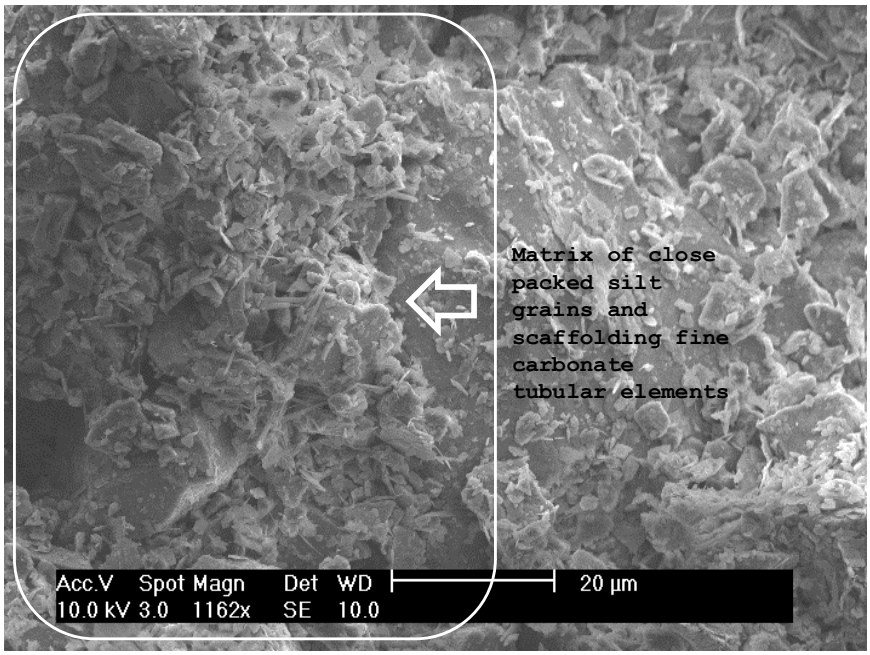

Fig. 4.21 Tubular carbonate bridges after flooding

4.3.3 Dry Stress-State Surface

Laterally-confined stressing to 12.5 kPa (less than the threshold stress at which grains commence splitting) led to compression of fine silts (0.8 to 20µm). This can be observed on Fig. 4.22, where the population of <20 µm grains decreased on loading.

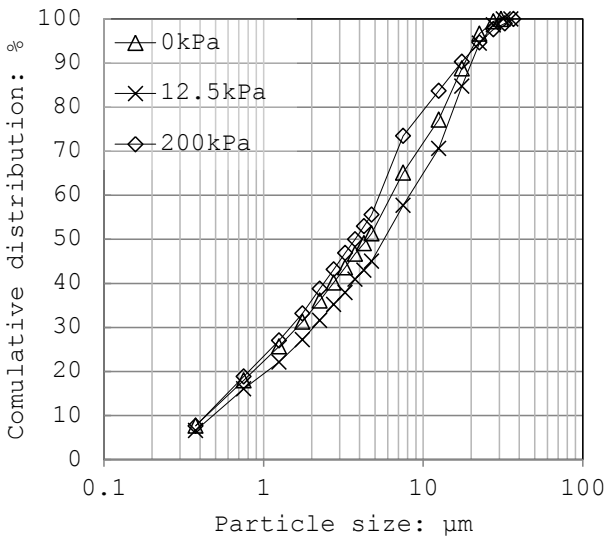

Fig. 4.22 Loss in population of 0.8-20µm grains upon stressing to 12.5kPa

Early changes to packing state were associated with the grains' re-arrangement rather than collapse. Buttress units survived under relatively low levels of skeletal forces. Assemblages took a dispersed association and the size of clusters slightly decreased (Fig. 4.23-4.24): Four assemblage units are shown in hatched lines in Fig 4.23(a). Within each assemblage, chains of silt-bond-silt surround macro-pores. This is schematically illustrated in Fig. 4.23(a). In Fig. 4.23(b) (post-stressing re-arranged assemblage), silt chains arch macro-pores of reduced volume. This is schematically illustrated in Fig. 4.24.

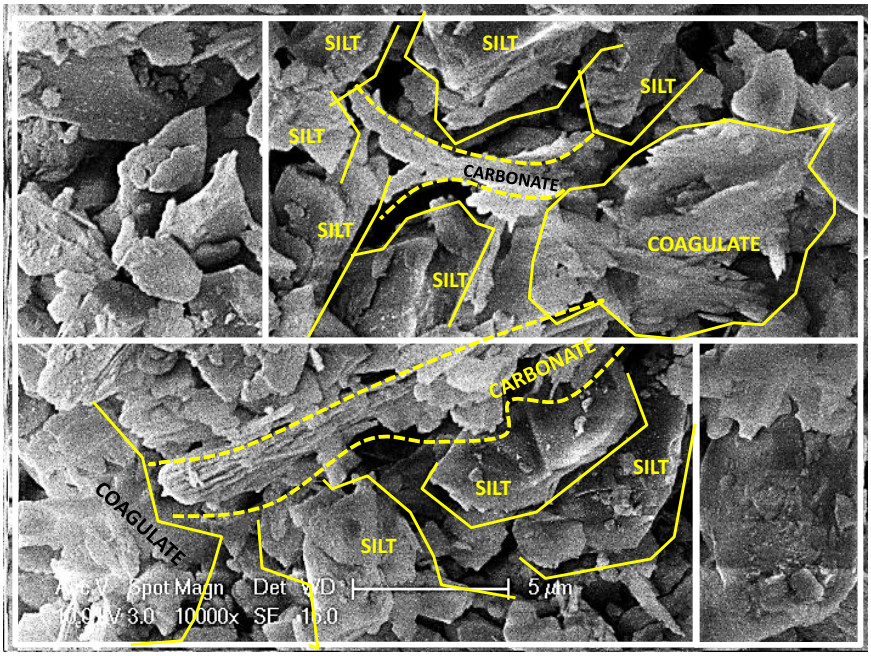

Fig. 4.23(a) Initial packing (before compression)

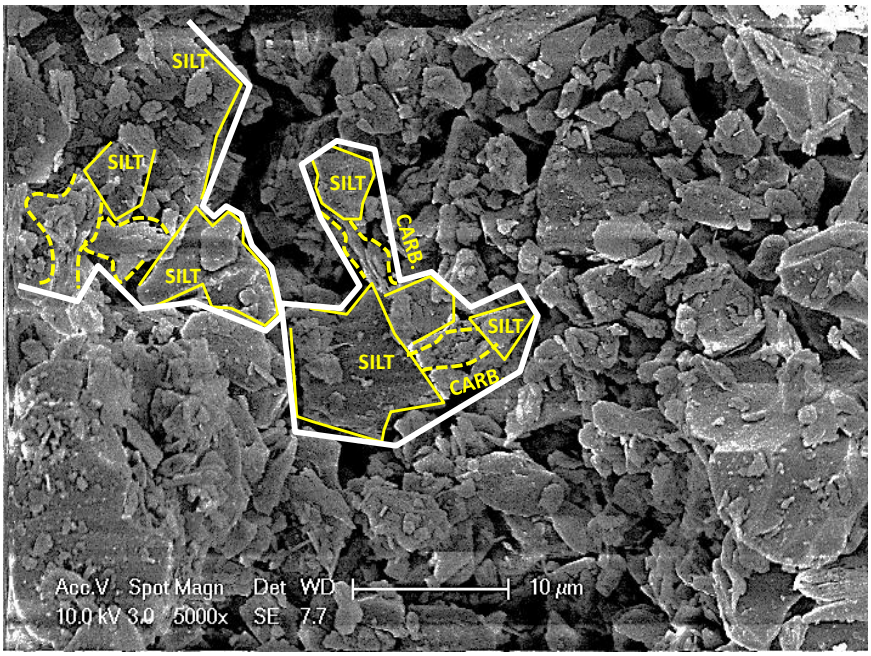

Fig. 4.23(b) Post-stressing packing

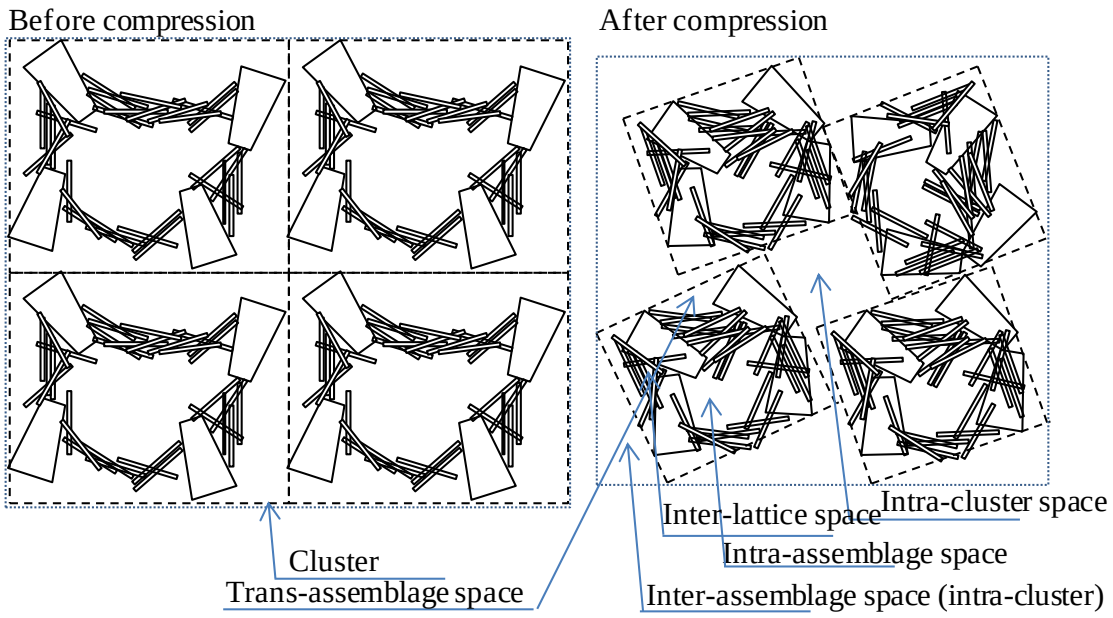

Fig. 4.24 Schematic of particle arrangement before and after pre-wetting laterally confined loading

A further increase in net stress to 200 kPa led to the breakage of silt grains. This was reflected in increased mass of 1 to 20 μm grains (Fig. 4.22). Crushing continued, but with a decelerating rate, with an increase in the net stress to 2100 kPa (Fig. 4.25).

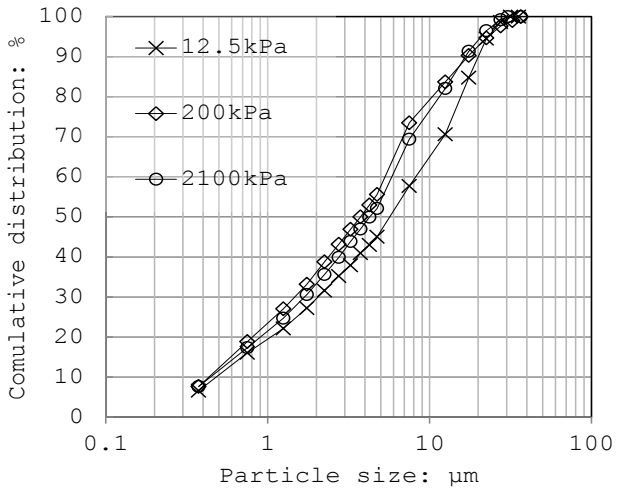

Fig. 4.25 Particle size distribution on dry surface

With reference to Fig 4.26, a multi-modal pore size distribution was obtained for stress levels beyond 200 kPa.

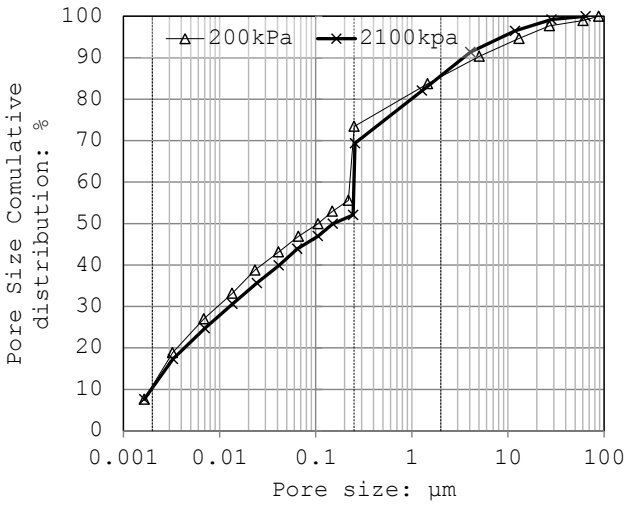

Fig. 4.26 Pore size distribution on dry-surface

From a micromechanical perspective, the soil medium consists of a number of clusters, each containing assemblages of silts bonding together with carbonate/clay (Fig. 4.24). Upon stressing to 2100 kPa, trans-assemblage pore spaces were destroyed due to air expulsion. This is mirrored in the decrease in population of 0.25 to 2 µm pore spaces (Fig. 4.26). Silt grains were forced into the buttress units, which reduced the intra-assemblage pore spaces. This implements the drop in the population of 0.001 to 0.25 µm void spaces. Clusters rotated and approached to contact points, forming new inter-assemblage pores. The increase in abundance of 2 to 20 µm pores was attributed to the formation of these inter-assemblage spaces.

4.3.4 Wet Stress-State Surface

The dynamics of packing state on the post-wetting stressing shall be viewed in the light of stress-hydraulic history. The $(e_f-e_0)/e_0$ is plotted against the flooding pressure in Fig. 4.27, where e_f is the void ratio at 2100 kPa under saturated condition and e_0 is the void ratio before stressing at the dry state. The enhanced consolidation for 12.5 kPa flooding stress is due to the marked loss of void ratio in the event of wetting. A further increase in consolidation for 25 kPa flooding stress is due to a relatively high dry-state compression in addition to the high content of collapse upon wetting. From a different perspective, the marginal difference between the compressibility of specimen pairs on dry-state at 12.5 and 25 kPa, and also the higher degrees of

wetted collapse at 12.5 kPa than 25 kPa, highlighted the dependency of coefficient of volume compressibility (m_v) to the flooding pressure.

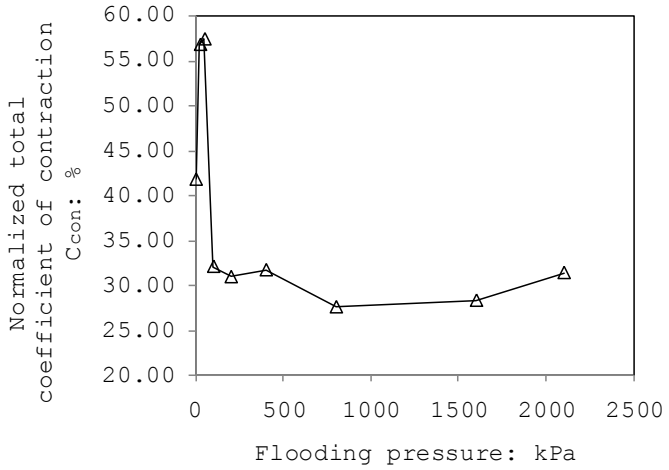

Fig. 4.27 Plot of normalized total contraction upon pre-wetting stressing, wetting, and post-wetting stressing for varied flooding pressures: $(e_0-e_f/1+e_0)/e_0$ vs. flooding pressure

4.3.5 Concluding Remarks

The ideal loess (containing 70% silt, 20% carbonate, and 10% kaolinite) was used to examine the dynamics of pore spaces in the event of laterally-confined loading, self-weight wetting, wetting under varied stress, and post-wetting laterally-confined loading. Key findings are reviewed in this section:

Four levels of pore size intervals were introduced, within which pore population changed upon self-weight wetting had a particular pattern: (1) trans-assemblage pores (>1.5 µm, corresponding to >40 µm grains), (2) macro-pores (0.3-1.5 µm corresponding to 0.65-7.0 µm grains), (3) meso-pores (0.001-0.25 µm corresponding to 7-40 µm grains), and (4) micro-pores (<0.001 µm corresponding to <0.65 µm grains).

Pre-wetting loading failed to fully restrict the collapsing structure. Wetting at any stress level led to aggregation (in >30 µm grains), and a subsequent increase in pore volumes. Enhanced pore volumes could induce some degree of collapsibility in the event of drying. However, the ideal loess showed maximum densification after wetting under 25 kPa stress.

4.4 Dynamics of Silt-Bond Interface

4.4.1 Fundamental Concepts

In the previous section, 4.3.5, a brief account of the interplay between hydraulic hysteresis and pronounced pore sizes was introduced. A single wetting-drying cycle re-arranged the micro-fabric in the test specimen and led to the hydraulic hysteresis, as the result of an increase in the pore sizes and the consequent decrease in the matric suction. This means a slight increase in the post-wetting void ratio over a drying season. Section 4.3.5 also showed how washed carbonates can re-precipitate again and restore the collapsibility to some degree. The extent to which collapsibility could be restored, is a factor of silt-bond interface properties. The 'number' and 'quality' of silt-to-silt contact points has a significant control on the quality of re-stored bonds: The 'number' of contact points is a factor of silt size distribution, while the 'quality' of contact points is controlled by silt's textural properties. This section further examines this hypothesis.

4.4.2 Results

Coefficient of collapsibility was measured in identical pairs of loess specimens (similar composition and stress history but of varied silt component grading). Standard oedometer test results revealed a higher dry stiffness for clayey silt and calcareous clayey silt loess soils when containing uniformly graded (UG) silt components (see Fig. 3.7 and Fig. 3.8). Uniform grading is analogous to poor sorting. The higher stiffness in the presence of UG silts can be seen in Table 4.3, where total contraction for 0 to 200 kPa confined stressing were measured higher in specimens made up of NG silt component. In Fig. 4.28, the decreasing trend of normalized coefficient of contraction against stress increments in soils with silt-components' natural grading (NG) shows that bonds failed under initial low stresses. On contrary, the increasing trend of normalized coefficient of contraction against stress increments in soils with silt-components' uniform grading (UG) shows that bonds resist well against low stresses.

Table 4.3 Normalized C_{con} on dry-, wet-, and wetting- stress state surfaces

Sample No.		Dry Stress-State Surface						Wetting	Wet Stress-State Surface				
	From: kPa To: kPa	0 12.5	12.5 25	25 50	50 100	100 200	0 200		200 400	400 800	800 1600	0 800	0 1600
	Silt-Clay-Carb-Grading	C_{con}%						C_{col}%	C_{con}%				
1	60-10-30-UG	2.89	0.10	0.22	0.71	3.61	3.87	20.10	8.26	5.68	2.75	41.05	42.72
2	60-10-30-IG	0.80	0.12	0.39	0.92	3.15	5.21	20.07	3.86	3.54	2.85	25.49	28.72
3	70-10-20-UG	1.52	2.05	6.08	12.47	9.58	26.80	31.68	11.74	11.45	13.86	45.47	48.11
4	70-10-20-IG	0.36	0.61	1.12	3.11	4.64	9.35	23.32	5.60	4.43	3.97	34.54	36.38
5	75-10-15-UG	1.81	0.68	1.49	2.26	4.11	9.92	27.68	8.76	7.64	N/A	44.21	N/A
6	75-10-15-IG	1.43	1.46	1.42	2.12	5.75	11.26	13.16	4.31	3.41	N/A	26.21	N/A
7	80-10-10-UG	1.24	0.98	1.56	2.68	4.40	10.22	13.86	5.80	5.38	5.03	29.08	31.89
8	80-10-10-IG	1.12	0.90	0.64	1.63	4.66	12.14	9.62	11.85	3.55	N/A	25.40	N/A
9	90-10-0-UG	1.86	1.19	1.37	1.32	1.77	5.57	3.49	2.11	2.70	2.67	12.89	15.03
10	90-10-0-IG	7.72	2.94	2.80	2.71	2.48	17.69	6.09	2.05	3.98	2.11	24.91	26.16
11	90-10-0-IG	2.88	4.81	4.18	3.38	2.05	15.76	14.06	12.54	2.18	N/A	30.54	N/A

UG: Uniformly graded (poor sorting)

IG: Ideally graded (well sorting)

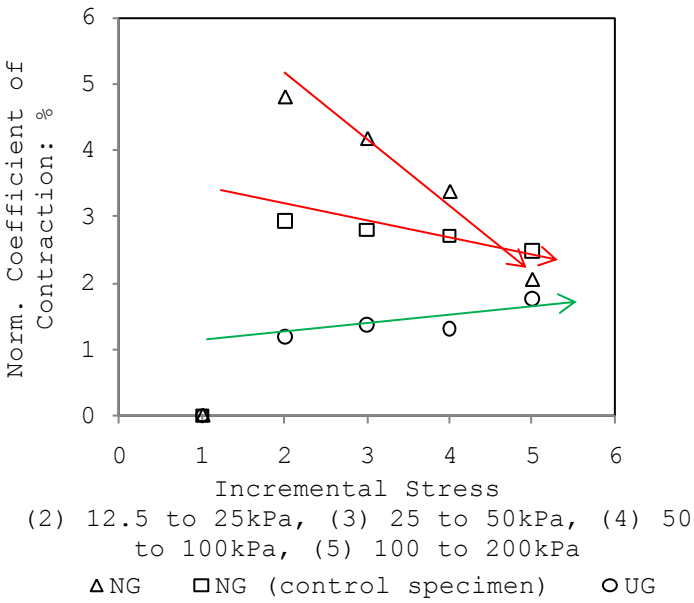

Fig. 4.28 $\left(\frac{e_i - e_{i+1}}{e_i}\right)/e_0$ versus loading increment (i to i+1): clayey silt specimens (10% kaolinite, 90% quartz silt)

4.4.3 Discussion and Conclusion

In Section 4.3, it was shown that Quartz sand and silt continuously break to finer grains in nature, irrespective of the value of applied energies. The breakage results in the formation of a well sorted quartz material (at 10-20 µm mode size). This section showed that loess soils made up of well sorted silt grains have higher collapse potential than similar loess soils made up of poor sorted silt grains. Such finding is supported by the results of single oedometer tests on loess soils containing 10% kaolinite, and 0 to 30% of carbonate. Higher collapsibility could be because of the formation of better quality bonds between well sorted silt grains. For compacted loess soils, grains crush to pronounced mode size of 10-20 µm. In the event of wetting, clay and carbonate migrate with water, and re-precipitate after subsequent drying. Re-precipitation can form good quality inter-particle bonds between well sorted crushed grains. Such phenomena can induce a hazardous degree of collapsibility in compacted loess fills.

4.5 Dynamics of Internal Forces

4.5.1 Fundamental Concepts

Section 4.2 showed the significance of skeletal forces (input energy) in the breakage of quartz silt, which make up loess. It was also shown that grains continuously break to form a repeatable pronounced particle mode size. Section

4.3 showed four levels of pronounced pore space sizes, which were surrounded with grains of repeatable marked mode diameters. This raised the question if specific forces apply to specific pore spaces in such a multi-porous medium.

This section examines the variation of inter-particle forces on the wetting stress-state surface. An 'ideal loess' was flooded via a steady-state flow followed by a phreatic phase (mode 3 as described in Section 3.3, Chapter 3). The use of temporary constant head flow was due to the need for magnifying the flow-associated internal forces and hence, to measure internal forces in a more generic hydraulic scenario. A similar experiment was conducted on an identical specimen, but through the capillary rise flow followed by a phreatic phase (mode 4 as described in Section 3.3, Chapter 3). Similar results to that of mode 3 were obtained, except with impacts of the early steady state flow. For this reason, and to avoid duplication, the mode 3 results are only explained throughout this section.

The internal forces were measured against the wetting time. The collapse trigger mechanism was then explained as a factor of the inter-particle forces. Eventually, these forces were closely examined to find their interplay with the micro-fabric. The results were used in Section 4.6, to re-define the effective stress as a factor of such internal forces.

4.5.2 Results and Discussion

The inter-particle forces were measured during wetting under the mode 3 condition on an ideal loess specimen (i.e. 70% quartz silt, 20% carbonate, 10% kaolinite). Fig. 4.29 illustrates the variation of void ratio, the internal and the super-imposed active (i.e. $F_{Skel} - F_D + F_W + F_U - F_B$) forces against the wetting time.

It can be observed that the drag force increased immediately after wetting and decreased thereafter by about half its peak value. Drag force was also measured against wetting under mode 4 condition, indicating the same rise and fall during the early course of wetting. The reduction in drag force led to a rebound volume change, and hence the expansion of pore spaces at the wetted lower-height of the test specimen. The number of solids available within the upper-height of the specimen increased consequently, giving rise to the weight

force, operating at the mid-height of the specimen. Consequently, the super-imposed active force was increased to the wetting course maximum (at minute 3.45). Reading the void ratio and active force graphs together infers that the maximum active stress failed to trigger the collapse (collapse triggered at the wetting time interval 7.0 to 8.5 minute). Net stress application gave rise to the skeletal forces (at minute 4). Hydraulic modification of connectors at grain contact points together with the increased axial skeletal force led to the migration of fines to macro-pores and hence a decrease in the number of solids standing in column above the specimen's mid-height. This led to a decrease in the weight force and consequently a decrease in the super-imposed active force. First collapse took place few minutes later, after 8.5 minutes of wetting. Fig. 4.30 illustrates the first collapse event: void ratio levelled off and remained constant at 1.40 throughout the time interval 7.0 to 8.5-minute. At the point of collapse, the mean water content was recorded 25.2%, giving a 'mean' saturation ratio of 42%. Super-imposed active force followed a declining trend towards the end of constant-head flow condition. The transition to the phreatic condition allowed the Super-imposed active force to climb back, before its second declining trend to the end of the suction decrease stage. The change of flow condition from constant-head to phreatic decelerated the bonds failure and allowed the contact relations to retrieve to carry greater forces. Further increase in the saturation ratio and thus further debonding led to a final declining trend in active forces.

Close inspection of the void ratio versus wetting time graph (Fig. 4.29) revealed three major time intervals in which void ratio gained a quite plateau trend: (1) 7.0 to 8.5-minute, (2) 382 to 447-minute, and (3) 1314 to 1419-minute. In micro-mechanical words, soil structure resisted against softening within the above three time intervals. The first and last time intervals were deemed to represent fully-mobilized pendular and funicular states of the water film, respectively. An explanation for such choice is that, on the wetting path, soil structure collapses due to an increase in the thickness of the thinnest possible water film (i.e. transition from the maximum pendular level to funicular state) and hence a decrease in matric suction under relatively a high and constant super-imposed active force.

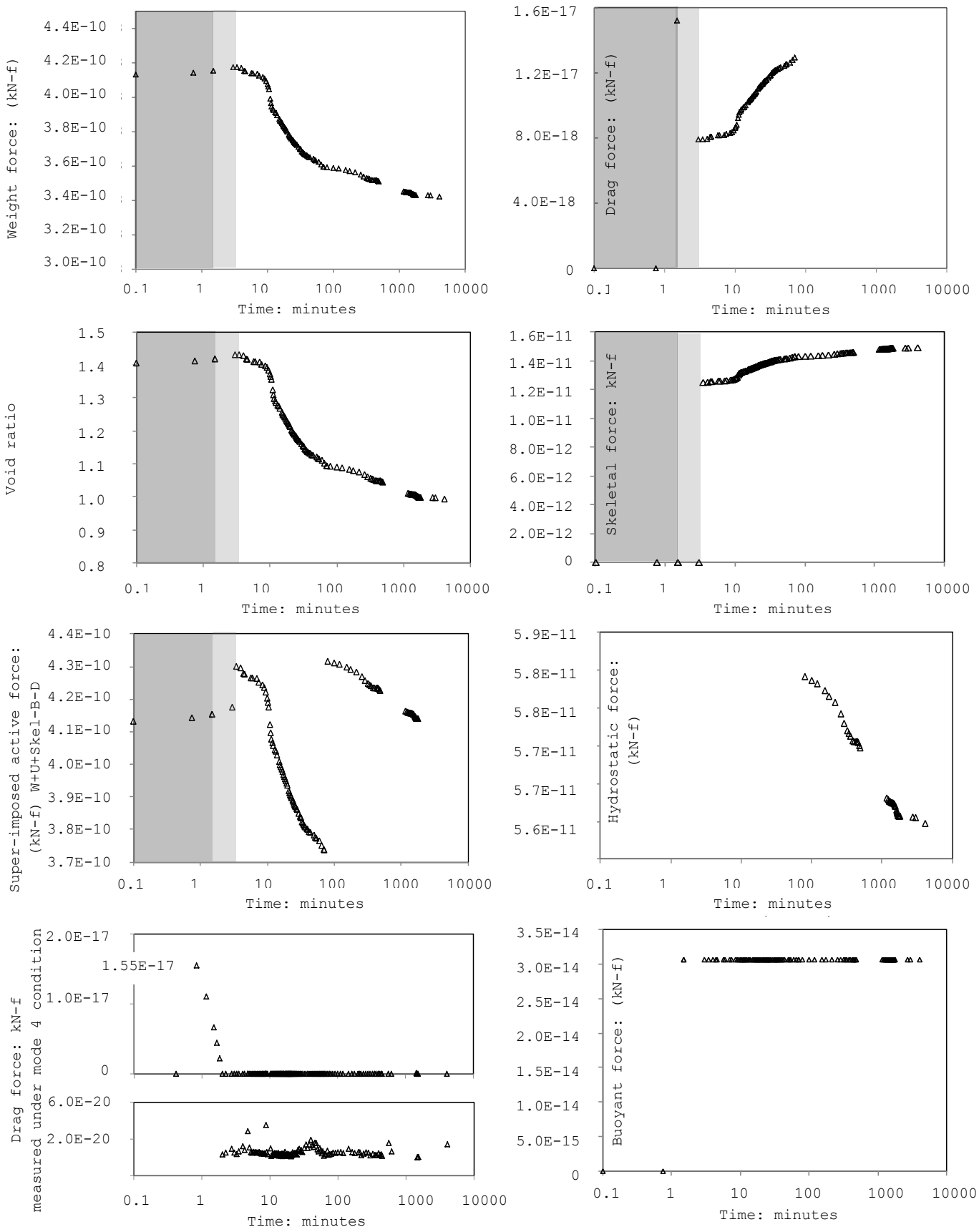

Fig. 4.29 Variation of internal forces upon wetting

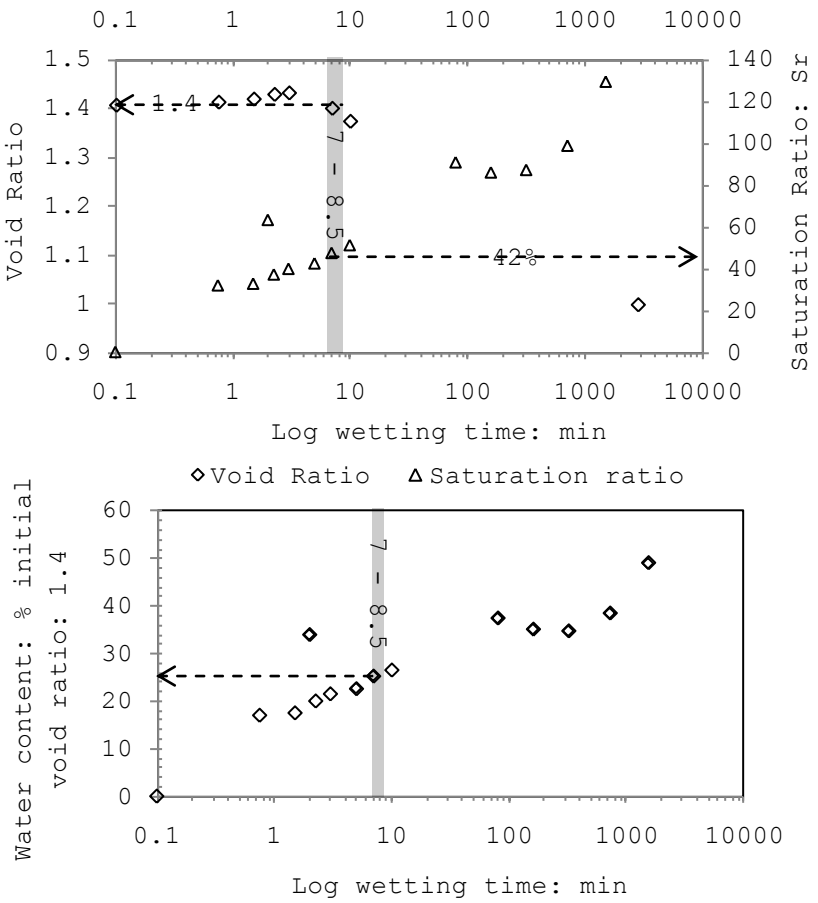

Fig. 4.30 (a) normalized water content against initial void ratio ($\frac{\omega}{e_i}$) versus wetting time, (b) water content versus wetting time (c) void ratio versus wetting time (d) saturation ratio versus wetting time

Soil structure experiences a final collapse event on the wetting path, when the curvature radii of the meniscus water tend to infinity and matric suction tends to zero (transition from the maximum funicular level to saturated state). The fully mobilized pendular state occurred at 25.2% water content (roughly analogous to 16-18% water content at the maximum mobilized effective apparent cohesion – see Dijkstra et al. (1994)) and 1.41 void ratio, while the final funicular state happened at 32.9% water content and 1.01 void ratio. A final collapse event occurred after integration of water films at saturation ratios beyond 95%.

To derive the maximum capillary force at the pendular level (7.5 to 8-minute interval), the mean pore diameter was first derived by plotting the mean pore diameter against the mean particle size at e=1.41 and $\gamma_d = 0.82\ ^{g}/_{cm^3}$, using the

Arya and Paris (1981) pedo-transfer function. Attaining a d_{pore}=0.0032 mm for D_{50}=0.018 mm, the pendular-level capillary force was formulated as:

$$F_{Cap} = \frac{\pi . T_s . {D_{50}}^2}{2 d_{Pore}} = 1.17985 \times 10^{-6} \quad kg - f \qquad Eq.\ 4.3$$

With the funicular level Arya-Paris pedo-transfer function was used to plot the derive the pore size corresponding to D_{50}=0.018 mm (at e=1.01 and $\gamma_d = 0.98\ {}^{g}/_{cm^3}$) and consequently the matric suction: 11.81 kPa. In the light of the geometry of the liquid bridge, we have,

$$\left(\frac{d_{pore}}{2} + R\right)^2 + f(r_1)^2 = (r_1 + R)^2, \qquad Eq.\ 4.4$$

$$\therefore f(r_1) = r_1 + \frac{1}{\frac{1}{r_1} - \frac{(u_a - u_w)_p}{T_s}} = r_1 + \frac{1}{\frac{1}{r_1} - \frac{11.81}{72.75 \times \frac{10^{-5} \times 10^{-3}}{10^{-2}}}} = r_1 + \frac{1}{\frac{1}{r_1} - 162336.7697}\ ,$$

$$\left(\frac{0.00032 \times 0.01}{2} + 0.0009 \times 0.01\right)^2 + (r_1 + \frac{1}{\frac{1}{r_1} - 162336.7697})^2 = (r_1 + 0.0009 \times 0.01)^2$$

$$1.1236 \times 10^{-10} + \left(\frac{2r_1 - 162336.7697{r_1}^2}{1 - 162336.7697 r_1}\right)^2 = {r_1}^2 + 8.1 \times 10^{-11} + 18 \times 10^{-6} r_1\ ,$$

$$\frac{4{r_1}^2 + 26353226797{r_1}^4 - 649347.0788{r_1}^3 + 2.961048563{r_1}^2 - 3.64803 \times 10^{-5} r_1 + 1.1236 \times 10^{-10}}{26353226797{r_1}^2 - 324673.5394 r_1 + 1}$$
$$= {r_1}^2 + 8.1 \times 10^{-11} + 18 \times 10^{-6} r_1$$

$$r_1 = 4.89E - 06m,\ r_2 = 2.37E - 05m$$

$$\delta = ArcCos\left(\frac{R + \frac{d_{pore}}{2}}{R + r_1}\right) = 0.70 \qquad Eq.\ 4.5$$

Assuming perfect wettability (Θ=0), the volume of the liquid bridge was estimated as 1.19E-28m^3. The capillary force at the maximum funicular level was calculated as 5.12E-09 Kg-f. The perfect wettability can apply to clean quartz grains, however, should one consider the capillary force at a cemented contact, the capillary force value would have a lesser value (see Eq. 3.13-3.15, Chapter 3).

In Fig. 4.31, the timed variation of capillary force is displayed, showing an early mobilization to a maximum value (i.e. pendular state), and a step-wise decline to the end of the wetting period.

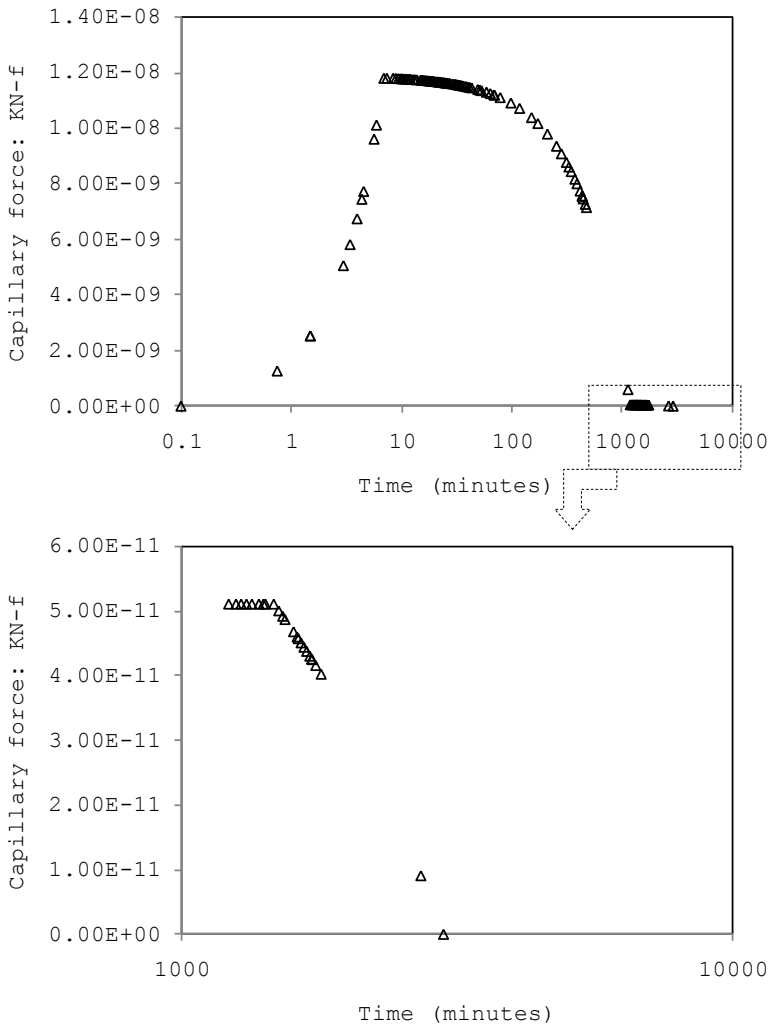

Fig. 4.31 Timed variation of the capillary forces

4.5.3 Concluding Remarks

Drag force is a product of changing stress or hydraulic environment. The wetting-induced drag force is independent from the external net stress (Fig. 4.29). It is a stand-alone control on the overall stress state at grain-to-grain contact points. The wetting-inducted drag force leads the overall active stress state to the wetting course maximum (Fig. 4.31), shortly after the water ingress (as shown in Fig. 3.15, drag force, temporarily decreases after an immediate increase right after water ingress). However, the mobilisation of capillary forces is not fast enough to sustain the soil's structure against

collapse under the decreased passive drag stress condition (Fig. 4.31). Therefore, in the presence of cementation (salts and carbonates – in agreement with Dijkstra et al.(1994)), the collapsible structure resists against the elevated stress state. Nonetheless, capillary forces can play the key role in postponing the collapse in the presence of relatively high kaolinite contents, which enhances the number of micro-pores and hence the tensile stresses.

4.6 Dynamics of Effective Stress

4.6.1 Fundamental Concepts

Reading the outputs of Section 4.3 suggested the control of certain pore spaces (of certain sizes) on the micro-fabric and hence matric suction change on wetting-drying, in a typical calcareous clayey loess soil. These pore sizes are among the four pore space levels naturally developed through continuous quartz grain breakage in nature (Section 4.2) together with post-depositional events (Section 4.4). Whether certain temporary internal forces (stresses) mobilize during the bypass of water from these pore spaces were studied in Section 4.5. This section is a closing to Chapter 4, and aims to examine the control of such temporary stresses on the effective stress[33].

---

[33] Fredlund and Rahardjo (1993) used four independent phases (i.e air, water, contractile skin, and soil grain) together with two stress variables to formulate the stress equilibrium equation in a unsaturated soil:

$$\frac{\partial \tau_{zx}}{\partial z}+\frac{\partial(\sigma_x-u_a)}{\partial x}+(n_w+n_c f^*)\frac{\partial(u_a-u_w)}{\partial x}+\frac{\partial \tau_{yx}}{\partial y}+(n_c+n_s)\frac{\partial u_a}{\partial x}-{F_{sx}}^w-{F_{sx}}^a+n_c(u_a-u_w)\frac{\partial f^*}{\partial x}=0$$

(*Continued from 20*): Where n was the porosity associated to each of the phases, ${F_{sx}}^w$ is the contact-level force between soil particles and water along the x-direction, ${F_{sx}}^a$ is the contact-level force between soil particles and air along the x-direction, and f^* equals to $\frac{A^*}{L^*.t}$. The horizontal area through the contractile skin is A^*, and the periphery of the contractile skin is L^*, and t is the thickness of contractile skin.

For a loess soil, the equilibrium equation can account for an individual assemblage (aggregate, globule, ped or pellet), under boundary-level forces. However, the test set-up in the present work matched better the conditions of Bishop Equation. For that reason, Bishops equation was chosen as the basis of the effective stress measurement.

4.6.2 Model Formulation

4.6.2.1 Double Porosity Concept: Threshold Saturation Ratio

Considering the Bishop form of the principle of effective stress, $\sigma' = (\sigma - u_a) + \chi.(u_a - u_w)$, a high matric suction at dry-state corresponds to a small content of the effective stress parameter (χ). This results in an effective stress of $(\sigma - u_a)$, which operates on particles when in a dry state. For soil containing clay, in the event of wetting, clay fragments attract the water first, due to their relatively higher surface area, finer pore diameters and hence higher degrees of matric suction. Water ingress reduces the suction in clayey micro-pores. However, no change to the air-volume at the macro-pore spaces occurs before the full saturation of micro-pore spaces. This is evidenced by close inspection of pore-size distribution curve together with the void ratio versus wetting time versus saturation ratio graph (Fig. 4.30) for the test loess specimen (70% silt, 20% carbonate, 10% kaolinite) under a steady state flow condition. According to Fig. 4.32, a pronounced mode size of 40 µm is followed by a minor pronounced mode at 7 µm and an early high particle concentration at 0.65 µm in the particle size distribution graph. According to the findings detailed in Section 4.3 on multi-porosity, >40 µm grains form trans-assemblage pores, 7-40 µm grains form meso-pores, 0.65-7 µm form macro-pores and <0.65 µm form micro-pores (intra-lattice spaces). These correspond to the four levels of pores (Section 4.3): Trans-assemblage pores of >1.5 µm diameter, macro-pores of 0.3-1.5 µm in diameter, meso-pores of 0.001-0.25 µm diameter, and micro-pores of <0.001 µm. According to the pore size distribution curves (Fig. 4.14), the macro-pores and micro-pores occupied 10% and 7.5% of the total voids' volume. The ratio of the macro-scale pores' volume (V_v^M) to micro-scale pores' volume (V_v^m) is,

$$\frac{V_v^M}{V_v^m} = \frac{0.10}{0.075} = 1.33 \qquad Eq.\ 4.6$$

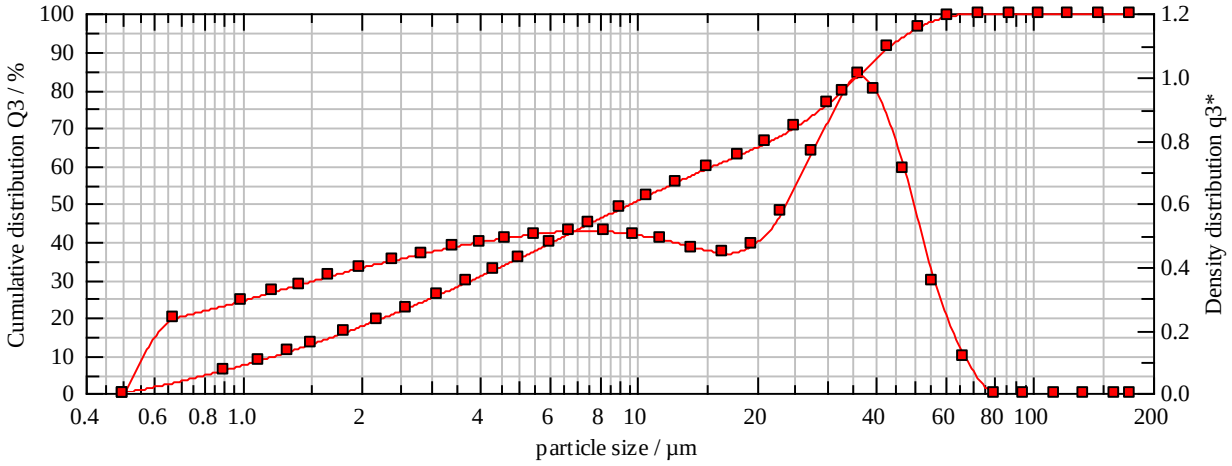

Fig. 4.32 Particle and mode size distribution, calcareous clayey silt[34]

Fig. 4.30 showed a *'mean'* threshold saturation ratio of 42%, which gives:

$$S_r = \frac{V_w}{V_v^m + V_v^M} = \frac{V_v^m}{V_v^m + V_v^M} \sim 0.42, \qquad Eq.\ 4.7$$

$$\therefore \quad \frac{V_v^M}{V_v^m} = 1.38 \approx 1.33 \qquad Eq.\ 4.8$$

where M and m denote macro- and micro-pore levels. This suggests a threshold saturation ratio (S_{r_T}) needs to be considered in the model, beyond which macro-pores start to accommodate water.

Fig. 4.30(c) shows a plateau trend of void ratio against wetting time for $S_r < S_{r_T}$. Collapse triggers after an increase in the effective stress to a value beyond its initial $(\sigma - u_a)$. The early resistance of packing suggested the possible constant value of effective stress. This suggested that χ preserves its initial zero content for $S_r < S_{r_T}$. From Eq. 4.6 to Eq. 4.8, the zero χ represents the reluctancy of macro-pores to accommodate water, before the saturation of micro-pore spaces. From this point on, χ rises to 1 and consequently, the effective stress marginally increases to $\sigma' = (\sigma - u_w)$, leading to the trigger of deformation in the packing state. To prove this, the wetting hydraulic path is herein explained mathematically in the framework of the double porosity concept (also see Alonso et al. (2010)).

[34] Q3 is the cumulative percent of grains, which size lesser than the associated mesh size. q3 is the population of certain-size grains in logarithm scale out of 100.

$$S_r = S_r^M + S_r^m \qquad Eq.\ 4.9$$

Where S_r^M is the macro-pores' degree of saturation and represents the inter-particle void spaces (surrounded by chains of silt particles) and S_r^m is the micro-pores' degree of saturation, which represents the intra-assemblage pore spaces within the clay bridges and grain coat structures. Let,

$$S_r = \frac{V_w^m}{V_v} + \frac{V_w^M}{V_v} = \frac{V_w^m}{AV_v^m} + \frac{V_w^M}{BV_v^M} = S_r^m + S_r^M \qquad Eq.\ 4.10$$

$$A = \frac{V_v}{V_v^m}, B = \frac{V_v}{V_v^M} \qquad Eq.\ 4.11$$

Silt grains are bridged together with bond. Therefore $S_r^M = 0$ at the initial dry state and during the saturation of intra-assemblage pore spaces ($S_r < S_{r_T}$). According to Alonso et al. (2010), χ may be written as S_r^e. Then:

$$\chi = S_r^e = \langle \frac{S_r - S_r^m}{1 - S_r^m} \rangle, \qquad Eq.\ 4.12$$

Where S_r^e is the effective saturation ratio, which implicates the amount of water available for occupying macro-pores. S_r^e is formulated in Eq. 4.13-4.15 for boundary conditions during the water inflow into connectors.

$$\chi = \lim_{S_r \to 0} S_r^e = \lim_{S_r \to 0} \langle \frac{S_r - S_r^m}{1 - S_r^m} \rangle = \lim_{S_r \to 0} \frac{\left(\frac{S_r - S_r^m}{1 - S_r^m}\right) + \left|\frac{S_r - S_r^m}{1 - S_r^m}\right|}{2} = 0 \qquad Eq.\ 4.13$$

$$\chi = \lim_{S_r^m \to a<1} S_r^e = \lim_{S_r^m \to a<1} \langle \frac{S_r - S_r^m}{1 - S_r^m} \rangle \quad \because a = \frac{1}{b}, \ni b \in N \qquad Eq.\ 4.14$$

$$\lim_{S_r^m \to a<1} S_r^m = \lim_{S_r^m \to a<1} \frac{V_w^m}{AV_v^m} = \lim_{S_r^m \to a<1} \frac{V_w^m}{\frac{V_v}{V_v^m} V_v^m} = a$$

$$V_w^m = aV_v \qquad and$$

$$S_r = \frac{V_w^m}{V_v} + \frac{V_w^M}{V_v} = a + \frac{0}{V_v} = a, \qquad Therefore.$$

$$\chi = \lim_{S_r^m \to a<1} \frac{\left(\frac{S_r - S_r^m}{1 - S_r^m}\right) + \left|\frac{S_r - S_r^m}{1 - S_r^m}\right|}{2} = \lim_{S_r^m \to a<1} \frac{\left(\frac{a - S_r^m}{1 - S_r^m}\right) + \left|\frac{a - S_r^m}{1 - S_r^m}\right|}{2} = 0$$

$$\chi = \lim_{S_r^m \to 1} S_r^e = \lim_{S_r^m \to 1} \langle \frac{S_r - S_r^m}{1 - S_r^m} \rangle \qquad Eq.\ 4.15$$

$$\lim_{S_r^m \to 1} S_r^m = \lim_{S_r^m \to 1} \frac{V_w^m}{AV_v^m} = \lim_{S_r^m \to 1} \frac{V_w^m}{\frac{V_v}{V_v^m} V_v^m} = 1 \Rightarrow V_w^m = V_v$$

$$S_r = \frac{V_w^m}{V_v} + \frac{V_w^M}{V_v} = 1 + \frac{0}{V_v} = 1,$$

$$\chi = \lim_{S_r^m \to 1} \frac{\left(\frac{S_r - S_r^m}{1 - S_r^m}\right) + \left|\frac{S_r - S_r^m}{1 - S_r^m}\right|}{2} = \lim_{S_r^m \to 1} \frac{\left(\frac{1 - S_r^m}{1 - S_r^m}\right) + \left|\frac{1 - S_r^m}{1 - S_r^m}\right|}{2} = 1$$

As shown in Eq. 4.13, the χ-parameter at the dry state gains the zero value, tends to 1 when clay connectors are fully saturated (Eq. 4.15). χ theoretically preserves a zero value during the saturation of connectors (Eq. 4.14).

4.6.2.2 Problem Statement

Having the χ values for progressing and boundary conditions, the current form of the principle, $\sigma' = (\sigma - u_a) + \chi.(u_a - u_w)$, appears to fail to explain the rebound volume change observed in Fig. 4.39 for $S_r < S_{r_T}$ ($S_r = 42\%,\ t = 6\,min,\ S_r^m = a < 1$). In other words, constant effective stress may justify the delay in contraction, but cannot explain the early rebound volume change. This limitation is sought to be relaxed by introducing a third stress variable: the outcome of micromechanical modelling carried out in this chapter (Section 4.5.3).

4.6.2.3 The Third Stress Variable

Drag force (or stress on a domain of unit-sized sides) operates on clay connectors to dissipate the wetting-induced positive excess pore water pressure, $\bar{u}_w^m$. The drag force is independent from net stress, but controls the overall stress state of soil at a given grain-to-grain contact point. The force gains value when either air or water travels between pores, separated by a clay/salt shield. Eq. 3.23 is re-written in Eq. 4.16 at the clay level:

$$F_D = \frac{3\pi\mu d_p . K_c . i}{n} \qquad Eq.\ 4.16$$

Where d_p is the particle diameter, K_c is the clay permeability under the $\sigma - u_a$ net stress, μ is the viscosity of water (0.001 N.S/m^2 at 20°C), n is the porosity and 'i' is the hydraulic gradient:

$$i = \frac{{u_w}^M - {u_w}^m}{t_b} \qquad Eq.\ 4.17$$

Where t_b is the thickness of clay bridge connector from which the water travels through. Porosity was formulated as,

$$n = \frac{V_v}{V} = \frac{\frac{4}{3}\pi\left(\frac{d_D - d_p}{2}\right)^3}{{d_D}^3} \qquad Eq.\ 4.18$$

Where d_D is the square domain's side ($d_D > 2d_p$). Substituting Eq. 4.17 and 4.18 into Eq. 4.16, we obtain,

$$At\ t = t_i{:}\ F_{D_i} = \frac{18\pi\mu d_p . {d_D}_i{}^3 K\left(\frac{{u_w}^M{}_i - {u_w}^m{}_i}{t_{b_i}}\right)}{\left(d_{D_i} - d_p\right)^3} \qquad Eq.\ 4.19$$

With unsaturated soils according to (Brooks and Corey, 1964),

$$K = K_{c-sat} \times \left\{\left(\frac{(u_a - u_w)_b}{(u_a - u_w)}\right)^{\lambda}\right\}^{\frac{2+3\lambda}{\lambda}} \qquad Eq.\ 4.20$$

Where $(u_a - u_w)_b$ is the matric suction value at the turning point of the water retention curve (i.e. air value), and λ is a constant greater than 1.0, which is recommended for loam silty soils about 1.82 (Brooks and Corey, 1964). With $S_r^M = 0$, the clay connectors adhere the bulk water, resulting in a decrease in the micro-pore matric suction. According to Khalili et al. (2005), the micro-pore saturation ratio attains a plateau trend at about '1', when the matric suction decreases beyond the air expulsion value, $(u_a - u_w)_{m(ex)}$. Likewise, with $0 < S_r^M < 1$, due to the expulsion of inter-assemblage air and intrusion of trans-assemblage water into the macro-pore, clay connectors stage a Pseudo-drying condition. Air flows through the water-filled clay[35], resulting in an increase in the micro-pore matric suction, which may go beyond the air entry value, $(u_a - u_w)_{m(ae)}$. As such, the coefficient of permeability is:

[35] As water begins to travel from the connector units (i.e. built up of micro-pores) to macro-pore spaces, a pressure forms within the connectors (i.e. air-entry value or displacement pressure), allowing the air to travel from macro-pores to micro-pores. A negligible mass of air may dissolve in water and flow back to the macro-pores, the mass of which is a factor of the absolute pressure of air at the macro-pore space.

$$K = K_{c-sat} \times \left\{\left(\frac{(u_a - u_w)_b}{(u_a - u_w)}\right)^{\lambda}\right\}^{\frac{2+3\lambda}{\lambda}} \quad for\ (u_a - u_w) \leq (u_a - u_w)_{m(ae)}, (u_a - u_w) \geq (u_a - u_w)_{m(ex)}$$

$$K = K_{c-sat} \quad for\ (u_a - u_w)_{m(ae)} < (u_a - u_w) < (u_a - u_w)_{m(ex)} \quad Eq.\ 4.21$$

With $S_r^M = 0$ and suction between the early maximum to the air expulsion value:

$$F_D = 18\pi\mu d_p lim_{S_r^m \to a < S_r^{m(ex)}} \frac{{d_D}^3 . K_{c-sat} \times \left\{\left(\frac{(u_a - u_w)_{m(ex)}}{(u_a - u_w)}\right)^{\lambda}\right\}^{\frac{2+3\lambda}{\lambda}} . ({u_w}^M - {u_w}^m)}{t_b \times (d_D - d_p)^3} \quad Eq.\ 4.22$$

With $0 < S_r^M < 1$ for suction values ranging from air entry value to its final:

$$F_D = 18\pi\mu d_p lim_{S_r^m \to a < S_r^{m(ae)}} \frac{{d_D}^3 . K_{c-sat} \times \left\{\left(\frac{(u_a - u_w)_{m(ae)}}{(u_a - u_w)}\right)^{\lambda}\right\}^{\frac{2+3\lambda}{\lambda}} . ({u_w}^M - {u_w}^m)}{t_b \times (d_D - d_p)^3} \quad Eq.\ 4.23$$

On the wetting-drying protocol soil water retention curves in clay, the drag force progresses in four stages during the water ingress phase: (1) $(u_a - u_w) \geq (u_a - u_w)_{m(ex)}$ (2) $(u_a - u_w) < (u_a - u_w)_{m(ex)}$ (3) $(u_a - u_w) \leq (u_a - u_w)_{m(ae)}$ (4) $(u_a - u_w)_{m(ae)} < (u_a - u_w)$: At constant t_b, and d_p, d_D attains a constant value. K_{unsat} (Fig. 3.12) and ${u_w}^M - {u_w}^m$ increase sharply and hence F_D soars (Fig. 4.29). This was also seen in Fig. 4.30, at the 0.1-1 minute time interval.

Upon water absorption, the clay fragment commenced to swell, giving rise to t_b[36] at constant d_p[37]. The $\frac{{d_D}^3}{t_b \times (d_D - d_p)^3}$ term consequently plunged to the end of the period and hence the F_D decreased. These can be seen in Fig 4.29 within the 1 to 6 minutes time interval. K attained the constant value of K_{c-sat}, and $u_w^M - u_w^m$ continued the declining trend at a decelerated rate. At a constant t_b, swelling led to the rearrangement of particles (Section 4.3) and therefore, a reduction in the d_D[38] and hence $\frac{{d_D}^3}{t_b \times (d_D - d_p)^3}$ occurred. F_D as the result increased, however not to a significant extent. This was recorded in the plot of normalized drag force ($\overline{F_{D_i}}$) against wetting time, where $\overline{F_{D_i}}$ equals $F_{D\,i}/(t_i - t_{i-1})$.

[36] i.e. Thickness of clay bridge connector from which the water travels through

[37] i.e. Particle diameter

[38] i.e. Square domain's side $(d_D > 2d_p)$.

Since the drag force was recorded at varied time intervals, normalization was deemed to provide the realistic pattern through the wetting time (Fig. 4.29). At constant d_p, t_b, and d_D, $u_w^M - u_w^m$ decreased after inflow of air packets through the saturated medium. Considering the constant value of K_{c-sat}, F_D decreased through the end of the period.

4.6.2.4 The New Form of the Principle

A new general form of the principle is presented in Eq. 4.24 and deemed capable of relaxing the limitation discussed in section 4.6.2.2.

$$\sigma' = \sigma - u_a + S_r^e.(u_a - u_w) + (1 - S_r^e)F_D \qquad Eq.\ 4.24$$

The variation of χ is 'schematically' demonstrated in Fig. 4.33. The graph is commented below, considering the discussions introduced in Section 4.6.4.3.

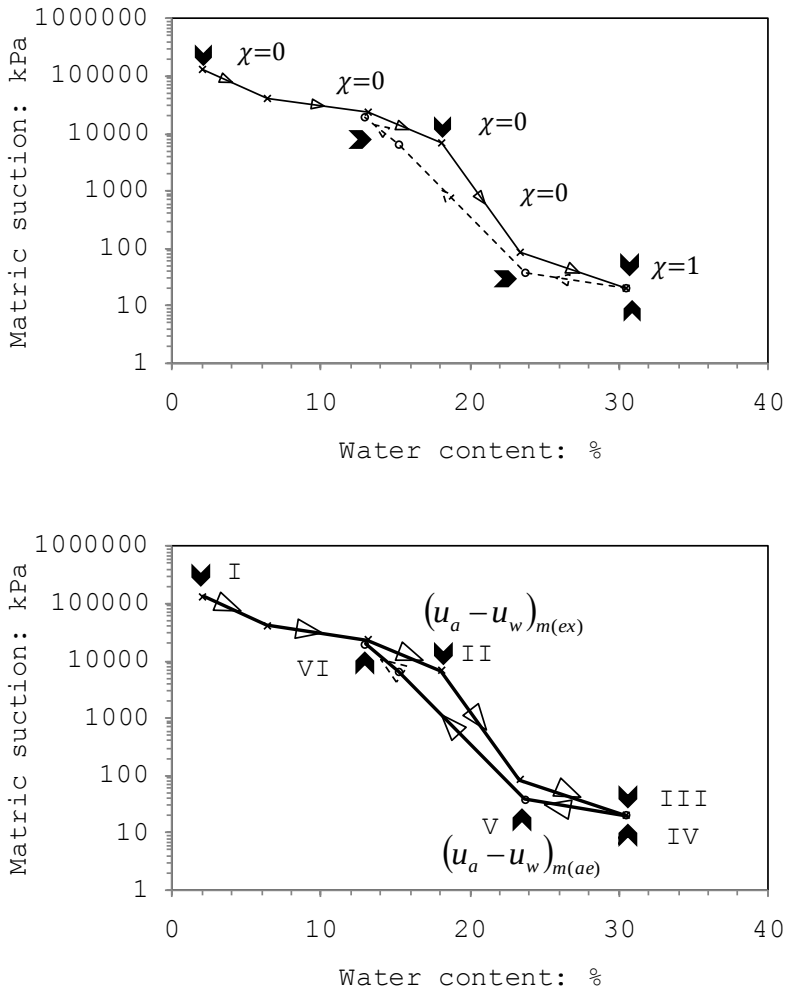

Fig. 4.33 χ-parameter on the wetting-drying path (the connector): calcareous clayey specimen 70% silt, 20% carbonate, 10% kaolinite

For $S_r^M = 0$, the principle is written below for fractions shown in Fig. 4.33:

$$I: \sigma' = \sigma - u_a + 0.(u_a - u_w) + (1-0)0 = \sigma - u_a$$

$$I - II: \sigma' = \sigma - u_a + 0.(u_a - u_w) + (1-0)F_D = \sigma - u_a + F_D(\nearrow\nearrow)$$

$$I - II: \sigma' = \sigma - u_a + 0.(u_a - u_w) + (1-0)F_D = \sigma - u_a + F_D(\swarrow)$$

$$II: \sigma' = \sigma - u_a + 0.(u_a - u_w) + (1-0)F_D = \sigma - u_a + F_D(minimum)$$

$$II - III: \sigma' = \sigma - u_a + 0.(u_a - u_w) + (1-0)F_D = \sigma - u_a + F_D(\nearrow)$$

$$III: \sigma' = \sigma - u_a + 1.(u_a - u_w) + (1-1)F_D = \sigma - u_w \qquad Eq.\ 4.25$$

Where $\nearrow$ denotes an increase, $\nearrow\nearrow$ denotes a considerable increase, and $\swarrow$ denotes a decrease. For $0 < S_r^M \leq 1$, to rewrite the principle during the saturation of macro-pore spaces, the boundary conditions for the χ parameter are first derived as outlined below.

$$\chi = \lim_{S_r^M \to a<1} S_r^e = \lim_{S_r^M \to a<1} \langle \frac{S_r - S_r^m}{1 - S_r^m} \rangle \quad \because 0 < S_r^m < 1, \quad \ni \mathrm{b} \in \mathbb{N}: \ a = \frac{1}{b}, \qquad Eq.\ 4.26^{39}$$

S_r^m tends to the residual saturation ratio ($S_{r\,Res}^m$), close to zero, as air bubbles intimately ingress into the intra-assemblage pore space. It is just before the destruction of connectors, where S_r^m tends to zero.

$$\lim_{S_r^M \to a<1} S_r^M = \lim_{S_r^M \to a<1} \frac{V_w^M}{BV_v^M} = \lim_{S_r^M \to a<1} \frac{V_w^M}{\frac{V_v}{V_v^M} V_v^M} = a$$

$$\therefore V_w^M = aV_v \ and \ S_r = S_r^m + \frac{V_w^M}{V_v} = S_r^m + a,$$

$$\chi = \lim_{S_r^m \to S_{r\,Res}^m, S_r^M \to a<1} \frac{\left(\frac{S_r - S_r^m}{1 - S_r^m}\right) + \left|\frac{S_r - S_r^m}{1 - S_r^m}\right|}{2}$$

$$= \lim_{S_r^m \to S_{r\,Res}^m, S_r^M \to a<1} \frac{\left(\frac{a + S_r^m - S_r^m}{1 - S_r^m}\right) + \left|\frac{a + S_r^m - S_r^m}{1 - S_r^m}\right|}{2}$$

$$= \frac{a}{1 - S_{r\,Res}^m} \qquad Eq.\ 4.27$$

Thus,

[39] S_r^m has decreased to a value below 1, due to the flow of air packets through the saturated clay (bond) bridge.

$$\sigma' = \lim_{S_r^m \to S_{r\,Res}^m, S_r^M \to a \to 1} (\sigma - u_a + S_r^e(u_a - u_w) + (1 - S_r^e)F_D)$$
$$= \sigma - u_a + \lim_{S_r^m \to S_{r\,Res}^m, S_r^M \to a \to 1} \frac{a}{1 - S_r^m}(u_a - u_w) + (1 - \lim_{S_r^m \to S_{r\,Res}^m, S_r^M \to a \to 1} \frac{a}{1 - S_r^m})F_D$$
$$= \sigma - u_a + \frac{a}{1 - S_{r\,Res}^m}(u_a - u_w) + \left(1 - \frac{a}{1 - S_{r\,Res}^m}\right)F_D \qquad Eq.\ 4.28^{40}$$

For $0 < S_r^M \leq 1$ (Fig. 4.33), having the variation of χ, the principle is written below:

$$III: \sigma' = \sigma - u_a + 0.(u_a - u_w) + (1 - 0)F_D = \sigma - u_a + F_D$$

$$III - VI: \sigma' = \sigma - u_a + \frac{a}{1 - S_{r\,Res}^m}(u_a - u_w) + \left(1 - \frac{a}{1 - S_{r\,Res}^m}\right)F_D \qquad Eq.\ 4.29$$

Where $\frac{a}{1 - S_{r\,Res}^m}$ increases slightly, while $(u_a - u_w)$, $\left(1 - \frac{a}{1 - S_{r\,Res}^m}\right)$ and F_D gradually decrease.

$$V: \sigma' = \sigma - u_a + 1(u_a - u_w) + (1 - 1)F_D = \sigma - u_w \qquad Eq.\ 4.30$$

4.6.2.5 Drying-Wetting Cycles - Principle Adaptation

Migrated clay flakes at the inter-assemblage pores adhere together. Upon drying, the trans-assemblage pores pioneer to lose water. $F_D = 0$. It can be written:

$$\sigma' = \sigma - u_a + \chi \left\{ \lim_{S_r^m \to 1^-, S_r^M \to 0^+} \langle \frac{S_r^m + S_r^M - S_r^m}{1 - S_r^m} \rangle \right\} \times (u_a - u_w)_m + (1 - \chi)0 \qquad Eq.\ 4.31$$

For constant $\sigma - u_a$ and, $(u_a - u_w)_m$, and in the absence of an immediate head gradient, the effective stress decreased upon drying (Eq. 4.31). The stress relief, however, was countered by shrinkage. Considering the surface negative electrical charge of kaolinite flakes, free cations at the absorbed-water level form clouds surrounding the clay particle. In the event of drying, concentration of free cations and therefore the electrical conductivity increases, encouraging the clouds to approach the negatively charged surfaces. Due to the decrease in the thickness of cation cloud and hence the clay-to-clay repulsive forces, attractive forces take the lead and coagulate the negatively charged flakes, causing an overall shrinkage. Due to shrinkage,

[40] Principle of effective stress on the drying protocol of SWCC

surrounding quartz grains were pulled together. This is observed in the 15% loss of void ratio in the clayey silt specimen upon self-weight wetting and drying (Fig. 4.34).

Upon wetting, the void ratio increased, and this can be attributed to the effective stress relief. Waterfronts first occupied the macro-pores and then sought to access the clay aggregates at the inter-assemblage pore spaces (i.e. the physical outer-to-inner, macro- to micro-pore route of bypassed water):

$$\chi = \lim_{S_r^m \to a<1,\, S_r^M \to 1^-} \langle \frac{S_r - S_r^m}{1 - S_r^m} \rangle = \lim_{S_r^m \to a<1,\, S_r^M \to 1^-} \langle \frac{S_r^m + S_r^M - S_r^m}{1 - S_r^m} \rangle = \frac{1}{1-a}$$

$$\because a = \frac{1}{b}, \ni b \in N \qquad Eq.\ 4.32$$

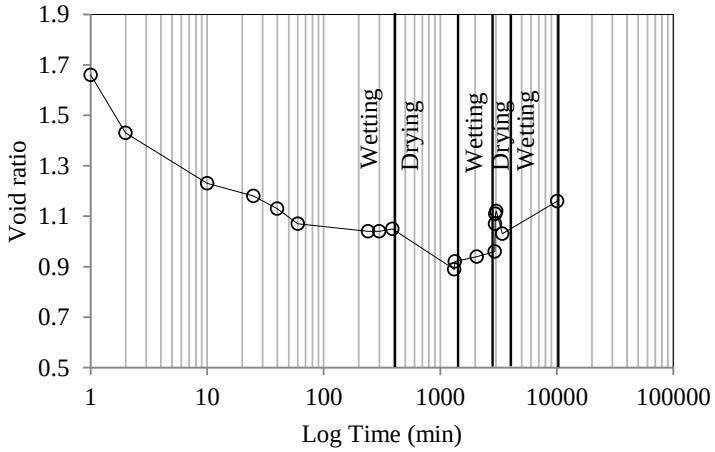

Fig. 4.34 Oedometer test results: at 90% silt, 10% kaolinite

In Eq. 4.32, $(1-\chi)$ attains increasingly negative values with wetting time. Increasing the χ-parameter counters the decreasing matric suction and the net stress remains constant. At a constant $\frac{{d_D}^3}{t_b \times (d_D - d_p)^3}$, the coefficient of permeability increases, while ${u_w}^M - {u_w}^m$ changes to a minimum (i.e. due to the accumulation of clays at macro-pores, instead of appearing as a shield between macro-pores). Consequently, F_D increases, leading to a superimposed $(1-\chi)F_D$ increase at a negative value. This remarkably decreases the effective stress (considering the control of the $(1-\chi)F_D$ term in the effective stress expression – Eq. 4.24), resulting in a heave volume change (see Fig. 4.42). The second and third drying cycles led to a further increase in the void ratio (Fig. 4.42). This was attributed to the effective stress relief discussed in Eq. 4.32. The over-consolidated clay aggregates (after shrinkage during the

first drying stage) was deemed to exhibit much less shrinkage, giving room to the effective stress to take over the volume change.

4.6.3 Concluding Remarks

Accurate interpretation of collapse in loess, requires accurate determination of the effective stress. Since 1959, much effort is placed into the formulation of such parameter. However, with unsaturated collapsing soils, the concept is still a matter of dispute.

Section 4.6 critically reviewed the major recent contributions: the association of microfabric to effective stress and the double porosity concept. Both concepts have been much appreciated, but not quantitatively developed. A new formulation is written for one working domain, two clusters of pores, four constituents (two solids and two fluids), and four phases along each hydraulic path. The formulation is rigorously examined against three subsequent wetting-drying cycles. Deriving from the double porosity concept, a third stress variable is introduced to the model, which operated during the transition of fluid between pair of neighbouring pore subspaces. The new formulation satisfies the hydraulic hysteresis and collapse-rebound volume change.

4.7 Summary

The present chapter has explained a framework for collapse mechanism modelling using classical terms associated with a modified form of the principle of effective stress, for representative loess soil of both clay and carbonate constituents. The principle in its new form is written by means of inputs attained after investigating three micromechanical indices associated with different stress state surfaces. Key findings are outlined here.

The efficiency of the skeletal forces in crushing grains is inversely proportional to the grain size. However, grain crushing continues in the absence of all-around confinement (with clay), increasing the mass of 10-20 μm particles and thus improving the sorting quality. A well sorted quartz silt is a favourable medium for oxides and salts to re-precipitate during drying seasons. Seasonal wetting-drying allows tubular carbonates (in loess soil

containing silt, clay, carbonates, etc) to re-precipitate into a scaffolding framework and form re-stored carbonate bridges. Clays, however, do not re-precipitate into inter-particle bridges, since secondary clay-silt laminated deposits normally form at macro-pore spaces upon a single cycle of wetting-drying. Formation of re-crystallized carbonate cements however impacts the efficiency of compaction in calcareous deposits. On other hand, pronounced 10-20 μm mode size of grains in loess (due to the stress environment operating on loess as detailed above) leads to the development of large macro-pores: A ideal loess, containing 20% carbonates, 10% clay, and 70% silt occurred to possess four levels of pore spaces, including trans-assemblage pores (>1.5 μm in diameter), macro-pores (0.3-1.5 μm in diameter), meso-pores (0.001-0.25 μm in diameter), and micro-pores (<0.001 μm in diameter). Stress applications to calcareous clayey silts (loess) up to 2100 kPa at dry state (more than 3-times the static equivalent energy of 25 Proctor blow number) forms trans-assemblage pores of 2-20 μm diameter at the expense of the loss of 0.001-0.25 μm and 0.25-2 μm void spaces. Upon wetting, in the presence and absence of external loads, >30 μm silt, carbonates and clay coagulate into pellets, which further increases the volume of the macro-pore spaces. Upon drying, the void spaces become prone to collapse. This has impact on the efficiency of compaction when applied to loess soils (specifically in calcareous loess).

Collapse upon wetting is a delayed process. Upon wetting, an excess positive pore water pressure ($\bar{u}_w^m$) develops. This pressure dissipates at the expense of formation of drag pressure (i.e. drag forces (F_D) operating in a domain of unit size). The effective stress attains a decreasing trend ($\sigma' = (\sigma - u_a) + 0(u_a - u_w) + (1-0)F_D;\ F_D \to 0$) for saturation ratios less than a threshold ($S_r^M = 0,\ S_r^m > 0,\ S_{rT} = 0.42$: specific to loess containing 20% carbonate and 10% clay), beyond which macro-pores accommodate water (i.e. theoretically proved in Section 4.6.2.1). Formation of water films and mobilization of ion-electrostatic forces provide a short period of steady stress state. At the threshold state, a hydraulic gradient encourages the flow of water from the outer macro-pores to the inner macro-pores, through the clay connectors (micro-pores). This induces an excess positive pore water pressure in the clay connectors, and hence a subsequent drag force. Once more, the drag force gains in value, increasing the effective stress, which could also be regarded as the 'net'

skeletal force ($\sigma' = (\sigma - u_a) + 0(u_a - u_w) + (1 - 0)F_D$). The 'net' prefix refers to the superimposed effect of skeletal forces and drag forces. The increased active stress is simultaneous to the loss of much of the matric suction. Clays migrate with the flowing water into the macro-pores, and hence the loss of cementation appears as an additional problem. An enhanced active stress state therefore leads to the collapse. Collapse triggers at the threshold saturation ratio, where $S_r^m \to S_r^m{}_{Res} \to 0$. The shearing of connectors (under escalating skeletal forces) is formulated in the context of effective stress principle at micro-scale (i.e. the clay connector clusters) for suction values less than the air entry value ($(u_a - u_w) \leq (u_a - u_w)_{m(ae)}$).

The principle then determined the hazardous post-collapse behaviour of clayey silt soils upon seasonal drying-wetting. Since clay fragments supply much of the matric suction and as secondary clays accumulate in inner macro-pore spaces, drying does not control the matric suction. Hence, at a constant net stress and in the absence of hydraulic gradient between pairs of distinct pore spaces, drying causes a relief in the effective stress. In contrast, secondary normally consolidated (due to a history of migration after the first phase of wetting) clays shrink upon drying due to a rise in the electrical conductivity (loss of water and the consequent increase in cations). This suggests that drying causes further void ratio loss in collapsed clayey silts. However, drying causes rebound volume changes in the collapsed clayey silts of over-consolidated secondary (due to a history of drying and hence an increase in effective stress at a residual state) clays. Post-collapsed wetting results in an upsurge trend in $(1 - \chi)F_D$ of negative value, and hence the effective stress relief. Consequently, a rebound volume change occurs in response to this stress relief.

Chapter 5 | LEVEL II: CLASSIFICATION AND COLLAPSE MICRO-MECHANICAL MODELLING

5.1 Introduction

Treatment to remove collapse often involves densification techniques. However, such approaches have been reported (Wynne, 2007, Roohnavaz et al., 2011) not effective enough to fully combat the collapse problem. This stems from a lack of in-depth understanding of geochemistry and structure (and the interplay of packing and suction), the result of which is an oversimplification of the complex geotechnical and geological interactions. In particular, the current practice ignores the increasing evidence of the restoration of the collapsing microfabric (granular soils in Valdes (2002), clayey granular soils in Mellors (1995), calcareous grounds in Roohnavaz et al (2011)), upon seasonal wetting-drying in both calcareous and non-calcareous soils (detailed in Chapter 4).

This chapter aims to develop a better understanding of the above geochemical-constituent controls, through the synthesis and analysis of a wide range of artificial fine-grained soils. Fine soils are systematically classified into 11 main classes. Specific modes of collapse, which correspond to specific soil groups are then identified and explained within the framework of the collapse mechanism, which is addressed earlier in Chapter 4.

Chapter 5 reports the oedometer test results, the baseline data that establishes two criteria: Firstly to systematically classify fines on the basis of chemical, micro-morphological, and mechanical properties. Secondly to derive the collapse mechanism for each of the classes, by using mechanical and chemical test results, microscopic observations, and analytical methods.

5.2 A New Classification System for Fine Soils

5.2.1 Expected Impacts

Approaching the classification from a perspective of soil as an engineering material neglects the available literature on micro-morphology, geo-chemistry,

and packing indices; those have been much evident in similar classification criteria from the perspective of soil as a resource.

Modern soil classification for engineering purposes aims an easy transformation of field logging data into groups of materials with similar engineering behaviour. Approaching soil classification from the perspective of soil as a material, which contains characteristics at certain combinations of grain size – wet consistency makes it comprehensive, concise, and meaningful. Classification might be based on the proportions of gravel-, sand-, silt-, and clay-sized particle (e.g. National research Council, 1947, BS 1377), or on the basis of both particle size proportions and soil plasticity (e.g. USCS[41], AASHTO[42]). Physical and mechanical properties are conventionally derived through the use of tailored testing procedures for each of the soil classes. Such an approach in classification however has reportedly not always been accurate. Identical soil types (i.e. clayey silt) may differently respond under loading/wetting, due to their mineralogical, morphological, geochemical, and fabric differences. Failures are reported after taking the size-consistency approach, including the Teton Dam failure due to the wrong choice of fill material (Smalley, 1992) and re-stored collapsibility of engineered loess fills in Karachaganak gas processing complex (Roohnavaz et al. (2011)). As such, following key questions need to be addressed:

(1) What would be the control of minerals on the yield surface and hence the collapse? Would the simplified undrained analysis be sufficient enough in the geotechnical design, or are the geo-chemical, micro-morphological, and packing constituents of soil are needed to overcome such simplifications? Is the coefficient of consolidation obtained by the Terzaghi oedometer test a true representative of the most critical stress-hydraulic combination for fine soils?
(2) How can the increasingly reported collapse volume changes in engineered fine-grained fills be explained?

As such, the present section proposes a modified classification system for <63 µm soils (particularly silt-size range), which considers the interplay of geo-

[41] Unified Soil Classification System
[42] American Association of State Highway and Transportation Officials

chemistry and shape of minerals with the mechanical properties, as well as the conventional size criterion. The new system differs from those in the soil science discipline, as basic standard geotechnical tests are proposed to allow an easy identification of soil type from field logging data.

5.2.2 Inputs and Criteria

Based on the proportions of silt-, kaolinite-, and carbonate constituents, the testing material (i.e. a representation of sub 63 μm fragment within the BSCS[43]) was divided into eleven classes on a ternary diagram (Fig. 5.1). Any given <63 μm soil sample plots as a point within or along the sides of the diagram, depending on its specific composition (also Table 5.1). The proposed classification is worked out through examining the standard collapse potential of engineered artificial soil specimens. The variation of any of the three main soil components, in each (sub-) class results in repeatable trends of collapse potential (philosophy behind such classification). These trends along with boundary constituent contents (in bold typeset) are detailed throughout this chapter (and also in Chapter 6).

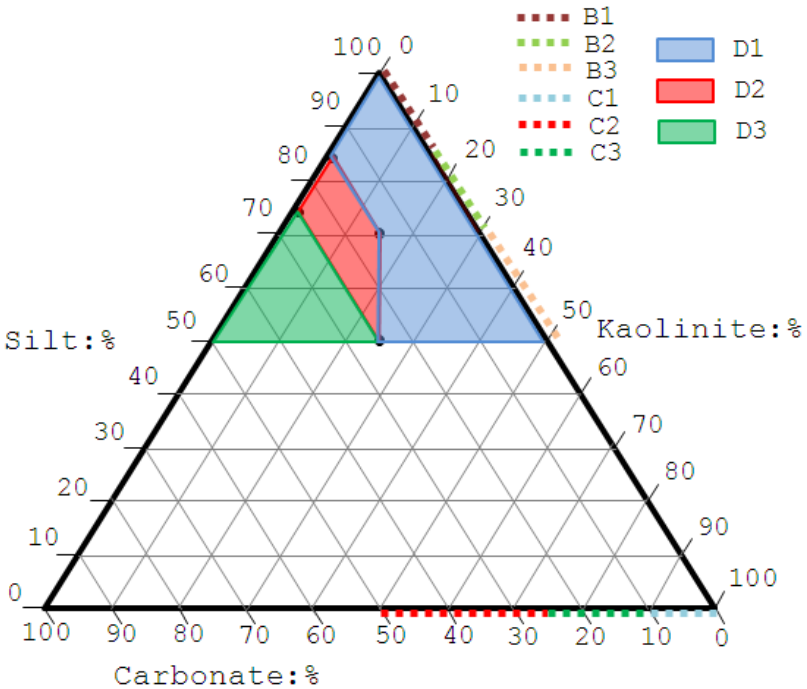

Fig. 5.1 Proposed classification system for soil class A (silt - E and F), B (G and H), C, and D (I and J), and K (clay) on a ternary diagram

[43] British Soil Classification System

Table 5.1 Proposed classification system and the criteria

(SUB)CLASS			TYPE	DESCRIPTION		CRITERIA	
A	-	-	SILT	-		100%: 2μm<D<63μm	
B	B1	-	CLAYEY SILT	SLIGHTLY CLAYEY		Clay<15%	
	B2	-		CLAYEY		15%≤Clay<30%	
	B3	-		VERY CLAYEY		30%≤Clay<50%	
C	C1	-	CALCAREOUS SILT	SLIGHTLY CALCAREOUS		Carb<[5-15]%	
	C2	-		CALCAREOUS		[5-15]%≤Carb<[20-30]%	
	C3	-		VERY CALCAREOUS		50%>Carb≥[20-30]%	
D	D1	-	CLAYEY CALCAROUS SILT	SLIGHTLY CALCAREOUS		Carb<15% OR 15%<Carb<25% & Clay≥15%	
	D2	-		CALCAREOUS		15%<Carb<25% & Carb>Clay	
	D3	-		VERY CALCAREOUS		Carb>25% & Clay≤25%	
E	EM	-	SILICA-INDURATE SILT	MILD	-	100%:2-63 μm	260cc/Hr loss
	EH	-		HOT	-		90cc/Hr loss
F	FM	FM1	METAL-BASED SULPHATED SILICA-INDURATE SILT	MILD	-	260cc/Hr loss	
	FH	FH1		HOT	-	90cc/Hr loss	
G	GM	GM1	SILICA-INDURATE CLAYEY SILT	MILD	SLIGHTLY CLAYEY	Clay<15%	260cc/Hr loss
		GM2		MILD	CLAYEY	15%≤Clay<30%	
		GM3		MILD	VERY CLAYEY	30%≤Clay<50%	
	GH	GH1		HOT	SLIGHTLY CLAYEY	Clay<15%	90cc/Hr loss
		GH2		HOT	CLAYEY	15%≤Clay<30%	
		GH3		HOT	VERY CLAYEY	30%≤Clay<50%	
H	HM	HM1	METAL-BASED SULPHATED SILICA-INDURATE CLAYEY SILT	MILD	SLIGHTLY CLAYEY	Clay<15%	260cc/Hr loss
		HM2		MILD	CLAYEY	15%≤Clay<30%	
		HM3		MILD	VERY CLAYEY	30%≤Clay<50%	
	HH	HH1		HOT	SLIGHTLY CLAYEY	Clay<15%	90cc/Hr loss
		HH2		HOT	CLAYEY	15%≤Clay<30%	
		HH3		HOT	VERY CLAYEY	30%≤Clay<50%	
I	IM	IM1	SILICA-INDURATE CLAYEY CALCAREOUS SILT	MILD	SLIGHTLY CALCAREOUS	Carb<15% OR 15%<Carb<25% & Clay≥15%	
		IM2		MILD	CALCAREOUS	15%<Carb<25% & Carb>Clay	
		IM3		MILD	VERY CALCAREOUS	Carb>25% & Clay≤25%	
	IH	IH1		HOT	SLIGHTLY CALCAREOUS	Carb<15% OR 15%<Carb<20% & Clay≥20%	
		IH2		HOT	CALCAREOUS	15%<Carb<20% & Carb>Clay OR Carb>25% & Clay≥25%	
		IH3		HOT	VERY CALCAREOUS	Carb>25% & Clay≤25%	
J	JM	JM1	METAL-BASED SULPHATED SILICA-INDURATE CLAYEY CALCAREOUS SILT	MILD	SLIGHTLY CALCAREOUS	Carb<15% OR 15%<Carb<25% & Clay≥15%	
		JM2		MILD	CALCAREOUS	15%<Carb<25% & Carb>Clay	
		JM3		MILD	VERY CALCAREOUS	Carb>25% & Clay≤25%	
	JH	JH1		HOT	SLIGHTLY CALCAREOUS	Carb<15% OR 15%<Carb<20% & Clay≥20%	
		JH2		HOT	CALCAREOUS	15%<Carb<20% & Carb>Clay OR Carb>25% & Clay≥25%	
		JH3		HOT	VERY CALCAREOUS	Carb>25% & Clay≤25%	
K	KM	-	CLAY (KAOLINITE)	MILD	-	In-situ ω < Compaction ω	
	KH	-		HOT	-	In-situ ω > Compaction ω	

A suite of standard conventional tests is proposed for the purpose of classification as listed below:

- Hydrometer and wet sieving (or alternatives): BS1377:2-1990|9.2,9.5
- Particle density: BS1377:2-1990|8
- Liquid/plastic limits: BS1377:2-1990|4,5
- Natural water content: BS1377:2-1990|3
- Natural density: BS1377:2-1990|7
- Carbonate content: BS1377:3-1990|6.3
- Sulphate and Chloride Content: BS 1377:3-1990,5.3,7.2
- Proctor compaction: BS1377:4-1990|3

5.2.3 Case History

Wynne (2007) and Roohnavaz et al. (2011) described the North West Kazakhstan loess (30 km from Aksai city within the Karachaganak oilfield) as calcareous clayey silt, containing 20% to 40% clay, 10% to 20% Calcium Carbonate, and 0% to 5% sand. Serridge and Synac (2006) described the upper Karachanganak Loess (0-2 m deep) as a lumpy loam (very silty clay) with gypsum inclusions, containing 20% sand, 55% silt, 24% clay, and 12-80% carbonate. These combinations suggested a range of sub-classes, including Class C1, D1, and D2 (Fig. 5.1). More specifically, the combination detailed in Serridge and Synac (2006) suggests a soil class D1 (60% quartz, 25% clay, and 15% carbonate). According to the predictive graphs presented in Chapter 6, the maximum possible normalized[44] collapse potential for class C1, D1 and D2 material is between 15% and 25% (7.2 and 12.1% for the mean 0.48 void ratio reported in Wynne (2007)). This agrees with the 6.4% collapse potential (at 200 kPa) reported in Serridge and Synac (2006), bearing in mind that graphs represent the maximum collapse potential occurring at roughly zero water content, while the 6.4% represents the collapse potential at 10% natural water content.

The site location is shown in Fig. 5.2(a) while the loess face is shown in Fig. 5.2(b).

[44] As there were differences in the initial void ratios among the test specimens, the clay/carbonate content versus coefficient of contraction may not be comparable. Hence, normalized values of coefficient of contraction are reported throughout the chapter.

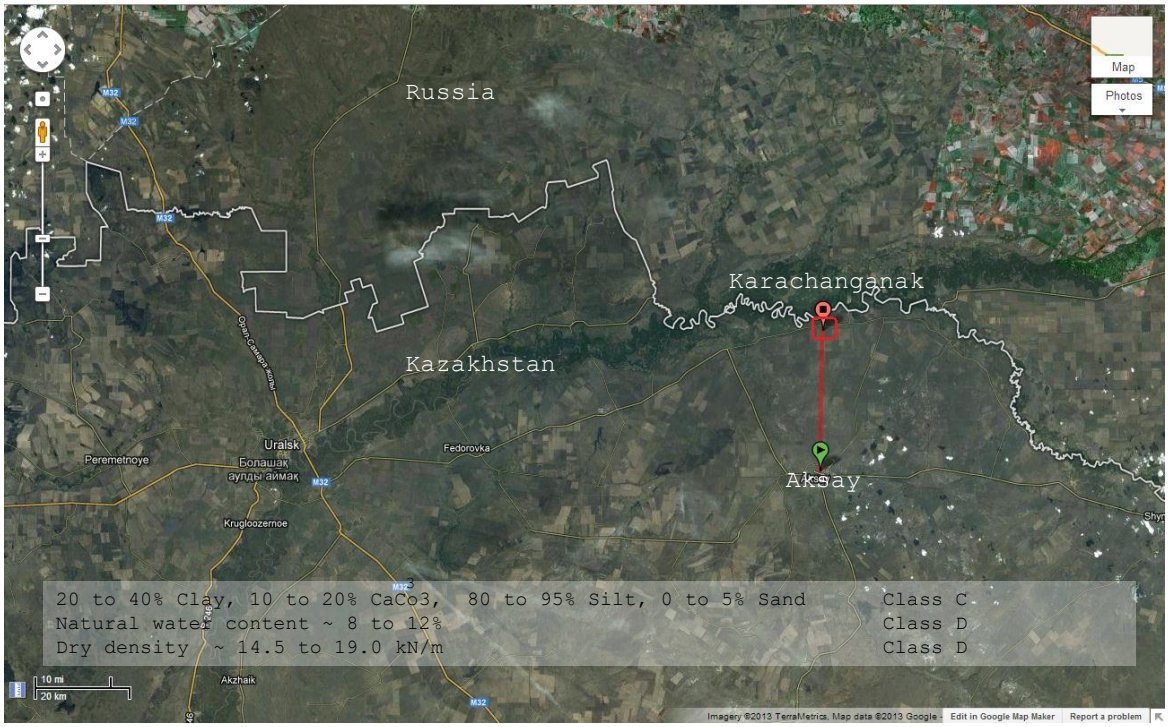

Fig. 5.2(a) Case study site location: Karachanganak, Kazakhstan, South Ural

Fig. 5.2(b) Karachanganak upper loess, Kazakhstan: 0-2 m top crust, deluvial (i.e. on slopes) loess, very silty clay with gypsum (Serridge and Synac, 2006)

5.3 Micromechanics of Collapse

5.3.1 Expected Impacts

In this section, the predominant role of clays in the collapsibility in particularly calcareous fine soils is argued. This agrees with the findings presented in Chapter 4, which showed the early migration of clayey flakes from the connector sites to the macro-pore spaces and the contribution of Calcium Carbonate scaffold structures in retaining the porous structure until capillary forces dropped (see Sections 4.3, 4.5, 4.6). It is also shown that the only fine tubular carbonates (also see (Grine and Glendinning, 2007)) are

capable of binding the silt particles (and therefore generate collapsibility). This indicates the significance of micro-morphology and the chemical properties of the bonding agents. The significance of minor bonding agents, including amorphous silica and sulphate phases are then discussed. As these minor phases are typically the products of chemical weathering, analyses are enhanced by the use of a temperature control, which in turn affects the micro-morphology. The chemical interplay among various combinations of major and minor bond types is then detailed.

5.3.2 Class ‘A’, ‘B’, ‘C’

5.3.2.1 Class ‘A to B’ – Clayey Silts (B1, B2, B3)

The clay content was increased in clayey silt specimens. The silt-with-clay substitution increased the volume of the micro-pores at the expense of a decrease in macro-pores volume. The initial unimodal pattern of the particle (and hence pore) size distribution (showed in Chapter 3 for crushed sand after ten 60 s of milling) attained a bi-modal form for an increase in the clay content. This was due to the clay’s relatively lower specific gravity (the average specific gravity of kaolinite was measured as 2.61), which allowed higher volumes of solids to accommodate in a domain of fixed dimensions. The honeycomb face-to-face and/or edge-to-face arrangement of clay flakes formed the micro-pores.

Increasing the clay content from 0 to 15% marginally reduced the dry-state compressibility, but gave rise to collapsibility. **At 15%** clay content, the silt grains were finely coated with clay (Fig. 5.3, Table 5.1 Row 2). Coatings occurred upon the first cycle of post-depositional drying, which allowed suction forces to draw clay-contained bulk water into fine pore openings. At 15% clay content, the air-filled macro-pores provided minimum support to the peripheral arching chain of clayey coated silts, while clay fragments radiated from the grains’ surface to the grains’ contacts and formed a suite of clay bridge/buttress units. Water ingress led to the migration of clays into macro-pore spaces. This opened a gap space between pairs of silt grains. Carrying high skeletal forces at 200 kPa net stress; silt grains travelled this gap space and collided at the asperity tip points upon wetting. Chipped quartz grains also migrated into the macro-pores with the flowing bulk water.

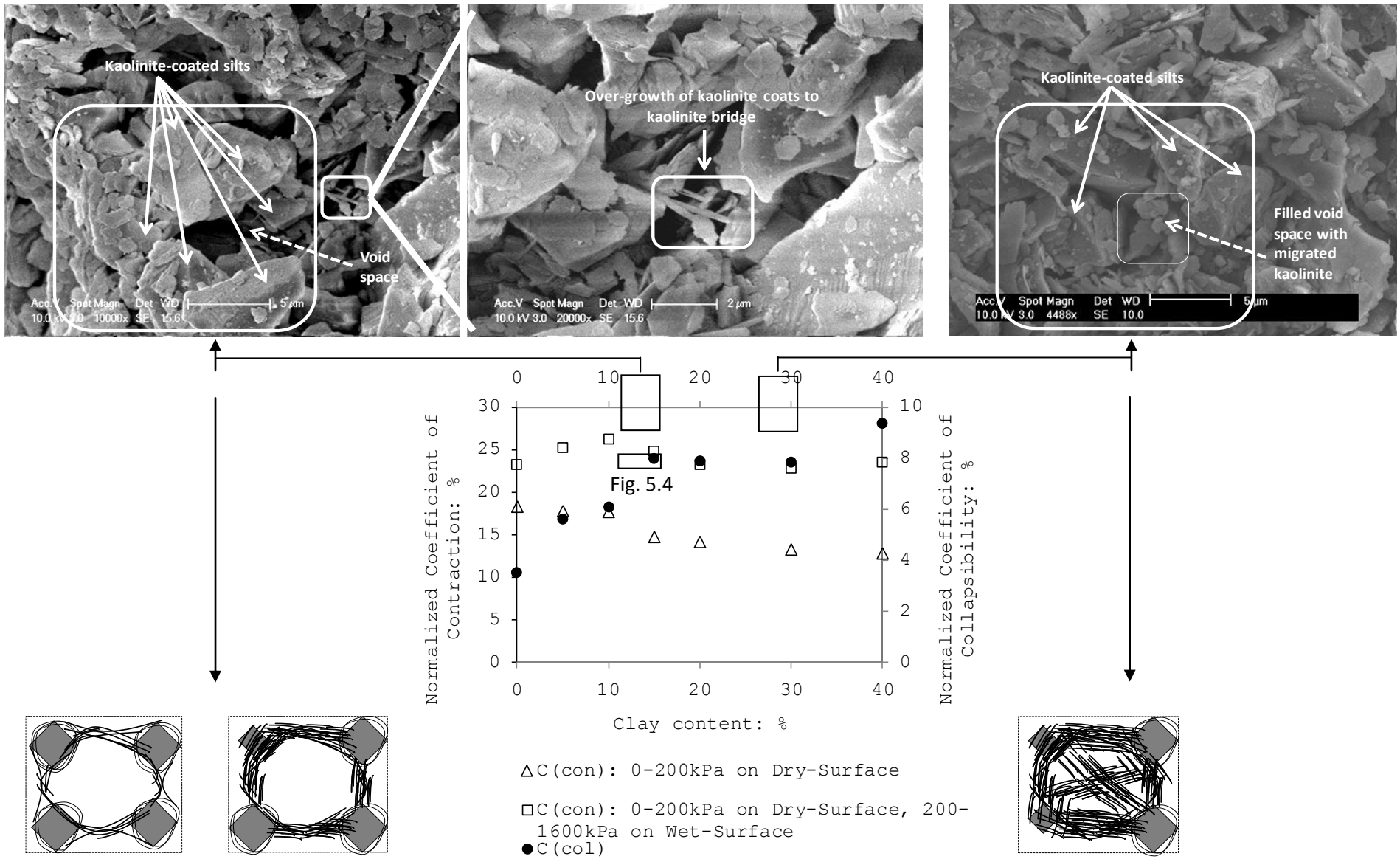

Fig. 5.3 Class B: schematic micro-fabric illustrations and SEM image micro-graphs before wetting (from left to right class B1, B2, and B3) on the plot of kaolinite content versus normalized collapse potential

Increasing the clay content from 0 to 15% marginally reduced the dry-state compressibility, but gave rise to collapsibility. **At 15%** clay content, the silt grains were finely coated with clay (Fig. 5.3, Table 5.1 Row 2). Coatings occurred upon the first cycle of post-depositional drying, which allowed suction forces to draw clay-contained bulk water into fine pore openings. At 15% clay content, the air-filled macro-pores provided minimum support to the peripheral arching chain of clayey coated silts, while clay fragments radiated from the grains' surface to the grains' contacts and formed a suite of clay bridge/buttress units. Water ingress led to the migration of clays into macro-pore spaces. This opened a gap space between pairs of silt grains. Carrying high skeletal forces at 200 kPa net stress; silt grains travelled this gap space and collided at the asperity tip points upon wetting. Chipped quartz grains also migrated into the macro-pores with the flowing bulk water.

A further increase in the clay content **from 15 to 30%** reduced the dry-state compressibility, and stopped the increasing trend of collapsibility (Table 5.1 – Row 2, second criteria). At >15% clay, remnant clays (to coatings) radiated into macro-pores (Fig. 5.3). Aggregated clay at macro-pores provided some degree of lateral support to the arching chain of clayey coated silts. This decreased the share of skeletal forces, which was carried by contacts. Given the lower air-volume at macro-pores, lower contents of grains moved to macro-pores, and thus a decrease in collapsibility was recorded.

Fig. 5.4 and Fig. 5.5 show the post-collapse micro-fabric of class B soil at 10% clay content (i.e. class B1). The micromechanism of collapse detailed above is further discussed through commenting these two images as below. Clusters of closed-packed, clean, and angular 2 to 4 µm silt grains were spotted immediately next to 20 to 30 µm of grains with concave surface features (Fig 5.4, see the sand grain immediately above the clayey matrix). These possibly are the footprints of edge chipping events after wetting. The new microfabric was tightly packed, providing high inter-locking forces, which impede any further migration of silt grains. The presence of clean large silts and irregular aggregates and silt bridges among them indicated the fine migration. This is also supported by the heavily clay-coated matrix composed of perturbed parallel clayey flakes and crushed silts (Fig 5.4).

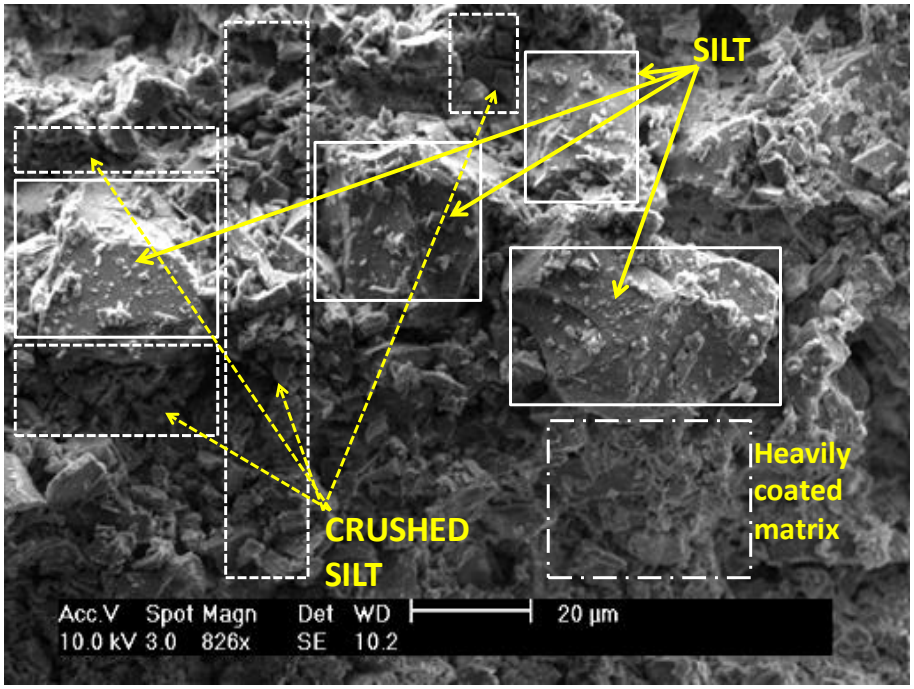

Fig. 5.4 Class A-B: SEM image at 10% clay content after collapse event

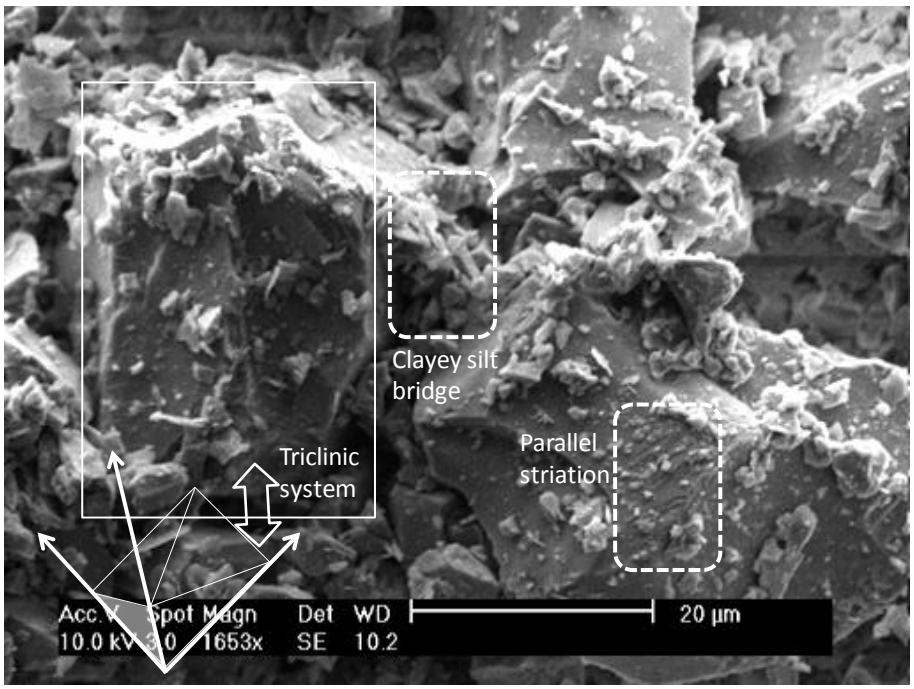

Fig. 5.5 Class A-B: clay 10-15%, (a) intermediate fabric level, (b) clay-size level

At higher magnifications (Fig. 5.5) the fresh fracturing features of silt are seen more clearly. Triclinic crystallography, sub-angular textures and parallel striation surface features support the significance of grain breakage at 15% clay content. Clayey buttress units vanished. However, the presence of inter-particle silt chains suggested the possible susceptibility to further crushing under skeletal stresses. The clayey nodules attached to the quartz surfaces confirmed the formation of secondary clay coagulates upon wetting.

5.3.2.2 Class 'C' – Calcareous Silts (C1, C2, C3)

Owing to the contribution of suction during the first post-depositional drying stage, the bulk water with colloidal sodium carbonates travelled to grains' contact points, where the pore diameter was a minimum (and hence the matric suction was a maximum). Further wetting-drying with high di-electric chloride solution, led to nucleation of lithogenic Calcium Carbonates at contact points. Fig. 5.6 summarizes the output of oedometer tests conducted on calcareous loess specimens, containing 0 to 40% carbonate. Fabric arrangements are illustrated in schematic drawings and by microscopic images.

Increasing the carbonate content from 0 to 5% remarkably reduced the dry-state compressibility and slightly increased the collapsibility. This is an indication of relatively stronger carbonate bonds than inter-locking forces in clean silts. Increasing the carbonate content from 5 to 15% gave rise to dry compressibility. This is due the higher compressibility of carbonate matrix than quartz structures. However, the increasing trend of collapsibility (seen at <5% carbonates) continued to 15% carbonate content, giving the marked collapsibility at a carbonate content between 10 and 15%. This is mainly due to the increase in gap space between pairs of silt grains, allowing silts to travel a longer distance and take a higher kinematic momentum before colliding in the event of wetting. As such, a classification boundary at **5-15%** carbonate was considered in Table 5.1, which divides soil classes C1 and C2. Plateau trends in both compressibility and collapsibility were observed for soils containing carbonates between **5-15% and 20-30%**. Increasing the carbonate content **beyond 30%** decreased the dry compressibility. Remnant carbonates at macro-pores provided lateral support to the surrounding arching chain of carbonate coated silts, which then improved the dry-state stiffness. The increased collapsibility is due to the limited dry-state compression and hence higher preserved voids' volume, which then were compressed on wetting. This, however, was deemed to occur more at micro-pores within the carbonate units, rather than in macro-pores, and thus may not be regarded as collapsibility: The decrease in ultimate void ratio loss (Fig. 5.6, between 30 to 40% carbonate content) is in agreement with the deemed decrease in collapsibility.

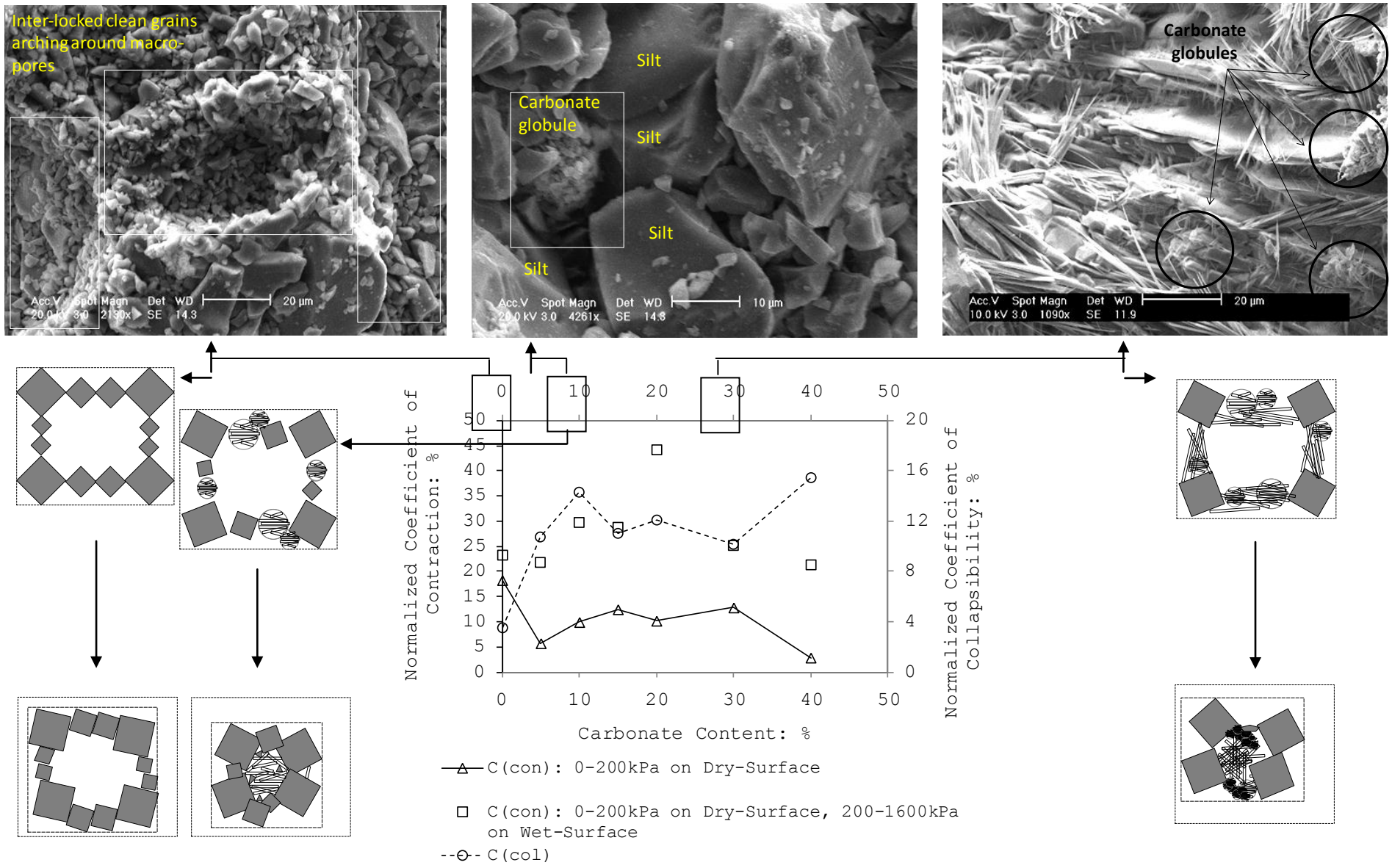

Fig. 5.6 Class A and C: schematic micro-fabric illustrations and SEM image micro-graphs before wetting (from left to right class A, C1, and C3) on the plot of carbonate content versus normalized collapse potential

5.3.2.3 Discussion: Significance of the Cement Type

To compare the contribution of kaolinite and carbonate in loess compressibility/collapsibility, single oedometer test was conducted on seven pairs of specimens, at 60%, 70%, 80%, 85%, 90%, and 95% content of quartz silt constituent. Silt was combined with either kaolinite or carbonate, forming the pair of specimens at certain silt content. Oedometer test results conducted on specimen pairs (containing certain silt content) are presented in Fig. 5.7.

Higher dry-state compressibility, collapsibility and wet-state compressibility were recorded in calcareous silts compared to in clayey silts, both comprising same contents of constituents at a same initial void ratio (following a try and error specimen preparation process). Carbonates contribute to the soils' stiffness in the absence and presence of water more than the contribution of clays of similar content.

5.3.3 Class 'D'

5.3.3.1 Crystallization of Bonds: Key Difference between Class 'D' and 'B & C'

As described in section 4.6 Chapter 4, a single cycle of post-depositional wetting-drying can drive the primary clays from contact points into macro-pore spaces. Therefore, in the absence of post depositional wetting-drying cycles, clay in a clayey silt system tends to congregate at the grains' contacts. An increase in the clay content radiates the excess clay into the macro-pores. In contrast, clay in calcareous clayey silts tends to accumulate at macro-pores, bracing the inner perimeter of void spaces. An increase in clay content gives a rise to the thickness of bracing units and provides a higher degree of lateral support to surrounding grains. Crystallization of carbonates commences from the grain contacts. This was deemed from the EDS-SEM data (Fig. 5.8), showing the minimum population of Ca^{++} cations at macro-pore spaces. Accumulation of carbonates at grain contact points is due to the early crystallization of Anhydrous Sodium Carbonates at contact points, which then change into Calcium Carbonates after interacting with the infiltrating Calcium Chloride electrolyte. Any increase in carbonate content therefore allows the excess carbonates to occupy the macro-pore spaces.

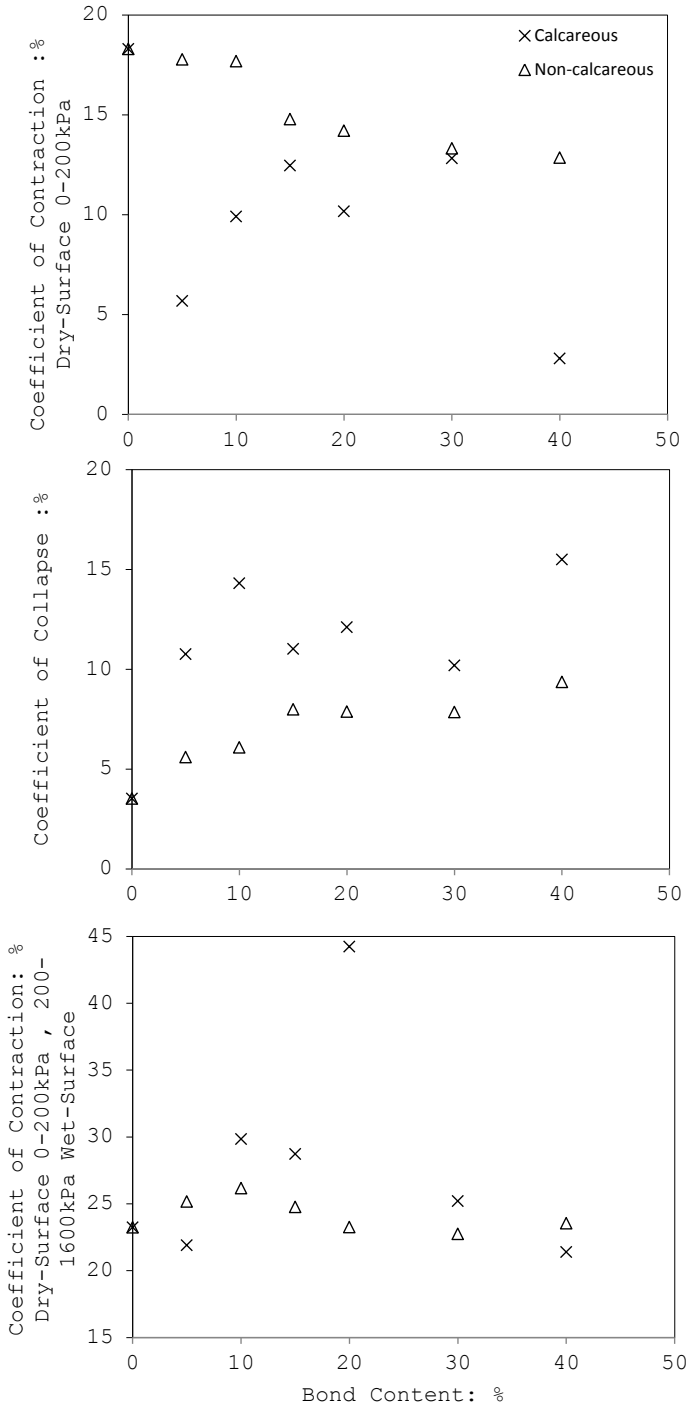

Fig. 5.7 Class A-B-C: kaolinite versus carbonate bonding agents

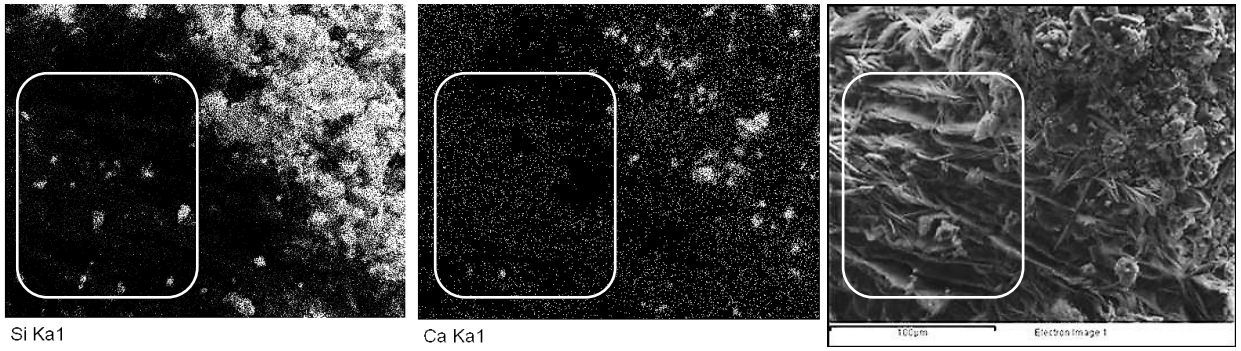

Fig. 5.8 Energy-dispersive X-ray and ESEM images of calcareous loess specimen, showing low population of Calcium at micro-pores

5.3.3.2 Slightly Calcareous Clayey Silt (D1)

Varied Clay Content

Carbonates in D1 soil provide additional reinforcement to clay units rather than exhibiting as individual connectors. In other words, the dominating clay content allows clay fragments to play the major role in the soil's structural stiffness and hence the degree of collapsibility. Carbonates nucleate on clay coatings (Fig. 5.9, and Eq. 5.8), though a chemical interaction detailed in section 5.3.3.4.

Oedometer test results and ESEM images revealed:

- For D1 loess of clay contents within +5% of carbonate (**Clay<20%**), existing clayey connectors received reinforcement from carbonate globules, which were attached to the clay's surface. This was evidenced after the decreased dry-state compressibility and increased collapsibility for 5 to 10% increase in clay fraction (see also Fig. 5.9 and Fig. 5.10).
- The plot of dry-state compressibility against clay content for <10% clay in conjunction with the plot of collapsibility against clay content for <15% clay (both in Fig. 5.9), suggests **a threshold of 15%** (same threshold for clay content as in class B material – see Table 5.1; also see Fig. 5.9), at which carbonate scaffold units were fully formed and grains gained both lateral and axial support from macro-pore bracings and over-grown clay coatings, respectively. Further increase in clay content led to the occupation of macro-pores (Fig. 5.9) and reduced the collapsibility (Fig. 5.9), providing a more ductile behaviour in the absence of water (as can be seen in the dry-state compressibility versus clay content for >20% clay in Fig. 5.9).

Given the minor contribution of carbonates, the overall behaviour of class D1 soil was expected to resemble that of Class B soil to some degree. Fig. 5.9 and Fig. 5.10 show the maximum collapsibility in D1 soil, taking place at **15% clay content**. In other words, soil exhibited its maximum collapsibility at 15% clay content, **at zero or <15% carbonate content.**

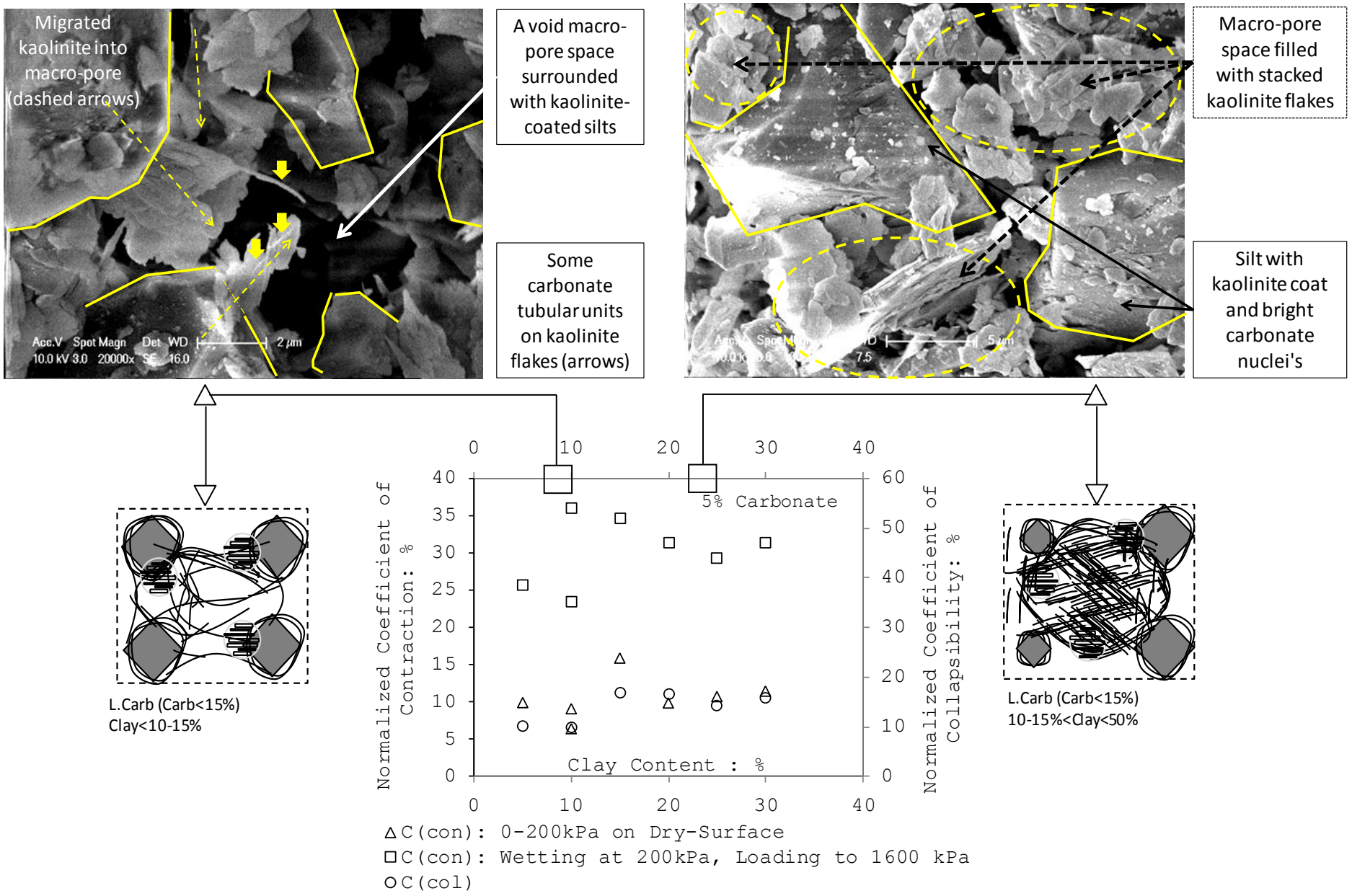

Fig. 5.9 Class D1: schematic micro-fabric illustrations and SEM image micro-graphs on the plot of kaolinite content versus normalized collapse potential at 5% carbonate content

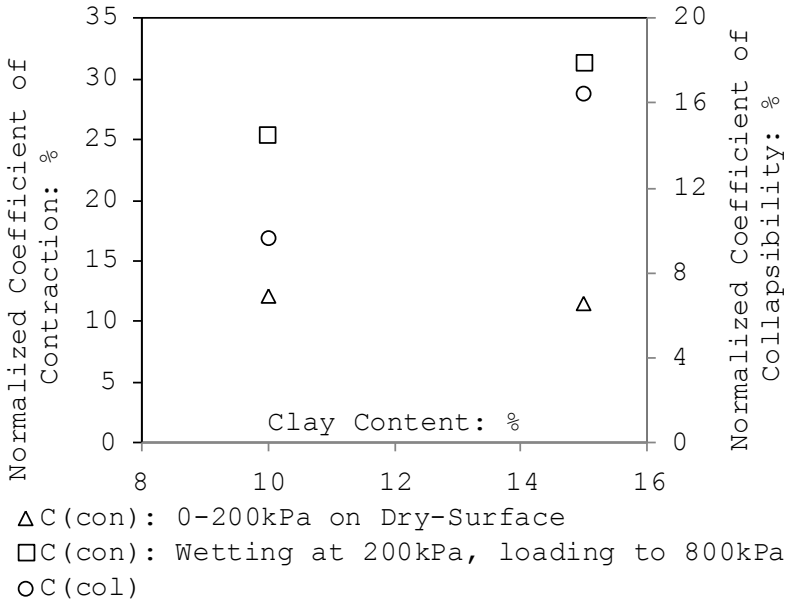

Fig. 5.10 Class D1: Control of clay content at 10% carbonate: Maximum collapsibility at 15% clay

Varied Carbonate Content

As discussed in the above section, the combination of fragile macro-pore bracing units and relatively strong clay bridges generated collapsibility in D1 soils. The carbonates reinforced the clay connectors; instead of forming individual bridge/buttress units. In the light of the carbonates' crystallization regime (detailed in Section 5.3.3.1), silt-carbonate replacement occurred at the grains' contact points. This is schematically illustrated in Fig. 5.11. **Carbonate content** is first varied to **15%** (less than clay content in D1 soil) at the 15% clay content (the threshold developed in the previous section above and reflected in Table 5.1).

Increased carbonate content from 5 to 15% led to the reinforcement of existing kaolinite connectors (rather than formation of macro-pore bracing units). For this, a reverse relationship between dry compressibility and carbonate content was recorded (Fig. 5.11). With respect to the pronounced control of carbonates on the time lag between wetting and collapse (the collapse framework in Section 4.6, Chapter 4), the collapse occurred relatively earlier at lower carbonate contents. This allowed higher degrees of drag forces to contribute and hence, owing to the greater degrees of grain breakage (under the combined drag and skeletal stresses), higher degrees of collapsibility was recorded.

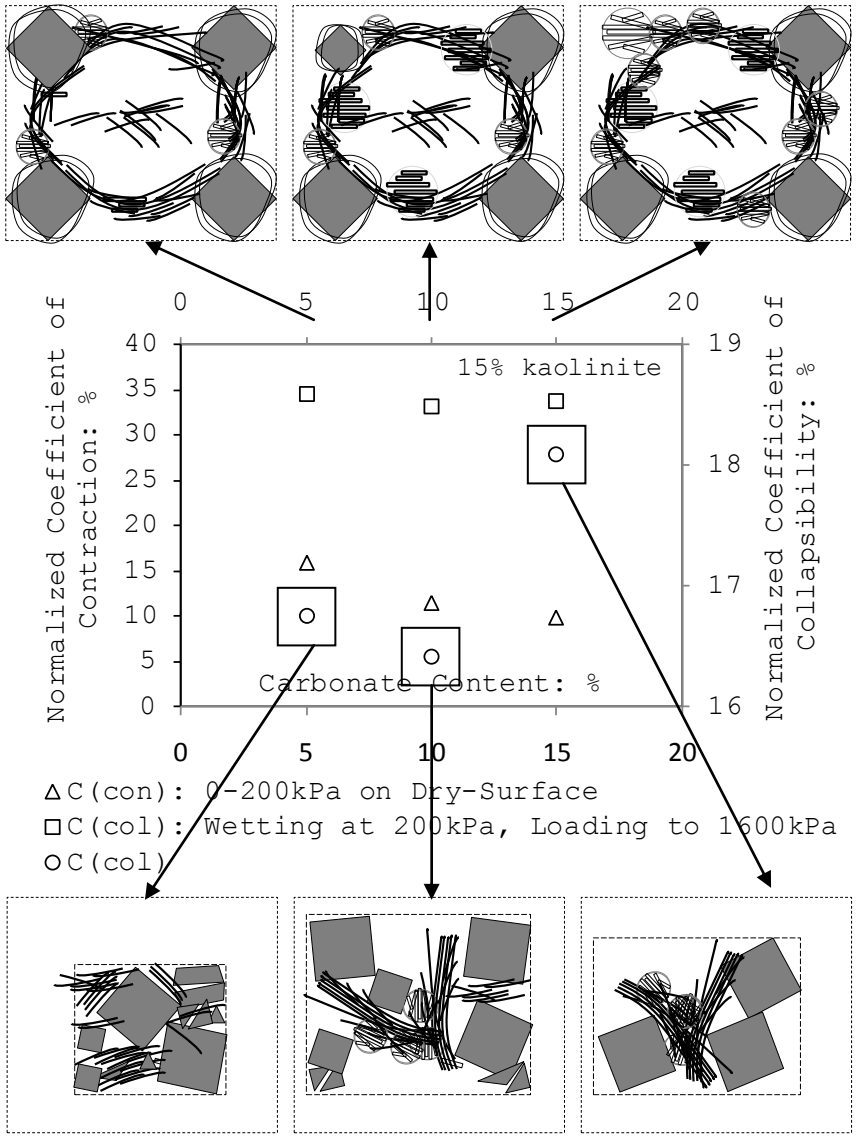

Fig. 5.11 Class D1: schematic micro-fabric illustrations on the plot of carbonate content versus normalized collapse potential at 15% kaolinite content

At >15% clay content, clay fragments filled more macro-pore spaces in the form of bracing units, and connectors received further reinforcement from carbonates. Furthermore, carbonate globules replaced some silt grains (Fig. 5.12).

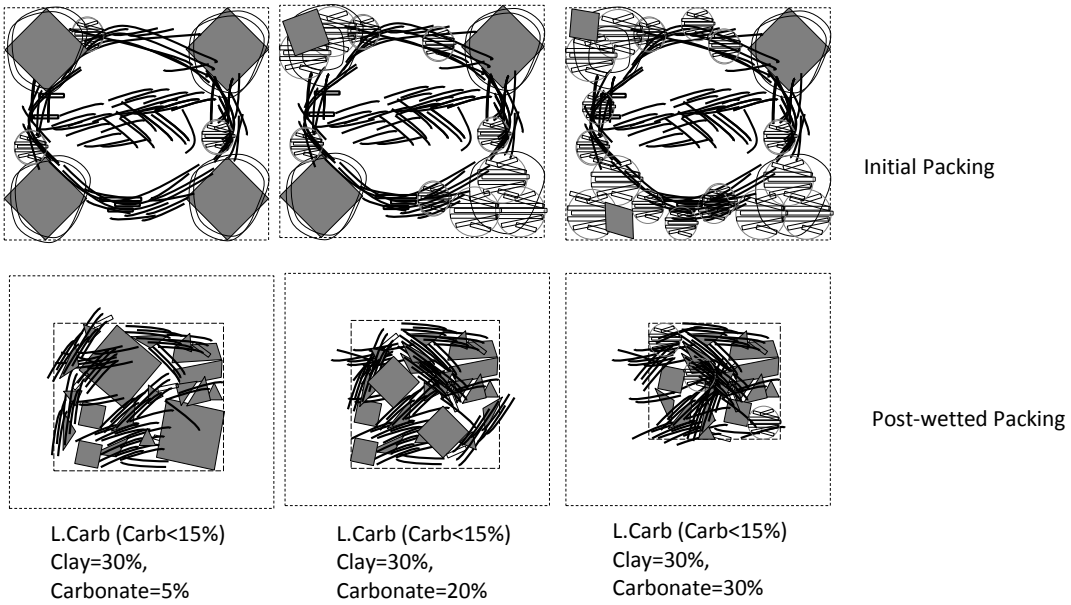

Fig. 5.12 Class D1: Schematic domain at varied carbonate content and 30% clay content - Before and after wetting (to be read in conjunction with the ESEM images)

The abundant clay-carbonate coagulates reduced the dry-state compressibility. A reduced rigid silt content allowed the post-wetting residual void spaces to decrease to a minimum (Fig. 5.13). Carbonates and clays formed fine matrix bodies and covered the residual void spaces.

Varied Cement (Clay vs. Carbonate) Content

Increasing the carbonate content at the expense of decreasing clay content increased the dry-surface compressibility and decreased the collapsibility in D1 loess (Fig. 5.14). This is due to the decreased content of the main cement (clay), which in turn decreased the soils' stiffness and hence increased the pre-wetting void ratio loss and consequently decreased the collapsibility.

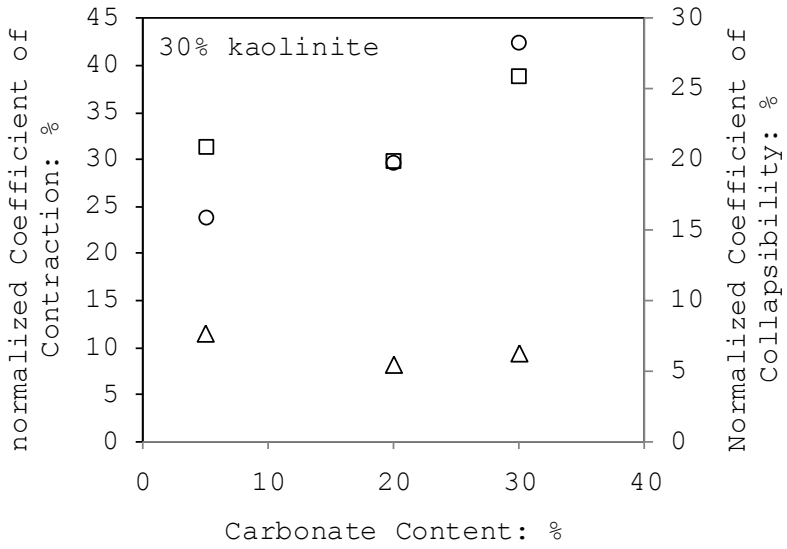

△C(con): 0-200kPa on Dry-Surface
□C(con): Wetting at 200kPa, Loading to 1600kPa
○C(col)

Fig. 5.13 Class D1: Control of carbonate content at 30% clay content

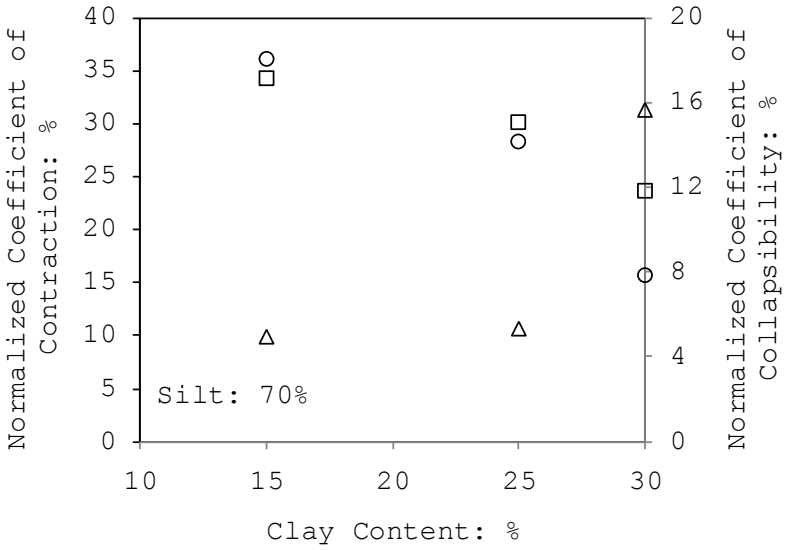

△C(con): 0-200kPa on dry-surface
□C(con): Wetting at 200kPa, Loading to 1600kPa
○c (col)

Fig. 5.14 Class D1: Control of clay/carbonate ratio at 70% silt content

5.3.3.3 Calcareous Clayey Silt (D2)

Collapse on Microscopic Images

Calcareous loess was found to be the most collapsible form of calcareous loess, within which the carbonate takes the major control on the soil's mechanical response. Electron microscopy imaging was used to understand the delicate micro-fabric features of test specimens before and after the wetting:

- Tubular bridge units tied pairs of silt grains (Fig. 5.15) together. The network of grains formed macro-pore spaces, which may remarkably collapse, with much of the skeletal forces stored as a potential energy, should wetting/loading be established.
- Encrusting carbonate tubes and bracing units (Fig. 5.15) conveyed the skeletal forces in axial compressive-tensile form and hence was responsible for the low dry-state compressibility.
- Carbonate buttress structures were originated from the over-growth of carbonate coatings as displayed in Fig. 5.15.

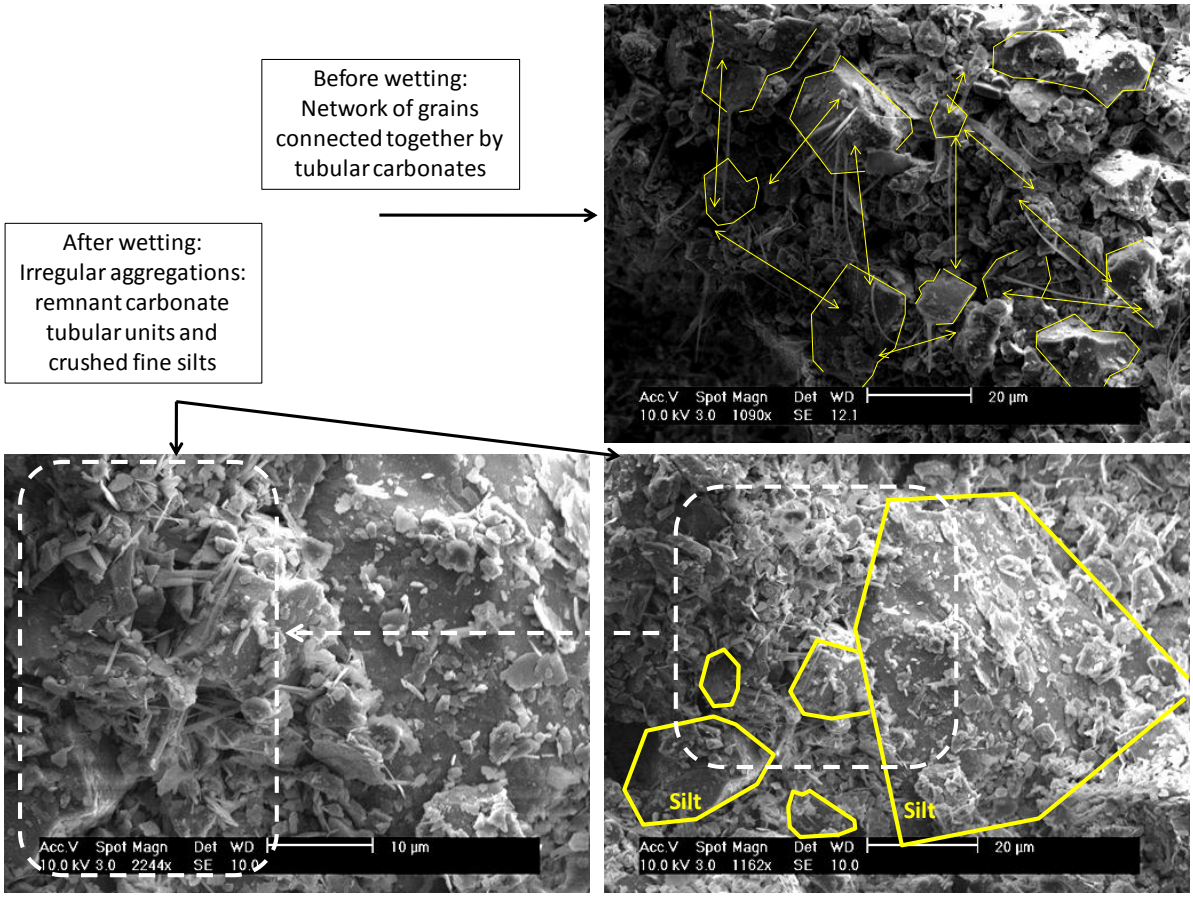

Fig. 5.15 Class D2 – SEM image of specimen made up of 25% carbonate and 10% kaolinite – before versus after wetting

The key findings after inspecting the wetted microfabric were:

- Irregular aggregations were found among survived silts, which were composed of crushed silts, coagulated clays and carbonates (Fig. 5.15).
- The presence of tubular carbonate remnants and nodular units (carbonate re-precipitated aggregates) implemented the migration of colloidal carbonates through the pore-network (Fig. 5.15). The surviving particles were finely coated. Some tubular carbonates still encrusted the grains, showing a residual degree of collapsibility.

Varied Carbonate Content

At constant clay content, an increase in carbonate led to a decrease in the silt content. This expanded the micro-pores' volume, while a matrix of nodular and interwoven tubular carbonates accumulated at macro-pores (Fig. 5.16).

At lower carbonate contents, a suite of porous scaffold structures were formed while at higher carbonate contents, closely packed clusters were generated (Fig. 5.16). Higher carbonate contents decreased the dry-state compressibility (Fig. 5.16) due to the better structural integrity grained by the closer packing. At **>20% carbonate** content (>30% cement content), carbonates possibly radiated into the macro-pore spaces, while connectors received further reinforcement. Occupation of macro-pores with crystallized carbonates provided an additional degree of lateral support to the surrounding silt grains. This decreased the collapsibility, after its peak at **20% carbonate** content.

Varied Clay Content

Increasing the clay content allowed clays at macro-pores to expand and provide better lateral support to surrounding grains (Fig. 5.17). For this, the dry-state compressibility marginally decreased with clay content (Fig. 5.17). At **10% clay content**, the combined effect of poor macro-pore bracing, lubricating act of grains' clay coatings, and strong carbonate connectors generated the maximum collapsibility.

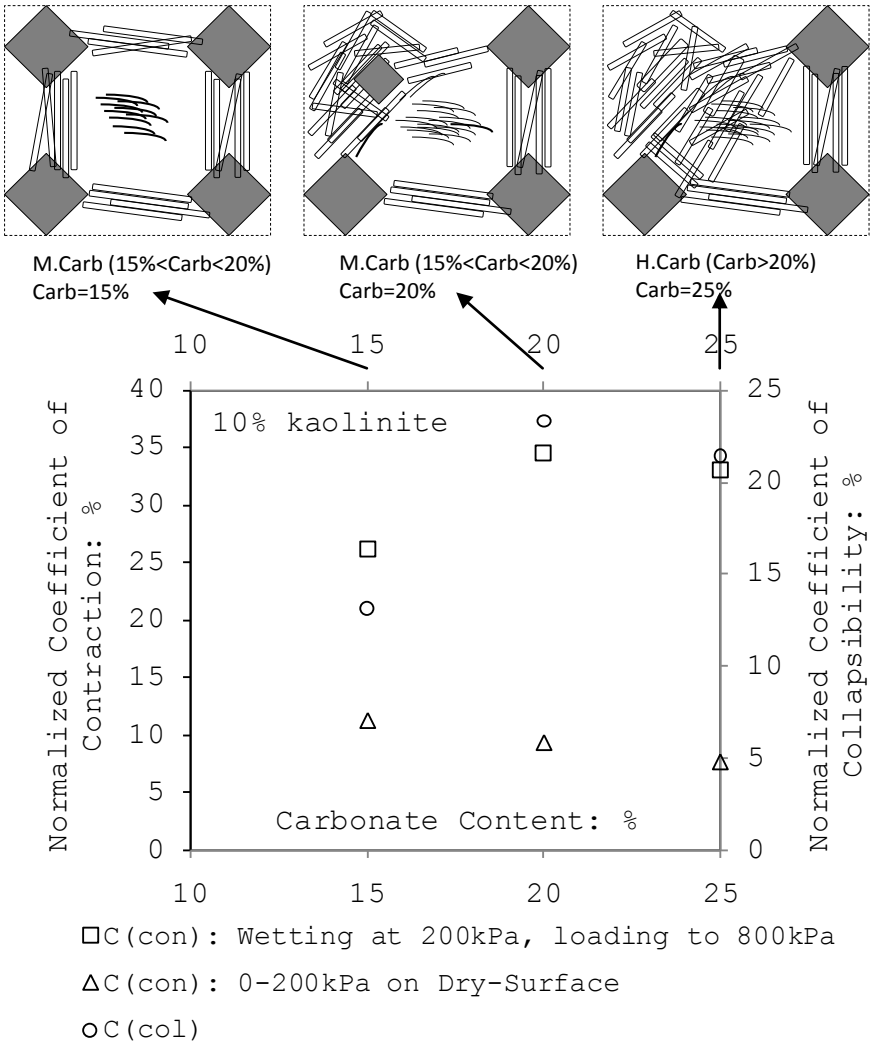

Fig. 5.16 Class D2: schematic micro-fabric illustrations on the plot of carbonate content versus normalized collapse potential at 10% kaolinite content

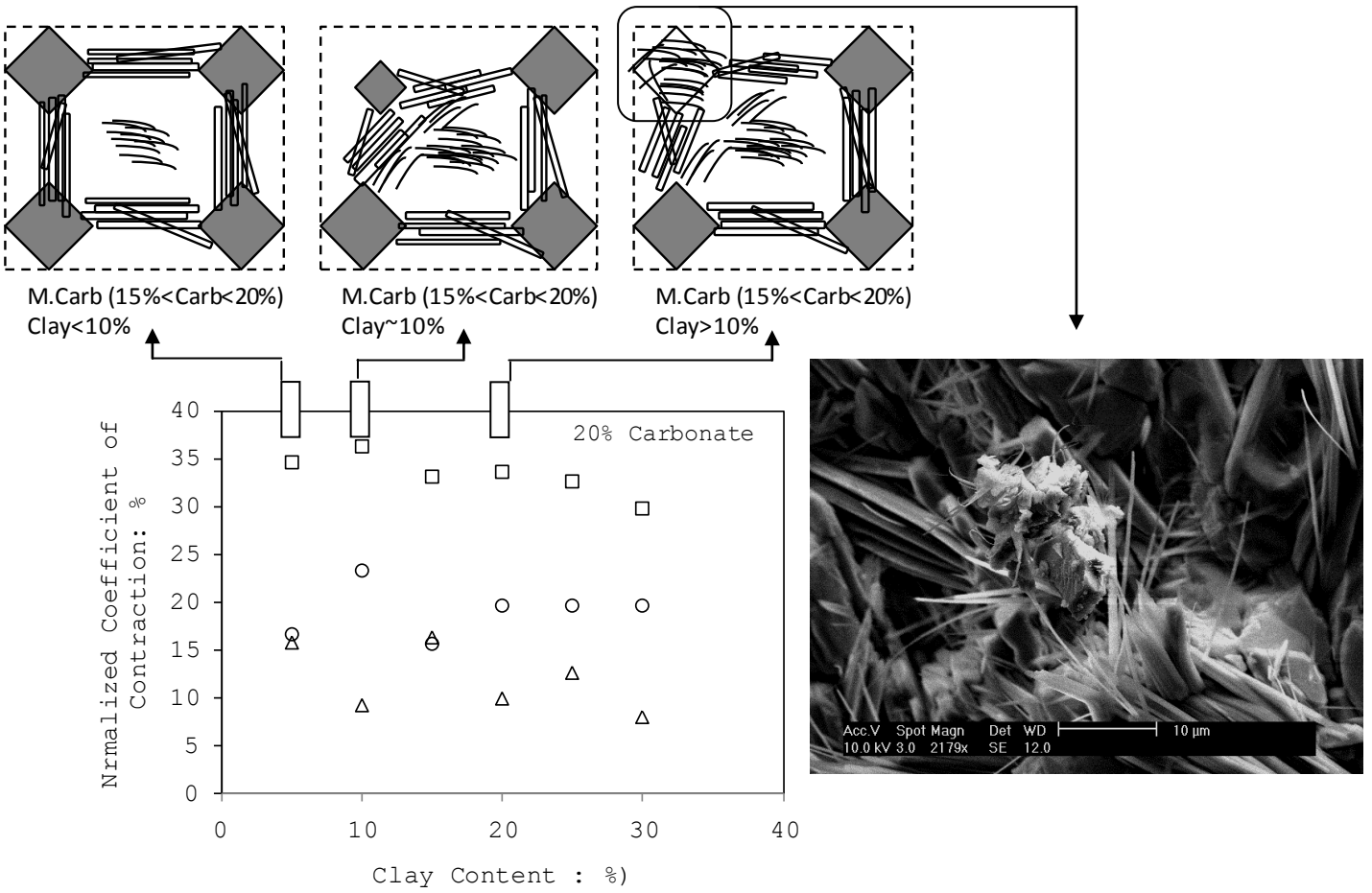

Fig. 5.17 Class D2: schematic micro-fabric illustrations on the plot of kaolinite content versus normalized collapse potential at 20% carbonate content

For >10% clay, the clay-carbonate pellet units were replaced with silt grains (Fig. 5.17) while receiving an enhanced lateral support from clay bracing units in the macro-pores. This decreased the dry-state compressibility. Although this lower degree of void space loss was expected to give rise to the collapsibility, since macro-pores contained less space to accommodate solids and water (due to the accumulated clays), only a marginal increase in collapsibility occurred. This marginal increase in collapsibility was generated by the lubricating effect of clay, as a less pronounced cement, and facilitation of silt-to-silt and silt-to-carbonate slippage on wetting.

Varied Cement (Carbonate vs. Clay) Content

Substitution of carbonates for clays at a constant cement content increased the dry-state compressibility and reduced the collapsibility. This was evidenced in a specimen pair containing 75% silt content, for 5% drop in carbonate content. The decrease in carbonates resulted thinner carbonate connectors and hence lower critical pressure on the dry surface. Meanwhile, the consequent increase in clay contents resulted in a higher volume of accumulated clay at the macro-pore spaces, and less room for washed substances upon flooding.

5.3.3.4 Very Calcareous Clayey Silt (D3)

Varied Carbonate Content

Increasing the carbonate content led to congregation of tubular into nodular carbonates, at macro-pores and the replacement of carbonate porous nodules with rigid silt grains (Fig. 5.18).

Higher lateral support to the chain of particles led to lower degrees of compressibility on the dry-surface. Carbonate-filled macro-pores left minimum room for fines to enter upon wetting. This decreased both the collapsibility and compressibility on the wet stress-state surface (Fig. 5.18).

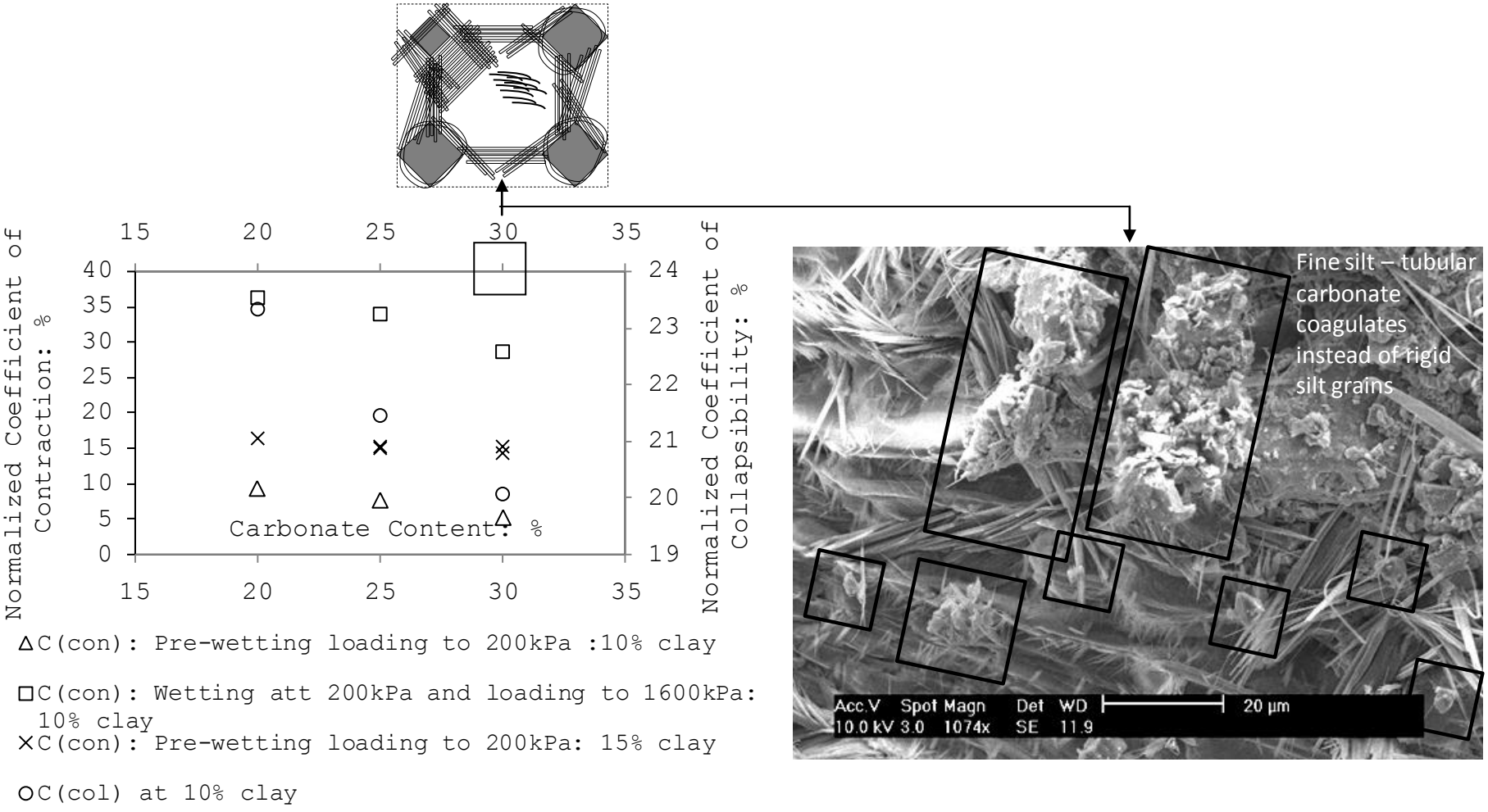

Fig. 5.18 Class D3: schematic illustration and SEM micro-fabric on the plot of carbonate content versus normalized collapse potential at 10 to 15% kaolinite content

Varied Clay Content

At high clay contents (about 50% silt), a homogeneous matrix of cements surrounded the grains, conducting a decent portion of skeletal forces (see chapter 3, skeletal force distribution discrete elements model) and providing a decent degree of lateral support to the particle chains. This reduced the impact of the clay content variation. Any increase in clay content beyond 20% (silt<50%) changed the structure of soil from granular to fine-grained, allowing clay-carbonate matrix to take over the structural stiffness (as a calcareous clay, a potential sub-class of class K material). An increase in clay content from 20% to 30% gave rise to consolidation volume change. This is due to the substitution of less-compressible rigid silts with highly compressible saturated clays (Fig. 5.19).

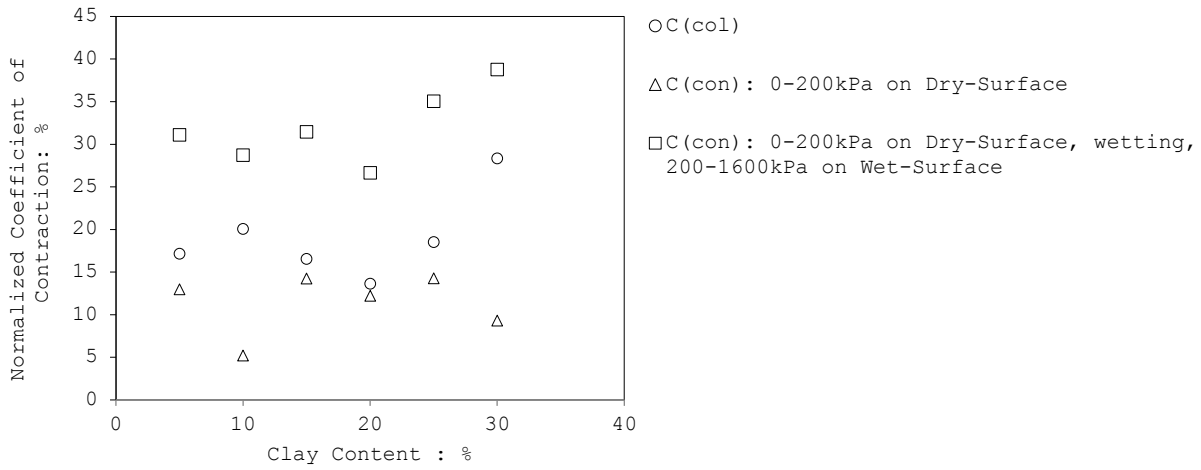

Fig. 5.19 Class D3: Control of clay content at 30% carbonate content

Varied Cement (Carbonate vs. Clay) Content

Substitution of carbonates with clays in D3 soils decreased both the compressibility at the dry-state, and the collapsibility. This may be viewed from a geochemical prospective. Tubular carbonates were transformed into nodular carbonates as more Na^{+} sites hosted Ca^{++}-enriched di-electric fluid for the cation exchange process (Fig. 5.20 to Fig 5.21). EDS examination revealed why such a change in the minerals took place. Fig. 5.20 shows the distribution of carbon, calcium, silicon, sodium, oxygen, and chloride elements. The mapping domain is shown in the electron microscopy image in Fig. 5.21, which indicates two distinct arrangements. Homogeneous distribution of chloride (i.e. fine white spots) suggested the satisfying multi-directional inflow of

$CaCl_2$ reactant fluid. The heterogeneous distribution of sodium, however, suggested a limitation to the sample preparation technique. This is possibly an indication of pellet structures formed during the depositional phase after crystallization of sodium carbonate by adsorbing the hygroscopic moisture. Sporadic white patches of calcium matches the nodular micro-morphology of carbonates. The plain distribution of the calcium matches the tubular micro-morphology of carbonates, containing lesser contents of calcium. This suggested that high contents of calcium may change the micro-morphology of carbonates from tubular into nodular. The distribution of silica suggests the encrusting act of tubular carbonates. These obscured the quartz grains while nodular carbonates accommodated in the macro-pores, exposed the quartz grains to the electron beam. In Fig. 5.20, nodular calcites appeared at Ca^{++}-enriched clusters while Na^{+}-enriched clusters possessed remarkably more contents of tubular carbonates (Aragonite) compared to nodular carbonates (calcites). These showed the interplay between morphology and chemistry in carbonates.

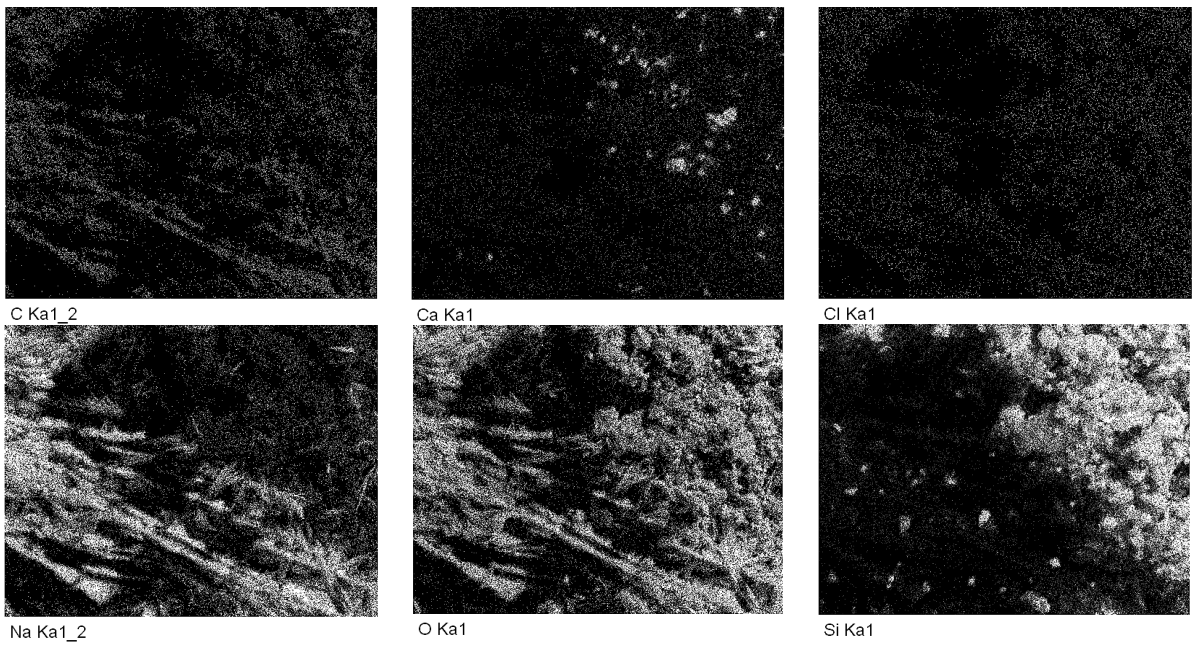

Fig. 5.20 EDS mapping on a Class B2 soil (10% kaolinite, 25% carbonate)

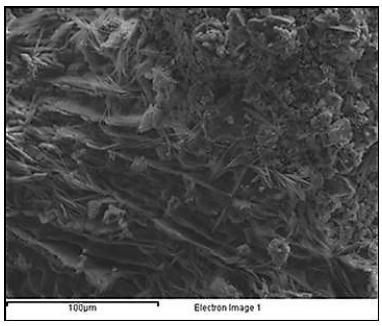

Fig. 5.21 SEM micrograph at initial state

In the XRD micro-graphs (Fig. 5.22 and Fig. 5.23), increasing carbonate content led to an increase in calcite's concentration, while changes to Aragonite concentration were found to be marginal.

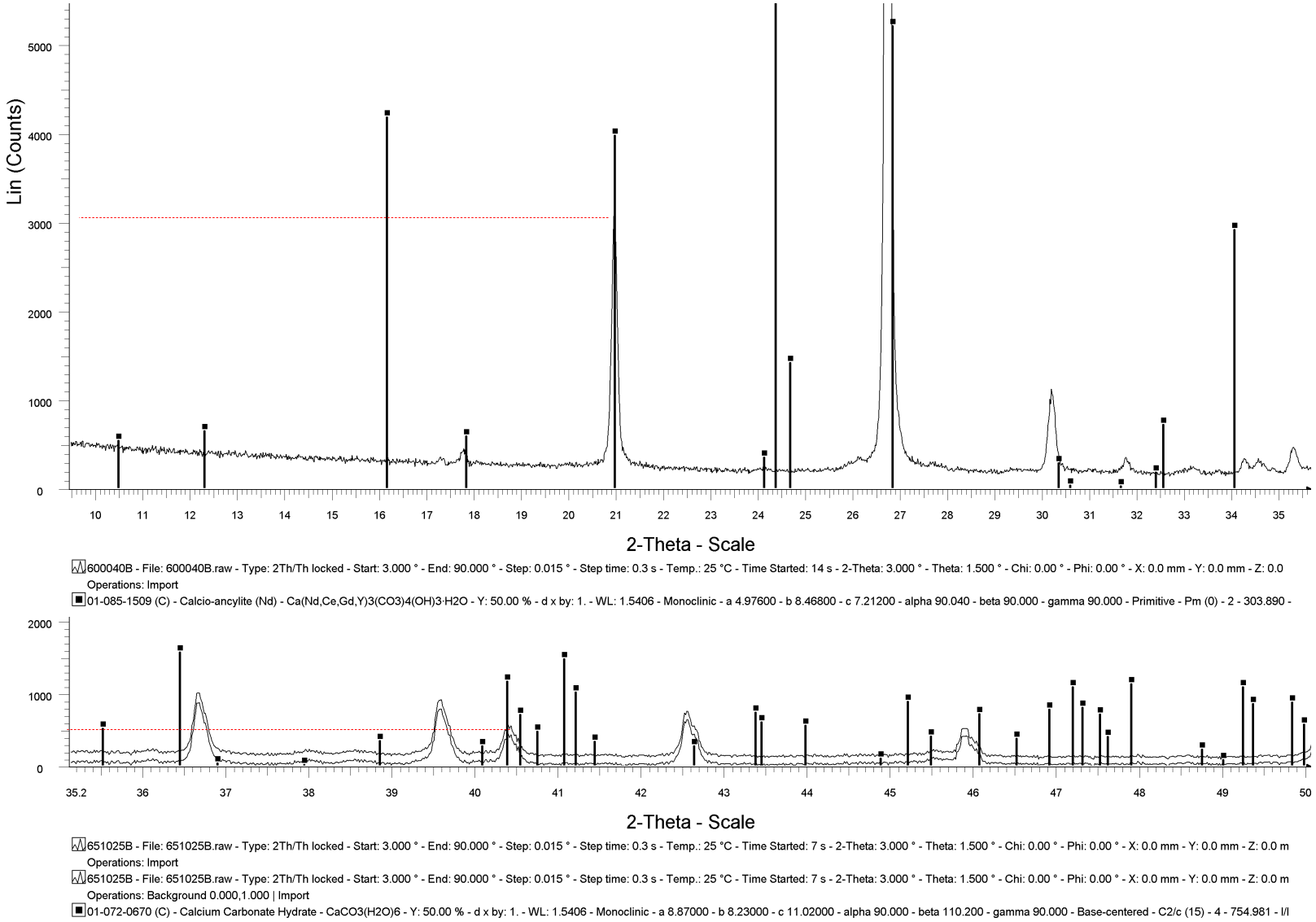

Fig. 5.22 (Up): XRD graph at 40% carbonate content (Down): XRD graph at 25% carbonate content: Calcium Carbonate Hydrate

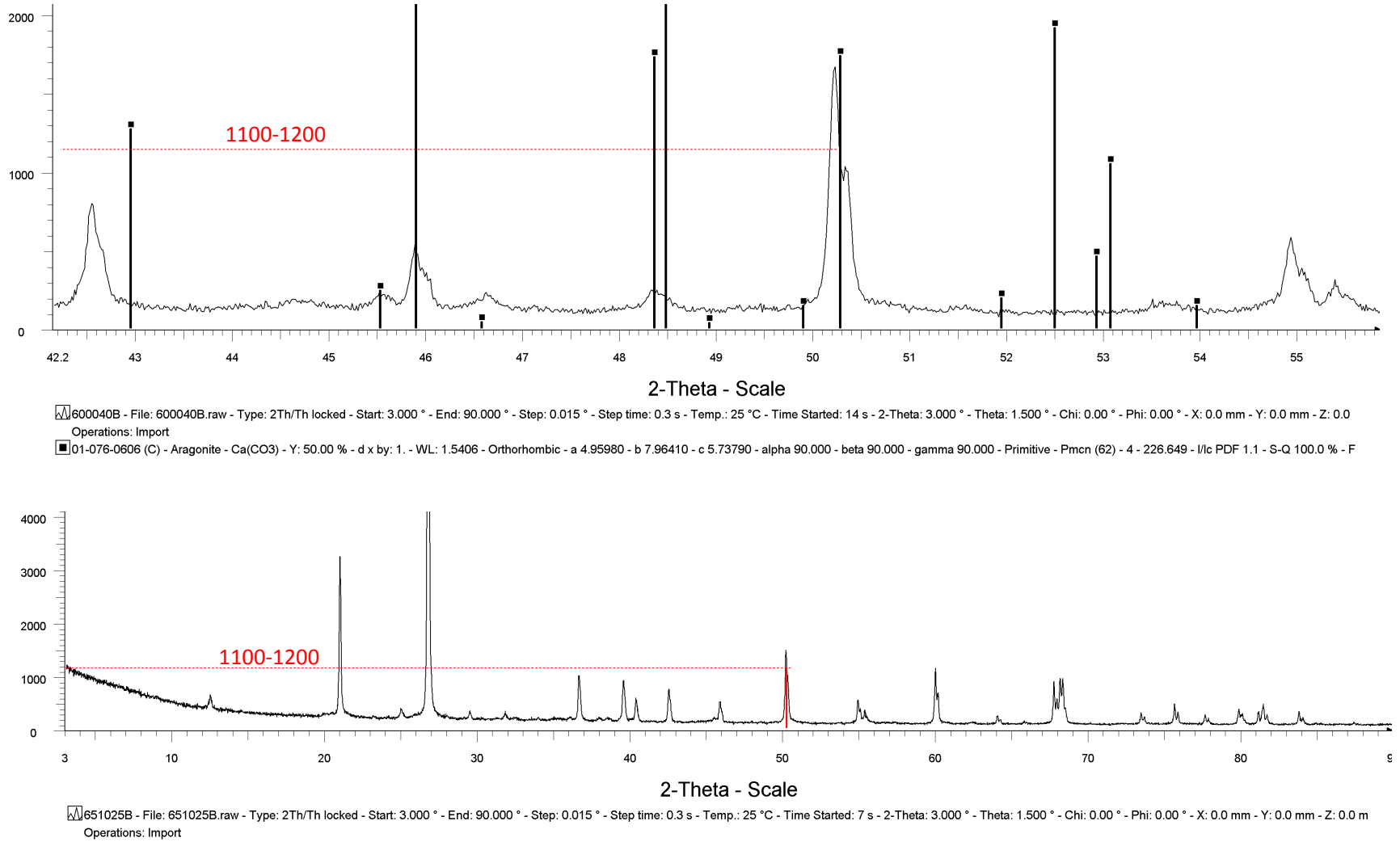

Fig. 5.23 (Up): XRD graph at 40% carbonate content (Down): XRD graph at 25% carbonate content: Aragonite

5.3.3.5 Discussion: Clay – Carbonate Interaction

The ingress of calcium-enriched electrolytes into a kaolinite matrix triggers short-term and long-term pozzolanic reactions (Broms and Boman, 1977, Little, 1995). Pozzolanic reaction is a suite of ion exchange events, specifically associated with pH-dependent charges on clays' edge: The pH-dependent positive charge on the edge of kaolinite flakes can change to negative after an increase in the pH of soil solution and the subsequent deprotonation at hydroxyl sites (Van Olphen, 1977). Mitchell and Soga (2005) suggested that these charges are responsible for the clay platelets' associations.

Any pozzolanic reaction needs a pozzolan, which is a source of silica or alumina. Deprotonated kaolinite (after donation of hydrogen atom by the hydroxyl tail in an alkaline environment) is a pozzolan. The reaction also needs a source of calcium ion. This can be supplied by the residual calcium within the soil, or by an external source ($CaCl_2$ in the present study):

$$Cl..Ca..Cl + H..\ddot{O}..H \xrightarrow{yields} .Ca.+ H..\ddot{O}. +.Cl+.Cl + H.+H..\ddot{O}. \qquad Eq.\ 5.1$$

Ca^{2+} exchanged with monovalent Na^{+} at the stern layer. Liberated Na^{+} reacted with the free hydroxyl anions, giving rise to the pH of the environment. High pH encouraged the liberation of hydrogen atoms from the clay's hydroxyl tail (i.e. deprotonation). Excess calcium ions then attached to exposed silica sheets and formed Calcium Silicate Hydrate (CSH) gels, as well as exposed alumina sheets to form Calcium Aluminate Hydrate (CAH) gels. Another type of gel, which might have formed in the absence of clay crystal breakage, is the Calcium Alumino-Silicate Hydrate (CASH), which also binds kaolinite clusters.

5.3.4 Class 'E', 'F': [Metal-based Sulphated] Silica-indurate Silt

Deep chemical weathering forms amorphous silica precipitates and therefore alters the mechanical properties. Table 5.2 displays the oedometer test results on silica-indurate soils (Class E to J). For class E and F material, silica-indurate silts were found to be less compressible and more collapsible than clean silts of identical stress history. Even higher degrees of collapsibility were recorded under hot climates. In the presence of metal-based sulphates, higher degrees of collapsibility were recorded under mild climates.

Table 5.2 Oedometer test results (silica-indurate specimens)

	Phases		Climate		Specification			Normalized relative contraction			
	With Sulphate	Without Sulphate	Mild	Hot	Silt	Clay	Salt	Dry surface 0-200kPa	Wetting surface at 200kPa	Wet surface 1600kPa	Wet surface 2100kPa
1					100	0	0	18.3	3.52	23.23	-
2	X		X		100	0	0	15.99	5.39	23.69	24.24
3	X			X	100	0	0	15.55	3.89	21.79	22.27
4		X	X		100	0	0	18.37	3.36	23.59	-
5		X		X	100	0	0	13.25	8.63	23.85	24.51
6					90	10	0	17.69	6.09	26.16	-
7	X		X		90	10	0	16.59	5.36	23.71	-
8	X			X	90	10	0	17.22	5.62	24.6	-
9		X	X		90	10	0	17.1	5.42	23.71	-
10		X		X	90	10	0	17.37	5.84	24.73	-
11					80	20	0	14.2	4.98	21.10	21.74
12	X		X		80	20	0	14.74	6.14	23.09	23.72
13	X			X	80	20	0	16.02	6.26	24.07	24.63
14		X	X		80	20	0	14.51	6.37	22.09	22.59
15		X		X	80	20	0	19.08	7.22	27.02	27.54
16					60	40	0	13.07	9.51	23.93	-
17	X		X		60	40	0	16.00	9.61	27.62	28.15
18	X			X	60	40	0	12.18	7.86	22.21	22.82
19		X	X		60	40	0	20.36	9.62	31.49	32.21
20		X		X	60	40	0	13.26	5.28	20.04	20.63
21					50	50	0	5.95	2.94	27.24	30.00
22	X		X		50	50	0	13.23	8.39	24.06	24.82
23	X			X	50	50	0	13.76	9.28	25.43	26.03
24		X	X		50	50	0	14.65	6.66	22.18	22.65
25		X		X	50	50	0	13.47	7.70	22.49	23.41
26					85	10	5	9.04	9.89	23.5	24.57
27	X		X		85	10	5	8.10	13.32	28.52	29.67
28	X			X	85	10	5	5.98	15.48	27.84	28.66
29		X	X		85	10	5	7.58	10.81	24.57	25.23
30		X		X	85	10	5	11.02	10.08	26.75	27.41
31					70	10	20	9.35	23.32	34.54	36.38
32	X		X		70	10	20	6.10	18.29	31.12	31.96
33	X			X	70	10	20	3.70	14.71	24.11	24.91
34		X	X		70	10	20	12.78	12.19	27.24	28.18
35		X		X	70	10	20	13.05	11.72	30.03	30.62
36					60	10	30	5.21	20.07	25.49	28.72
37	X		X		60	10	30	16.00	9.61	27.62	28.15
38	X			X	60	10	30	6.35	17.67	27.7	28.51
39		X	X		60	10	30	15.68	18.38	38.48	39.23
40		X		X	60	10	30	12.67	14.89	29.54	-

In practice and as an example, silica-indurate silts under hot climates represent the deposits in Merredin, east of Perth, Western Australia (Singh and Gilkes, 1993).

In the absence of clay, quartz and amorphous silica interacted physically. Silica coats act as inter-particle beddings. While higher extents of skeletal forces were conveyed on the dry-surface, particles slipped more readily on the wet-surface as less inter-locking forces operated on grains. Lower inter-locking forces were due to the particle edge chipping, which occurred upon wetting. Wetting led to larger loss of void ratio. This was attributed to the small deformations on the dry-surface, and hence greater degrees of stored skeletal forces. Upon the release of silica beddings, grains travelled the gap space and collided.

According to the microscopic observations, fast re-precipitation of silica (i.e. in a hot environment) formed spherical sub-rounded flocs (in agreement with Singh and Gilkes (1993)). These were accommodated in inter-particle trapdoors and macro-pore spaces. Flocs (Fig. 5.24) were highly porous and thus highly permeable.

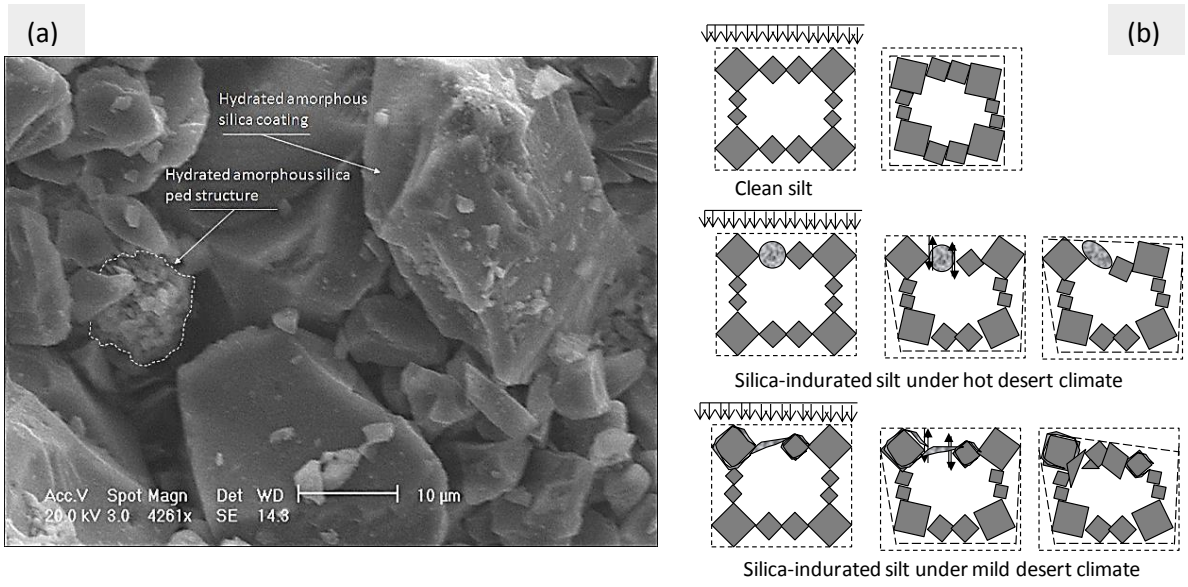

Fig. 5.24 Class E: (a) Horizontal alignment, silica-indurate silt in hot environment (b) Schematic view of collapse progression in silica-indurate silts

These carried larger skeletal forces than laminated silica units, as skeletal stresses were converted into compressive stresses carried on the flocs' spherical surface. Upon an increase in the stress level, grains rotated, and

hence shear stresses at the grains' contact points with stationary neighbouring flocs were developed. The stress was then conveyed to the adjacent out-of-plane grains through sets of compressive surface stresses. In contrast, slow re-precipitation of silica (under mild climate) formed laminated coat units. An overgrowth of coats generated buttress structures, which were much susceptible to shear failure (Fig. 5.24 and Fig. 5.25).

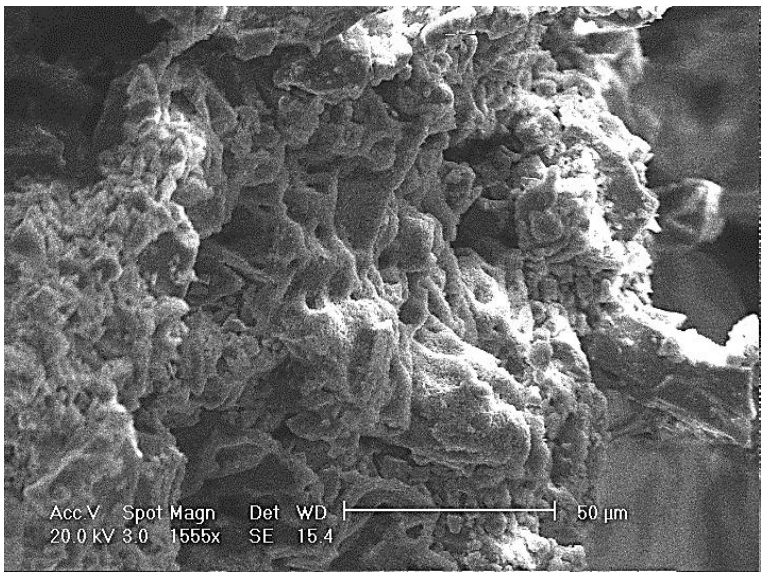

Fig. 5.25 Class F: ESEM image showing a vertical alignment of silica-indurate sulphated silt in mild environment

In presence of $[M - SO_4^{2-}]$ phases (Class F), sulphates bridged either fully hydrated $[H_4SiO_4]$ or partially hydrated $[SiO_2.OH]_n$ clusters: While neither Na^+, Ca^{2+}, and Mg^{2+} ions (M) could be exchanged with H^+ of hydroxyl tail (cation exchange), the [-OH] was released and replaced with $[SO_4^{2-}]$ via ligand exchange (anion exchange). The release of hydroxyl gave rise to the pH. The basic environment encouraged the de-protonation of the silica – sulphate chain. Consequently, donation of H^+ ion by the hydroxyls slightly decreased the pH. Presence of free Na^+ ions in the soil solution kept the environment slightly alkaline. The net negative charge of the resulting compound and the slight alkalinity of the soil solution needed to be balanced. Upon a second ligand exchange ([-OH] with $[SO_4^{2-}]$), and the sodium-oxygen bond formation, the charge was balanced and the environment attained a neutral pH (see Eq. 5.2-5.3)

$$\left[:\ddot{O}=Si\left|\begin{matrix}OH\\OH\end{matrix}\right.\right]^{\pm 0}+\left[\begin{matrix}.O-\overset{\overset{O.}{\|}}{\underset{\underset{O.}{\|}}{S}}-O.\end{matrix}\right]^{2-}+\dot{N}a\xrightarrow{yields}\left[:\ddot{O}=Si\left|\begin{matrix}OH\\O-\overset{\overset{O.}{\|}}{\underset{\underset{O.}{\|}}{S}}-O.\end{matrix}\right.\right]^{1-}+:\ddot{O}..H+\dot{N}a$$

$$\therefore pH\gg 7\xrightarrow{yields}\left[:\ddot{O}=Si\left|\begin{matrix}O.\\O-\overset{\overset{O.}{\|}}{\underset{\underset{O.}{\|}}{S}}-O.\end{matrix}\right.\right]^{2-}+:\ddot{O}..H+\dot{H}+\dot{N}a\qquad\therefore pH>7\qquad Eq.\ 5.2$$

$$\left[:\ddot{O}=Si\left|\begin{matrix}O.\\O-\overset{\overset{O.}{\|}}{\underset{\underset{O.}{\|}}{S}}-O.\end{matrix}\right.\right]^{2-}+\dot{N}a+O\left|\begin{matrix}H\\H\end{matrix}\right.+\left[O=Si\left|\begin{matrix}OH\\OH\end{matrix}\right.\right]^{\pm 0}$$

$$\xrightarrow{yields}\left[:\ddot{O}=Si\left|\begin{matrix}O..Na\\O-\overset{\overset{O.}{\|}}{\underset{\underset{O.}{\|}}{S}}-O..\underset{5}{\overset{OH}{\dot{S}i}}=\ddot{O}:\end{matrix}\right.\right]^{\pm 0}+:\ddot{O}..H\qquad\therefore pH\approx 7\qquad Eq.\ 5.3$$

Irrespective of sulphate content, higher degrees of compressibility occurred in mild environments. This, however, did not cause failure in connectors as instead packing re-arranged. Considering the control of kinetics on crystal quality, precipitation under lower temperatures allowed time for crystallization of O-Si-O rings. This was deemed responsible for the higher degrees of structural stiffness recorded on the dry-surface.

5.3.5 Class 'G' and 'H'

In the presence of clay, the role of amorphous silica relies on the relative abundance of clay. Based on the protocol developed earlier for clayey silts, three levels of clay content were investigated: slightly clayey, clayey and very clayey silts. The B1 class accounts for clay contents of less than 15% (10% as for representative testing specimen). The B2 class is associated with 15% to 30% clay content (15% inclusive with 20% as for representative testing specimen). The B3 class accounts for soils of more than 30% clay content (40% and 50% as for representative testing specimens). The micro-mechanism of collapse is modelled for each class. The silica-indurate clayey silts in a hot environment closely mirrors the natural deposits occurred in Russian steppe

landscapes (i.e. North Caucasus), which occurred with strongly salinized clay, containing chlorides, sulphates, magnesium and sodium.

5.3.5.1 [Metal-base Sulphated] Silica-indurate Slightly Clayey Silt

Generally, silica-indurate clayey silts were less compressible and less collapsible than clayey silts of identical stress history. Irrespective of sulphate content, collapsibility and compressibility in silica-bearing soils gained higher degrees in hot environments. Irrespective of weathering temperature, lower records of collapsibility applied to deposits containing sulphate phases.

The results were in a good agreement with the works of (Sokolovich, 1965, Sokolovich and Gubkin, 1970) on application of 'silicatization-carbonation method' to arrest the collapsibility in Russian loess. The injection of amorphous silica (re-precipitated silica gel) into the sulphate-bearing clayey silty loess under mild desert steppe climate was reported an appropriate approach to mitigate the collapsibility. The mechanisms that are responsible for such behaviour are discussed in detail below.

The kaolinite surface charge distribution is schematically illustrated in Fig. 5.26 and Eq. 5.4. Formulations also display the silica-kaolinite bonding mechanism at the diffused double layer level.

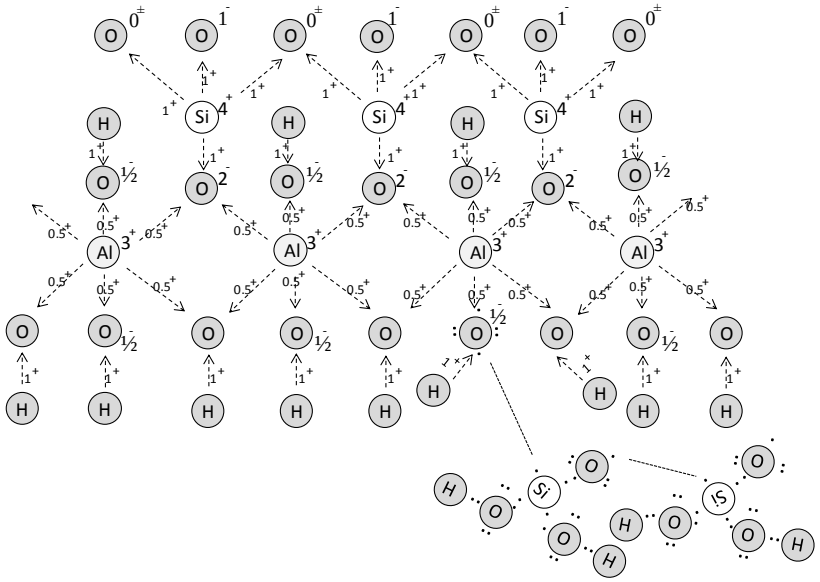

Fig. 5.26 Schematic of surface charge distribution of kaolinite clay: Lewis structure of orthosilicate anion sharing electron with the edge oxygen atom of aluminium octahedral unit (Si-O-Si-O rings)

Layers of stacked $H_4Si_2O_6$ orthosilicate anion share bond with a kaolinite Chrystal (see also (Tossell and Vaughan, 1992)). As demonstrated in Eq. 5.4 (dashed area), silicon cannot share covalent bonds in reality and hence carries a net negative charge, which allows it to share chains of Si-O-Si (also see Fig. 5.27).

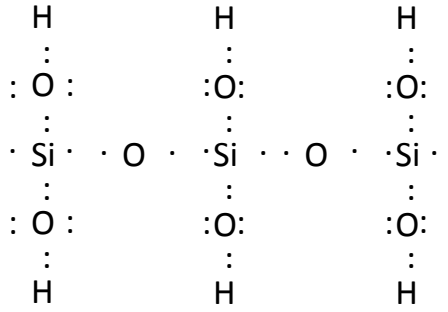

Fig. 5.27 Si-O-Si-O Rings on Lewis structure scale

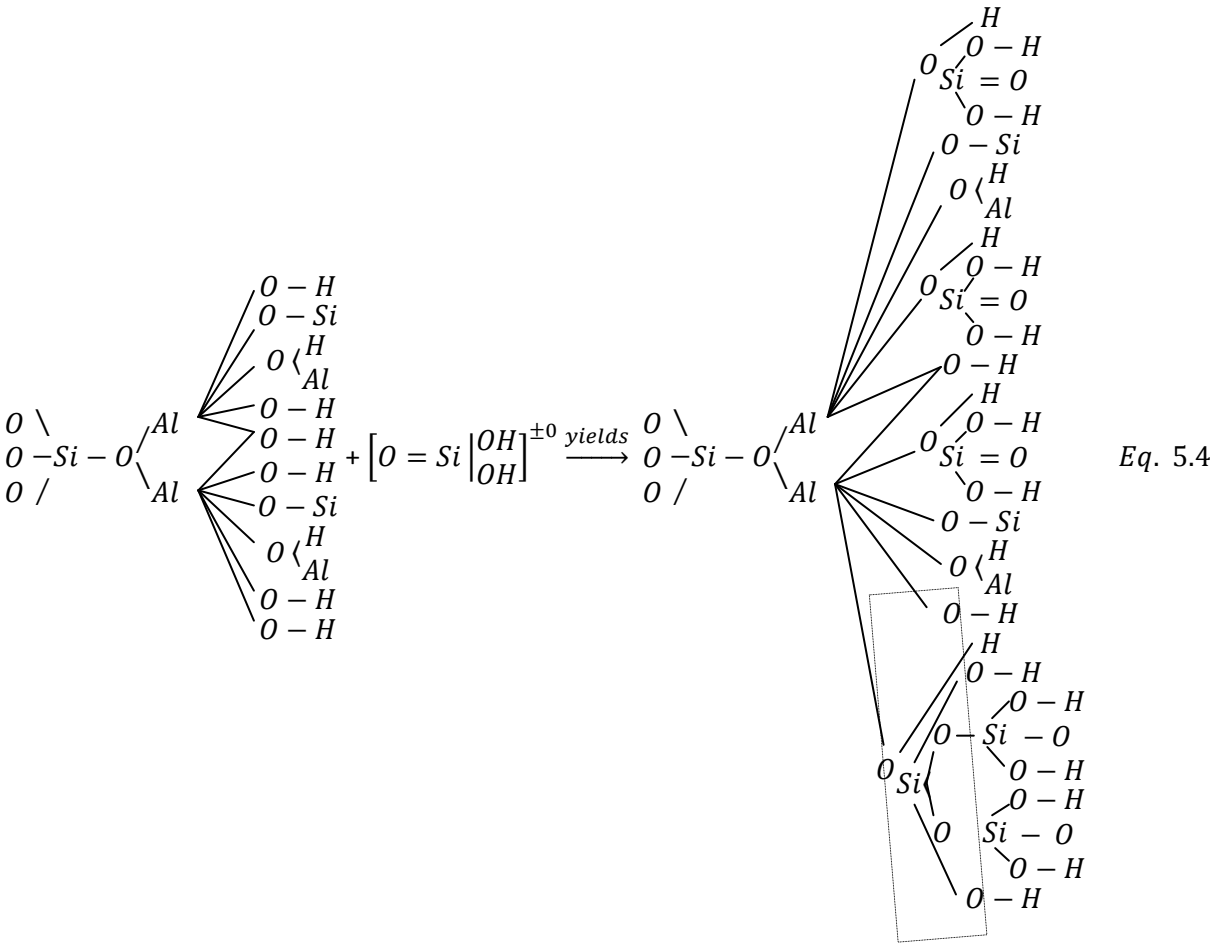

$Eq.\ 5.4$

The compressibility on both dry- and wet- stress surfaces declined in silica-indurate clayey silt. From a geo-chemical perspective, this refers to the

improved the structural stiffness through the formation of multi-layer silica-hydroxyl bonds (Eq. 5.4). From a physical perspective, accumulation of silica in inter-assemblage pore spaces (i.e. macro-pores) resulted in lesser degrees of void ratio loss.

Lower weathering temperatures provided a slower re-precipitation rate for silica. This let more Si-O-Si-O bonds to form, resulting in lesser void ratio loss upon net stress increase.

Lower weathering temperatures provided a higher abundance of Si-O-Si-O rings and therefore greater degrees of excess negative charge neutralization. Lesser negative surface charge decreased the liquid limit. Consequently, lower volumes of bulk water were needed to change the soil's state into plastic. Early shear failure of silica-indurate clayey bonds brought neighbouring grains into contact while the excess positive pore water pressure was not fully dissipated and hence the skeletal forces were not at their maximum value. Lower skeletal forces resulted in lower driving efforts and thus moderated the grain collision.

For silica-indurate LC loess with metal-based sulphate phases, compressibility and collapsibility were recorded slightly lower values than simple silica-indurate LC soils. The phenomenon was viewed from two different perspectives. Given the scarcity of kaolinite flakes, strong multi-layer silica-hydroxyl bonds gave rise to the dry stiffness. Bonds received even more strength after the clays' tetrahedral silicon tail shared its middle oxygen atom with dissolved cations. The cations themselves adsorbed free anions. Consequently, a poly-mineral connector shaped in which kaolinite-silica-kaolinite clusters (Fig. 5.28) were sandwiched between a layer of re-precipitated metal-based sulphates and chlorides (Fig. 5.29-5.30). High dry stiffness and low water solubility was recorded along the single oedometer tests, which further confirmed the significance of readily soluble salts stabilizing the void ratio.

From the second perspective, H^+ ions might have been released by exposing small amounts of kaolinite to water (Eq. 5.5). Interaction of acid silisic and kaolinite generated further H^+ (Eq. 5.6). The negative surface charge of clay

platelets tended to be balanced by adsorbing these free H^+ ions. This ultimately resulted in a reduction in liquid limit.

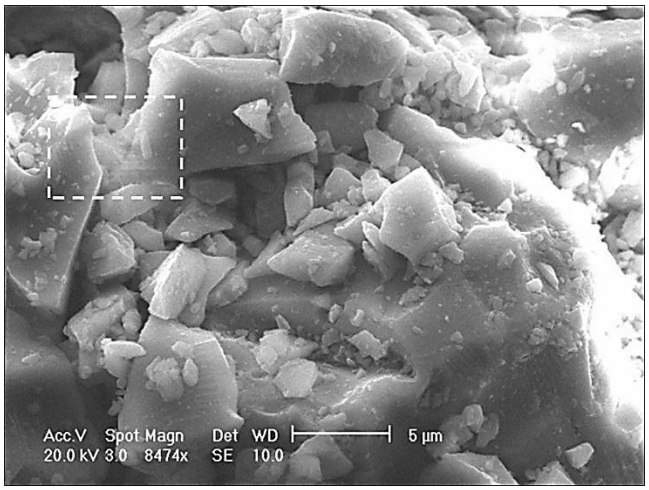

Fig. 5.28 Clay-silica-clay connectors between a pair of clay coated quartz silt

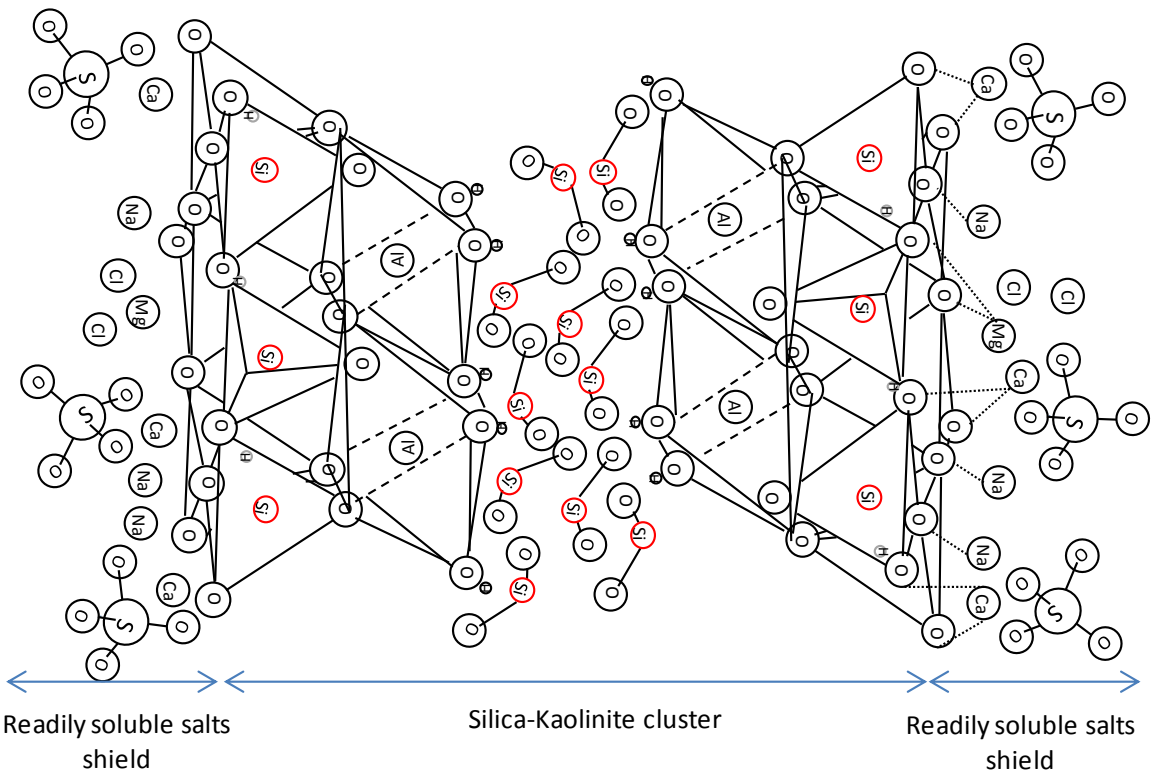

Fig. 5.29 Diagrammatic sketch of poly-mineral silica impregnated kaolinite – slightly clayey silt

$$Al_2Si_2O_5(OH)_4 + 5H_2O \xrightarrow{yields} 2Al(OH)_3 + 4H^+ + 2H_2SiO_4 \qquad Eq.\ 5.5$$

$$3H_2SO_4 + Al_2Si_2O_5(OH)_4 \xrightarrow{yields} 2SO_4^{2-} + 6H^+ + 2Al^{3+} + 2SiO_2 + O^{-2} + 4OH^- \qquad Eq.\ 5.6$$

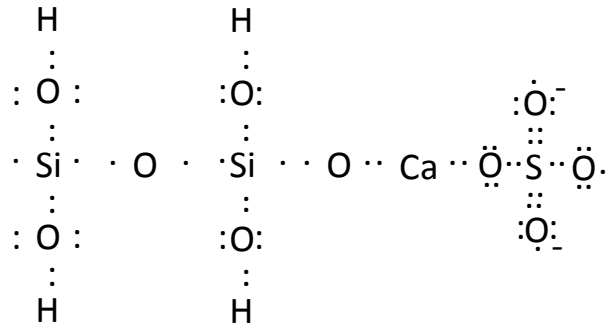

Fig. 5.30 Lewis structure of the Si-O-Si-O-M-Anion bonds

5.3.5.2 [Metal-base Sulphated] Silica-indurate Moderately to Very Clayey Silt

Silica-indurate moderately to very clayey silts were found more compressible and more collapsible than clayey silts of identical stress history. This is in contrast with silica-impregnated slightly clayey silts. Irrespective of sulphate content, collapsibility and compressibility was measured even higher in hot weathering environments.

However, with clay contents more than 45%, the soil state changed from a clayey granular to a clayey material with granules. For silty clays, an increase in weathering temperature reduced both compressibility and collapsibility. Furthermore, silty clays showed lower total consolidation settlements after impregnation with amorphous silica.

At >15% clay content and irrespective of the weathering temperature, collapsibility did not attain a regular trend against sulphate content. This was attributed to two simultaneous countering interactions between sulphates and clay system. Compressibility, however, took lower degrees in the presence of sulphate phases. This, however, did not apply to soils with clay contents beyond 45%.

Technically, no stand-alone amorphous silica cluster was found as kaolinite flakes hosted the entire impregnating polymers at their hydroxyl sites. A thin layer of silica therefore adsorbed the hydroxyl planes and weakly welded the neighbouring clay platelets together. The relatively low contents of silica and thus Si-O-Si-OH bonds allowed the silica to act as a hinge rather than a binding element. Silica polymers acted as hinges among stacked layers of clay

platelets, facilitating the particle re-arrangement in the absence of water. This gave rise to the void ratio loss through the densification of macro-pore spaces.

The presence of sulphates together with calcium, magnesium and sodium cations in clayey silt loess decreased the compressibility. This might be due to either the formation of Al-HO-Si-O-Si-O-M-Anion rings, or the formation of Al-HO-Anion-O-Al-O rings. Cations tended to absorb to silicon tetrahedral units (O-Si-O-M-Anion), as illustrated in Fig. 5.31 and Eq. 5.7.

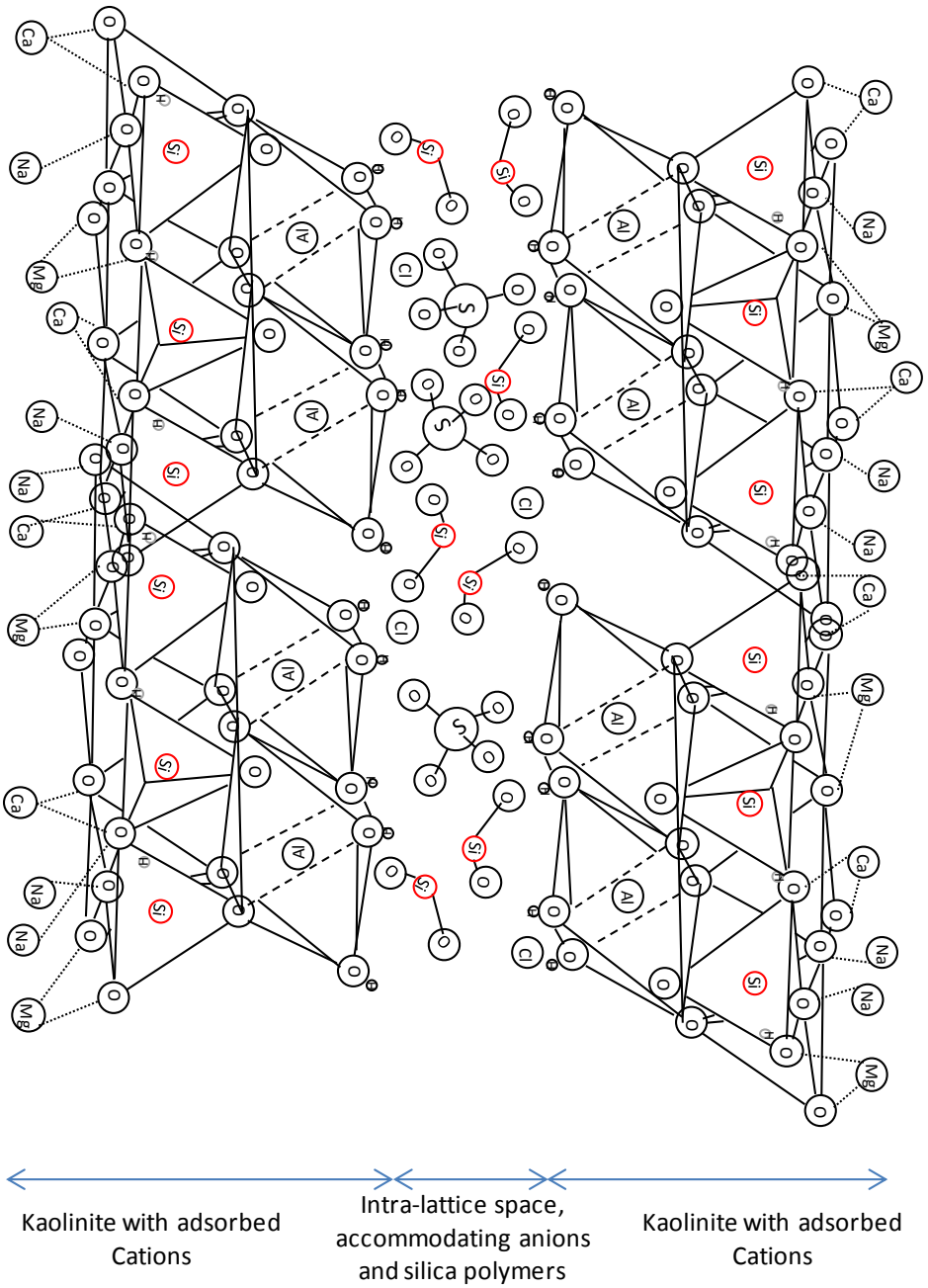

Fig. 5.31 Diagrammatic sketch of poly-mineral silica impregnated kaolinite - clayey silt loess

Such interactions justify the softening behaviour of Octahedral-anion-Octahedral rings in presence of water and in the absence of metal bonds. Water ingress allowed the formation of series of plastic hinges in intra-lattice space. Clay platelets slipped and migrated into the macro-pores. Sudden failure of trapdoors (i.e. connectors), brought the adjacent silts into contact. Collision and particle breakage led to further loss in macro-pores. The mechanism, however, was coupled with the mechanism discussed for LC soils, where Cations had a control on liquid limit and hence collapsibility. The two simultaneous mechanisms were deemed responsible for the lack of a regular collapsibility trend in presence of sulphate phases.

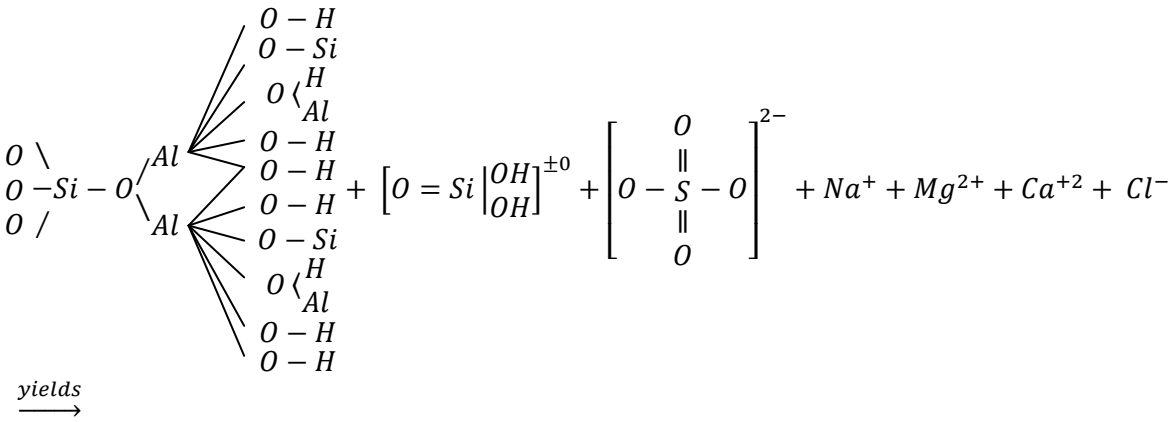

Eq. 5.7

5.3.6 Class 'I' and 'J'

In the presence of both clay and carbonates, the contribution of amorphous silica in collapse was investigated for three levels of carbonate contents. These are detailed in Table 5.1.

5.3.6.1 [Metal-based Sulphated] Silica-indurate Slightly Calcareous Clayey Silt.

Generally, silica-indurate calcareous clayey silts were found less compressible and more collapsible than calcareous clayey silts of identical stress history. Irrespective of sulphate content, silica precipitation (weathering) in mild environments resulted in lower compressibility and higher collapsibility than in hot (under high temperatures) environments. Irrespective of precipitation temperature, in presence of sulphate phases, lower degrees of compressibility and higher degrees of collapsibility were recorded.

The mechanical behaviour is a factor of the diagenesis of material. With deposits without sulphate phases, the zero-time air-fall deposited material comprised clay, silt, and Anhydrous Sodium Carbonate. The sodium content gave rise to the pH of the soil solution. As pH exceeded the point of zero net charge (PZNC), according to (Sudhakar and Sridharan, 1984), hydroxyl tails of clay commenced to donate protons. The release of H^+ allowed the deprotonated oxygen atoms to absorb the free Na^+. Formation of Sodium Aluminium Silicate hydrate zeolites ($NaAlSiO_4.H_2O$) implicated the Na-clay interaction (Fig. 5.32). Upon wetting by acid silisic, silicon ions also shared an electron with deprotonated oxygen atoms, forming Al-O-Si-O bonds. pH balanced. Soil then was enriched with Ca^{2+} ions; where aqueous $CaCl_2$ was introduced to solid anhydrous Na^+ CO_3^{2-} precipitates. Ca^{2+} replaced the Na^+ on tetrahedral unit due to its higher cation exchange capacity. This induced an excess positive charge, allowing the absorption of $-CO_3^{2-}$ anions. Hence, Calcium Carbonate nucleated on the surface of kaolinite clay (Fig. 5.33). Released Na^+ ion reacted with the free Cl^- anions to form Sodium Chloride precipitates (Fig. 5.32), coating the silica-indurate calcareous clayey connectors. The complex was less compressible than calcareous clayey silts as O-Si-O bonds assisted hydrogen

bonds within the clay intra-lattice space. Moreover, clay was sandwiched between a layer of Calcium Carbonate and Sodium Chloride. This provided much higher degrees of stiffness on the dry-surface. Hence, much of the macro-pore-spaces remained susceptible to collapse, with many of the carbonate and chloride coat units still intact. The 200 kPa stress level at which flooding took place provided high potential skeletal forces to crush the grains upon water ingress. This implemented the observed higher degrees of collapsibility than in calcareous clayey silts. Mild climates provided better quality of O-Si-O bonds, and hence improved the dry-stiffness and collapsibility.

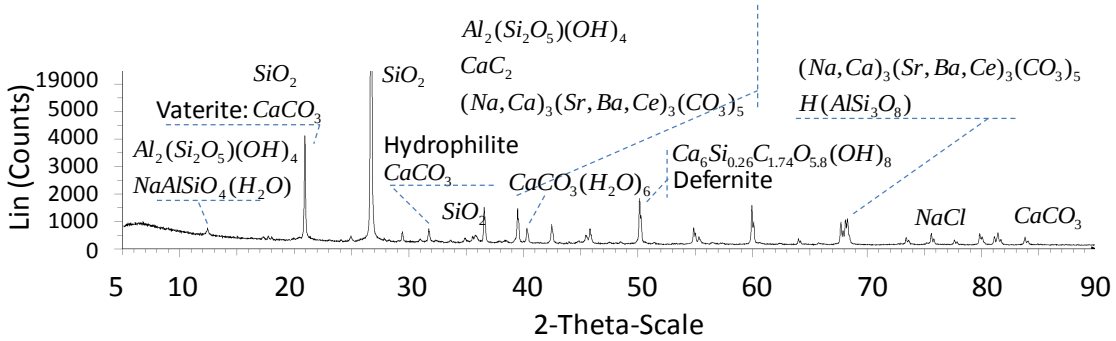

Fig. 5.32 XRD pattern showing Zeolite $NaAlSiO_4.H_2O$ (Specimen class IM1)

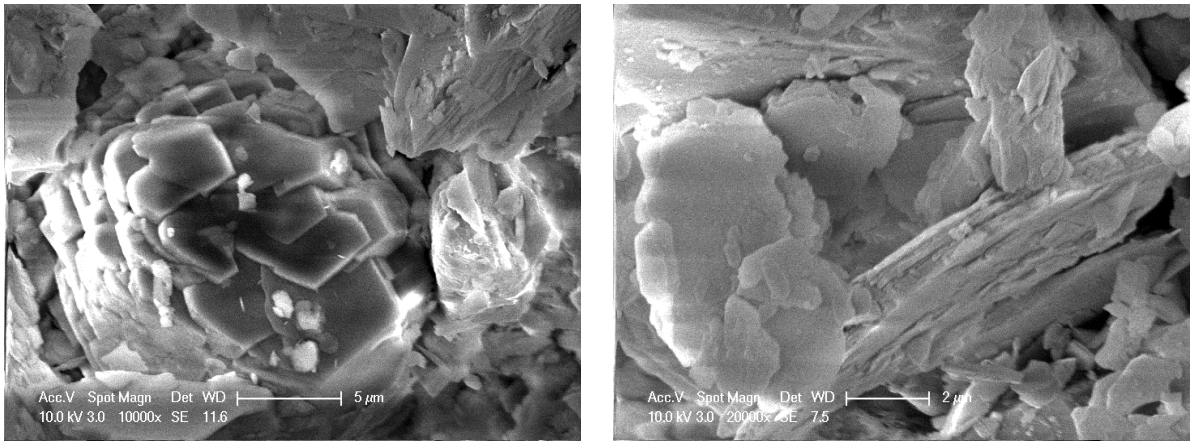

Fig. 5.33 Calcium Carbonate nucleation on kaolinite in electron microscopy image (left): carbonate nodules absorbed by the clay flake surface and overgrowth of carbonate tubular next to the clay laminated aggregate (right): Carbonates bonding with the clay platelets

The mechanism discussed in this section applies to deposits with and without sulphate phases. However, upon metal-based sulphate liquid ingress, ligand exchange took place between the hydroxyl tail of clay and sulphates. The consequent net negative charge was balanced with the formation of chains of anions, cations, and neighbouring clay platelets (Eq. 5.8 – last line). Lower

levels of compressibility and higher degrees of collapsibility in presence of sulphates were attributed to the contribution of the latter ligand exchange. The mechanism is schematically illustrated in Eq. 5.8.

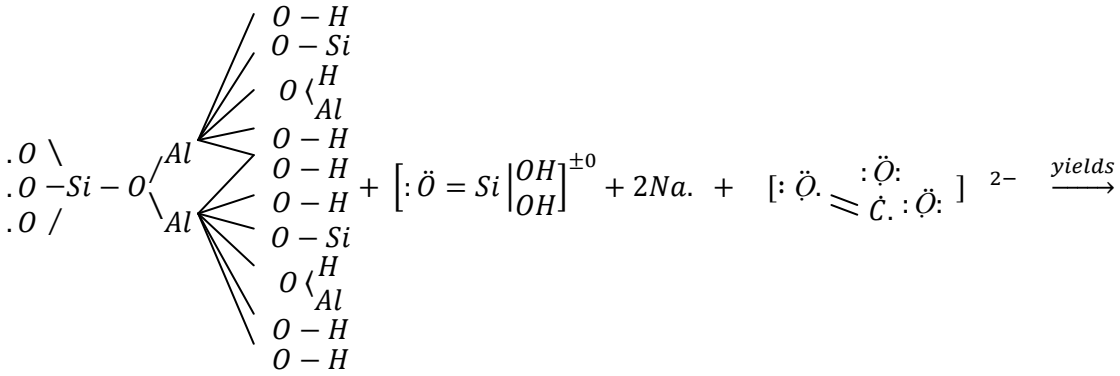

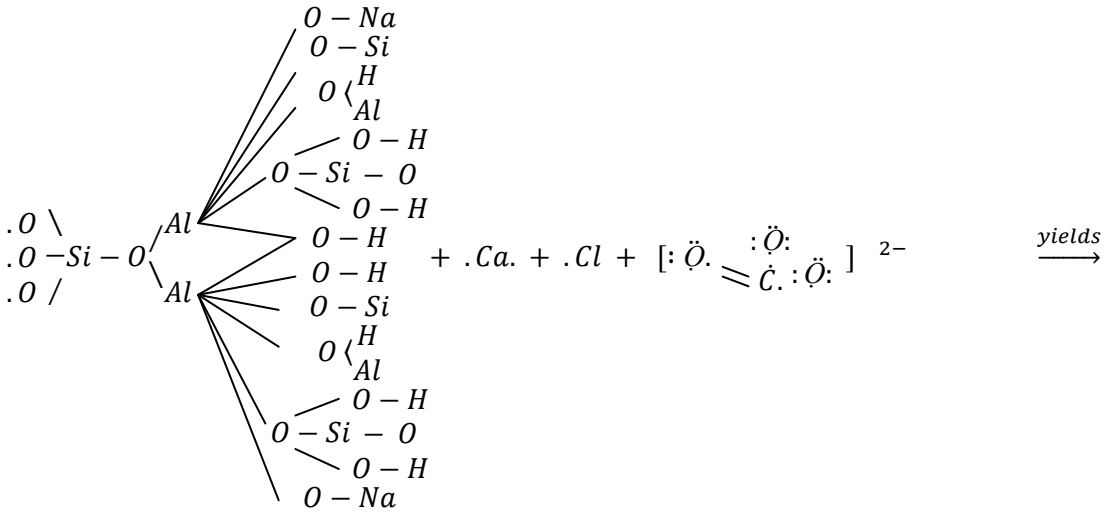

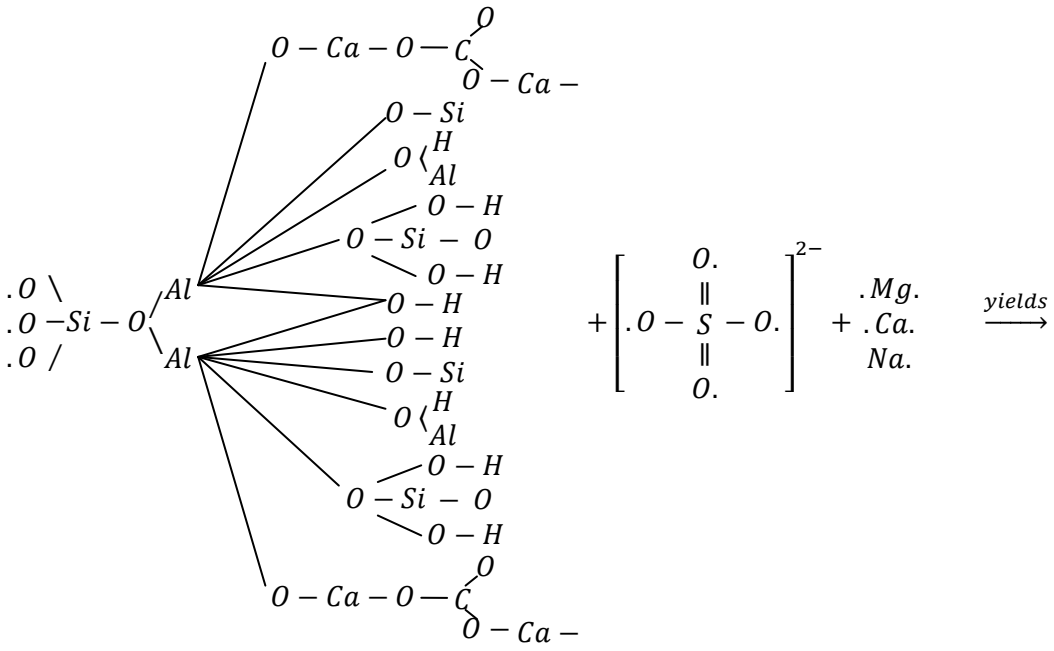

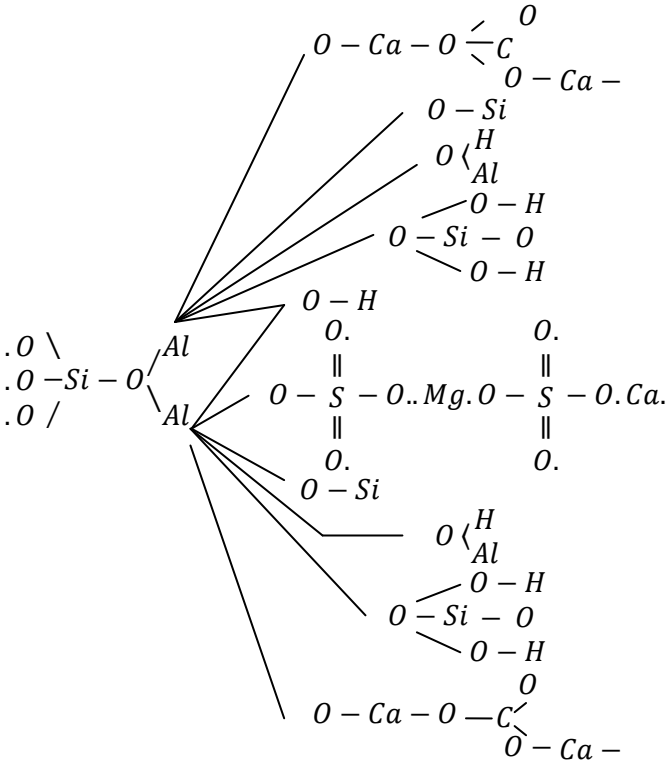

Eq. 5.8

5.3.6.2 [Metal-based Sulphated] Silica-indurate Moderately to Very Calcareous Clayey Silt

In contrast to silica-indurate slightly calcareous clayey silts, at higher carbonate contents, silica-indurate soils were found more compressible and less collapsible than identical calcareous clayey silts. Irrespective to the precipitation temperature (environment), presence of sulphate phases lowered the compressibility and thus gave rise to the collapsibility.

With reference to the outlined results, silicatization stabilization policies can only be applied to calcareous clayey silts, irrespective of the applying climatic condition.[45]

The bond formation mechanism is similar to what at low carbonate clayey silts. However, since Calcium Carbonate exceeded the kaolinite in content, less free -OH tails contributed in the chemical interaction. Silicon atom of $H_4Si_2O_6$ orthosilicates could not share electron with hydroxyls and instead, nucleated between clay platelets and carbonate clusters. This distracted the clay-to-

[45] Very calcareous deposits are excluded because the addition of amorphous silica at already high fine content (clay and carbonate) would enhance the consolidation settlement, which is not favourable in the engineering practice. This was observed in the present oedometer test results.

clay hydrogen and Van der Waals (Lal, 2005) bonds, clay-to-quartz electro-static and adhesion surface (Hardy, 1925) bond, clay-to-carbonate silicon bond, and carbonate-to-quartz crystal bonds. The distraction was responsible for the higher recorded degrees of compressibility. Consequently, upon potential skeletal stress relief, lower kinematic stress contributed in the collapse upon wetting.

In the presence of sulphates, basic salt polymers coated the connectors. The scarcity of free hydroxyl tails did not allow any chemical interaction to take place. This improved the dry stiffness through the formation of a polymer shield, while preserved much of the macro-pore spaces.

5.4 Chapter Highlights

This chapter proposed a new classification system for the fine-grained soils, ranging from basic silt to basic clay. The chapter then discussed the physical modelling results for the artificial material. The collapse mechanism was described in the framework of the principle of effective stress, which was developed in Chapter 4. To describe the chemical interactions among clay, carbonate, silica, and sulphates, Lewis structure analysis was utilized.

This chapter showed that a change to the relative content of major and minor clay-sized cements (made up of various minerals) as well as the placement and in-situ climate can remarkably affect the soil's mechanical properties. This is due to the complex chemical interactions occurring between clay-sized minerals, which control the strength and the erodibility of poly-mineral cements in soil. To relax the limitations with the current soil classification practice, geo-chemical indices of cements were aimed to be considered in the fine-grained soils' classification in addition to the conventional grain size criteria. A novel classification system was proposed, for engineering purposes, which in particular address the problematic collapsing soils, as well as inactive swelling clays. Standard testing methods are suggested to be undertaken for to explain the field logging output in meaningful geotechnical soil classes.

According to the oedometer test results, clean silt is compressible (i.e. crushable). The addition of Calcium Carbonate to the silty matrix remarkably decreased the compressibility (to lower degrees than that of the addition of same content of clay caused), at the expense of a significant increase in collapsibility. The higher the clay content, the more the clayey silts exhibited collapsibility. Carbonates had the same effect, except with moderate contents of carbonates, at which collapsibility first decreased but then climbed back with increasing carbonate content. Among the various combinations, the maximum collapsibility occurred at 10-15% clay content and about 20% carbonate content. In general, increasing carbonates and/or clays reduced the compressibility. Both compressibility and collapsibility, however, dropped with carbonate content when the soil composition changed into the fine-grained zone (silt content approaching 45-50%). Work on silica-indurate specimens and Lewis structures analyses showed that Silicatization (classic Russian ground improvement technique – see Chapter 2) could be effective in stabilization of sulphated slightly clayey silts under mild climate conditions. The technique can be used with cautious for slightly clayey silts in mild environments, silty clays (clay>45%) in hot environments, and clayey calcareous silts in the absence of sulphate phases. Calcium Carbonate implant in silty clays and clayey soils restricts the collapsibility and improves the compressibility. Generally speaking, carbonate implants in clayey calcareous silts restricts the collapsibility.

The mechanisms are used to assess the current practice in more details and to develop individualized mitigation techniques in Chapter 6.

Chapter 6 | LEVEL III: ENGINEERING PRACTICE – EARTHWORK STRATEGIES

6.1 Introduction

This chapter demonstrates, through a case study, the application of the fundamentals established in Chapter 4 and collapse micro-mechanical modelling presented in Chapter 5 to engineering practice.

This Chapter is arranged in the below order:

1. Predictive contours of collapse/swell for Quaternary fine-grained soils (class A to J) as well as kaolinite soils (class K)
2. Identification of constraints to compaction practice
3. Earthwork design to overcome the constraints to the common practice for soil classes A, B, C, D and K.

The oedometer test results discussed in Chapter 5 were used to develop predictive contour plots. For soil class A and B, outputs of coupled oedometer - standard compaction (BS1377-4, 1990, ASTM:D698-12, 2012, AASHTO T 224-01, 2001) experiments were employed to assess the efficiency of the common practice. The results were interpreted by both fundamental and micromechanical modelling outputs (discussed in Chapter 4 and 5). These outputs were also used to criticize the current compaction practice in soil classes C and D (Charles and Watts, 2001). Finally, modelling outputs were used to design modified water treatment - grading change - densification schemes as well as a tentative chemical modification - gassing scheme, which is expected to mitigate the collapsibility permanently. These are seen as tentative solutions to overcome current limitations with (1) (BS-EN-ISO-14688-2:2004, 2007), (2) (BS EN 1997-1:2004, 2004), (3) (BS-6031:2009), and (4) (SHW600, 2009) codes. Finally, a case study example is detailed to show how the proposed tentative earthwork guideline can be practically applied.

The guideline is illustrated in Box 6.1.

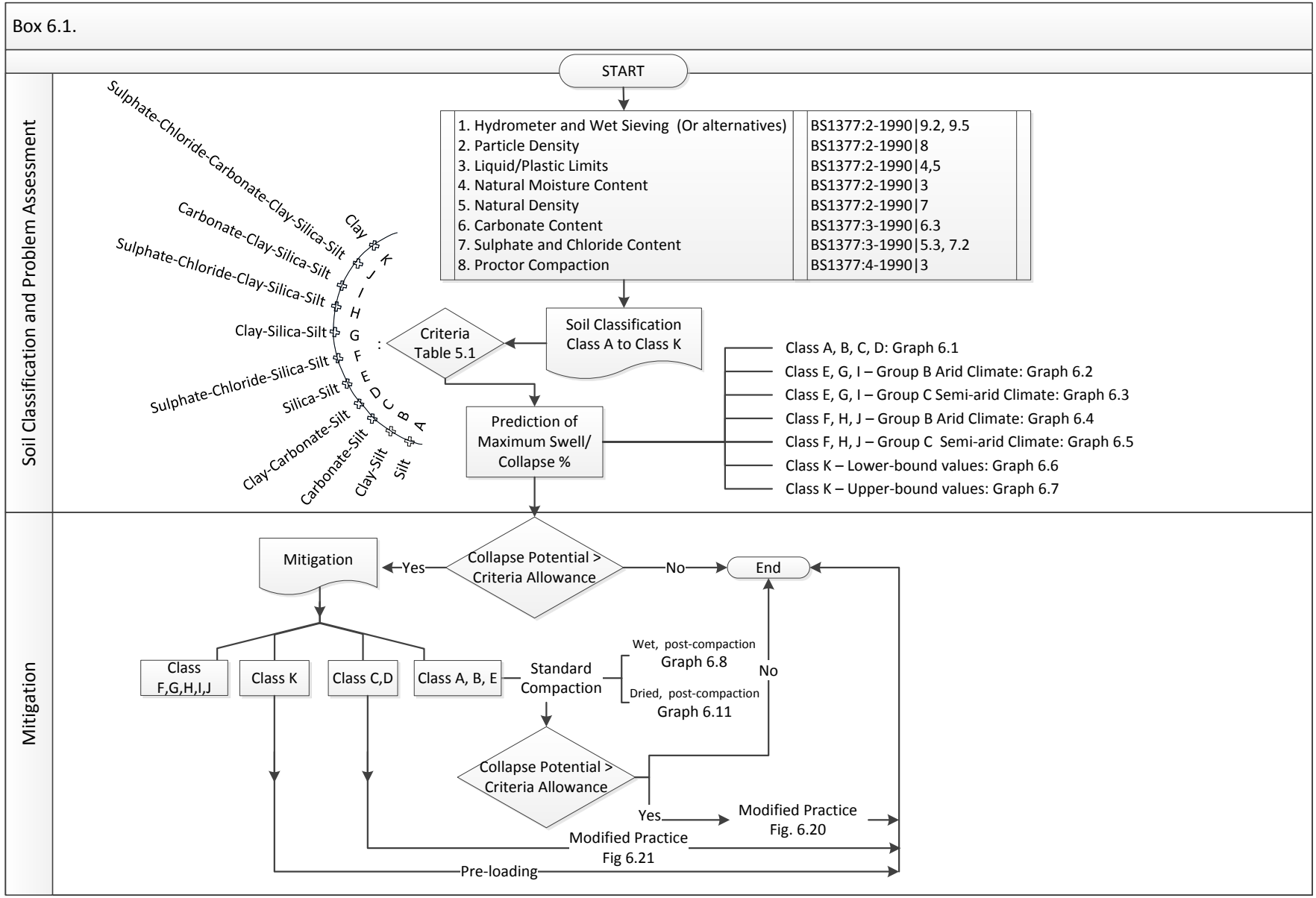

Box 6.1 Proposed pathway for ground investigation and improvement for fine-grained fills/lands

6.2 Prediction

A suite of diagrams are presented in this section to allow engineers to estimate the volume change potential in the absence of specific tests in naturally occurring fine-grained soils. Collapsibility in unweathered aeolian soils (class A, B, C, and D), and weathered aeolian soils (class E, F, G, H, and I) as well as kaolinite clay (class K) are plotted against the constitutive properties: with aeolian soils, collapsibility is plotted as a function of naturally occurring void radio, clay, silt, and carbonate content. With clayey soil, collapsibility is plotted as a function of embedment depth (i.e. total vertical stress) and placement water content. Collapsibility in clay spanned lower-bound values to upper-bound values, depending on the in-situ conditions.

With silica-indurate non-calcareous soils (Class G and H), the database used to generate the contour lines (Fig. 6.2-6.5) includes the collapse potential values of clayey silt specimens at four clay contents, representing the three classes of lightly-, moderately, and very clayey soils (Table 5.2). Likewise, with silica-indurate calcareous soils (Class I and J), the database used to generate the contour lines (Fig. 6.2-6.5) includes the collapse potential values of clayey calcareous silt specimens at three carbonate contents, all containing a fixed 10% of clay fragments, and representing the three classes of lightly-, moderately, and very calcareous soils (Table 5.2). Since the core aim of the present study was to explain the collapse mechanism in engineered and systematically classified fine-grained soils through such trends (Fig. 6.2-6.5 and Sections 5.3.4 to 5.3.6 of Chapter 5), the collapse potential values for other points (gaps in Fig. 6.2-6.5) remain to be determined, although the general trends are expected to remain the same. This is due to the prime contribution of clays and carbonates in the collapse. Kaolinite and carbonate contents are plotted against the normalized collapse potential for aeolian deposits in Fig. 6.1-6.5.

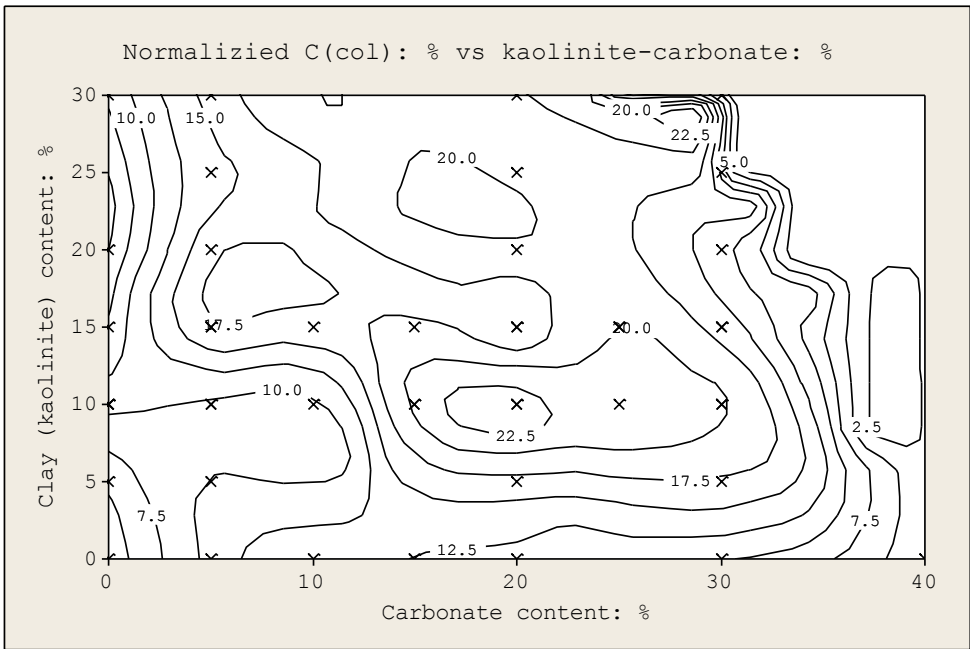

Fig. 6.1 Normalized Coefficient of Collapsibility against clay and carbonate content in soil class A, B, C and D

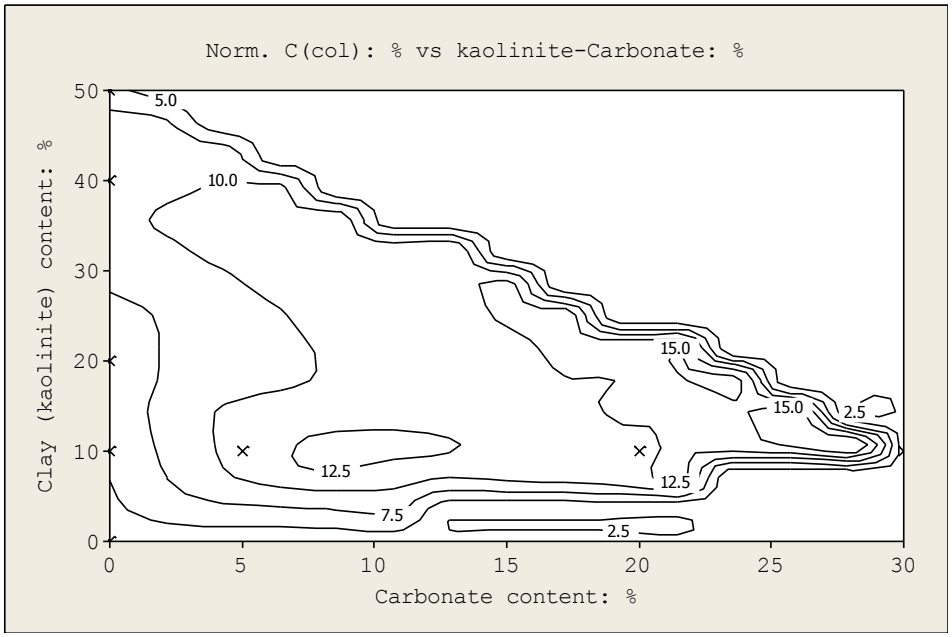

Fig. 6.2 Normalized Coefficient of Collapsibility against clay and carbonate content in soil class E, G, I under hot climate (see Table 3.7 and Table 5.1) conditions

When present, combination of kaolinite and carbonate bonding materials contribute to the collapse behaviour in a complex way depending on the predominant bonding material (Chapter 5). It is therefore important to determine the dominant chemical component of the clay-size fraction. There is a strong support in Fig. 6.1 for the view that the dominant component of clay-grade particles in loess takes charge of its behaviour. For a sample consisting of 15% carbonates, high contents of collapsibility appeared (Norm. C_{col}=10-15% - also see Fig. 5.11 in Chapter 5) at 0% clay. With a sufficiently

strong bond structure provided by the congregated carbonate tubular units, an increase in net stress to 200 kPa was not followed by significant loss of void spaces and therefore, higher contents of collapse volume change occurred (10-15% normalized collapsibility) in the event of wetting, releasing much of the great stored skeletal forces. With an increase in clay content to 10% (Class D2 material – See Table 5.1), clay fragments at macro-pore space provided increasing lateral support to surrounding grain-carbonate-grain chains. This slightly decreased the pre-wetting compressibility at the expense of increasing collapsibility. Increasing clay content, however, led to the accumulation of more clay fragments at macro-pores and hence less room for solids to accumulate after wetting. Less air-filled macro-pores led to the decreased collapsibility for clay contents exceeding 13%. For clay contents greater than 15%, clay fragments radiated to grain contact points, forming clay bridges covered with carbonate encrusting units. Given the pronounced contribution of clay to structural stiffness, an increase in clay content gave rise to collapsibility (see Fig. 6.1 for clay contents between 15 to 25% when Norm C_{col} ranges from 15 to 25%). At 25% clay and 15% carbonates (40% cement), any further increase in the clay content led to a decrease in collapsibility. This was due to the formation of matrix fabrics instead of porous granular matrix, and transformation of soil from clayey silt to silty clay, which decreased the collapsibility, and remarkably increased the consolidation.

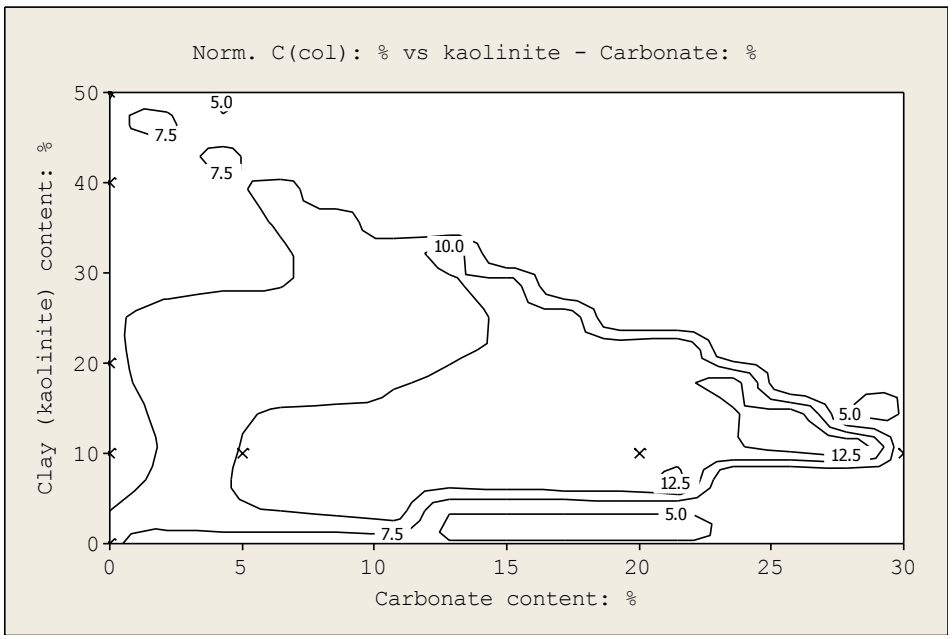

Fig. 6.3 Normalized Coefficient of Collapsibility against clay and carbonate content in soil class E, G, I under mild climate (see Table 3.7 and Table 5.1) conditions

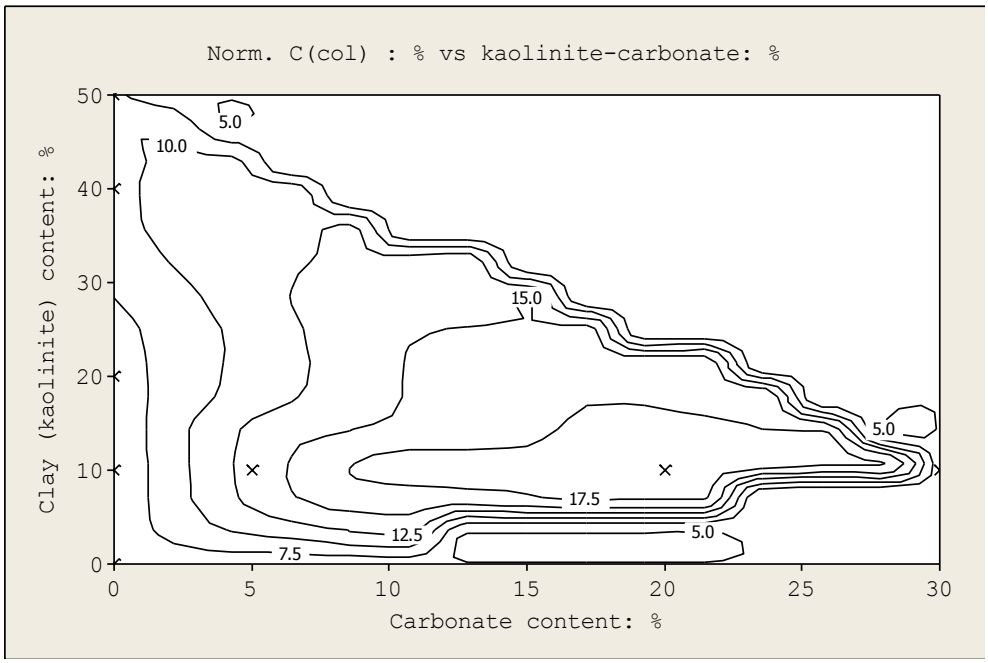

Fig. 6.4 Normalized Coefficient of Collapsibility against clay and carbonate content in soil class F, H, J under hot climate (see Table 3.7 and Table 5.1) conditions

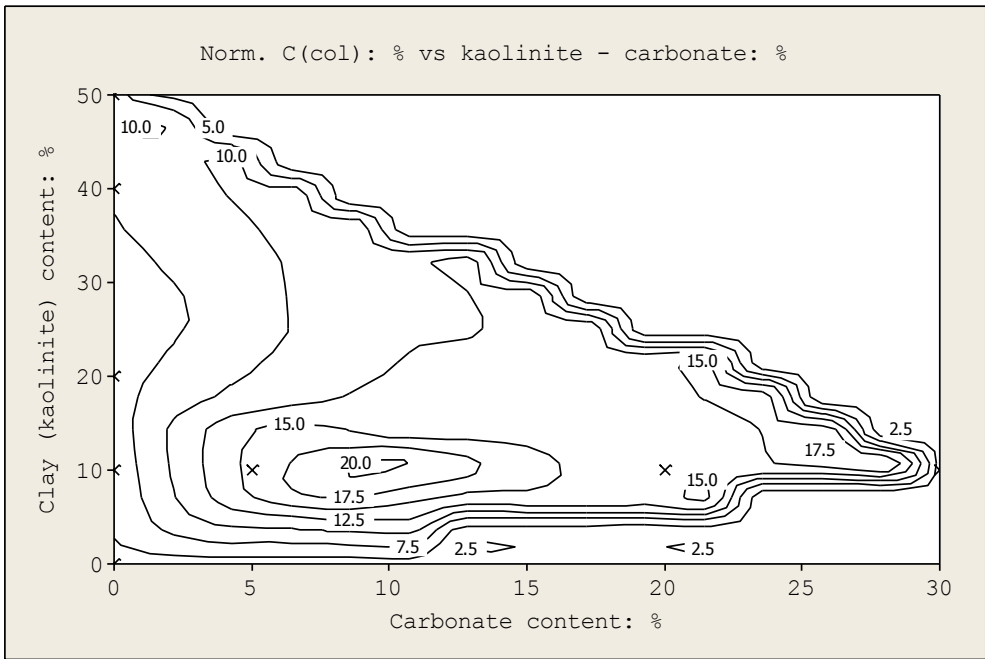

Fig. 6.5 Normalized Coefficient of Collapsibility against clay and carbonate content in soil class F, H, J under mild climate conditions

Collapsibility in kaolinite (i.e. the minus values of swelling potential occurring at 200 kPa effective stress and low water contents of 0-5% as well as high water contents of 40-45%) spanned lower-bound values as in Fig. 6.6 to upper-bound values as in Fig. 6.7, depending on the in-situ conditions. Increasing placement pressure (and hence dry density) led to greater swelling

potential. This increase was more marked in dried kaolinite specimens. Implementation of low compressive effort (i.e. 200 kPa) and low placement water content (i.e. about 5%) led to the formation of a collapsing structure in both wet and dry specimens. Similar collapsing structure formed at high placement water content (i.e. 40-45%) when specimen was dried.

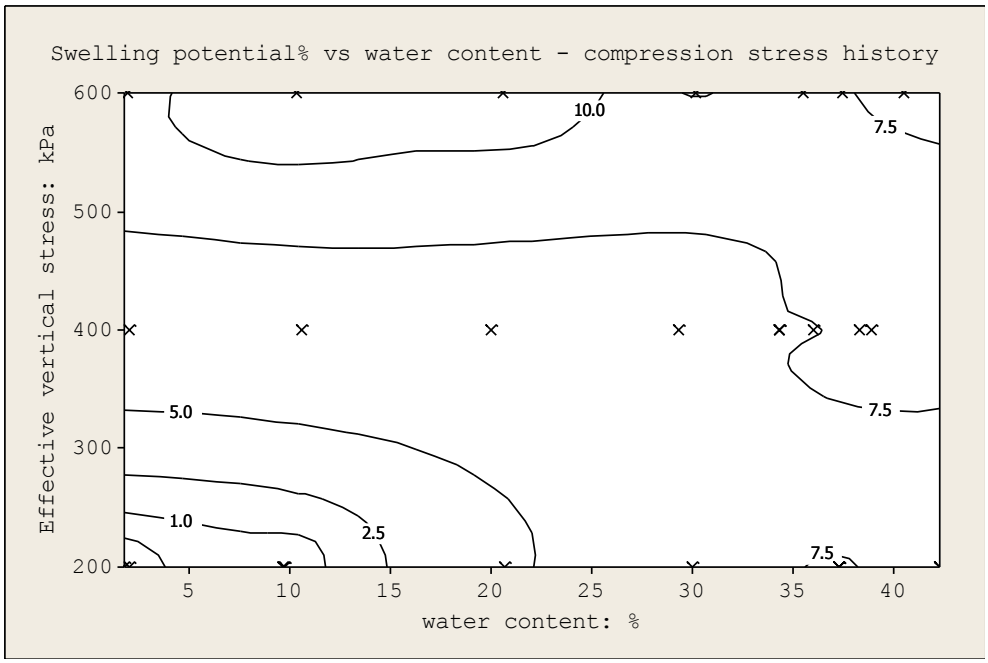

Fig. 6.6 swelling potential against effective stress (σ'_v) and water content: minimum values for equal in-situ and present-day water contents

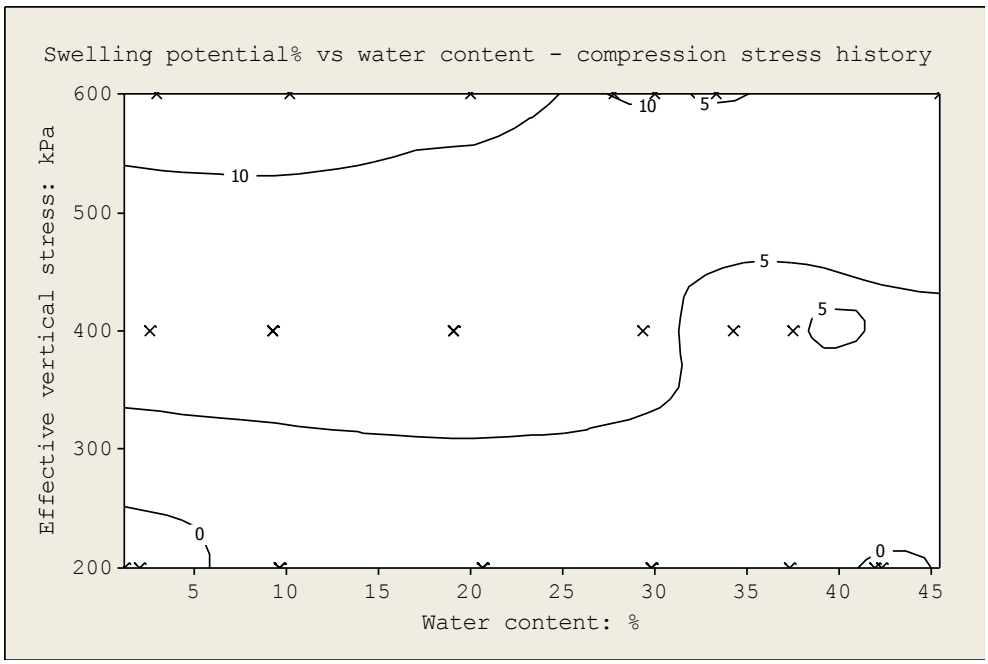

Fig. 6.7 swelling potential against effective stress (σ'_v) and water content: maximum values for drying conditions under in-situ state

6.3 Constraints to the Common Compaction Practice

6.3.1 Non-Calcareous Fines

According to BS-6031:2009, the most commonly practiced criteria in composite fills is pre-consolidation (also BS-EN-14688-2:2007), densification or pre-loading (Jefferson et al., 2005). However, efficiency of these techniques is a factor of compaction water content, post-compaction water content, clay content, climate, and the loading environment (Charles and Watts, 2001).

6.3.1.1 Compaction Water Content

Coupled compaction-oedometer experiments revealed a <1% residual collapse potential ($C_{col} = \left(\frac{e_{i+1} - e_i}{1 + e_i}\right) \times 100$ upon wetting at 200 kPa) in clayey silts compacted through the standard proctor practice at varied compaction water contents (Fig. 6.8). Residual collapsibility took higher degrees on the dry side of the proctor curve. This weak response appeared again in Fig. 6.9, where compressibility increased with decreasing compaction water content on the dry-of-optimum tail. This was previously observed in micro-mechanical models (Chapter 5), where compressibility increased with a decrease in the 'compaction water content' below $S_{r(comp)} = 15\%$ (Fig. 6.10). This is due to the delayed mobilization of capillary forces at low water contents (Fig. 4.35).

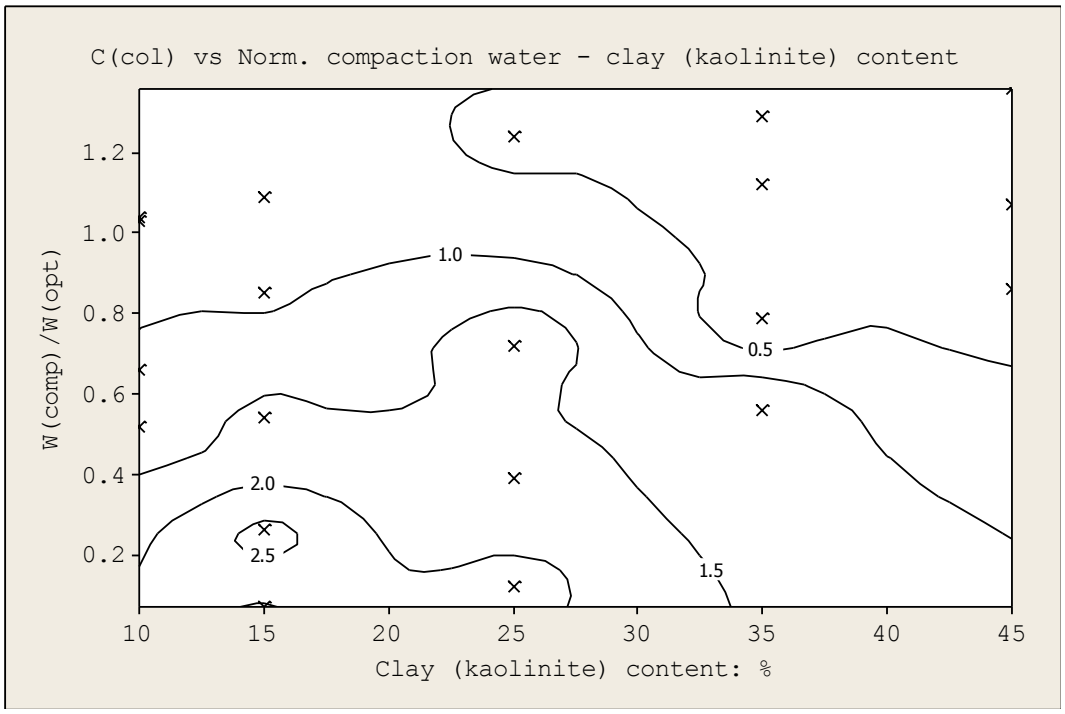

Fig. 6.8 Coefficient of Collapsibility C_{col} for $\omega_{in-situ} = \omega_{Compaction}$

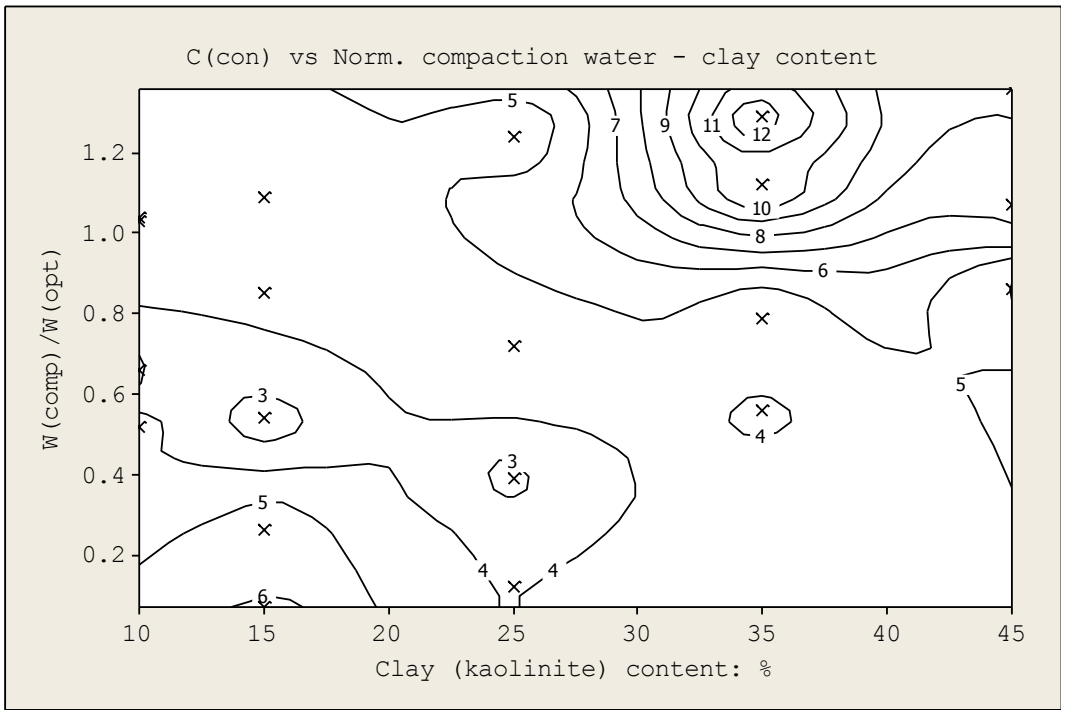

Fig. 6.9 Coefficient of Contraction C_{con} (200 kPa) for $\omega_{in-situ} = \omega_{Compaction}$

To recap, at optimum water content, compaction results in less than 1% collapse potential. Wet-of-optimum compaction would not increase the collapse potential. Dry-of-optimum compaction however increases the collapse potential from 1% to 3%, particularly for <25% clay content and $\omega_{Comp}/\omega_{opt}$ < 0.4.

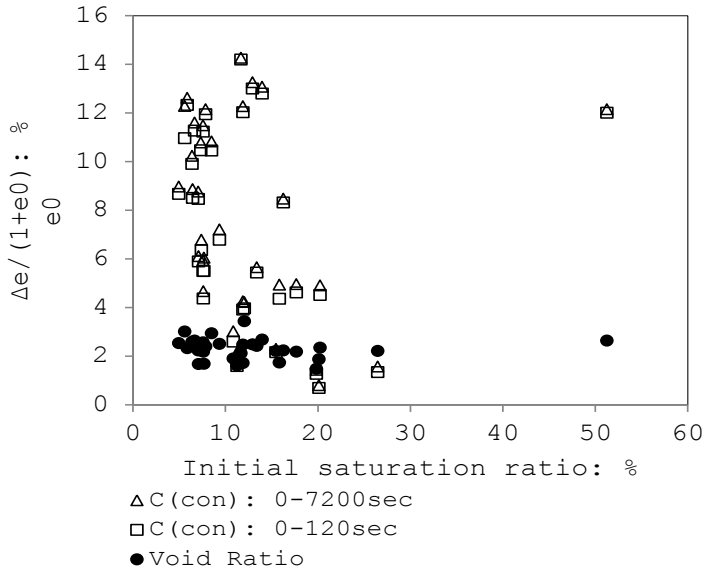

Fig. 6.10 Deficiency of compaction at sub-25% saturation ratios to minimize the air volume (AV), at 0 to 30% carbonates, 10 to 30% clay, and 45 to 90% silt

6.3.1.2 Clay Content

Fig. 6.9 showed a compressible zone ($C_{con} > 6\%$) at 15% clay content on the dry-of-optimum curve. This agrees with the output of micromechanical modelling (Chapter 5 – Class B), which showed that the soil's structure gains considerable stiffness between 15% to 25% (higher end) clay content (which may promote the resistance against the applying compaction forces). Clay forms strong connectors and supports the volume of macro-pores. Earlier, (Miller, 2002) reported negligible void ratio loss in clayey silts (see Section 2.3.2 for specimen preparation method) containing 10-15% (lower end) clay content upon loading to 200 kPa under dry conditions. Optimum compaction failed to tackle the compressibility at >25% clay contents (Fig. 6.9). This is due to the silt-with-clay replacement, which decreased the overall stiffness.

In Fig. 6.8, the residual collapsibility in compacted soils at the optimum water content decreased in specimens containing >25% clay content. This is in agreement with collapse models (Chapter 5 – Class B3), since clay radiates from contact points into macro-pores (Fig. 5.5 and Eq. 4.24). From a micromechanical perspective, reduced collapsibility at elevated clay contents can also be attributed to the contribution of skeletal force contribution. This is explained through the stress distribution DEM outlined earlier in Chapter 4, where the skeletal force equals: $\sigma'.f\{e,d\} = \sigma'.\frac{\pi}{2}d^2.A.exp\left(B.e + C\sqrt{e}\right)$. For d=$d_{50}$, an increase in the clay content reduces the void ratio and d_{50}. Although $A.exp\left(B.e + C\sqrt{e}\right)$ increases, $\frac{\pi}{2}d^2.A.exp\left(B.e + C\sqrt{e}\right)$ decreases. Hence, at a constant σ', $F_{(N)ske}$ and consequently the skeletal forces (potential stress stored in grains before wetting) decreases. On the other hand, the contribution of grain crushing is also evident. Lower $F_{(N)ske}$ supply lower energy inputs to grains (see Section 4.2), which leads to a lower Hardin's B_r index, and hence less crushing in grains. From the effective stress principle viewpoint, drag forces (a factor of clay content) also play a key role. The force was formulated in Chapter 3 as $3\pi \times 10^{-3} \times d \times \frac{K_i \times i_i}{n_i}$. For d=$d_{50}$, as increase in clay content reduces the d, K_i and n_i consequently decrease. Consequently, a higher content of clay constituent results in lower degrees of wetting-induced drag force, for a given hydraulic gradient. A lower drag force produces a lower collapse potential.

6.3.1.3 Post-compaction Water Content

Coupled compaction-oedometer experiments showed a maximum of 3% normalized collapse potential in specimens compacted at the optimum water content, for <20% clay contents (Fig. 6.8). Collapse potential increased after drying (Fig. 6.11), to values as high as 4-5% for 25 to 40% clay contents. Fig. 6.12 shows the pre-wetting compressibility for the similar drying condition.

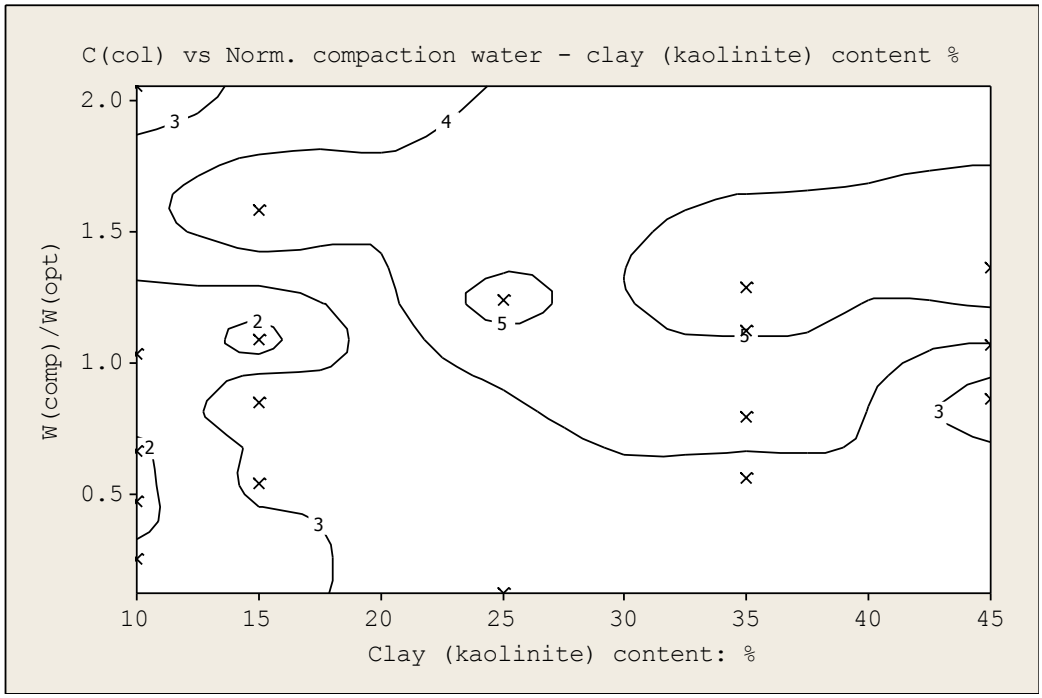

Fig. 6.11 Coefficient of Collapsibility C_{col} for $\omega_{in-situ} < \omega_{compaction}$

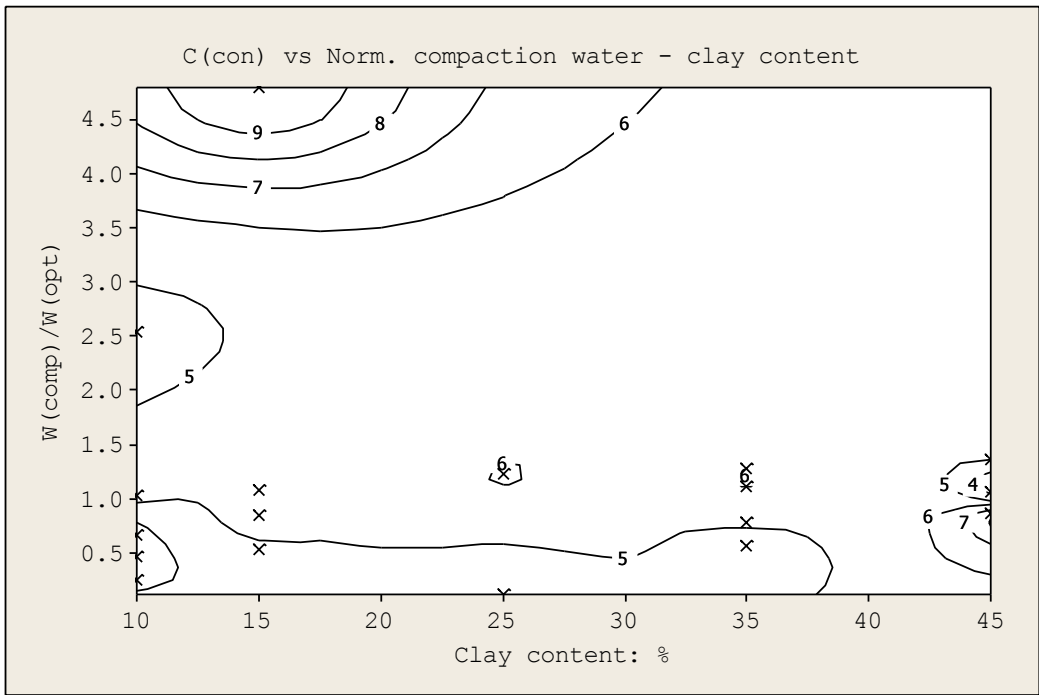

Fig. 6.12 Coefficient of Contraction C_{con} (200 kPa) for $\omega_{in-situ} < \omega_{compaction}$

It is evident that for >30% clay content, wet compaction of fines might be ineffective, when dry conditions apply (Fig. 6.11). This agrees with the 2007 work of the author (Assadi, 2007) on residual clayey sandy silts containing 30% clay content (PI=38%) and residual moderately plastic sandy silty clays containing 55% clay content (PI=41%). In Fig. 6.13, the state of 17 soil specimens compacted on dry and wet sides of the standard proctor curve is illustrated. Among the specimens two identical specimens (PI=41%, clay=30%) are presented in bold marks, representing 60% and 96% saturation ratio at the void ration of 0.83. For 30% clay content, wet of optimum compaction resulted lesser residual void space volume. This is in agreement with increasing compressibility for higher compaction water content for clayey silts at 0 to 30% clay content in Fig. 6.12. On contrary, greater volume of residual voids were observed at wet of optimum compaction state in specimens at >30% clay content (Fig. 6.14b). This is in agreement with enhanced collapsibility of wet of optimum compacted specimens when clay content exceeds 30% (Fig. 6.11).

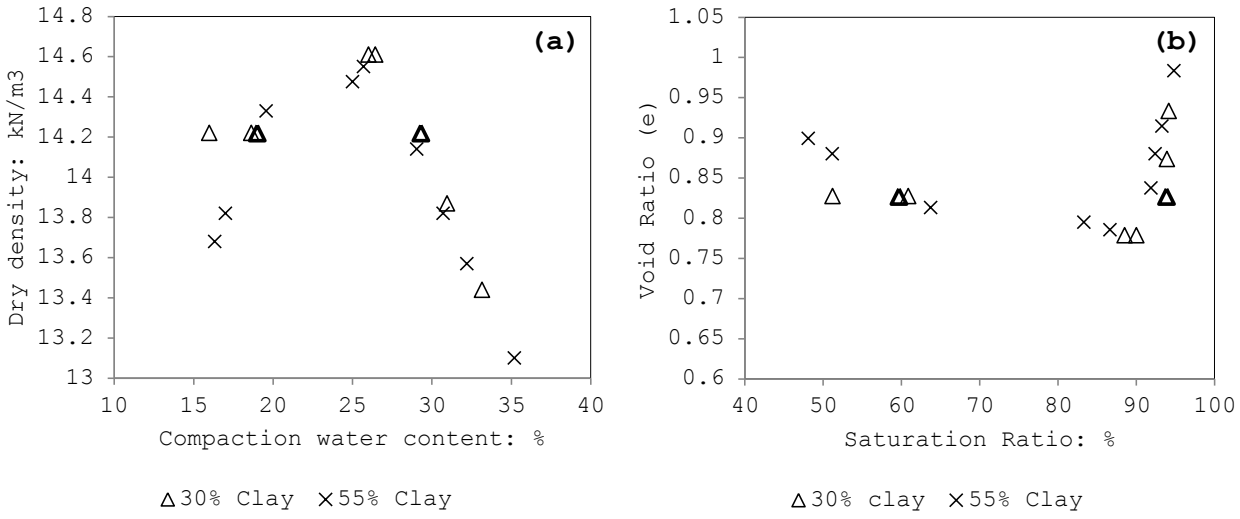

Fig. 6.13(a) Testing specimen pair on the proctor compaction curve, (b) Testing specimen pair on the void ratio – saturation ratio space

6.3.1.4 Climate

The modified effective stress principle developed for clayey silts in Chapter 4 suggests that void ratio increases in flooded and collapsed loess upon subsequent wetting-drying cyclic events. Self-weight flooding therefore may fail to fully remove the collapse risk in the long-term.

6.3.1.5 Loading Environment

With composite fines (<60% clay), consolidation of the subgrade is a well-practiced improvement scheme (BS-6031:2009). This reduces the soil's compressibility ($C_c = -\frac{\Delta e}{log\left(\frac{\sigma' + \Delta\sigma'}{\sigma'}\right)}$, see (BS-EN-ISO-14688-2:2004, 2007)) under an upper-bound stress level, which is slightly lower than the treatment (consolidation) stress. To examine the effectiveness of the consolidation practice in transient loading environments, this section looks into the variation of clayey silt stiffness with clay content (kaolinite) and the number of loading-unloading cycles.

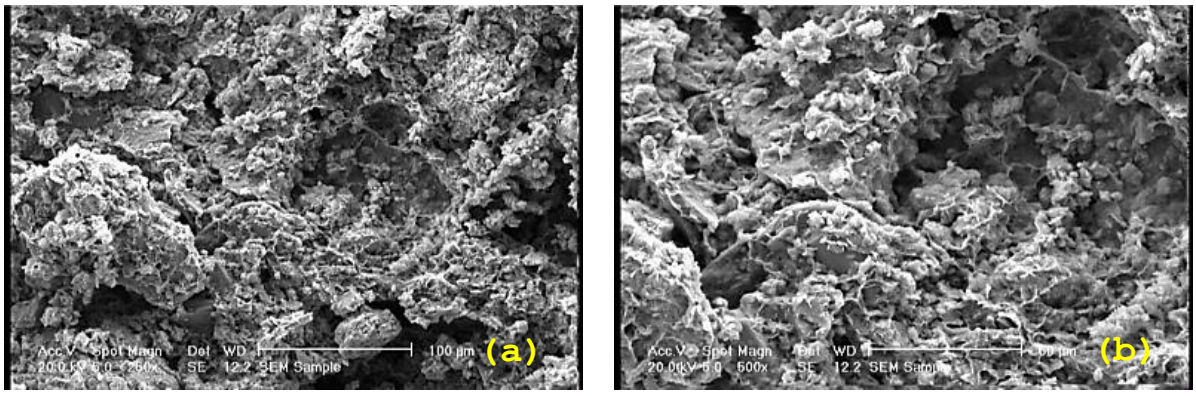

e_{comp}=0.83, $S_{r.i}$=0%, CP:30% (a) Dry curve: $S_{r.comp}$=60%, (b) Wet curve: $S_{r.comp}$=94%

Fig. 6.14(a) ESEM image of clayey silts at varied compaction water content

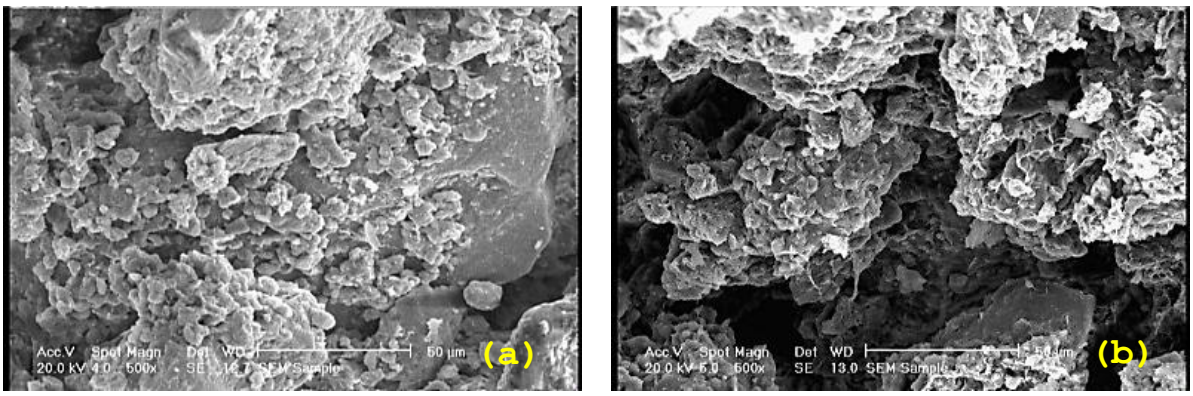

e_{comp}=0.88, $S_{r.i}$=0%, CP:55% (a) Dry curve: $S_{r.comp}$=51.2%, (b) Wet curve: $S_{r.comp}$=92.4%

Fig. 6.14(b) ESEM image of sandy silty clay at varied compaction water content

Initial Step-Loading (SL) before Wetting

In Fig. 6.15(a), at 5% clay content (B1), C_{con} (Coefficient of contraction for i^{th} loading cycle: e_i-e_{i-1}÷1+e_{i-1}) increased on two occasions at 12.5 kPa and 100

kPa. At higher clay contents, C_{con} increased once at 25 kPa. At 5%, 20%, and 40% clay content, C_{con} for 0 to 200 kPa loading was recorded as 17.8%, 14.2% and 12.9%, respectively. Hence the total void ratio loss upon stressing to 200kPa is inversely proportional to clay content (Rogers et al., 1994a).

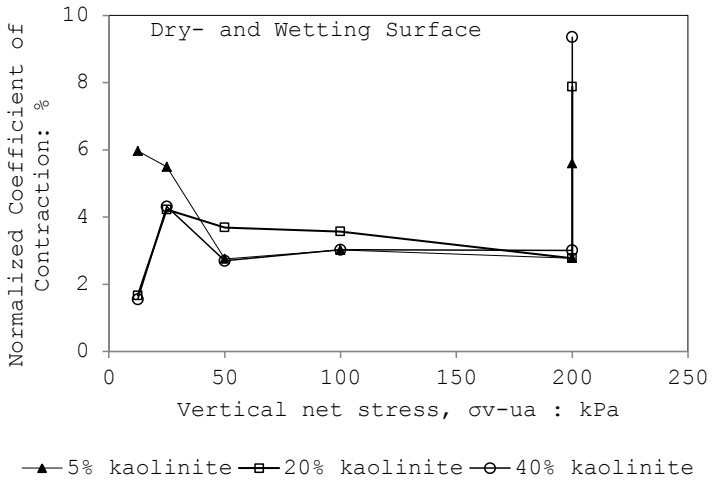

Fig. 6.15(a) Normalized coefficient of contraction against net stress, on pre-wetting-, wetting stress-state surface

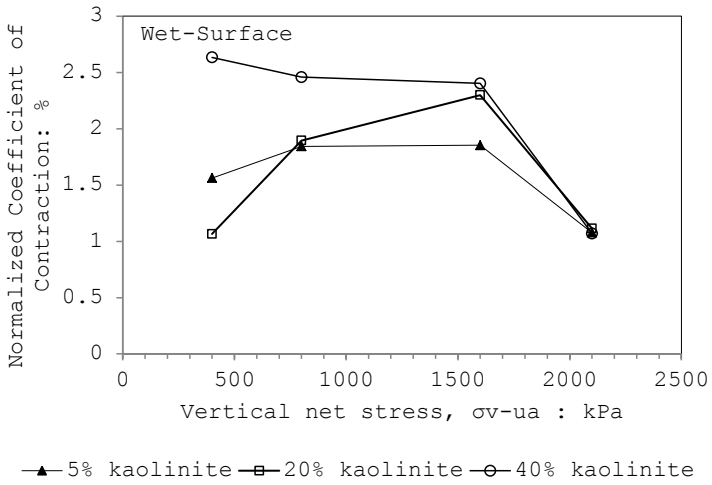

Fig. 6.15(b) Normalized coefficient of contraction against net stress, on post-wetting stress-state surface

Wetting and Loading on the Wet-Surface

At relatively higher clay contents (e.g. 40% instead of 5%), lower dry compressibility (e.g. 12.9% instead of 17.8% for 0-200 kPa loading) and thus relatively higher volume of preserved void ratio led to higher degrees of stored energy in grains, the release of which resulted greater value of collapse potential (Fig. 6.15(a)). On loading to 2100 kPa on the wet-surface,

patches of water in residual macro-pores (voids surrounded by survived larger silts through the inter-locking forces) were extracted from the pore network.

Step Unloading (SUL) on the Wet-Surface

Upon un-loading, the decreased net stress was countered with an excess negative pore water pressure (Fredlund and Rahardjo, 1993), at the early stages. This pressure gradient allowed water to flow into the micro-pores, which were most sensitive to water content changes (see (Munoz-Castelblanco et al., 2012)). Intra-lattice spaces in clay platelets expanded. The swelling of clay aggregates pushed the surrounding survived silt grains aside, providing room between pairs of silt particles (Chapter 4 – Section 4.3). This justifies the higher elastic rebound, which took place at higher contents of clay (6.3%, 6.2%, and 11.8% at 5%, 20%, and 40% clay content, respectively). Upon the subsequent re-compression, the increase in net stress was countered with an excess positive pore water pressure formed at early stages, the dissipation of which resulted in further consolidation. However, due to the consolidation history of the inter-assemblage clays, the clay was compressed to a lesser extent and therefore surrounding distant silt grains were only partially brought into contact. It justifies the lower compressibility of soil at identical stresses (<clay's pre-consolidation pressure) on the recompression curve than on virgin curve (Fig. 6.16).

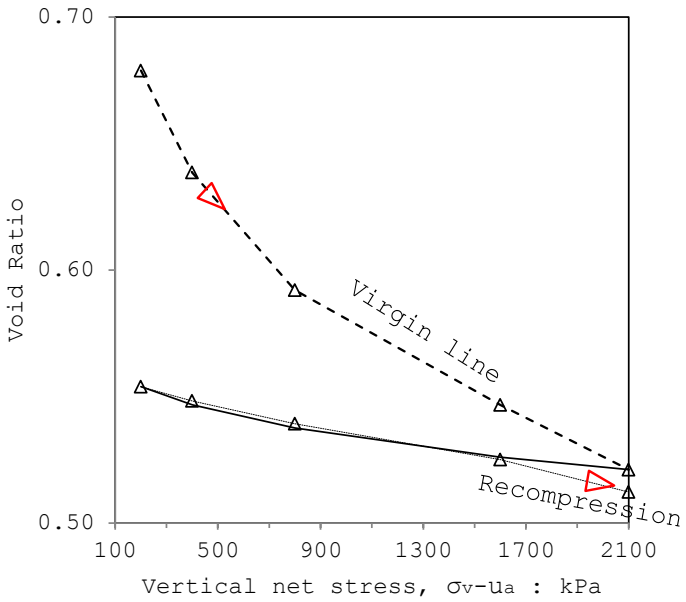

Fig. 6.16 Net stress versus void ratio plot for B1 soils (5% clay, 95% silt)

Step Reloading-Unloading (SL/SUL) on the Wet-Surface

According to Munoz-Casteblanco et al. (2012), the slope of the rebound curve in the elastic range and the slope of the reference compression curve in the plastic range define the stiffness (i.e. Barcelona Basic Model BBM-κ). At low clay contents, an increase in the number of SL/SUL cycles from 2 to 3 decreased the stiffness (i.e. increased BBM-k parameter – see Fig. 6.17). This was attributed to the fatigue effect and the continuous breakage of grains. Nonetheless, an exception with the high 200 kPa stress level occurred in which stiffness was improved by a rise in the number of cycles from two to three. This could be due to further breakage of silt grains upon an increase in stress from 1600 to 2100 kPa, leaving lesser chance to break for grains and thus enhanced inter-locking forces in proceeding cycles.

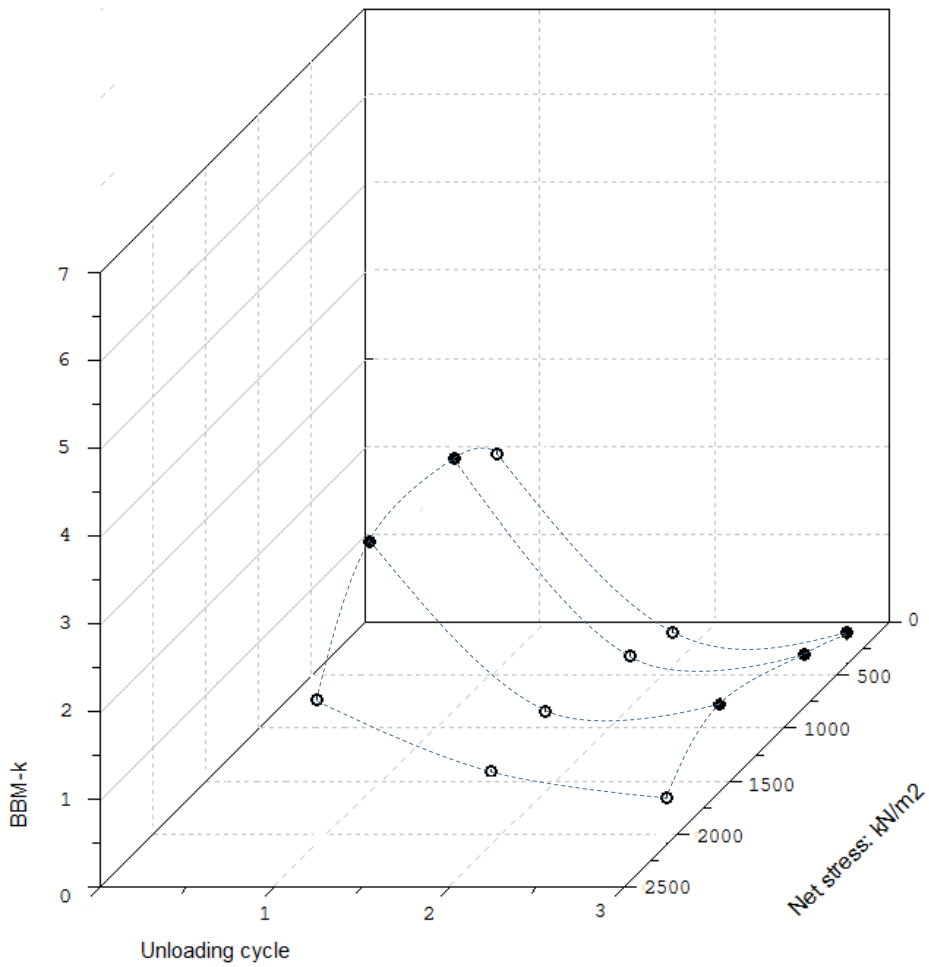

Fig. 6.17 Cycle – BBM κ - Net stress surface (5% clay content)

For higher clay contents (between 20% and 40%), stiffness was found to be directly proportional to the SL/SUL cycle number, although marginal changes

were recorded after the second cycle. This was attributed to the higher contents of clay at macro-pores, which damped the forces, enhancing the survival chance of grains (Fig. 6.18).

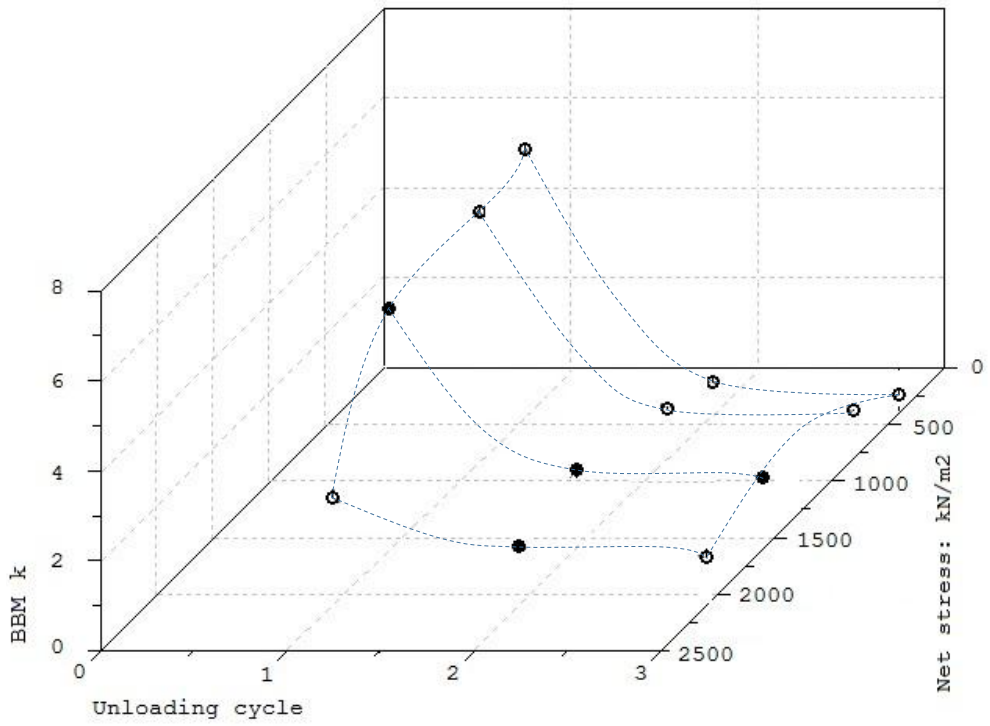

Fig. 6.18 Cycle – BBM κ - Net stress surface (40% clay content)

6.3.2 Calcareous Fines

In chapter 4, dry compression to 2100 kPa (equivalent to an energy of about three times the standard static Proctor compaction, 600 kPa), led to grain breakage (formation of 10-20 µm silt), loss of micro- and meso-pore spaces (0.001-0.25 µm and 0.25-2 µm), agglomeration and formation of macro-pore spaces (2-20 µm). Wet compression also led to strong coagulation in sub-30 µm silts, carbonates and clays, which further gave rise to the macro-pore spaces. Re-crystallization of carbonates upon drying led to the formation of bonding bridges. However, cyclic wetting and drying slightly decreased the void ratio. The findings were consistent with the recent work of (Roohnavaz et al., 2011) on natural calcareous loess. They outlined the earthwork challenges with calcareous clayey loess in Northwest Kazakhstan. A 16 km by 20 km development project was involved in grading and excavation to 3m below the existing ground. Excavated material, however, was stockpiled at the project site to

satisfy environmental protection legislations with organic soils. They reported a series of tests aimed at:

- Mitigation of collapse
- Mitigation of prolonged compressibility
- Potential reuse of site-won loess as earthworks material

They however realised that,

- Standard proctor compaction could not reduce the air volume from the in-situ extents. The lower-bound void ratio after compaction was found above the in-situ values, while the upper-bound dry density was below the in-situ values.
- Five additional passes of compaction at standard energy (2.5 kg) resulted in a 5% air volume at 16% optimum water content, but the soil swelled on wetting.
- Three additional passes of compaction at a modified energy (4.5 kg) did not reduce the air volume beyond 5% and the compacted soil still showed a remarkable swelling potential.

The above limitations with the compaction practice are generally consistent with the collapse models outlined in Section 5.4 and the stress path experiments outcome described in Section 4.3. The poor result of compaction is calcareous soils is partly due to the soil's extremely high dry stiffness, formation of 2-20 μm macro-pores under compression efforts as high as 3-times the static equivalent energy of 25 Proctor blows (Chapter 4), and restoration of carbonate tubular connectors upon wetting-drying. Meanwhile, dilatancy may be a second explanation of the potential for further volume change upon compaction. Compacted loess deposits are reported to show shearing expansion deformation before a subsequent softening (Shao et al., 2008). However, the rate of dilation is low for loose loess specimens, i.e. soils initially at a high voids ratio and therefore the contribution of dilatancy might not be significant. This however is a factor of the water content, degree of kinematical constrains, and consolidation history.

6.3.3 Conclusive Discussion

The mechanical behaviour of a fill relies on placement and in-situ conditions operating on it. Furthermore, these serve as baselines to design engineered fills. Such controls are systematically collated (Charles and Watts, 2001), reviewed and re-examined in calcareous and non-calcareous artificially synthesised collapsing soils.

6.3.3.1 Aging

According to Charles and Watts (2001), as time passes, soil might be subjected to changes in its environment, which influence its mechanical response. Age strengthening is associated with chemical bonding, grain slippage and increased interlocking. The length of time passed since fill placement has a major control.

From a geological perspective, prolonged flow of high di-electric Ca^{++}-enriched groundwater through a Na^{+}-enriched soil can form nodular carbonates and hence decrease the collapsibility. In case of thermal weathering, amorphous silica interacts better with kaolinite and sulphates over longer periods of time and in milder climates. This can increase the collapsibility. Similarly, in slightly alkaline environments, carbonate interacts better with kaolinite, which may then give rise to the collapsibility.

From a geotechnical perspective, an increase in the void spaces in clayey silts due to the effective stress relief upon drying-wetting cycles and formation of re-crystallized carbonate needle bonds are matters of concern.

6.3.3.2 Placement and in-situ water content

According to Charles and Watts (2001) excessive settlement of a compacted clay fill occurs upon saturation when placement water content is too low.

The current work also showed excessive subsidence upon wetting for high placement water content under a low compactive effort and sub-PL in-situ water content. With calcareous deposits, compaction at sub-PL placement water content under controlled compactive effort (i.e. particular roller type, rolling pass, rate, and lift) can minimize the air volume at low carbonate contents (or in soils with carbonate contents less than the clay content). Wet

compaction, however, fails to mitigate the collapsibility in calcareous collapsing soils. This is due to the strong chemical cementation and the tendency of carbonates to migrate with over-saturated bulk fluid and re-precipitates as secondary connector units.

Referring to Lawton et al. (1989), Charles and Watts (2001) concluded that compaction at optimum or slightly wet of optimum water content can fully mitigate the collapsibility for all types of collapsing soils for 'all usual stress levels'.

This, however, was shown herein not to be entirely true, as service water content and chemical composition have major controls on the post-compaction collapsibility of fill.

Lowering of groundwater may cause settlement due to an increase in the effective stress. It is classically believed (Charles and Watts, 2001) that higher levels of effective stress may lead to a higher chance for soil to collapse. This however was argued within the context of the newly proposed form of the effective stress principle. At a constant external net stress, constant micro-scale matric suction and zero hydraulic head gradient, effect stress decreases upon drying. This was reflected in wetting-drying oedometer experimental results, where an increase in the void ratio was recorded during the second and third drying cycles. Loss of void ratio over drying occurred only upon the first drying cycle, over which the contribution of enhanced electric conductivity and hence coagulation of clay fragment was more pronounced that the stress relief.

Charles and Watts (2001) indicated three major controls on collapsibility, namely: placement conditions (compaction conditions), water content history and stress history. The manual referred to a laboratory test programme, showing that proctor compaction to 95% of maximum density at slightly dry of optimum water content can fully mitigate the collapsibility in colliery spoil and mudstone fills (i.e. coarse-grain fills), but may result in a maximum of 2% collapse potential in clayey fills (i.e. fine-grain fills). In contrast, the current work showed a swelling potential of 10 to 15% for compacted kaolinite fills at zero service water content. For coarse grained soils, the present work showed a 0.5 to 1.0% collapse potential for clayey silts of up to

30% kaolinite clay content at a service water content equal to the placement water content. This increased to 3-5% after compacted fill was dried to water contents less than the plastic limit. Charles and Watts (2001) then concluded that there might be a need for a criterion of a placement water content greater than standard Proctor. However, the current work clearly showed that the collapse potential could rise over 5% in coarse-grain fills of >30% clay content compacted on wet-of-optimum.

6.3.3.3 Apparent versus True Cohesion

Plastic limit was defined in Charles and Watts (2001) analogous to the critical collapse water content on the dry stress-state surface. Soil at its plastic limit water content, beyond which capillary forces fail to sustain the soils' open structure, is susceptible to disintegration (collapse). However, the work in Section 4.5 showed that capillary forces do not play the key role in sustaining the structure. Chemical cementation is the first passive factor, which protects the soil against wetted-induced collapse before the mobilization of capillary forces, if the ion-electrostatic forces are regarded as capillary forces associated with the fine micro-pores between the clay platelets.

6.3.3.4 Grain Strength

Charles and Watts (2001) had a cursory glance at the significance of particle strength. Recent work showed that a clean quartz assemblage with internal crystalline defects (i.e. Quartz from an eutectic graphic granite source and a high-to-low quartz transformation under varied temperatures background) tend to crush over time and under applied stresses to form a final pronounced mode of 10-20 μm. The more the time elapses (or the energy applies), the more the concentration of 10-20 μm grains would be. Finer fragments may either be entrapped in macro-pores or flow as an avalanche through the network of pores. Under steady state flow conditions and in the absence of clays, sub-10μm grains may even be washed out of the soil if favourable drainage conditions (clean gravel beds) are available.

6.3.3.5 Placement Stress History

It is conventionally believed that (Charles and Watts, 2001) where a fill is preloaded to a stress level beyond the building design load, stiffness would be improved and hence less subsidence would be expected.

This work, however, showed that preloading at natural water content can improve the stiffness only under constant hydraulic conditions. Either wetting or drying disturbs the packing and consequently the engineering behaviour. Furthermore, where cementation is supplied by non-clayey non-capillary bonds, maximum densification can be achieved through over-consolidation at non-zero flooding stresses.

It is acknowledged in Charles and Watts (2001) that fill becomes more stiffer upon reloading to the previous maximum stress than on initial loading. This was further examined for wetted silty clays of low clay content. For low clay contents, an increase in the number of loading-unloading cycles from two to three decreased the stiffness (i.e. increased BBM-κ parameter). This was attributed to the fatigue effect and the continuous breakage in quartz grains. An exception, however, applied with the high 2100 kPa stress level, in which stiffness was improved by a rise in the number of cycles from two to three. This exception tied in with the fact that most quartz internal defects mobilize on the first loading cycle to 2100 kPa and hence, in the absence of further crushing, inter-locking forces improve in proceeding cycles.

6.4 Modification of the Common Compaction Practice

6.4.1 Non-Calcareous Fines

According to the micromechanical models (Chapter 5), for Class B1 and B2 soils, wetting at a stress level marginally inferior to the dry threshold stress (i.e. the stress at which soil's structure collapses in the absence of water), maximised the densification. The threshold stress is higher than the swelling pressure, and lower than the stress at the point of maximum curvature on the plot of dry void ratio versus logarithm of net stress. This is the backbone of efficient mechanical improvement of soil. The energy needed for ground improvement in transient loading environments can then be lowered to a

minimum by tackling the dependency of sub-grade's stiffness to the 'pre-loading stress.

In Section 6.3.1.5, experimental work showed that:

(1) Compressibility on the normally consolidated line is mainly controlled by the volume of residual macro-pores (roughly analogous to the concept of 'critical' void ratio as introduced in Dijkstra(2001)).

(2) For fine soils containing >30% clay, the stiffness is directly proportional to the number of SL/SUL cycles, irrespective of the stress level.

(3) Clay content is inversely proportional with C_{con} on the dry-surface, but is directly proportional with C_{col}.

In an attempt to reduce collapsibility and induce a direct relationship between soils' stiffness and loading-unloading cycles irrespective of stress level, a control on the residual void spaces was designed:

For B2 class soil specimens (see 6.3.1.5), the initial void ratio of 1.84 decreased to 0.59 at 2100 kPa on the wet stress surface. Upon unloading-loading cycles, void ratio decreased further to 0.58 and 0.57. The void volume associated with e=0.59 was calculated. The equivalent kaolinite clay solid mass to the void volume ($\gamma_w . G_{s(clay)} . V_{v(at\ e=0.59)}$) was added to the dry specimen and the assembly was statically compressed to the original initial total volume. The composite material included 50.6% silt and 49.4% clay, at the void ratio of 0.78 (instead of the previous 1.84). SL/SUL tests showed (Fig 6.19):

(1) The threshold stress increased from 25 kPa to 50 kPa.

(2) C_{con} decreased to 6%.

(3) Elastic rebound upon unloading increased to 14.6%.

(4) C_{col} was minimized.

(5) κ-parameter followed an inverse trend against the number of SL/SUL cycles, irrespective of the applying stress level.

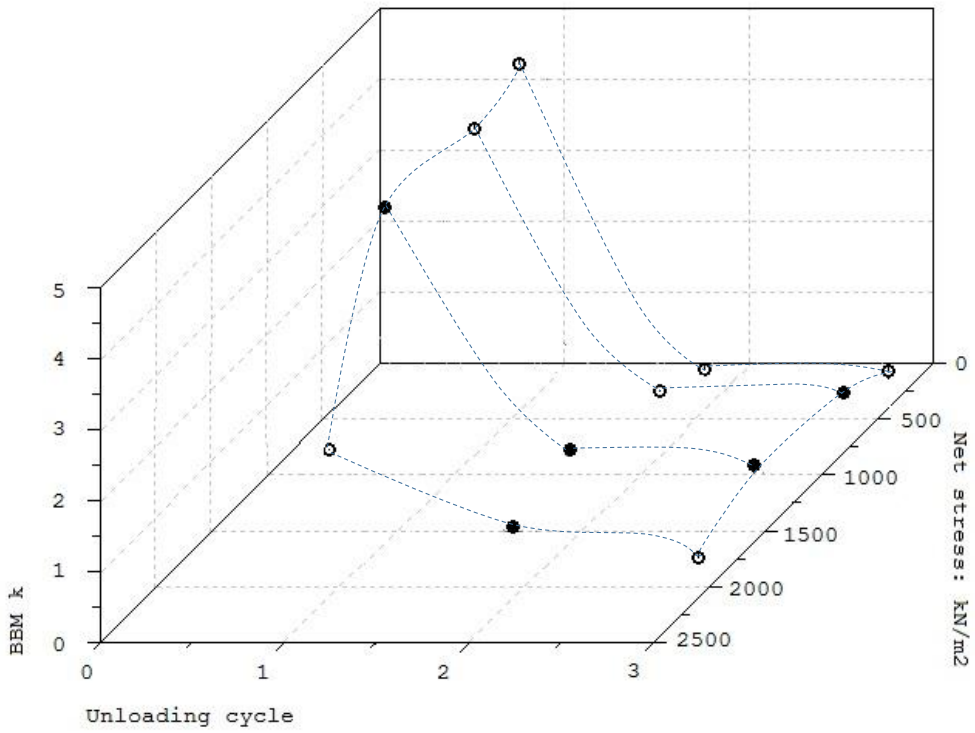

Fig. 6.19 Loading-unloading cycle number versus BBM κ - parameter

Table 6.1 summarizes the impact of the current compaction practice on fine-grained calcareous and non-calcareous soils. In Table 6.1, the efficiency of silicatization in mitigation of collapsibility is summarised and displayed with symbols: '✓✓✓' denotes 'very effective', '✓✓' represents 'effective', and '✓' denotes 'effective subjected to SOT control testing'. '✖✖✖' represents 'severe increase in collapsibility', '✖✖' denotes 'increase in collapsibility', and '✖' represents 'possible increase in collapsibility'.

Micromechanical modelling outputs (Chapter 5 and Table 6.1) and the results of the additional experiments (Section 6.4.1) were finally used to develop a tentative modification to the common compaction practice for class A, B, and K materials. Non-calcareous fines were classified into the six below groups:

- silt (<5% clay – Class A)
- Composite Slightly clayey silt (5-15% clay – Class B1)
- Composite clayey silt (15-35% clay – Class B2)
- Intermediate very clayey silt (35-50% clay – Class B3)
- Intermediate composite silty clay (50-60% clay – Class K)
- Kaolinite clay (>60% clay – Class K)

Table 6.1 Fine-grained soils' response to pre-wetting compression and silicatisation

(SUB)CLASS			TYPE	DESCRIPTION		SOIL RESPONSE [1]	
A	-	-	SILT	-		Highly compressible (well compactable)	
B	B1	-	CLAYEY SILT	SLIGHTLY CLAYEY		Collapsibility increases in compacted soils with an increase in the clay content	
	B2	-		CLAYEY		Collapsibility is rather high in compacted soils and remains high for increasing clay content	
	B3	-		VERY CLAYEY			
C	C1	-	CALCAREOUS SILT	SLIGHTLY CALCAREOUS		Collapsibility increases in compacted soils with an increase in carbonate content. 0-5% carb.: poor compressibility	
	C2	-		CALCAREOUS		Compressibility increases with carbonate content	Collapsibility in compacted soils marginally decreases with an increase in carbonate content.
	C3	-		VERY CALCAREOUS		Compressibility decreases with carbonate content	Collapsibility in compacted soils increases with an increase in carbonate content.
D	D1	-	CLAYEY CALCAROUS SILT	SLIGHTLY CALCAREOUS		Clay ~ 1/Compressibility Clay ~ Collapsibility (max: 15%) Carbonate ~ 1/compressibility	
	D2	-		CALCAREOUS		Carbonate ~ 1/compressibility Carbonate ~ collapsibility (max=20%) Clay ~ 1/compressibility Clay ~ collapsibility (max=10%)dropped & increase steadily	
	D3	-		VERY CALCAREOUS		Carbonate ~ 1/compressibility Carbonate ~ 1/collapsibility Clay↓, Carbonate↑ => compressibility and collapsibility decrease	
E	EM	-	SILICA-INDURATE SILT	MILD	-	×	×
	EH	-		HOT	-		××
F	FM	FM1	METAL-BASED SULPHATED SILICA-INDURATE SILT	MILD	-	×	××
	FH	FH1		HOT	-		×
G	GM	GM1	SILICA-INDURATE CLAYEY SILT	MILD	SLIGHTLY CLAYEY	✓✓	
		GM2		MILD	CLAYEY	×	
		GM3		MILD	VERY CLAYEY	×	
	GH	GH1		HOT	SLIGHTLY CLAYEY	✓	
		GH2		HOT	CLAYEY	××	
		GH3		HOT	VERY CLAYEY	××	
H	HM	HM1	METAL-BASED SULPHATED SILICA-INDURATE CLAYEY SILT	MILD	SLIGHTLY CLAYEY	✓✓✓	
		HM2		MILD	CLAYEY	×	
		HM3		MILD	VERY CLAYEY	×	
	HH	HH1		HOT	SLIGHTLY CLAYEY	✓	
		HH2		HOT	CLAYEY	××	
		HH3		HOT	VERY CLAYEY	××	
	K(G/H)		SILICA-INDURATE Silty Clay (>45%)	Mild		✓	
				Hot		✓✓	

Table 6.1 (Cont.) Fine-grained soils' response to pre-wetting compression and silicatisation

(SUB)CLASS			TYPE	DESCRIPTION		SOIL RESPONSE [1]
I	IM	IM1	SILICA-INDURATE CLAYEY CALCAREOUS SILT	MILD	SLIGHTLY CALCAREOUS	✖✖
		IM2		MILD	CALCAREOUS	✓✓
		IM3		MILD	VERY CALCAREOUS	✓✓
	IH	IH1		HOT	SLIGHTLY CALCAREOUS	✖
		IH2		HOT	CALCAREOUS	✓✓
		IH3		HOT	VERY CALCAREOUS	✓✓
J	JM	JM1	METAL-BASED SULPHATED SILICA-INDURATE CLAYEY CALCAREOUS SILT	MILD	SLIGHTLY CALCAREOUS	✖✖✖
		JM2		MILD	CALCAREOUS	✓
		JM3		MILD	VERY CALCAREOUS	✓
	JH	JH1		HOT	SLIGHTLY CALCAREOUS	✖✖
		JH2		HOT	CALCAREOUS	✓
		JH3		HOT	VERY CALCAREOUS	✓
K			CALCAREOUS CLAY		At constant clay%, carbonate ~ 1/compressibility	

Eight modified ground improvement strategies were conclusively written, addressing the above six soil groups (Fig. 6.20). Methods I to VI involve in the use of the existing fine soils. Method VII requires the access and use of a clay borrow, and hence is treated as an alternative to methods I-IV.

6.4.2 Calcareous Fines

Micromechanical modelling outputs (Chapter 5 and Table 6.1), the mechanism of classic Russian ground improvement technique (analysed in section 2.5.2.2), the outputs of the Russian technique examination (sections 5.3.4 to 5.3.6), and the micro-analytical test results on the control of carbonate micro-morphology on collapsibility (Sections 5.3.3.4.3) were used to develop a tentative modification to the compaction practice for Class C and D materials. The proposed strategies (Fig. 6.21) include the modified mechanical improvement as well as a new chemical treatment - soil gassing practice. The latter is detailed further in the present section.

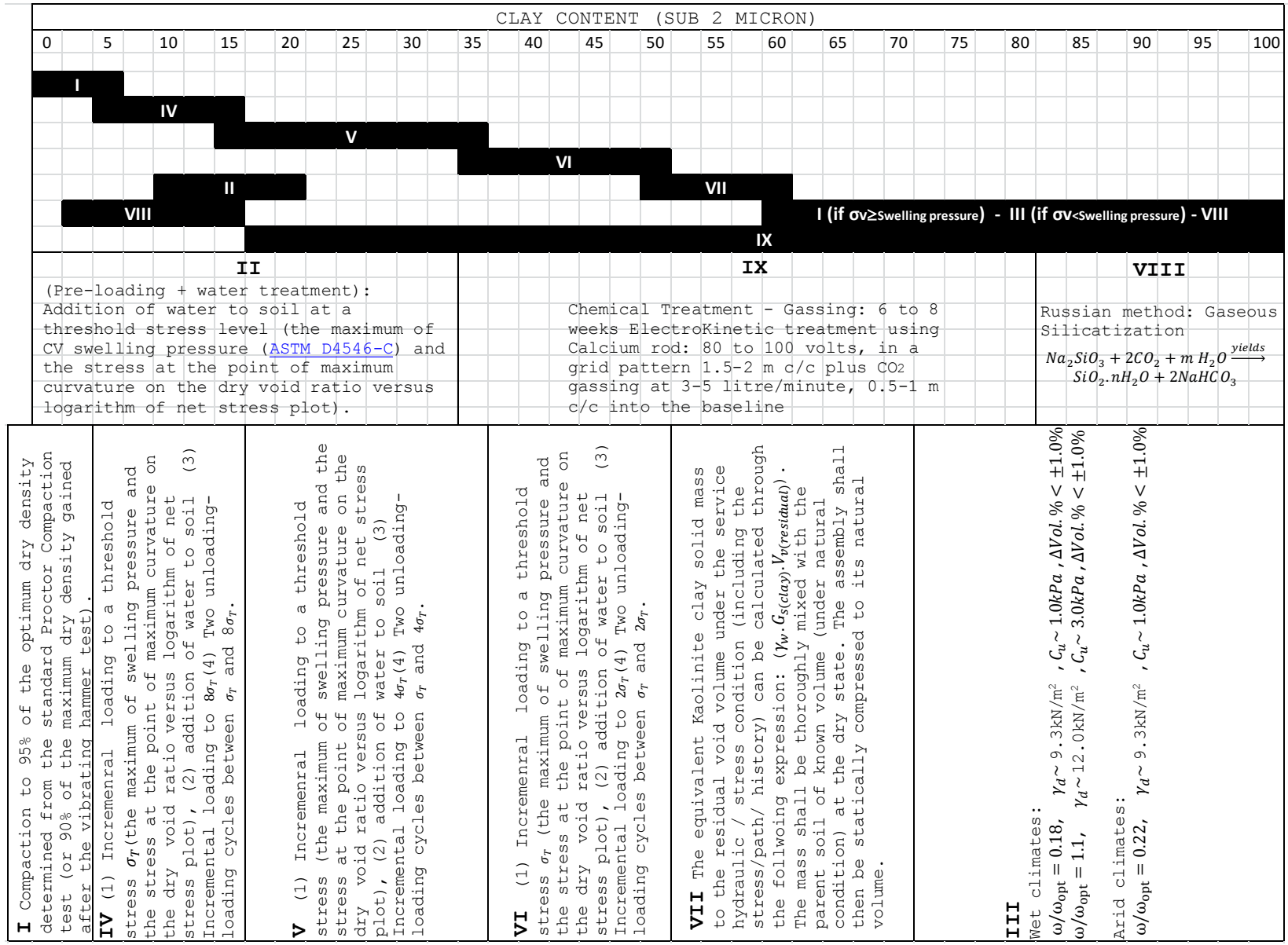

Fig. 6.20 Fine segmentation and the relevant earthwork strategies

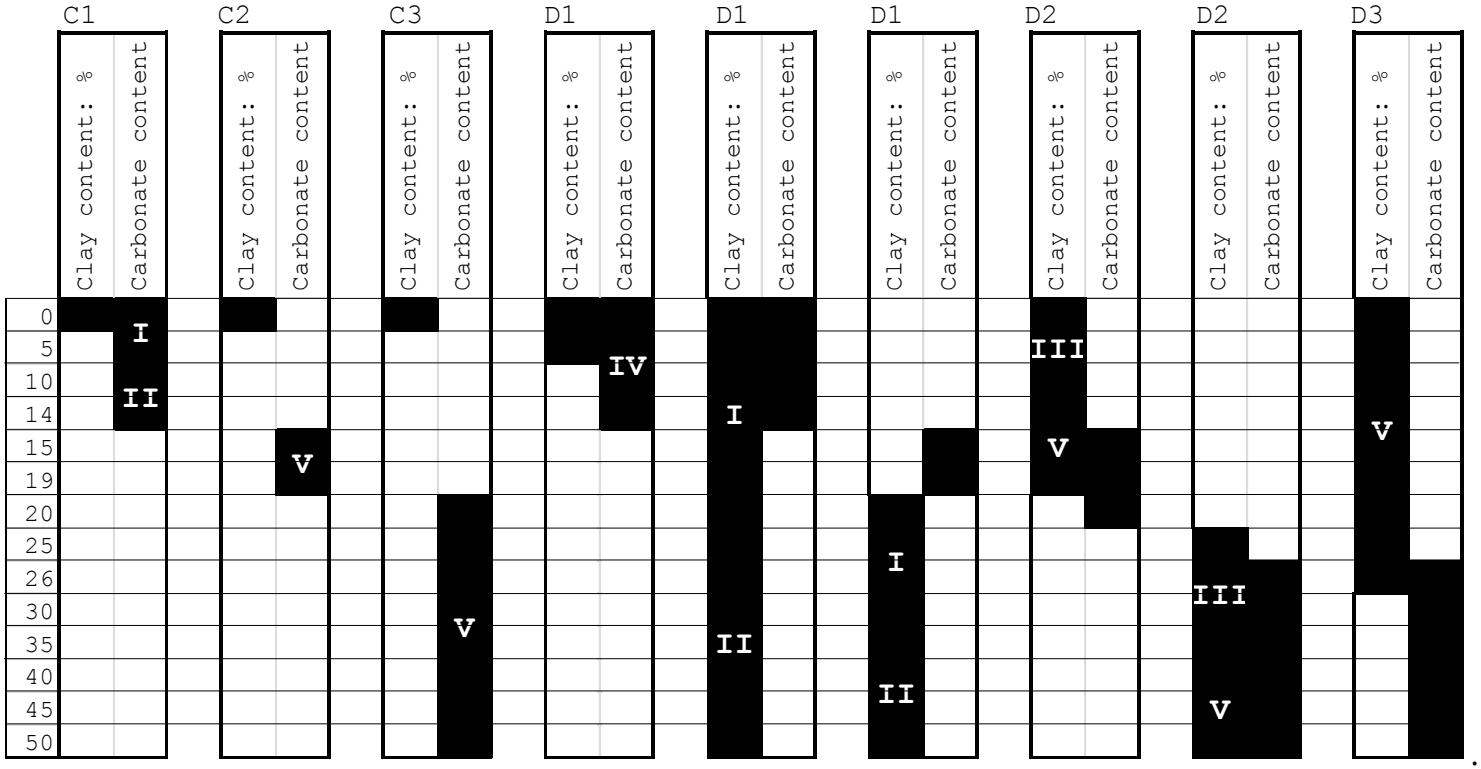

I. Pre-loading to 400 kPa or the standard compaction at 1.6 times the static energy, 640 kPa

II. Pre-loading to 25 kPa, flooding, and post-wetting incremental loading to 1600 kPa

III. Pre-loading to 25 kPa followed by flooding

IV. Compaction at the optimum proctor water content

V. Chemical Treatment - Gassing: 6 to 8 weeks ElectroKinetic treatment using Calcium rod: 80 to 100 volts, in a grid pattern 1.5-2 m c/c plus CO2 gassing at 3-5 litre/minute, 0.5-1 m c/c into the baseline

Fig. 6.21 Fine segmentation and the relevant earthwork strategies

6.5 Case Study

The upper Karachanganak Loess (detailed in Case History Section 5.2.3, Chapter 5), fits into a Class D1 material (60% sand and silt, 25% clay, and 15% carbonate – see Table 5.1. Using the graph in Fig. 6.1, the maximum possible normalized collapse potential for class D1 material is about 20% (9.6% for the mean 0.48 void ratio as reported in Wynne (2007)). Should such a collapse potential exceed the criteria allowance, the ground will need to be stabilized. For a D1 material, Fig. 6.20 shows a suite of recommended collapse mitigation practices. For 25% clay and 15% carbonate constituent, either Method I or II can be implemented immediately at the future foundation locations:

(1) Pre-loading to 400 kPa for single footings or compaction of ground by a Tamping Foot Roller at 1.6 times the static energy (i.e. 640 kPa) for earthwork purposes (e.g. passing the roller at a rate of 8 mph in five passes, to compact the soil in 15 cm thick layers)

(2) Pre-loading to 25 kPa, flooding through a set of installed vertical drains, and post-wetting compression to 1600 kPa for single footings.

6.6 Key Highlights

This chapter drew on the research presented in Chapter 4 and Chapter 5, and the analyses described in Chapter 2. The collated data were used to prepare a framework enabling the constitutive diagnosis of collapse. With non-calcareous fine soils, five by-and-large ignored controls on collapse were then studied. With calcareous fine soils, stressing and flooding were critically probed at the micro-pore scale. With the 'controls' and 'constraints-to-the-current-practice' in hand, the next step was to modify the current practice for specific soil sequences to treat the collapsibility. This led to the constitutive treatment of collapse. However, the proposals discussed herein are tentative. The chapter served as an example case study to show how the micromechanics of collapse can produce effective contribution to the ground improvement practice.

Chapter 7 | CONCLUSIONS AND FURTHER RESEARCH

Knowledge does not mean mastering a great quantity of information but understanding the nature of the mind.

This knowledge can penetrate each one of our thoughts and thus illuminate each one of our perceptions

Matthieu Ricard
Buddhist Monk

7.1 Introduction

There is a rich literature devoted to understanding collapse mechanisms from the physical i.e. bonds' modification (Feda (1988), Smalley and Dijkstra 1991, Rogers et al. (1994a), Bentley and Roberts (1995), Mellors (1995), Pye (1995), Boardman et al. (2001) and Zourmpakis (2005)) viewpoint, as well as mechanical i.e. effective stress (Jennings and Burland (1962), Alonso et al. (2010)) viewpoint. Nonetheless, research into the role of individual loess components and internal forces, which operate on them, has been much less evident and this raises several key questions:

(1) What would be the control of minerals on the yield surface and hence the collapse? What role does the geo-chemical, micro-morphological and packing constituents have on this collapse?

(2) How can reported collapse volume changes in engineered fine-grained fill be explained? What are the controls of aging? Can excavated poor-quality loess soils be used as embankment material under certain circumstances to promote the finance of development projects?

(3) How would the multi-porosity and hydraulic hysteresis be explained with the current form of the principle of effective stress? Can current limitations with the principle limit understanding of engineered loess fills under seasonal wetting-drying cycles?

(4) What are the reasons behind the failure of common practice to fully mitigate collapsibility? Can this failure be explained through micro-mechanics?

(5) How micro-mechanics can be applied to optimise current ground improvement practice?

As such, the aim of this thesis was to examine various modes of collapse in collapsing soils, including loess, from a micro-mechanical perspective, to answer the above questions, and ultimately optimize common mitigation practice applied to collapsible loess soils. The principal objectives were set as:

1. A better understanding of micromechanical indexes and the use of these in developing a collapse mechanism framework;
2. Modification of fine-grained soils' classification system with a particular focus on the interplay between the geochemical and mechanical properties of soils;
3. Examining various modes of collapse for individual soil types in the light of the framework developed in Objective 1, and other appropriate analytical techniques, and
4. Providing a tool for prediction of collapse potential together with identification of constraints to the common improvement practice, hence allowing appropriate mitigation strategies to be targeted more effectively.

These objectives have been carried out and detailed in the preceding chapters: Key findings and conclusions are described in this chapter. Subsequently, a pathway for future work is then proposed.

7.2 Conclusions

7.2.1 Changes to existing physical models and formulations

The latest technique to prepare an artificially collapsible silt soil (Zourmpakis et al., 2005) was modified and used to prepare the collapsible silty test specimens. Foremost, carbonates, shape-less silica, and metal-based sulphates were engineered under controlled conditions. The degree to which the engineered bonds represent the naturally formed bonds were verified through EDS-mapping, ESEM-imaging, and XRD spectroscopy. To probe the micromechanical

indexes on stress state surface), a number of formulations were developed to measure the skeletal and capillary forces. Formulations were based on models reported in Santamarina (2003) and Soulie et al.(2006). Importantly, constraints (the key ones being the capability to interpret the early heave volume change upon wetting and the later heave-contraction upon cyclic wetting-drying) to the existing form of the principle of effective stress were assessed and to overcome these. A new form was proposed, formulated and verified to describe the fundamental collapse mechanisms. The new form was an improvement to the Australian-Spanish attempts (Khalili et al., 2005, Bagherieh et al., 2009, Alonso et al., 2010).

7.2.2 Development of micromechanical interdisciplinary links

7.2.2.1 Quartz grains

Experiments confirmed that quartz breakdown is a fractal phenomenon. Sand and silt are neither the products of two different mechanisms (both can be produced to some extent by glacial grinding and the subsequent fluvial-aeolian abrasion), nor the final resistant products of glacial abrasion. These are inherently breakable materials (in presence of crystalline defects) for fractal dimensions less than an intrinsic maximum. These defects are independent from grain size and external energy input. Hence, breakage is not necessarily an energy-dependent process, although the efficiency of skeletal forces in crushing grains is inversely proportional to the grain size. Hence, collapse in loess is not restricted to the breakage of connectors, but also to the breakage of the frame (i.e. quartz) constituents. A control on the coordination number can, however, increase the damping effect, and stop the grains to further breakage. On the other hand, continuous quartz breakage improves the sorting quality. Solifluction and chemical weathering within a well-sorted granular soil can produce better quality secondary bonds, and hence can introduce a re-stored collapsibility.

From a sedimentary perspective, the UK genesis study (see Appendix A1-3) suggested that the present day silt and sand were supplied from different sources and were carried to their final deposition area through different transportation regimes. In particular, silt is more a product of long-distance aeolian actions while sand is more a product of local secondary/tertiary

fluvial-aeolian transportation actions. The long-distance aeolian migration of the present-day UK silt agrees with the results of grain strength experiments (presented in this thesis), where sand and silt were concluded products from a similar source, processed under different levels of operated high continuous energy levels over a short time period or low discontinuous energy levels over a long time period.

7.2.2.2 Inter-particle Forces

Moving water and stressing creates drag. The wetting-induced drag force, however, is independent from the external net stress. The drag force is a stand-alone control on the overall stress state at grain-to-grain contact points. The wetting-induced drag force leads the stress state to the wetting course maximum (i.e. the maximum value of stress during wetting), shortly after the water ingress. The mobilisation of capillary forces, however, does not react quickly enough to sustain the soil's structure against collapse at this stage. Therefore, in the presence of cementation (salts and carbonates – see Dijkstra et al.(1994)), the collapsible structure is sustained against the elevated stress state. Capillary forces can play the key role in postponing the collapse in presence of relatively high clay contents, which enhances the number of micro-pore spaces and hence the tensile stresses.

In short, new evidences do not support the pronounced contribution of capillary forces to the soils' stiffness, unless in the presence of relatively high clay contents. Cementation, however, can postpone the wetted collapse, although at the expense of a higher stored skeletal stresses within the granular structure.

7.2.2.3 Grain-Bond Interface

The quartz breakage timeline revealed that grains attain a well sorted distribution (at pronounced 10-20 μm size) upon stressing, although the abundance of 10-20 μm grains relies on the magnitude of input energy (i.e. magnitude and duration of applied stress). Oedometer tests, which were conducted on artificial loess specimens made up of certain proportions of silt, kaolinite, and carbonate, and varied silt particle size distribution, revealed that relatively higher degrees of collapsibility occur in soils with well sorted silt component. Since clayey- and calcareous bonds may

recrystallize (restore) over a post-wetting drying season, the quality of recrystallized bonds could be better than primary bonds. This is a potential risk to already-collapsed (or mechanically compacted) loess deposits, and should be considered in the design of earthwork strategies.

7.2.2.4 Packing State

Oedometer test results on identical calcareous clayey loess specimens on three stress state surfaces explained the contribution of distinct pore spaces to collapse. For a naturally occurring loess consisting of 70% silt, 20% carbonate, and 10% kaolinite clay, four levels of pore spaces were recognized: (1) trans-assemblage pores of >1.5 μm in diameter, (2) macro-pores of 0.3-1.5 μm in diameter, (3) meso-pores of 0.001-0.25 μm in diameter, and (4) micro-pores of <0.001 μm in diameter. As an example of the significance of multi-porosity concept, experiments showed that the water-retention properties are only reproducible upon wetting-drying in soils possessing pronounced pores of 0.001-0.25 μm and also 0.3-1.5 μm in diameter. Furthermore, since static compression can, via an equivalent energy, be considered analogous to dynamic compaction (i.e. standard proctor) (see Chapter 6) the viability of common compaction practice was examined for testing ideal loess material. Dry-compaction (even at energies beyond the standard compaction effort) is not sufficient enough to destroy the collapsing structure. Dry compaction in calcareous clayey loess soils leads to continuous grain breakage and thus improves the large macro-pores. For applied stresses up to 2100 kPa on the dry-surface (more than 3-times the static equivalent energy of 25 Proctor blows) large volumes of 2-20 μm pore spaces form (i.e. trans-assemblage pores) at the expense of the loss of 0.001-0.25 μm and 0.25-2 μm void spaces. Wetting at any stress level improves the aggregation (in >30 μm grains) and hence the pore volumes, leading to some degrees of post-drying collapsibility (i.e. void ratio increases beyond the threshold critical void ratio, as suggested in Dijkstra (2001)). Pre-loading to 25 kPa on the dry-surface followed by wetting however, guarantees the maximum degree of densification.

Microscopic observations revealed that any wetting-drying cycle allows some tubular carbonates to re-precipitate in a scaffolding framework and to form re-stored carbonate bridges. This however, does not happen in clays as

secondary clay-silt laminated deposits normally form at macro-pores upon a cycle of wetting-drying. Formation of re-crystallized carbonate bonds brings into question the efficiency of compaction in calcareous deposits.

7.2.3 Modification of fine-soils' classification system

A careful distinction among clay (>2 μm), carbonates, sulphates, amorphous silica and chlorides is needed, since moderately soluble to relatively insoluble cements behave differently than that of clays in a given granular system. As such, a new classification scheme was developed which is practice-friendly, whilst considering the geochemistry. The sub-63μm fragments was divided into 11 main classes based on the relative abundance of their major components (quartz, clay, carbonate), minor components (sulphates, chlorides, amorphous silica), and climate. A range of conventional property tests were then suggested for the purpose of classification.

7.2.4 Collapse mechanism: the framework

The major recent contributions to the principle of effective stress were critically reviewed in Chapter 4. Recent Australian-Spanish works particularly focused on the association of microfabric and the double porosity concept to effective stress. A new formulation was proposed in Chapter 4, which addressed one working domain, two clusters of pores, four constituents (two solids and two fluids), and four phases along each hydraulic path. The formulation was rigorously examined against three subsequent wetting-drying cycles. Owing to the double porosity concept, a third stress variable was introduced to the model, which operated during the transition of fluid between pair of neighbouring pore subspaces. The new formulation was then used to explain the collapse phenomenon in a typical calcareous clayey loess. Collapse upon wetting is a delayed process. Upon water ingress, an excess positive pore water pressure ($\bar{U}_w^m$) develops. This pressure dissipates at the expense of formation of drag forces (F_D). Effective stress follows a decreasing trend ($\sigma' = (\sigma - u_a) + 0(u_a - u_w) + (1-0)F_D;\ F_D \to 0$) for saturation ratios less than a threshold ($S_r^M = 0,\ S_r^m > 0,\ S_{rT} = 0.42$), beyond which macro-pores accommodate water as theoretically proved (see Section 4.6.2.1). Formation of water films and mobilization of ion-electrostatic forces provide a short period of steady stress state. At the threshold state, a hydraulic gradient encourages the flow

of water from the outer macro-pores to the inner macro-pores, by crossing the clay connectors (micro-pores). This induces an excess positive pore water pressure in the clay connectors, and hence a subsequent drag force. Once more the drag force gains value, giving rise to an increase in effective stress, which could also be regarded as the 'net' skeletal force ($\sigma' = (\sigma - u_a) + 0(u_a - u_w) + (1 - 0)F_D$). The 'net' prefix refers to the superimposed effect of skeletal forces and drag forces. An increased stress is simultaneous to the loss of much of the matric suction. Clay fragments trigger to migrate as water flows into the macro-pores, and hence the loss of cementation appears as an additional problem. Enhanced active stress state therefore leads to the collapse. Collapse triggers at the threshold saturation ratio, where $S_r^m \rightarrow S_r^m{}_{Res} \rightarrow 0$. Shearing of connectors (under escalating skeletal forces) is formulated in the context of effective stress principle at micro-scale (i.e. the clay connector clusters) for suction values less than the air entry value ($(u_a - u_w) \leq (u_a - u_w)_{m(ae)}$).

The model developed then allowed determination of the hazardous post-collapse behaviour of clayey silt soils upon seasonal drying-wetting. Since clay fragments supply much of the matric suction and as secondary (i.e. migrated) clays accumulate in inner macro-pore spaces, and drying does not control the matric suction. Hence, at a constant net stress and in the absence of a hydraulic gradient between pairs of distinct pore spaces, drying causes a relief in the effective stress. In contrast, secondary normally consolidated clays shrink upon drying due to a rise in the electric conductivity. Therefore, drying causes further void ratio loss in collapsed clayey silts of young secondary clays. However, drying causes rebound volume changes in the collapsed clayey silts of over-consolidated secondary clays. Post-collapsed wetting results in an upsurge trend in $(1 - \chi)F_D$ of negative value, and hence the effective stress relief. Consequently, a rebound volume change counters this stress relief.

7.2.5 Collapse mechanism

Addressing soil classes A to J (as defined in Table 5.1), a collapse volume change was described using the framework developed. ESEM-images together with Lewis structures were utilised, where needed, to describe the chemical

interactions between pairs of individual bonding agents and the nucleation processes during their formation. The latter manipulated the micro-morphology of chemical agents, the significance of which was then showed in Chapter 5.

In short, clean silt (A) was found compressible. Addition of Calcium Carbonate decreases the compressibility (more than clay of the similar content), but in-turn significantly increases the collapsibility. The more the clay, the more the clayey silts are collapsible. Carbonates have the same effect, except with moderate contents of carbonates (Class D2 in Table 5.1); at which collapsibility first decreases but then increases back with increasing carbonate content. This is a constraint to compaction practice, particularly in calcareous silts. Among various combinations, maximum collapsibility occurs at 10 to 15% clay content and at about 20% carbonate content. In general, increasing carbonates and/or clays reduces the compressibility. Both compressibility and collapsibility, however, drop with carbonate content as the soil approaches the fine-grained zone (silt content approaches to 45 to 50%). Lewis structures analysis, microscopic imaging, and mechanical test results suggested that Silicatization (classic Russian ground improvement technique – see Chapter 2) may be advised for sulphated slightly clayey silts under mild conditions (treatment at a slow rate). The technique can be used with caution for slightly clayey silts under mild conditions, silty clays (clay>45%) under hot conditions (treatment at a fast rate), and clayey calcareous silts in the absence of sulphate phases. EDS-ESEM analysis and mechanical tests revealed that Calcium Carbonate implant in silty clays and clayey soils can restrict the collapsibility and improves the compressibility. Generally speaking, carbonate implants in clayey calcareous silts restricts the collapsibility.

7.2.6 Common practice: problems and solutions

With non-calcareous fine soils, five, by-and-large currently ignored controls on collapse were identified. With calcareous fine soils, stressing and flooding were critically probed at the micro-pore scale. With the ‘controls’ and ‘constraints-to-the-current-practice’ established, the current practice was modified for specific soil classes (see 7.2.3).

With calcareous soils, the effectiveness of the current practice was confirmed for class D1 soils only. Pre-loading or dry compaction at controlled energy level (i.e. particular roller type, rolling pass, rate, and lift) was suggested for soil classes C1 and D1. A flooding follow-up stage was advised for soil class D2. A new tentative EK-gassing strategy was finally recommended for moderately to very calcareous soils. However, it should be noted that this approach is still unproven in detail in the field.

With non-calcareous soils, the current practice was found viable for class A (basic silts containing <5% clay content) and class K (basic clays containing >60% clay content under a surcharge greater than the swelling pressure) materials. A controlled pre-loading or dry compaction followed by a flooding scheme was suggested for soil classes B1 and B2 containing 10 to 20% clay content. A follow-up loading stage (wet-of-optimum compaction) was recommended for soil class B. Where transient design loads are involved, a supplementary loading-unloading set-up was detailed. Where application of such an energy is not feasible or where the scheme is not workable, an alternative soil-mixing strategy was detailed. For class K soils under low design surcharge loads, the standard compaction practice was constrained to a certain working water content to satisfy the swelling upon precipitation during the structure's service life.

7.3 Recommendations for future Research

In light of the research undertaken in this thesis and experience gained the following three areas for further investigations are suggested.

7.3.1 Loess constituents: Determination of collapse mechanism in loess containing active clays and oxides

Proposals can be made to understand the formation, the consequent micro-morphology, and the resulting mechanical response of other bonding materials, as individuals and combination, including montmorillonite, iron oxides, and calcium sulphates. However, having demonstrated the interplay between amorphous silica and clay/carbonate; iron oxides are expected to give rise to the liquid limit, and hence further delay the collapse. Active clays are

expected to collapse under skeletal stresses greater than the swelling pressure. However, since limited research has been taken place in the area of mixed (but controlled) minerals' behaviour, synthesis and examination of such artificial loess soils does certainly matter.

7.3.2 Collapse modelling: Explaining the collapse mechanism in loess in terms of small-strain stiffness instead of internal forces

Stiffness (resistance against deformation against applied load after Clayton (2011)) is conventionally expressed by the shear modulus under small strains, Gmax. According to Atkinson (2000), Gunn et al. (2006) and Yang et al. (2008), small strain shear modulus is controlled by the interaction between neighbouring particles within the solid framework of a soil. This can be measured by emitting an elastic wave after a small perturbation, while the original micro-fabric is kept intact (Lee et al., 2008). With loess soils, Gunn et al. (2006) developed a hybrid oedometer cell integrated with bender elements (i.e. acoustic oedometer) to study the structural stiffness of brickearths of Ospringe in North Kent, England. This approach, with some modifications, can be utilized to explain the wetted collapse process in terms of the real-time inter-particle forces, for controlled artificially synthesised loess specimens. Results can be read in conjunction with the outputs of Section 4.5 (real-time measurement of inter-particle forces).

Measurements can be made by using an integrated Bishop triaxial testing apparatus equipped with bender elements or a hybrid acoustic oedometer similar to that developed by the British Geological Surveys (Gunn et al., 2006).

Technically, the electrical excitation (i.e. a change in voltage) of a piezo-motor transducer (induced by a function generator) generates a bending motion. The motion of the two-layer cantilevered piezo-ceramic plates leads to an excitement, distortion, and generation of an elastic wave, which will travel through the medium. On the other end, a piezo-generator transducer will convert the detected received voltage to electrical signals, which thereafter will be recorded as waveforms on a digital oscilloscope. Each two-layer piezoelectric transducer (i.e. bender element) consists of a conductive metal shim sandwiched between two piezo-ceramic sheets and conductive outer electrodes. A suitable setting should include a parallel assemblage for the

transmitter probe to provide greater displacement and a series assemblage for the receiver probe to provide greater voltage.

The test procedure commences with signal calibration. Three single sinusoidal wave pulses of 2, 6, and 12 kHz target frequency will be transmitted from the Piezo-motor transducer attached to a pedestal. The received wave will be checked for the minimum distortion prior to the first major peak. After obtaining the minimum suitable target frequency, shear wave velocity will be calculated by dividing the tip-to-tip distance between the upper and the lower bender elements (i.e. specimen height minus the protrusion lengths) to the travel time from the transmit-receive pulse pair graph.

The maximum shear modulus of soil can be calculated as:

$$V_s = \sqrt{\frac{G_{max}}{\rho_b}} \implies G_{max} = V_s \times \rho_b \qquad Eq.\ 7.1$$

Specimen will then be gradually loaded at the initial dry state to 25, 50, 100, 200, 400, and 800 kPa. Repeated signal calibration shall be implemented prior to each proceeding loading increment.

For the wetting path, although the volume change of testing specimen along wetting under 200kPa is measureable, the volume of water which occupies the voids throughout the wetting cannot be measured and thus no estimation to the variations of void ratio, bulk density and thus small strain shear modulus could be made. To relax the problem, a 'self-weight suction decrease' followed by 'zero-suction compression' stress path can be implemented.

The maximum small strain shear modulus will be derived after self-weight suction decrease and for each stage of the load increments through:

$$H_s = \frac{M_s}{G_s.\gamma_w.A}, \qquad Eq.\ 7.2$$

Where the weight of solids, M_s, is derived by oven-drying an identical soil specimen.

$$H_{void(i)} = H_i - H_s, \qquad Eq.\ 7.3$$

Where H_i is the height of oedometer specimen.

$$e_i = \frac{H_{void(i)}}{H_s}, \qquad Eq.\ 7.4$$

$$\rho_{bulk(i)} = \frac{W_s + W_w}{H_i . A} = \frac{W_s + \frac{W_s . e_i}{G_s}}{H_i . A} = \frac{W_s . (G_s + e_i)}{G_s . H_i . A}, \qquad Eq.\ 7.5$$

$$G_i = {V_{s(i)}}^2 . \rho_{bulk(i)} \qquad Eq.\ 7.6$$

7.3.3 Engineering practice: Laboratory-scale simulation of EK-soil gassing practice

To examine the effectiveness of the proposed chemical treatment - soil gassing practice, artificially synthesised loess specimens (through the method detailed in Chapter 3) could be treated by a chemical approach (test set-up available in the Civil Engineering laboratory of Birmingham University). This would be a trial-and-error process, but a good starting point can be the treatment for 6 to 8 weeks on 80 to 100 volts, via steel pipe work. Undisturbed 75 mm oedometer specimens could then be obtained by tube-sampling. Specimens would be treated by soil gassing inside a modified oedometer cell, before conducting the standard single oedometer test. A modified oedometer which allows the gas flush and pH measurement is tentatively designed and schematically displayed in appendix A6.

APPENDICES

A1. Loess Soils in the UK: Genesis and Formation

Geographic and morphologic similarities of loess drapes of identical source in the West Europe were first introduced in 1839, when D'Archaic realized the similarity between the British Brickearth and the loess in continental Europe (Fall, 2003). Later, the relationship between the lower Thames Valley brickearth and the loess deposits of Central Europe was reported in Prestwich (1863). Meanwhile, it is widely believed that loess deposits, particularly those stacked on bedrocks and stable uplands bear the initial characteristics and hence source footprints Schaetzl (2013). As such, early works like that in Lyell (1852) suggested a fluvial origin for the British loess (based on the origin of the loess of Western Europe, which at the time were also considered to be fluvial). Pointing to the different levels on which loess occurred in England, Prestwich (1863) suggested the flood-water origin of the loess. Fall (2003) addressed other earlier theories of Wood (1882) on solifluction and colluviation (similar to thin loess colluvium in valleys surrounded by high topography in the Midwestern United States – reported in Schaetzl (2013)) under Periglacial conditions, Geikie (1905) on colluviation under temperate conditions, and Edmunds (1948) and Dines et al. (1954) on sheet flooding under wet condition of pre-existing loamy deposits. Some other early works are summarised in Table A1. The present section specifically sought the historic primary (i.e. syngenetic) and secondary (i.e. epigenetic) diagenesis of loess in South England. Available data on geographic signatures of loess drape as well as physical properties of loess deposits were used to draw a PTD (provenance, transportation, deposition) model.

Table A1.1 some of the early to recent studies on the origin of British brickearth

In	Origin of brickearth
White (1917) and Everard (1954) cited in Reynolds et al. (1996)	New Forest Brickearth was originated as river flood loams i.e. over bank deposits
Green and Calkin (1949) cited in Reynolds et al. (1996)	New Forest Brickearth was originated as purely aeolian
Lewin (1966), Swanson (1968), Fisher (1971), and Keen (1980) cited in Reynolds et al (1996)	New Forest Brickearth was originated as a mixed purely aeolian and river floodloams (fluvial)
Dalrymple (1960) in Fall (2003)	Much of the brickearth of Kent are of aeolian origin
Smart et al. (1996) cited in Fall (2003)	Brickearths of South East England were formed by solifluction
Coombe et al. (1956), Catt and Staines (1983),and Roberts (1984) cited in Fall (2003)	Lizard Loess in Cornwall contains two sequences: (1) massive classic loess on flat surfaces where solifluction activity was not pronounced and there was little post-depositional erosion of the loess (2) loess head where loess was deposited on geliflucted lobes flowing down the steep slopes
Harrod et al. (1973) in Fall (2003)	The mineralogical uniformity of silt-drift in Devon is an indication of possible single episode of deposition

A1.1 Syngenetic Events across North Kent and South Essex

Brickearth in Essex, North Kent, and probably London is more similar to the classic loess of Western Europe than the debris left by the British Ice. Parks and Rendell (1992) suggested that northward retreating British Ice was unlikely to have a pronounced effect, since deposits in North West France and South East England are genuinely similar and the thickness of the South East England brickearth is significantly more than that in the South, South West and North England. As such, Lill and Smalley (1978) stressed on the role of strong easterly winds formed from the anticyclonic conditions over

Scandinavia. Easterly winds carried glacially ground silts over large distances across Europe. Meanwhile, the cyclonic conditions operating on the West British Isles led to a decrease in the force of the easterly air flow, and thus the deposition of sparse and thin layers of dust over South East England. This closely mirrored a later work in Avery et al. (1982), which described the distinctly finer silts in deposits of North West London (i.e. north of River Thames – Chiltern Hills) of 16 to 32 μm mode size comparing with the typical 32 to 44 μm silt mode in Devensian loess of East England. Finer silts in the west are a signature of far-travelled dust (perhaps from a British Ice source), while the coarser silts in the east may suggest a short-travel background of dusts blown by easterly winds. Meanwhile in the north (i.e. Northern Wealden), Derbyshire and Mellors (1988) and Northmore et al. (1996) reported relatively higher contents of sand and larger mean sizes than that found in the south (i.e. Southern Wealden). The distribution pattern of sand may be attributed to a long-distance aeolian act from the British Ice source, in which strong prevailing north-west to south-east winds delivered and distributed the sand over the Wealden area. This however does not agree with the contribution of easterly and north-easterly winds, addressed as T1 stage (i.e. 'T' for Transportation) in Jefferson et al. (2003). The sand distribution pattern is here attributed to a potential short-distance aeolian migration from a secondary deposited area near Oxted to adjacent regions at an approximate radius of up to 60km (i.e. an area with three boundary points of Arundel to the west, Molash to the east, and Stambridge to the north east). In addition, as a secondary/tertiary transportation stage, silt particles deflated (or soliflucted) from a site close to Allington to the south west, north west, and north east. This is supported by the steady reduction of silt contents along theses directions. Likewise, silt particles deflated from east coasts of Pegwell Bay and Reculver Cliff and blown to South West, and North West. This agrees with the easterly wind flow in Lill and Smalley (1978).

A1.2 Syngenetic Events across Hampshire Basin

According to Lill and Smalley (1978), brickearths of East Yorkshire, East Lincolnshire, North Norfolk and Devon, are made up of silts supplied by

outwash deposits left after retreatment of the Weichselian glaciers. This could be the source of quartz in the Hampshire Basin.

As for the sand, the east end of the Hampshire Basin contains relatively lower contents, which agrees with the trend of sand distribution in the South Wealden (Fall, 2003). As for the silt, Reynolds et al. (1996) reported the 1978 work of Catt, showing the westward decrease in mode size of aeolian silt (blown by easterly winds from a source in the North Sea basin) in the late Devensian loess of West Hampshire. The long-distance aeolian distribution of sand may have formed sand drape at Lepe Point, Ocknell Plain, and Wootton Heath (Reynolds et al., 1996), but had less control on the most of the surface sandy drape at the Hampshire Basin. This is highlighted in irregularities in the increasing trend of sand content to the west (Fall, 2003). Sand was deemed a product of fluvial secondary and tertiary actions of rivers and river mouths (also see Smalley et al. (2009)), and the subsequent localised short-distance aeolian deflation-deposition. This conforms to the work of Reynolds et al. (1996) on brickearth deposits at New Forest in South Hampshire, as well as the works by West and Mills (2009) and West et al. (2010) on brickearth at High Cliffe, Barton-on-Sea, Chilling Cliff, Brownwich Cliff, and Hill Head.

A1.3 Epigenetic Processes across North Kent and South Essex Area

The recent work of Milodowski et al. (In Press) revealed fresh evidences on the history of epigenetic processes at North Kent. They reported signatures of Illuvial migration of fines, a source to the modern clay-bridges and detailed signatures of cryoturbation including the presence of coarse quartz grains, which were caped with a thin layer of silt and clay in a stable arrangement. Footprints of soft pellets, disappeared clay bridge/buttress connectors, destroyed cryogenic fabrics, and decreased plasticity indices were described by acknowledging a background of solifluction, which finally shaped the present-day upper non-calcareous brickearth. Milodowski and colleagues ruled out the recent theories of carbonate corrosion, dissolution and leaching after reporting a descent content of primary detrital carbonates in the upper brickearth sequence. This however might be argued since aragonites carbonates could change into calcite (i.e. detrital) carbonates if the sequence was

washed with high-dielectric Ca^{++} enriched water (Assadi and Jefferson, 2013). Within the lower calcareous brickearth, Milodowski et al. (In Press) reported loose open-packed ped structures, which were formed by cryoturbation, a product of Periglacial freeze-thaw cycles. Similarity in mineralogical characteristics of this lower sequence and the Tertiary substrata suggested that a significant proportion of the quartz silts (particularly in Pegwell Bay) nay have been produced through frost shattering within the underlying chalk and Thanet Sand Formation (also see Derbyshire and Mellors (1988)).

Bell et al. (2003) described the local post-depositional history of Maidstone brickearth in North Kent. The valley-ward movement of the underlying Atherfield Clay Formation in conjunction with the dissolution of the overlying Hythe Beds Formation formed gulls along fissures. Gulls were filled with river gravel, brickearth, and solifluction remnants. Subsequently, fill deposits slowly subsided into the gulls by disappearance of Perglacial conditions at the end of the Devensian as the ground ice melted. Similar sets of characteristics could be found to the west. Looking into further north and north-west, Avery et al. (1982) tentatively correlated the Chiltern Hills deposits with the brickearths of South and East England. They listed a set of post-depositional events operating on all these deposits, including cryoturbation, solifluction and temperate weathering: Local footprints of cryoturbation were realized in irregular admixture of loess with stones and fines from underlying sequences including drifts and clay-with-flint. The high clay content in Chiltern Hills loess was attributed to deposits' cryoturbation with adjacent clay formations including Reading Beds or Plateau Drift. Weathering, slumping, cryoturbation and solifluction of the Plateau Drift decreased in the thickness of the Reading Bed Clay strata and hence exposed the chalk to weathering. Dissolution of chalk led to the formation of funnels and slumps, which then housed the deep lying brickearth materials. For South Essex, Northmore et al. (1996) described the brickearths at north and north east of the region. These were found capping the Quaternary terrace gravels formation as well as Eocene London Clay formation. Solifluction caused by rapid slope degradation in outcrops of Tertiary deposits possibly incorporated with the formation of the head brickearth.

According to Fall (2003), the clay-size fragments in Wealden increases from east to the west, between Pegwell Bay and Teynham, then locally decreases at Allington (Maidstone, Kent), and climbs back along the west margin of the Wealden. This can also be seen in relatively higher clay contents (see Table B2 Appendix B) at Ospringe (upper sequence) than that at Pegwell Bay (McKervey and Kemp, 2001, Milodowski et al., In Press). In Table B4 (Appendix B), the plasticity index (PI) increased from 13.0 at Pegwell Bay and Recurver to 22.0 at Sturry and 35.0 at South Essex. Close to Maidstone, PI decreased to 13.0 at Northfleet. Milodowski et al. (In Press) attributed the low clay content within the Pegwell Bay upper non-calcareous brickearth to solifluction reworking and colluvial-alluvial activities. Bell et al. (2003) attributed the low clay content in Allington to its unique reworking background. Clay might be of an in-situ weathering origin, Eocene origin, or a product of decalcified chalk around Molash and south of the River Thames (Gallois, 2009). Flints might be a product of chalk dissolution. Nonetheless, it is likely that aeolian silts were originally mixed with clay and clay-with-flint fragments, by modification through cryoturbation and solifluction.

A1.4 Epigenetic Processes across Hampshire Basin Area

Unlike the Wealden area, the clay content decreases from east to west across the Hampshire Basin (Reynolds et al., 1996, Fall, 2003).

A <35cm thick often discontinuous Late Devensian loess caps a continuous nearly impermeable pre-Devensian loess in South-West Hampshire, a region between Southampton Water and Avon Valley (i.e. the New Forest). The upper brickearth contains footprints of surface runoff and erosion, while its sand fragments are mineralogically identical to that of in the Tertiary bed (Reynolds et al., 1996). Flint fragments could be a product of frost heave or cryoturbation. In Holbury (i.e. east margin of the region) Reynolds et al. (1996) suggested that a relatively older brickearth deposit was geliflucted over the lower younger deposit from an adjacent but slightly higher parts of the terrace, and sandwiched a stone line or a discontinuous fragipan.

According to the simplified geological map of Hampshire Basin (described in West and Mills (2009)), Hampshire Basin is surrounded by Reading, London Clay, and Chalk Formations, and is in association with local river system (e.g. River Meon, River Hamble, River Itchen, River Test, River Avon, and River Stour), which suggests the control of solifluction reworking on the formation of clay constituents at high contents (Derbyshire and Mellors (1988) also insisted on the interaction of quaternary brickearth and Tertiary beds). This agrees with the findings of Fall (2003), which attributed the high plasticity of South England Brickearth to Sussex deposits in Hampshire Basin. West et al. (2010) pointed to the mineralogical resemblance between the Hill Head Brickearths at east margins of Southampton Water and the chalk formations. This suggested a history of solifluction in Chalk outcrops of Portsdown Hill. This area (between Hill Head and Southampton water) is covered with a 1m thick non-calcareous loess blanket (i.e. in Chilling and Brownwich Cliffs according to West and Mills (2009)), which caps the Pleistocene river Gravel Terrace, a sequence on top of the Middle Eocene bioturbated marine sandy clay formation. Given the resemblance of clay mineral assemblages with that of chalk, clay may have been washed or blown as dust over the cliffs. To the north, the thickness of brickearth increases to 3 to 5.5 m in Salisbury. These deposits are calcareous and possess variable masses of flint and chalk, Late Pleistocene fauna, and signatures of solifluction reworking. To the west, head brickearths of Barton-on-Sea and High Cliffe possess cryoturbation structures.

A2. Loess Soils in the UK: Geochemistry and Mineralogy

A2.1 Mineralogical Inputs

Fall (2003) pointed to the constant ratio of clay content to plasticity index, which suggests the presence of identical clay minerals in the major two areas. Commonly occurring minerals in the two areas are listed in Table B1. The mineralogical composition of brickearths in Wealden and Hampshire areas are described in more details in Table B2 and Table B3. These can be read in conjunction with the consistency limits of deposits as demonstrated in Table B4. As discussed earlier, plasticity index generally increases from the east coast to the west in the Wealden, with an exception of Maidstone of different topography, where different post-depositional actions operated. In tables B2 and B3, higher dolomite and calcite contents were recorded within the lower brickearth sequences in two sites of Pegwell Bay and Ospringe. In contrast, higher kaolinite contents were recorded within the upper brickearth sequence. From a wider perspective, brickearth deposits over South England (Reynolds et al., 1996) contain five heavy mineral groups of Garnet, Amphiboles, Clinozoisite, Zoisite, and Epidote, which are abundant in fine sand and coarse silt fractions. The mixture of heavy minerals and surface sand and silt is a signature of cryoturbation and solifluction reworking. Catt (1978) indicated a mainly westward increase in the proportion of sheet silicate minerals (i.e. micas and chlorites) and a concomitant decrease in other minerals. Abundance of sheet silicates (i.e. phyllosilicates) in the west confirms the genuine difference between the epigenetic diagenesis of loess of South East and South.

Table A2.1 Mineralogy of the brickearth of North Kent, South Essex and Hampshire Basin (Fall 2003)

	Quartz	Feldspar	Mica muscovite	Mica Biotite	Zircon	Rutile	Ilmenite	Pyrite	Palygorsk-ite
Wealden	✓	✓	✓	✓	✓	✓	✓		
Hampshire Basin	✓	✓	✓	✓	✓	✓	✓	✓	✓

Table A2.2 Quantitative whole-rock mineralogy analysis of brickearth at Kent and South Essex

In	Location		Bulk Minerals: %														
			quartz	Mica	chlorite	K-feldspar	albite	calcite	dolomite	smectite	kaolinite	hematite	rutile	plagiocalse	Glauconite	Muscovite	Flint
(McKervey and Kemp, 2001)	Pegwell Bay	Lower	66	3	1	5	5	14	2	1	3	nd	<1	-	-	-	-
		Upper	62	16	<1	3	6	1	nd	1	11	<1	<1	-	-	-	-
	Ospringe		67	2	nd	7	8	<1	<1	3	14	nd	<1	-	-	-	-
(Bell et al., 2003)	Pegwell Bay		77	-	-	19	-	-	-	-	-	-	-	-	1	1	2
	Kent	Ford	82	-	-	14	-	-	-	-	-	-	-	-	1	2	1
		Allington	85	-	-	11	-	-	-	-	-	-	-	-	1	2	1
		Ashford	84	-	-	12	-	-	-	-	-	-	-	-	1	2	1
		Teynham	79	-	-	18	-	-	-	-	-	-	-	-	1	1	1
(Miller, 2002)	Star Lane		56	-	-	-	-	-	-	-	-	-	-	8	-	-	-

Table A2.2 (*Continued*) Quantitative whole-rock mineralogy analysis of brickearth at Kent and South Essex

In	Location		Bulk Minerals: %														
			quartz	Mica	chlorite	K-feldspar	albite	calcite	dolomite	smectite	kaolinite	hematite	rutile	plagiocalse	Glauconite	Muscovite	Flint
(Milodowski et al., In Press)	Ospringe	Upper	66	13	-	7	7	-	0.7	1.2	13	-	-	-	-	-	-
	Ospringe	Lower	59	14	-	5.5	5	8.4	3.1	1.3	4.4	-	-	-	-	-	-
	Pegwell Bay	Upper	62	13	0.5	4.4	5.7	0.5	-	1.5	7	0.5	-	-	-	-	-
	Pegwell Bay	Lower	63	11	-	5	3.5	-	1.7	1	2	-	-	-	-	-	-

Table A2.3 Quantitative clay-size mineralogy analysis of brickearth at Kent and South Essex

In	Location		Clay mineral: %			
			Smectite	Illite	Chlorite	Kaolinite
(McKervey and Kemp, 2001)	Lower	Pegwell Bay	50	27	7	16
	Upper		40	30	9	21
	Ospringe		43	22	0	36
(Miller, 2002)	Star Lane		28		0	4
(Milodowski et al., In Press)	Upper	Ospringe	53	22	8	19
	Lower		58	21	6	16
	Upper	Pegwell Bay	62	17	7	14
	Lower		55	25	6	14

Table A2.4 Consistency limits of brickearth at South Essex and Kent

In	Location	LL	PL	PI
(Derbyshire and Mellors, 1988)	Pine Farm Quarry, Kent	32.0	22.0	10.0
	Ford, Kent	34.0	19.0	15.0
	Pegwell Bay, Kent	29.0	18.0	11.0
	Pegwell Bay buried channel, Kent	33.0	20.0	13.0
	Reculver, Kent	33.0	20.0	13.0
	Sturry, Kent	44.0	22.0	22.0
	Northfleet, Kent	32.0	19.0	13.0
	Kent (average)	34.0	20.0	14.0
(Boardman et al., 2001)	Pegwell Bay, upper non-calcareous	25.6	18.6	7.0
	Pegwell Bay, lower calcareous	26.6	18.5	7.1
(Milodowski et al., In Press)	Ospringe, upper non-calcareous	36.0	23.0	13.0
	Ospringe, lower calcareous	28.0	NP	NP
(Assallay, 1998)	Britain (average)	28-	17-	9-28
(Northmore et al., 1996)	South Essex (average)	35.2	19.8	15.0
(Northmore et al., 1999)	Upper Claygate Beds, South Essex	60.0	25.0	35.0
	Middle Claygate Beds, South Essex	60.0	27.0	40.0
	Lower Claygate Beds, South Essex	70.0	25.0	45.0

A2.2 Lithological Inputs

According to Catt (1978), an almost ubiquitous loess layer covers the landscapes on the chalk formations of southern England. More specifically, Fall (2003) showed that brickearth in Wealden caps London clay (South Essex), Thanet Sand (North Kent), quaternary terrace gravels (South Essex) and Chalk Formations (North Kent). In Hampshire Basin however, brickearth caps a wide spectrum of formations ranging from upper Cretaceous to Oligocene. As an example, for the deposits in Barton-on-Sea and High Cliffe, West and colleagues in 2010 described these beddings as Pleistocene Plateau Gravel and Eocene Headon Hill (marl and clay with sandy layers), Barton Sand and Barton Clay Formations. In Chilling and Brownwich Cliffs, West and Mills (2009) detailed the substrata as Pleistocene Gravel, Barton Clay, and Selsey Sand Formations. In New Forest (Reynolds et al., 1996) beddings are reportedly made up of flinty terrace gravel.

A2.3 Geochemical Inputs

Geochemistry of loess sequences may reflect both their provenance characteristics and their evolution since deposition.

For the South England brickearth, Fall (2003) reported varied contents of CaO, P_2O_5, MnO, Na_2O, and MgO over the region, while SiO_2 content changed to a minimum extent. This may be a signature of mixing surface and bedding sequences, such as the interaction between loess and the underlying chalk outcrops, which consequently led to the regional variation of CaO content. Large variations may also implicate the intensity of weathering and leaching conditions (e.g. capability of soluble salts to be easily leached out of the brickearth upon weathering for CaO, MgO, and Na_2O variations). This agrees with earlier works of Assadi and Jefferson (2013a) and Assadi and Jefferson (2013b), where the gravity inflow of calcium enriched high di-electric ground water were shown a potential source of the upper non-calcareous and lower-calcareous brickearth sequences across the Wealden.

For North Kent and South Essex, Fall (2003) reported the declining trend of Zirconium content in a west to east direction with an exception for the Pegwell Bay. Less heavy minerals in east might be an indication of either younger or heavily reworked deposits. For Hampshire Basin, the concentration of TiO_2, Zirconium, Chromium, and Niobium decreases to the west. Higher concentration of Al_2O_3 in the Hampshire Basin area suggests the higher concentration of Alumina-Silicate minerals in brickearth. This agrees with the relatively higher clay contents.

Since the age of deposits in both Wealden and Hampshire Basin areas are not significantly different, the initial thickness of loess in South East England was possibly more than that of South and South West England. This might be due to the simultaneous act of silt Aeolian deposition and Thanet Sand frost shattering in Wealden. Relatively higher thickness of loess in Wealden justifies its lesser interaction with the Tertiary Clay formations and hence, the lesser clay content. In South and South West England however, the relatively lesser thickness of loess led to a much more effective cryoturbation and solifluction events, bringing the Tertiary heavy minerals as well as Tertiary clay to the surface. Silt in the South and South West is more

a product of Aeolian deposition from the margin of the British Ice. Local river system brought the sub-rounded sand grains, while the silt fraction relatively sizes more than that of the Wealden. This agrees with the short Aeolian transportation distance between Hampshire Basin and British Ice margin, far lesser than the distance between the Scandinavian Ices and South East England.

A3. Loess Soils in the UK: Geographical Distribution

County	District	Reference	Notes
Hampshire	South Hampshire	Key (1939) [1]	
	South Dawns	(Jefferson et al., 2003)	Thin primary loess deposits
	Southeast Hampshire	Key (1939), Hodgson (1967), Hodgson (1967), after (Reynolds et al.,	80 cm thick brickearths, particularly at the east banks of Southampton water
	Southwest Hampshire	(Reynolds et al., 1996)	Few patches, 30 to 80 cm thick bounded by Southampton water and at the Barton-on-Sea
	Between Hamble-le-Rice and Netley, South of Bursledon		
	East of Warsash, west of Hill Head on farming lands		
	North End, Hilsea, north Portsmouth and south Cosham		
	North of Redbridge causeway, northernmost Southampton water		
	New Forest, Higher Terraces		Area between Stoney Cross, Fritham and Picket Post
	New Forest, Lower Terraces		Area between coast and the towns of Burley, Brockenhurst, and Beaulieu
	Near Portsmouth	Palmer and Cooke	
	Lepe Beach, West Solent, Wessex coasts	(West et al., 2010)	Mix of wind-deflated sands from locally exposed Tertiary deposits and far-travelled late Devensian silts
	Brownwich & Chilling Cliffs, Barton-on-sea, Southampton water	West and Mills (2009)	On gravel terrace deposits, aeolian and fluvial, containing chalk and mixed layer clays
	Fisherton, Salisbury	Reid (1903) [3]	Brickearth with flint & chalk, 3 to 5.5 m
Sussex	Parts of Sussex	Hodgson (1967) [1]	
	Coastal Plains	(Jefferson et al., 2003)	Tertiary coastal Loess from Catchment of Arun, Weald
	West - Rother Valley	Wooldridge (1932)[2]	Tertiary, Loamy soil regions
	East - Port of Rye	(Jefferson et al., 2003)	From Rother catchment
	East - Seaford Head	(Shepherd and Randell, 2010)	10m thick orange stained accumulation of loess and coombe deposits (frost-shattered chalks)
Berkshire		Jarvis (1968) [1]	
Kent	-	Green and Fordham (1973)[1]	
	West Kent, Sevenoaks	Wooldridge (1932)[2]	On the hythe Beds – Loath

County	District	Reference	Notes
Kent	North Kent	Gruhn et al. (1974)[1]	On Calcareous substrata
		(Jefferson et al., 2003)	Tertiary, from Thames catchment
	Pegwell Bay	(Deakin, 1986, Gunn et al., 2006)	Also east of Canterbury
	Ospringe – South East of Faversham		
	Ford and Sturry	(Dibben, 1998)	Near Canterbury
	Reculver Cliffs	(Dibben, 1998)	
	Ramsgate, Monkton Quarry & Dumpton Gap Pine Farm Quarry	(Dibben, 1998)	East Kent
	Dover	(Dibben, 1998)	South East Kent, metastable glacial solifluction head loess-like deposit
	Northfleet	(Dibben, 1998)	
	Between Chatham and Thanet	Wooldridge (1932)[2]	Tertiary, Loamy soil regions
	Medway Valley, Tonbridge to Maidstone	(Deakin, 1986)	Tertiary, Loamy soil regions
	Hoo Peninsula between rivers Thames and Medway	(Deakin, 1986)	Also Conyer (south of peninsula), Funton (south of Sittingbourne), Murston (east of Sittingbourne)
Oxfordshire	Chilterns Hills	Avery et al. (1969)[1]	
Devon	East Plateau	Harrod (1971)[1]	
	-	Harrod et al. (1973)[1]	On Budleigh Salterton Pebble
		Harrod et al. (1973)[1]	On Haldon Gravels – Haldon
		Harrod et al. (1973)[1]	On Dartmoor Granite
		Harrod et al. (1973)[1]	On Devensian Limestone Plateau
Essex	North and northeast of south Essex	(Northmore et al., 1996)	Up to 8m thick in a circular area with a diameter of about 10Km, being centered around Stambridge. Including four main metastable regions: 1. South, southwest, west, northwest Rochford 2. Southeast Stambridge to the River Roach 3. Southeast of Paglesham 4. Patches south of the River Roach centered around Great Wakering
	Roding Valley	Sturdy (1971)[1]	
	South east	Gruhn et al. (1974)[1]	On Calcareous substrata
	South west	Wooldridge (1932)[2]	Tertiary, Loamy soil regions
	Parts of North Essex	King (1969)[1]	Loess occurring in river valleys
	South	(Jefferson et al., 2003)	Site for 2nd London Airport – 8m
		Perrin et al. (1974)[1]	Calcareous substrata

County	District	Reference	Notes
		(Jefferson et al., 2003)	Tertiary, from Thames catchment
	Tendring Hundred	Wooldridge (1932)[2]	Tertiary, Loamy soil regions
Dorset		(Catt, 1978)	On Chalk formation substrata
		(Jefferson et al., 2003)	Tertiary coastal Loess from Catchment of Arun, Weald
Isle of Wight		(Catt, 1978)	On Chalk formation substrata
Somerset	Between Somerset, Levels & Avon Valley	Findlay (1965)[1]	On limestone hills (carboniferous Limestone)
Derbyshire		Bullock (1971)[1]	On carboniferous limestone
Yorkshire			On carboniferous limestone
North Yorkshire	Yorkshire Wolds	Catt et al. (1974)[1]	Thin loess deposits devoid of sands
East Yorkshire		Penny et al. (1969)[1]	
	Vale of York	Perrin et al. (1974)[1]	Coversand
East Riding of Yorkshire	Yorkshire Wolds	Catt et al. (1974)[1]	Thin loess deposits
Wales	Coast near Aberystwyth Cardigan Bay	Watson and Watson (1967)[1]	A thin loess layer not extending to Inland
Lincolnshire	Lincolnshire Wolds		Loess devoid of aeolian sands
	West Lincolnshire	Perrin et al. (1974)[1]	Coverdsand
Hertfordshire	North-east	King (1969)[1], Thomasson (1969) [1]	Loess occurring in river valleys Calcareous substrata
	Chiltern plateau	Wooldridge (1932)[2]	Tertiary, Loamy soil regions list
Suffolk			Coversand , Calcareous
	South	King (1969)[1]	Loess occurring in river valleys
	North Thames estuary	(Jefferson et al.,	
Nortfolk		Perrin et al. (1974)[1]	Coversand , Calcareous
		(Jefferson et al.,	Loess material added to soils
	Cromer moraine	Wooldridge (1932)[2]	Tertiary, Loamy soil regions
Greater London	London	Wooldridge (1932)[2]	Tertiary, Loamy soil regions
Middlesex	South	Wooldridge (1932)[2]	Tertiary, Loamy soil regions
Surrey	West	Wooldridge (1932)[2]	Tertiary, Barget Beds, Loamy region
	Horsley	(Charles and Watts, 2001)	Mudstone/Sandstone opencast backfill (2% collapsibility)
Durham	Warren House Gill	(Davis, 2009)	Primary Loess
	West Auckland	(Charles and Watts,	Clay/shale opencast backfill

[1] Quoted in (Catt, 1978)

2 Quoted in (Jefferson et al., 2003)

[3] Quoted in (West and Mills, 2009)

A4. Reproducibility of Laser Diffraction Outputs

Laser diffraction (LD) measurements were repeated twice, using two 8-10g soil specimens from a larger batch. Reproducibility of results (concerning the device and interpretations) were assured by repeating LD analysis on random specimens. An example of such repeating test output is shown below for an ideal loess specimen (containing 70% silt, 20% carbonate, and 10% kaolinite).

- Mode size and particle size distribution pattern was observed reproducible.
- Marked mode sizes (i.e. grain size with maximum population) were reproducible.

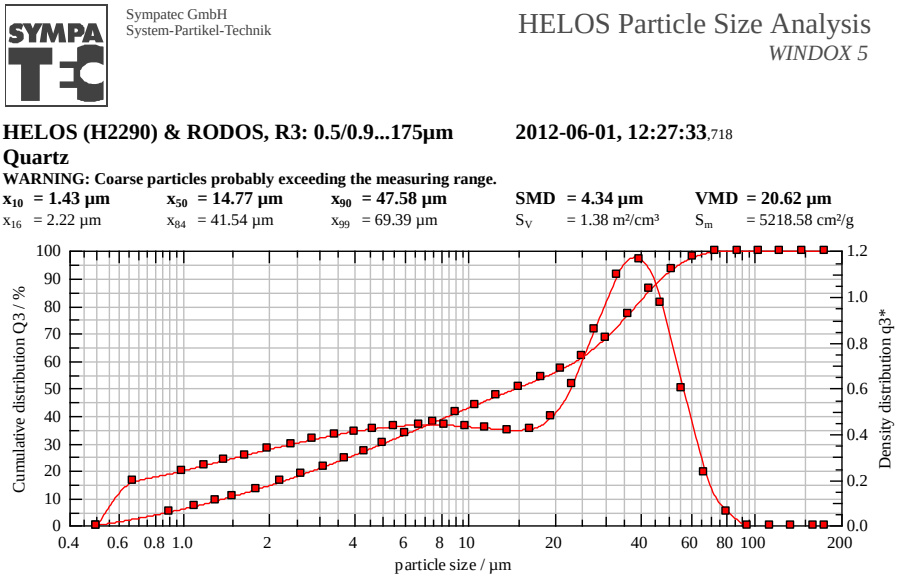

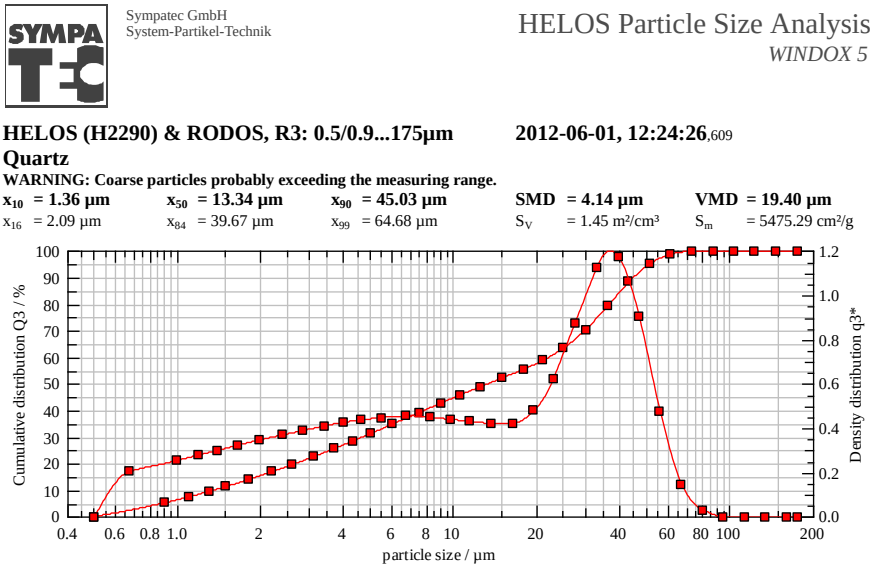

A5. Arya-Paris Pedo-Transfer Function

A5.1 Concept and Formulation

The Arya-Paris Model is the most commonly used (Delleur, 2007) pedo-transfer function for the in-direct determination of pore-size distribution in a soil. The model involves dividing the cumulative particle-size distribution curve into a number of fractions, each representing a mean pore radius (r_i) and water pressure head (ψ_i). Arya and Paris (1981) proposed a nonlinear expression to relate the pore radius (r_i) to the mean particle radius (R_i):

$$r_i = R_i.\left(\frac{4.e.{n_i}^{1-\alpha}}{6}\right)^{0.5}$$

where e is the void ratio; and n_i is the number of particles in each size fraction derived from:

$$n_i = \frac{W_i}{Spherical\ Particle\ Volume \times Particle\ density} = \frac{W_i}{\left(\frac{4}{3}\pi.{R_i}^3\right).\frac{W_s}{V_s}} = \frac{3W_i}{4\pi.{R_i}^3.\gamma_s}$$

where W_i is the solid mass (per unit sample mass) associated with R_i (i.e. in each given size fraction), in such a way that the sum of the W_i is unity. γ_s is the particle density taken equal to $G_s.\gamma_w$. Specific gravity (G_s) was directly measured in accordance with the BS 1377.

The empirical factor of α_i is termed 'scaling factor' (i.e. tortuosity factor). ${n_i}^{\alpha_i}$ represents the number of particles which trace the pore length. The scaling parameter is selected in accordance with the empirical study of Arya et al. (1999) on more than 1000 soils taken from the unsaturated soil hydraulic database known as UNSODA (Leij et al., 1996). The database contained both the water retention and particle-size distribution curves. The tortuosity parameter, α_i, was formulated for five different soil textural classes of the USDA soil texture triangle, namely sand, sandy loam, loam, silt loam, and clay. Loess, in the present study, is considered a silty loam material. To determine the α_i, a regression expression was used, which is the latest form presented by the function developers. Haverkamp et al. (2002) examined the validity of this expression and confirmed that the scatter between the

predicted and calculated α-values were satisfyingly low in all soil textural classes. Arya et al. (1999) regression expression is formulated as below:

Let

$$Y = Log\ N_i = Log\ {n_i}^{\alpha_i}$$

$$x = Log\ n_i$$

Then

$$Y + \Delta Y = \frac{Y_F . Y_i}{Y_i + \left(Y_f - Y_i\right) exp[-\mu(x + \Delta x)]}$$

to determine the Y (and subsequently the α_i), below table was proposed by Arya et al. (1999) to extract ΔY, Y_f, Y_i, μ and Δx for five soil textural groups,

	Y_i	Y_F	μ	ΔY	Δx
Sand	0.966	16.602	0.609	1.734	0.00032
Sand loam	0.559	16.983	0.553	2.492	1.849
Loam	0.628	16.614	0.510	2.242	1.977
Silt loam	0.719	19.686	0.457	1.902	0.684
Clay	1.993	21.685	0.289	4.766	2.648

The parameters for Loess (being a silt loam), are hatched on the above table.

The Arya-Paris Model suggests that the radius of a given pore is a factor of the mean radius of particles surrounding that pore, in a soil of certain void ratio and specific gravity. For a domain made up of a mesh of equally dimensioned squares, both particles (solids) and pores (voids) can be modelled as squares, the number of which are assumed equal. Hence, the population of the particles could be deemed equal to the population of pores. Arya and Paris (1981) used this simplification to plot the pore-size distribution curve from a given particle size distribution function.

A5.2 Model Limitation

Although the Arya-Paris model is extremely easy to use, it has a number of limitations outlined in Haverkamp and Parlange (1982), Delleur (2007), and Mingbin et al (2009). These are briefly discussed in Chapter 3 of this thesis. Most important of all, the use of the semi-logarithmic presentation of data in Arya-Paris model poses a visual problem, which is discussed in this section.

The problem lies in the fact that Arya and Paris (1981) used the conventional semi-logarithmic presentation of particle size distribution curve to produce the size fractions (see their working example detailed in Arya and Paris (1982)). Although a correct population of specifically sized pore spaces can be determined as a factor of particle size, because of the greater mass of solids available in a size interval of 1µm (e.g. 9 to 10µm) than a size interval of 10µm (e.g. 10 to 20µm), a 'visual' leap in the pore size distribution envelope appears when particle size intervals expand 10 times in size. Such leap could have been removed if both variables (i.e. cumulative population and size) had been plotted at a linear scale (see below plots). However, next section (A5.3) shows that this error has no impact on the data interpretation within the present work.

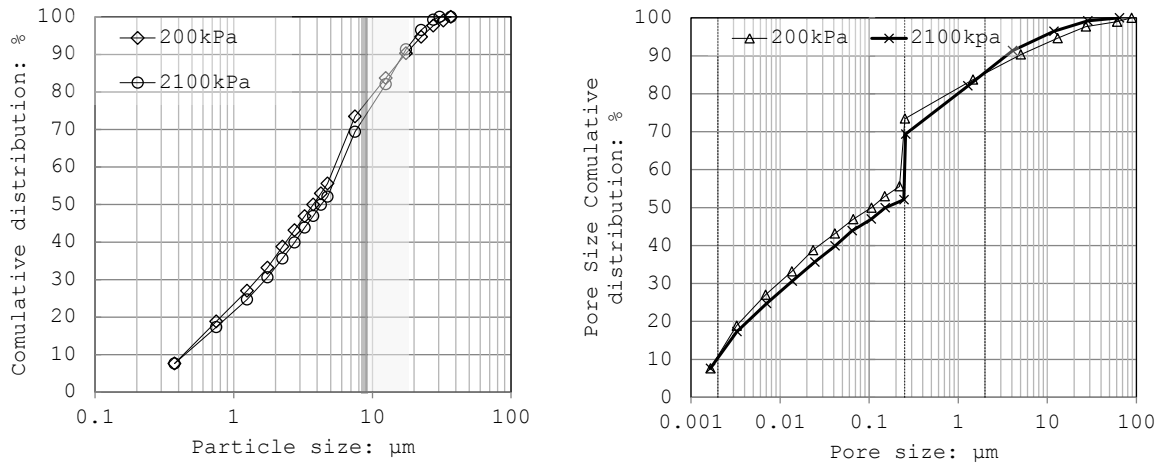

Fig. A5.1. a 'visual' leap appears between the 9.0-10 µm size fraction and 10-20 µm size fraction

A working example of model computation is explained below for a confined 'ideal loess' specimen under 200kPa of vertical stress.

Dry Stress State Surface: 200 kPa

$W_s = 74.1\ g$

$e = 1.05, \gamma_w = 0.001\ g/mm^3, G_s = 2.65$

$\gamma_s = 2.65 \times 1 = 2.65\ g/cm^3$

D_i: μm		$\bar{R}_i$: cm	W_i		Passing %	n_i	Y	α_i	$n_i^{1-\alpha_i}$	r_i: cm
0.5	1.0	3.75E-05	0.0765	0.0765	7.65	1.3062E+11 *	15.67431 **	1.4100 ***	2.7650E-05	1.6488E-07 ■
1.0	2.0	0.000075	0.1123	0.1888	18.88	2.3991E+10	14.95218	1.4405	2.6784E-05	3.24569E-07
2.0	3.0	0.000125	0.0814	0.2702	27.02	3755859806	13.93841	1.4557	4.3281E-05	6.87653E-07
3.0	4.0	0.000175	0.0615	0.3317	33.17	1033259315	13.08376	1.4514	8.5201E-05	1.35073E-06
4.0	5.0	0.000225	0.0562	0.3879	38.79	444655155	12.45914	1.4407	0.00015448	2.33846E-06
5.0	6.0	0.000275	0.0434	0.4314	43.14	188135734	11.7707	1.4225	0.00031898	4.10702E-06
6.0	7.0	0.000325	0.0377	0.4690	46.90	98854309	11.2244	1.4039	0.00058958	6.59881E-06
7.0	8.0	0.000375	0.0307	0.4997	49.97	52424842	10.6628	1.3813	0.00113957	1.05855E-05
8.0	9.0	0.000425	0.0300	0.5297	52.97	35243650	10.3008	1.3649	0.00176303	1.4922E-05
9.0	10	0.000475	0.0260	0.5558	55.58	21896948	9.8579	1.3429	0.00303679	2.18881E-05
10	20	0.00075	0.1788	0.7345	73.45	38178091	10.3743	1.3683	0.00161252	2.51838E-05
20	30	0.00125	0.1025	0.8371	83.71	4730481	8.3857	1.2563	0.01946169	0.000145817
30	40	0.00175	0.0661	0.9032	90.32	1110438	6.9735	1.1535	0.1180204	0.000502717
40	50	0.00225	0.0433	0.9456	94.56	342384	5.8533	1.0576	0.47994500	0.001303424
50	60	0.00275	0.0303	0.9768	97.68	131309	4.9795	0.9728	1.37635407	0.002697771
60	70	0.00325	0.0131	0.9899	98.99	34303	3.8395	0.8465	4.96366216	0.006054688
70	77	0.00367	0.0101	1.0	100.00	18368	3.3486	0.7853	8.23024414	0.008815989
			Sum=1							

* $n_i = \dfrac{3 \times 0.0765}{4\pi.(3.75 \times 10^{-5})^3.2.65} = 1.3062 \times 10^{11}$

** $Y = \dfrac{Y_F.Y_i}{Y_i + (Y_f - Y_i)exp[-\mu(x + \Delta x)]} - \Delta Y = \dfrac{19.686 \times 0.719}{0.719 + (19.686 - 0.719).e^{\{-0.457 \times (0.684 + Log\,(1.3062 \times 10^{11}))\}}} - 1.902 = 15.67431$

*** $\alpha_i = \dfrac{Log\ N_i}{Log\ n_i} = \dfrac{Y}{Log\ n_i}$

■ $r_i = 3.75 \times 10^{-5} \sqrt{\dfrac{4 \times 1.0488 \times 2.765 \times 10^{-5}}{6}} = 1.6488 \times 10^{-7}\ cm$

RL 1.3 Impact of the visual error in Arya-Paris model on the data interpretation in the present work

An important output of Section 4.3, dynamics of stress and hydraulic history, is the multi-porosity features of the ideal loess material. As such, in the concluding section 4.3.5, four levels of pore size intervals are introduced, within which the pore population changes with the pore size in a particular trend upon self-weight wetting. These four levels are shown in below plot (a reproduction of Fig. 4.14):

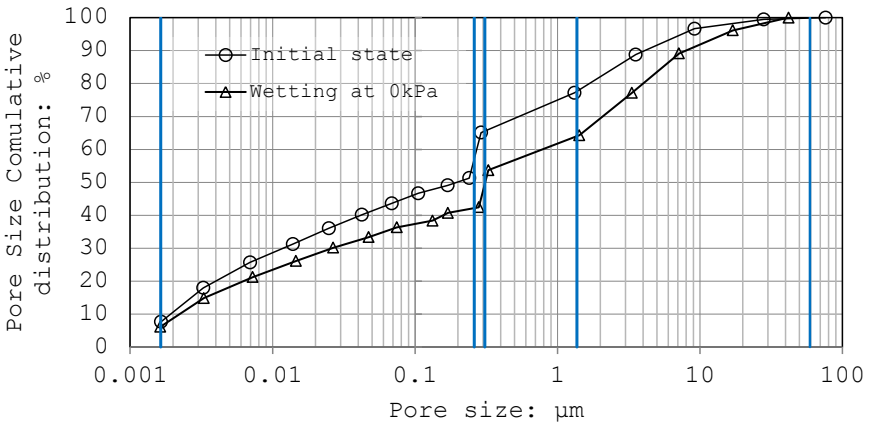

Fig. A5.2 A a reproduction of Fig. 4.14

From this plot, following observation were made:

- Pore spaces of less than 0.0016 µm (associated with particles sized between the minimum grain size and 1/2 µm: a resolution in accordance with the Arya-Paris model for loess soils – see Mingbin et al. 2009), were termed here as **micro-pore spaces (Zone 1).**

- For pore spaces of 0.0016 to 0.25 µm in size, larger pores lose relatively higher degrees of their population in the event of wetting **(meso-pore spaces - Zone 2).**

- For pore spaces of 0.26 to 0.31 µm in size, *the visual irregularity in the plot was observed*, which was attributed to the semi-logarithmic presentation of data (as fully discussed above).

- For pore spaces of 0.33 µm to 1.47 µm in size, no significant change in the degree to which the population of certain-sized pores decrease upon wetting was observed **(macro-pore spaces - Zone 3).**

- For pore spaces of 1.47 µm to 59.15 µm (i.e. maximum pore size in the testing material), larger pores lose relatively lower degrees of their population in the event of wetting (**trans-assemblage pore spaces - Zone 4**).

Since *the size interval associated with the visual leap* in the particle size distribution is not considered in graph interpretation, such error was deemed to have no control on the developed multi-porosity concept in the concluding Section 4.3.5.

A6. Schematic drawings of the proposed oedometer cell for future works

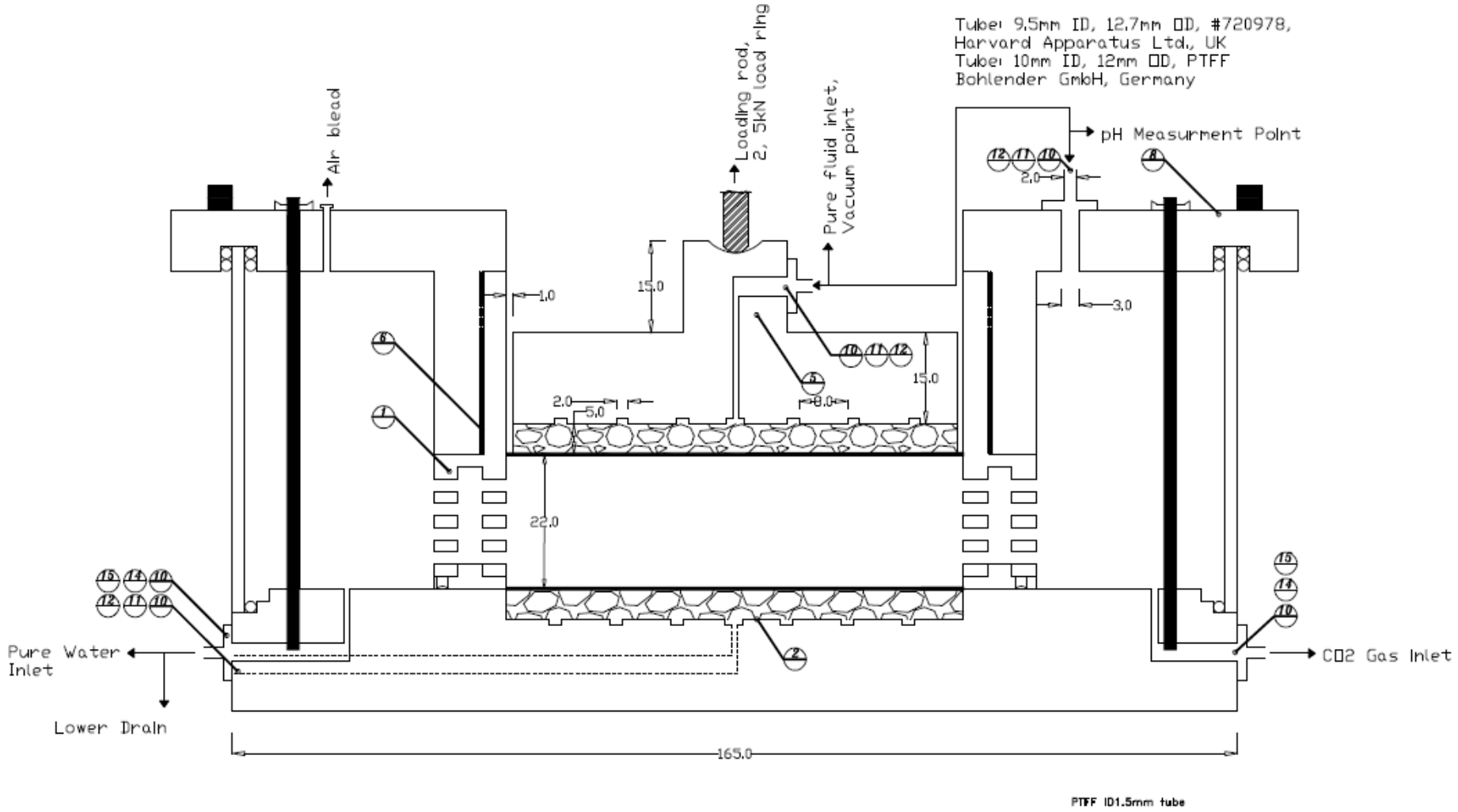

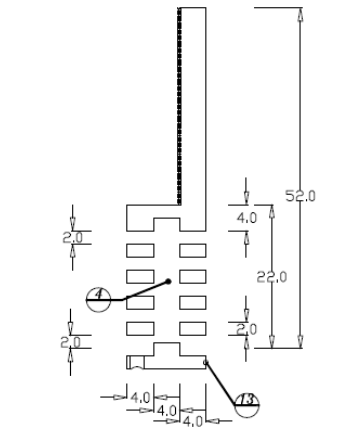

DET.2 POROUS RING

Sc.: 5.0mm

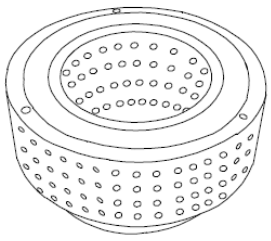

DET.2 POROUS RING
Front 3D view (2-pieces required)

NOT TO SCALE

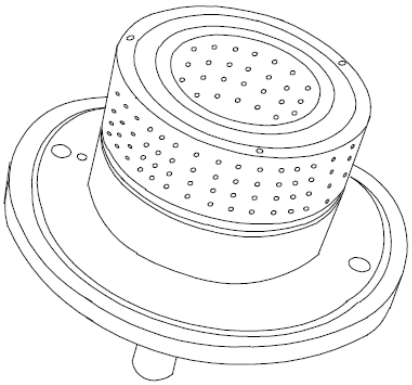

DET.6 SCREW, ASSEMBLY OF LOWER AND UPPER CELL BODY

NOT TO SCALE

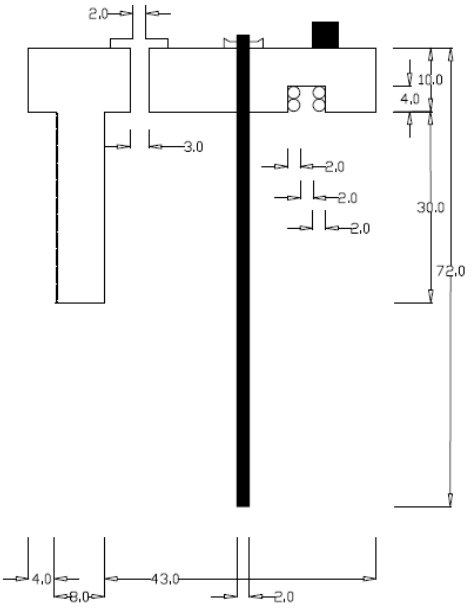

DET.8 UPPER CELL BODY

Sc.: 5.0mm

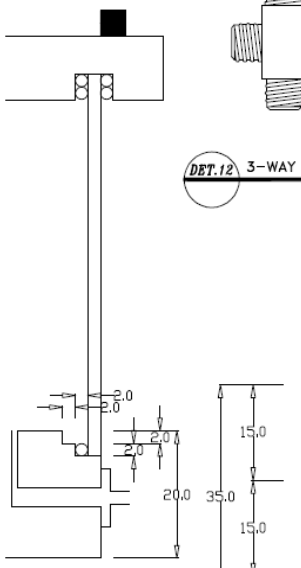

DET.9 LOWER CELL BODY

Sc.: 5.0mm

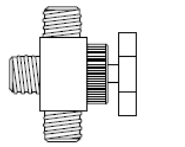

DET.12 3-WAY BALL VALVE

NOT TO SCALE

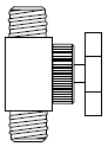

DET.14 2-WAY BALL VALVE

NOT TO SCALE

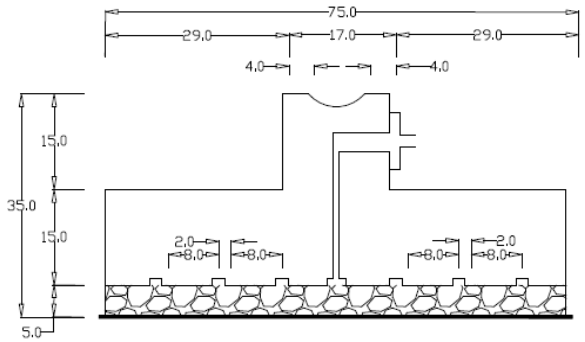

DET.5 SEQUENCE OF FILTER PAPER POROUS STONE, TOP CAP

Sc.: 5.0mm

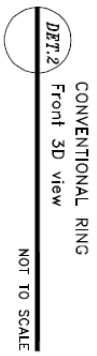

DET.2 CONVENTIONAL RING
Front 3D view

NOT TO SCALE

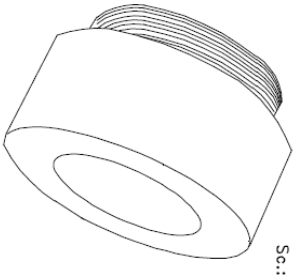

DET.2 GROOVED BASE

Sc.: 10.0mm

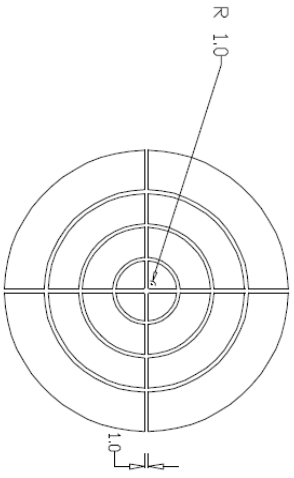

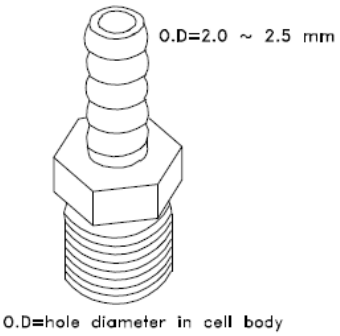

DET.10 STAINLES STEEL BARB CONNECTOR MALE TUBE

NOT TO SCALE

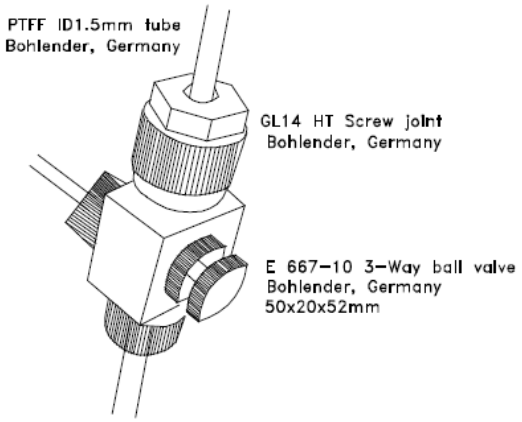

DET.11 ASSEMBLY OF TUBES 8mm SCREW JOINTS TO 3-WAY BALL VALVE

NOT TO SCALE

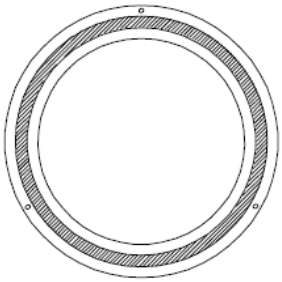

DET.13 LID

Sc.: 5.0mm

DET.4 Geotextile/Fine Sand

NOT TO SCALE

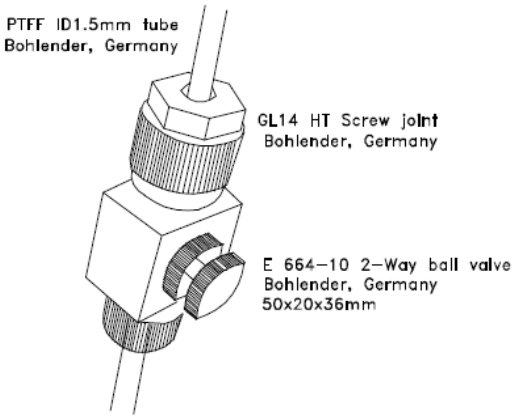

DET.15 ASSEMBLY OF TUBES 8mm SCREW JOINTS TO 2-WAY BALL VALVE

NOT TO SCALE

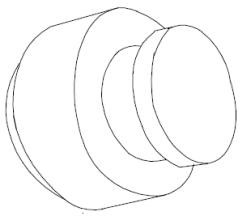

DET.A STATIC COMPRESSION PISTON

Sc.: 5.0mm

A7. Outputs (List of Publications)

Journal Publications

- ASSADI, A., JEFFERSON, I., O'HARA DHAND, K., & SMALLEY, I., 2013, Micromechanics of Quartz Sand Breakage in a Fractal Context, ***Geomorphology***, 211, 1-10.

- ASSADI, A., & JEFFERSON, I., 2013, Collapsibility in Calcareous Clayey Loess: A Factor of Stress-Hydraulic History, ***International Journal of Geomaterials****, 5(1),* 619-626.

- ASSADI, A., 2013, Discussion: Quantitative Evaluation of Microstructure Characteristics of Cement Consolidated Soil (*by)* CHEN, H., ZHANG, J., & YAN, H., (*in)* ***Bulletin of Engineering Geology and Environment***, (DOI: 10.1007/s10064-013-0558-4).

Conference Presentations

- O'HARA DHAND, K., ASSADI, A., JEFFERSON, I., SMALLEY, I., 2013, the control of loess grain shape in size distribution data, In: NIELD, J, & WILSON, R. (eds.) ***19th Windy Day****: UK aeolian research community meeting*, University of Southampton.

- ASSADI, A., & JEFFERSON, I., 2013, the Loess Genome Project. In: O'HARA-DHAND, K. & MCLAREN, S. (eds.) ***INQUALoess2013*** *Workshop: Loess & Dust: Geography-Geology-Archaeology*. University of Leicester: Print Services, University of Leicester.

Submitted

- ASSADI, A. 2014. Shear Strength in Terms of Coulomb C-Intercept, ***Applied Geology***, 10 (1)

- ASSADI, A., & JEFFERSON, I., 2014. A modified form of the principle of effective stress for collapsing soils, ***Soils and Foundations****,* SANDF-D-14-00036.

Ready for Submission

- ASSADI, A., & JEFFERSON, I, Implementation of a novel inter-particle force measurement method to model soil collapse, ***Géotechnique Letters***.

- JEFFERSON, I., ASSADI, A., GILBERT, P., ALOBAIDI, I. Identification and Risk Assessment of Unsaturated Collapsing Soils, ***Engineering Geology***.

- ASSADI, A., JEFFERSON, I., GILBERT, P. Constraints to the Current Compaction Practice in Fine-grained Fills. , ***Bulletin of Engineering Geology and Environment***.

Planned/Under Preparation

- JEFFERSON, I., NORTHMORE, K.J., CULSHAW, M., ASSADI, A., & FALL, D.A., 2014. Loess Soils in the UK: Genesis and Formation, ***Quarterly Journal of Engineering Geology and Hydrology***.

- ASSADI, A., McLAREN S., O'HARA DHAND, K., JEFFERSON, I., & SMALLEY, I., Sand: 63µm-2mm, 1-4Φ, ***Earth Science Reviews***.

- JEFFERSON, I., ASSADI, A., GILBERTS, P., ALOBAIDI, I., Modified Ground Improvement Practice in Collapsing Soils: A Proposal, ***Quarterly Journal of Engineering Geology & Hydrogeology***

REFERENCES

AASHTO T 224-01 2001. Standard method of test for correction for coarse particles in the soil compaction test, Standard specifications for transportation materials and methods of sampling and testing, Part II: Methods of Sampling and Testing. Washington, D.C.: American Association of State Highway and Transportation Officials.

ABBIREDDY, C. O. R. & CLAYTON, C. R. I. 2009. A review of modern particle sizing methods. *Proceedings of the Institution of Civil Engineers-Geotechnical Engineering,* 162**,** 193-201.

ABDULLAH, W. S., ALZOUBI, M. S. & ALSHIBLI, K. A. 1997. On the physicochemical aspects of compacted clay compressibility. *Canadian Geotechnical Journal,* 34**,** 551-559.

AITCHISON, G. D. Year. Relationship of moisture stress and effective stress functions in unsaturated soils. *In:* Pore Pressure and Suction in Soils, 1960 London, Butterworths. 47-52.

AKILI, W. & TORRANCE, J. K. 1981. The development and geotechnical problems of Sabkha, with preliminary experiments on the static penetration resistance of cemented sands. *Quarterly Journal of Engineering Geology,* 14**,** 59-73.

AL-RAWAS, A. A. 2000. State-of-the-art review of collapsible soils. *Science and Technology,* Special Review**,** 115-135.

AL-RAWAS, A. A. & MCGOWN, A. 1999. Microstructure of Omani expansive soils. *Canadian Geotechnical Journal* 36**,** 272-290.

ALONSO, E. E., PEREIRA, J. M., VAUNAT, J. & OLIVELLA, S. 2010. A microstructurally based effective stress for unsaturated soils. *Geotechnique,* 60**,** 913-925.

ARKELL, W. J. & TOMKEIEFF, S. I. 1953. "English rock terms", 139 pp. University of Durham Publications, Oxford University Press, . *Geological Journal,* 1**,** XXI-XXI.

ARYA, L. M., LEIJ, F. J., VAN GENUCHTEN, M. T. & SHOUSE, P. J. 1999. Scaling parameter to predict the soil water characteristic from particle-size distribution data. *Soil Science Society of America Journal,* 63**,** 210-519.

ARYA, L. M. & PARIS, J. F. 1981. A physicoempirical model to predict the soil moiture characteristic from particle-size distribution and bulk density data. *Soil Science of America Journal,* 45**,** 1023-1030.

ARYA, L. M. & PARIS, J. F. 1982. Reply to comments on: A physicoempirical model to predict the soil moisture characteristic from particle-size distribution and bulk density data. *Soil Science Society of America Journal,* 46**,** 1348-1349.

ASGHARI, E. 2002. *Effect of cementation on shear strength and deformation parameters of course grained soils with reference to Tehran alluvium.* Unpublished thesis - Doctor of Philosophy (Ph.D.), Tarbiat Modares University.

ASKALONOV, V. V. 1949. Silicatization of loess soils [in Russian] in Sokolivich, V. E., 1965, Silicatization of loess soils, Soil Mechanics and Foundation Engineering, Vol. 2 (1), pp. 3-7. *Mashstroiizdat*.

ASSADI, A. & JEFFERSON, I. 2013. The loess genome map. *In:* O'HARA-DHAND, K. & MCLAREN, S. (eds.) *INQUALoess2013 Workshop: Loess & Dust: Geography-Geology-Archaeology.* University of Leicester: Print Services, University of Leicester.

ASSADI, L. A. 2007. *Effect of chemical pollution, side friction, specimen size, drainage conditions and microfabric on swelling pressure.* Unpublished thesis - Master of Science (MSc.), Tarbiat Modares University.

ASSADI, L. A. 2009. Ground heave investigation of Pars Chemical Plant - causes, rehabilitation and maintenance. Tehran, Iran: POR Consulting Engineers.

ASSADI, L. A. & YASROBI, S. S. 2007. Effect of acidic-alkaline pollution intrusion into an unsaturated expansive soil mass on swelling pressure parameter. *60th Canadian Geotechnical Conference* 1940-1947.

ASSADI, L. A. & YASROBI, S. S. 2010. Microfabric transformation of Teleqan white clay under constant volume swelling condition *Engineering Geology***,** 116, 207-217.

ASSADI, L. A. & YASROBI, S. S. 2012. Drainage Controlled Uniaxial Swelling Cell. *ICE Geotechnical Engineering (Thomas Telford),* 166 (4), 357-364.

ASSALLAY, A. M. 1998. *Structure and Hydrocollapse behaviour of loess.* Unpublished thesis - Doctor of Philosophy (Ph.D.), Loughborough University.

ASSALLAY, A. M., ROGERS, C. D. F. & SMALLEY, I. J. 1996. Engineering properties of loess in Libya. *Journal of Arid Environments,* 32**,** 373-386.

ASSALLAY, A. M., ROGERS, C. D. F., SMALLEY, I. J. & JEFFERSON, I. F. 1998. Silt: 2-62 µm, 9-4 phi. *Earth-Science Reviews,* 45**,** 61-88.

ASTM 2003. standard test method for measurement of soil potential (suction) using filter paper, D 5298-03 West Conshohocken, PA: ASTM International.

ASTM:D698-12 2012. Standard Test Methods for Laboratory Compaction Characteristics of Soil Using Standard Effort.

AVERY, B. W., BULLOCK, P., CATT, J. H. & A.H., W. 1982. Composition and origin of some brickearths on the Chiltern Hills, England. *Brauschweig,* 9**,** 153-174.

BAGHERIEH, A. R., KHALILI, N., HABIBAGAHI, G. & GHAHRAMANI, A. 2009. Drying response and effective stress in a double porosity aggregated soil. *Engineering Geology,* 105**,** 44-50.

BARDEN, L., MCGOWN, A. & COLLINS, K. 1973. Collapse mechanicsm in partly saturated soil *Engineering Geology,* 7**,** 49-60.

BEAR, J. 1972. *Dynamics of fluids in porous media,* Dover, New York.

BELL, F. G., CULSHAW, M. G. & NORTHMORE, K. J. 2003. The metastability of some gull-fill materials from Allington, Kent, UK. *Quarterly Journal of Engineering Geology and Hydrogeology,* 36**,** 217-229.

BENTLEY, S. P. & ROGERS, A. J. 1995. Consideration of the possible contribution of Amorphous phases to the sensitivity of Glaciomarine clay. *In:* DIJKSTRA, T. A. & SMALLEY, I. (eds.) *Genesis and properties of collapsible soils.* Netherlands: Kluwer Academic Publishers.

BETTIS III, E. A., MUHS, D. R., ROBERTS H. M., WINTLE, A. G. 2003. Last glacial loess in the conterminous USA. *USGS Staff Published Research*, University of Nebraska – Lincoln.

BISHOP 1959. The principle of effective stress. *Teknisk Ukeblad,* 106**,** 859-863.

BISHOP, A. W. & BLIGHT, G. E. 1963. Some aspects of effective stress in saturated and partly saturated soil. *Geotechnique,* 13 (3)**,** 177-197.

BLATT, H. 1970. Determination of mean sediment thickness in the crust: a sedimentologic method. *Geological Society of America Bulletin,* 81**,** 255-262.

BLATT, H., and SCHULTZ, D.J., 1976. Size distribution of quartz in mudrocks. Sedimentology 23, 857-866.

BLATT, H., 1987. Oxygen isotopes and the origin of quartz. Journal of Sedimentary Petrology 57 (2), 373-377.

BLYTH, F. G. H. & DE FREITAS, M. H. 2006. A geology for engineers *In:* ARNORLD, E. (ed.) Seventh ed. Oxford: Elservier.

BRABY, C. E. 2001. Coccolithophorids: Quick facts [report]. Monterey Bay Aquarium Research Institute. Moss Landing, California, USA.

BOARDMAN, D. I., ROGERS, D. F., JEFFERSON, I., ROUAIGUIA, A. & XV ICSMGE, X. I. 2001. *Physico-chemical characteristics of British loess,* Leiden, A a Balkema Publishers.

BOLTON, M. D. 1999. The role of micro-mechanics in soil mechanics. *International workshop on soil crushability.* Yamaguchi University, Japan.

BORJA, R. I. 2004. Cam-Clay plasticity. part V: A mathematical framework for three-phase deformation and strain localization analyses of partially saturated porous media. *Comp. Mech. Appl. Mech. Engng.* 193 (48-51), 5301-5338.

BORJA, R. 2006. On the mechanical energy and effective stress in saturated and unsaturated porous materials. *Int. J. Solids Structs.* 43 (6), 1764-1786.

BORJA, R. I. & KOLIJI, A. 2009. On the effective stress in unsaturated porous continua with double porosity. *Journal of the Mechanics and Physics of Solids,* 57**,** 1182-1193.

BROMS, B. B. & BOMAN, P. 1977. Stabilisation of soil with lime columns. *Ground Engineering,* 12**,** 23-32.

BROOKS, R. J. & COREY, A. T. 1964. Hydraulic properties of porous media. *Hydrol. Pap.,* 3.

BROWN, G. J., MILES, N. J. & JONES, T. F. 1996. A fractal description of the progeny of single impact single particle breakage. *Minerals Engineering,* 9**,** 715-726.

BROWN, P. E. 2008. *Rhizoliths* [Online]. University of Wisconsin-Madison. [Accessed].

BS1377-4 1990. Methods of test for soils for civil engineering purposes: Compaction-related tests. BSi.

BS-6031:2009 Code of practice for earthworks. *BSI Standards Publication.* United Kingdom BSi.

BS-EN-ISO-14688-2:2004 2007. Geotechnical investigation and testing - Identification and classification of soil, Part 2: Principles for a classification *BSi British Standard*

BS 1377-2 1990. Methods of test for Soils for civil engineering purposes: Classification tests. BSi.

BS 1377-5 1990. Methods of test for Soils for civil engineering purposes - Part 5: Compressibility, permeability and duribility tests. BSi.

BS EN 1997-1:2004 2004. Eurocode 7. Geotechnical design. General rules. BSi.

BURLAND, J. B., CHAPMAN, T., SKINNER, H. & BROWN, M. (eds.) 2012. *ICE manual of geotechnical engineering, Vol. 1., Geotechnical engineering principles, problematic soils and site investigation,* Glasgow, Great Britain: Institute of Civil Engineers (ICE).

CASEY, W. H., WESTRICH, H. R. & HOLDREN, G. R. 1991. Dissolution rates of plagioclase at pH=2.0 and 3.0 *American Mineralogist,* 76**,** 211-217.

CATT, J. A. 1978. The contribution of loess to soils in lowland Britain. *In:* LIMBREY, S. & EVANS, J. G. (eds.) *The effect of man on the landscape: the lowland zone.* London: Council for British Archaeology, The Chameleon Press Limited.

CATTELL. A.C. 1997. The development of loess-bearing soil profiles on Permian Breccias in Torbay. *Annual Conference of the Ushher Society*. 9, 168-172.

CGS. 2001. Evaporite karst subsidence. Colorado Geological Survey ROCKTALK, 4(4), 6-8

CHANDRASEKHAR, S., RAGHAVAN, P., SEBASTIAN, G. & DAMODARAN, A. D. 1997. Brightness improvement studies on kaolin based zeolite 4A. *Applied Clay Science,* 12**,** 221-231.

CHARLES, J. A. & WATTS, K. S. 2001. *Building on fill: geotechnical aspects by BRE Centre for Ground Engineering and Remediation*, Construction Research Communications Ltd: by permission of Building Research Establishment Ltd.

CHENG, Y. P. 2004. *Micromechanical investigation of soil plasticity.* Doctoral of Philosophy (unpublished thesis), Cambridge University.

CHOU, C. W., SEAGREN, E., AYDILEK, A. & MANUGEL, T. 2008. Bacterially induced calcite precipitation via Ureolysis. Washington DC, USA: American Society for Microbiology.

CLEVENGER, W. 1958. Experience with loess as foundation material. Transactions, American Society of Civil Engineers, ASCE, 123, 151-170

COLLINS, K. 1978. *A scanning electron microscopy study of natural engineering soils.* Unpublished thesis - Doctor of Philosophy (PhD), University of Strathclyde.

COOP, M. R. & ALTUHAFI, F. N. 2011. Changes to particle characteristics associated with the compression of sands. *Geotechnique,* 61**,** 459-472.

COOPER, J. 1998. Particle size analysis - the Laser Diffraction technique. *Material World,* 6 (1)**,** 5-7.

COSTANTINI, E. A. C., PRIORI, S., URBAN, B., HILGERS, A., SAUER, D., PROTANO, G., TROMBINO, L., HÜLLE, D. & NANNONI, F. 2009. Multidisciplinary characterization of the middle Holocene eolian deposits of the Elsa River basin (central Italy). *Quaternary International,* 209**,** 107-130.

COUSSY, O. 2007. Revisiting the constitutive equations of unsaturated porous solids using a Lagrangian saturation concept. *Int. J. Numer. Analyt. Meth. Geomech.* 31 (15), 1675-1694.

COX, D. R. & HINKLEY, D. V. 1974. *Theoretical Statistics*, Chapman & Hall.

CRONEY, D., COLEMAN, J. D. & BLACK, W. P. M. 1958. Movement and distribution of water in soil in relation to highway design and performance. *Water and its conduction in soils,* Special Report No. 40**,** 226-252.

CUI, Y. I. & DELAGE, P. 1996. Yielding and plastic behaviour of an unsaturated compacted silt. *Geotechnique,* 46**,** 291-311.

CUNDALL, P. A. & STRACK, O. D. L. 1979. DISCRETE NUMERICAL-MODEL FOR GRANULAR ASSEMBLIES. *Geotechnique,* 29**,** 47-65.

D'ARCHIAC, A. 1839. Observations sur le groupe moyen de la formation crétacée. *Paris, F.G. Levrault,* .

D'ONZA, F., GALLIPOLI, D., WHEELER, S., CASINI, F., VAUNAT, J., KHALILI, N., LALOUI, L., MANCUSO, C., MAŠÍN, D., NUTH, M., PEREIRA, J. M. & VASSALLO, R. 2011. Benchmark of constitutive models for unsaturated soils. *Geotechnique* [Online], 61.

DAVIS, B. 2009. *The glacial history of Northern England* [Online]. Durham: Durham University. [Accessed].

DEAKIN, W. H. 1986. Kent minerals subject plan, Brickearth, Written Statement. Springfield, Maidstone.

DELAGE, P., CUI, Y. J. & ANTOINE, P. 2006. Geotechnical problems related with loess deposits in Northern France. *International conference on problematic soils.* Famagusta, North Cyprus.

DELLEUR, J. W., 2007. The handbook of groundwater engineering. 2nd Edition, CRS Press, Taylor & Francis Group, United States of America.

DENISOV, N.Y. 1951. The engineering properties of loess and loess loams, Gosstroiizdat, Moscow

DERBYSHIRE, E., Carrillo, T., Menendez, I., Engelbrecht, J. P., Romero, L. E., Mayer, P. L., Caballero, E., Rodriguez de Castro, F. C. B. 2013. *In:* O'HARA-DHAND, K. & MCLAREN, S. (eds.) *INQUALoess2013 Workshop: Loess & Dust: Geography-Geology-Archaeology.* University of Leicester: Print Services, University of Leicester.

DERBYSHIRE, E. & MELLORS, T. W. 1988. Geological and geotechnical characteristics of some loess soils from China and Britain - a comparison *Engineering Geology,* 25**,** 135-175.

DERBYSHIRE, E., MENG, X. & DIJKSTRA, T. A. 2000. *Landslides in the thick terrain of north-west China,* Chichester, West Sussex, England, John Wiley & Sons, Ltd.

DERBYSHIRE, E., MENG, X. M., WANG, J. T., ZHOU, Z. Q. & LI, B. X. 1995. Collapsible loess on the Loess Plateau of China. *In:* DERBYSHIRE, E., DIJKSTRA, T. & SMALLEY, I. J. (eds.) *Genesis and Properties of Collapsible Soils.* Dordrecht: Kluwer Academic Publ.

DEYNOUX, M., MILLER, J. M. G., DOMACK, E. W., EYLES, N., FAIRCHILD, I. J. & YOUNG, G. M. 1994. Earth's glacial record. Press syndicate of the University of Cambridge.

DIBBEN, S. C. 1998. *A microstructure model for collapsing soils.* Unpublished thesis - Doctor of Philosophy (PhD), Nottingham Trent University.

DIJKSTRA, T. A. 2001. Geotechnical thresholds in the Lanzhou loess of China. *Quaternary International,* 76–77**,** 21-28.

DIJKSTRA, T. A., ROGERS, C. D. F., SMALLEY, I. J., DERBYSHIRE, E., LI, Y. J. & MENG, X. M. 1994. The loess of north-central China: Geotechnical properties and their relation to slope stability. *Engineering Geology,* 36**,** 153-171.

DIPOVA, N. & DOYURAN, V. 2006. Assessment of the collapse mechanisms of tufa deposits. *Engineering Geology,* 83**,** 332-342.

EMERIAULT, F. & CHANG, C. A. 1997. Interparticle forces and displacements in granular materials. *Computers and Geotechnics,* 20**,** 223-244.

EN13286-2:2010 2010. Unbound and hydraulically bound mixtures - Part 2: Test methods for laboratory reference density and water content - Proctor compaction. *CEN/TC 227 - Road materials.* European Committee for Standardization.

EROL, O. A. and EL-RUWAIH, I. A. 1982. Collapse behaviour of desert loess. Proc. 6th Congress International Association of Engineering Geology, 1, New Delhi, 443-448.

ESHEL, G., LEVY, G. J., MINGELGRIN, U. & SINGER, M. J. 2004. Critical Evaluation of the Use of Laser Diffraction for Particle-Size Distribution Analysis. *Soil Science Society of America Journal,* 68**,** 736-743.

EVSTATIEV, D. 1995. Design and treatment of loess bases in Bulgaria. *In:* DIJKSTRA, T. A. & SMALLEY, I. (eds.) *Genesis and properties of collapsible soils.* Netherlands: Kluwer Academic Publishers.

FALL, D. A. 2003. *The geotechnical and geochemical characterisation of the Brickearth of Southern England.* Unpublished thesis - Doctor of Philosophy (PhD), University of Portsmouth.

FEDA, J. 1966. Structural stability of subsident loess soil from Praha-Dejvice. *Engineering Geology,* 1**,** 201-219.

FEDA, J. 1964. Colloidal activity, shrinking and swelling of some clays. Proceedings of Soil Mechanic Seminar, Loda, Illinois, 531-546.

FEDA, J. 1988. Collapse of loess upon wetting. *Engineering Geology,* 25**,** 263-269.

FINK, J. 1974. INQUA Loess Commission Circular Letter. *Beilage 1 Quadrenniel Report*

FRATTA, D. & SANTAMARINA, J. C. 2005. Strains due to coupled phenomena - Particle-level analyses. *In:* ULM, F. J., ABOUSLEIMAN, Y. N., ALEXANDER, H. & CHENG, D. (eds.) *3rd Biot Conference on Poromechanics.* Norman, Oklahama, USA: Taylor & Francis.

FREDLUND, D. G. & RAHARDJO, H. 1993. *Soil mechanics for unsaturated soils*, John Wiley & Sons Inc.
FUENTES, W. & TRIANTAFYLLIDIS. 2013. On the effective stress for unsaturated soils with residual water. *Geotechnique.* 63 (16), 1451-1455.
FUERSTENAU, M. C., HAN, K. N. 2003. *Principles of mineral processing,* Colorado, USA, Society of Mining, Metallurgy, and Exploration, Inc.
FUKUE, M., NAKAMURA, T. & KATO, Y. 1999. Cementation of soils due to calcium carbonate. *Soils and Foundations,* 39**,** 55-64.
FUKUE, M., SATO, Y., YAMASHITA, M., YANAI, M. & FUJIMORI, Y. 2003. Change in microstructure of soils due to natural mineralization. *Applied Clay Science,* 23**,** 169-177.
GALAI, B.F. (1987). Procedure and results of modelling of the collapsibility of aeolian loess soils. In: Soil Properties and Engineering Geological Properties of Loesses and Loess-Like Loams (in Russian), 102-109, Nauka, Moscow.
GALLIPOLI, D., GENS, A., SHARMA, R., & VAUNAT, J. 2003. An elastoplastic model for unsaturated soil incorpotaying the effects of suction and degree of saturation on mechanical behaviour. *Geotechnique*, 53 (1), 123-135.
GALLOIS, R. W. 2009. The origin of the clay-with-flints: The missing link. *Geoscience on South-West England,* 12**,** 153-161.
GENS, A. 2010. Soil environment interactions in geotechnical engineering. *Geotechnique.* 60 (1), 3-74.
GHERBI, M., GOURVES, R. & OUDJEHANE, F. Year. Distribution of contact forces inside a granular material. *In:* Proceedings of 2nd International Conference on Micromechanics of Granular Media, 1993 Birmingham, UK. Powders and Grains, 93, Elsevier, Amsterdam, 167-171.
GIBBS, H.J. 1961. Properties which divide loose and dense uncemented soils. Earth Laboratory report em-658, Bureau of Reclamation, US Department of the Interior, Washington, D.C.
GIBBS, H.J. and BARA, J.P. 1962. Predicting surface subsidence from basic soil tests. Special Technical publication No. 322, American Society for Testing and Materials (ASTM), 231-247.
GIBBS, H. J. & HOLLAND, W. Y. 1960. Petrographic and engineering properties of loess. Colorado: United States Department of the Interior Bureau of Reclamation.
GILBERT, P. 2010. Understanding the implications of the updated BS 6031 for earthworks designs. *Slope Stability 2010.* London, United Kingdom: Atkins Global Newsletter.
GILBERT, P., ALOBAIDI, I., JEFFERSON, I. & ASSADI, L. A. 2012. Earthwork challanges with calcareous loess in Kazakhstan. *Personal Communication At Atkins Geotechnique, 31th August 2012.* Birmingham, United kingdom.
GLASSEY, P. J. 1986. *Geotechnical properties of lime stabilised loess, Port Hills, Canterbury.* Master of Science (unpublished thesis), University of Canterbury.
GOCKE, M., PUSTOVOYTOV, K. & KUZYAKOV, Y. 2010a. Effect of CO2 concentration on the initial recrystallization rate of pedogenic carbonate -- Revealed by 14C and 13C labeling. *Geoderma,* 155**,** 351-358.
GOCKE, M., PUSTOVOYTOV, K. & KUZYAKOV, Y. 2010b. Carbonate recrystallization in root-free soil and rhizosphere of Triticum aestivum and Lolium perenne estimated by 14C labelling. *Biogeochemistry*.
GOUDIE, A.S., and MIDDLETON, N.J. 2001. Shaharan dust storms: nature and consequences. *Earth-Science Reviews*. 56, 179-204.
GOUDIE, A. S. 1983. Calcrete in: Chemical sediments and geomorphology. *In:* GOUDIE, A. S. & KENNETH, P. (eds.). Academic Press Inc.
GRABOWSKA-OLSZEWSKA, B. 1988. Engineering geological problems of loess in Poland. *Engineering Geology,* 25**,** 177-199.
GRABOWSKA-OLSZEWSKA, B. 1989. Skeletal microstructure of loesses - its significance for engineering-geological and geotechnical studies. *Applied Clay Science,* 4**,** 327-336.
GRAF, W. H. 1984. *Hydraulics of sediment transport,* Highlands Ranch, Colorado, Water Resources Publications.
GREGERSEN, O. 1981. The quick clay landslide in Rissa, Norway: the sliding process and discussion of failure modes. Norwegian Geotechnical Institute, Oslo, No. 135.
GRINE, K. & GLENDINNING, S. 2007. Creation of an artificial carbonate sand. *Geotechnical and Geological Engineering,* 25**,** 441-448.

GUNN, D. A., NELDER, L. M., JACKSON, P. D., NORTHMORE, K. J., ENTWISLE, D. C., MILODOWSKI, A. E., BOARDMAN, D. I., ZOURMPAKIS, A., C.D.F., R., JEFFERSON, I. & DIXON, N. 2006. Shear wave velocity monitoring of collapsible loessic brickearth soil. *Quarterly Journal of Engineering Geology and Hydrogeology,* 39**,** 173-188.

HAINES, W. B. 1925. Studies in the physical properties of soils II. A note on the cohesion develped by capillary forces in an ideal soil. *The Journal of Agrecultural Science,* 15**,** 529-535.

HALDORSEN, S. 1981. Grain-size distribution of subglacial till and its relation to glacial crushing and abrasion. *Boreas,* 10**,** 91-105.

HANDY, R. L. 1973. Collapsible loess in Iowa. *Soil Science Society of America Journal,* 37**,** 281-284.

HARDIN, B. O. 1985. Crushing of soil particles. *Journal of Geotechnical Engineering, Proc. ASCE,* 111**,** 1177-1192.

HARDY, F. 1925. Cohesion in colloidal soils. *The Journal of Agrecultural Science,* 15**,** 420-433.

HAVERKAMP, R., REGGIANI, P., ROSS, P. J., and PARLANGE, J. Y. 2002. Soil water hysteresis prediction model based on theory and geometric scaling. In Environmental Mechanics: Water, Mass and Energy Transfer in the Biosphere, RAATS, P. A. C., SMILES, D., and WARRICK, A. W. (Eds.), Geophysical Monograph 129, American Geophysical Union, Washington, 213-246.

HAVERKAMP, R. & PARLANGE 1982. Comments on: A physicoempirical model to predict the soil moisture characteristic from particle-size distribution and bulk density data. *Soil Science Society of America Journal,* 46**,** 1348-1349.

HILLEL, D. 1998. *Environmental siuk physics: Fundamentals, applications and environmental considerations*, Academic Press Inc.

HOULSBY, G. 1997. The work input to an unsaturated granular material. *Geotechnique.* 47 (1), 193-196.

HOUSTON, S. L., HOUSTON, W. N., ZAPATA, V. E., & LAWRENCE, C., 2001. Geotechnical engineering practice for collapsible soils. *Geotechnical and Geological Engineering*, 19, 333-355.

HOWARTH, J. J. 2010. The shape of loess particles reviewed. *Central European Journal of Geosciences,* 2(1)**,** 41-44.

HUE, N. V. 1995. Soil chemistry. University of Hawaii System.

HUTTER, K., LALOUI, L. & VULLIET, L. 1999. Thermodynamically based mixture models for saturated and unsaturated soils. *Mech. Cohesive-Frictional Mater.* 4 (4), 295-338.

HYSLIP, J. P. & VALLEJO, L. E. 1997. Fractal analysis of the roughness and size distribution of granular materials. *Engineering Geology,* 48**,** 231-244.

IRCOLD 1999. *Geotechnical design for collapsible soils and the importance in dam foundation,* Tehran, Iran.

ISAEV, B. N., ZELENSKII, V. Y., SHUVALOVA, L. P. & SEMENOV, Y. I. 1979. Stablization of saturated loess soils. *Fundamenty i Mekhanika Gruntov,* 2**,** 4-6.

ISMAIL, M. A., JOER, H. A., RANDOLPH, M. F. & MERITT, A. 2002. Cementation of porous materials using calcite. *Geotechnique,* 52**,** 313-324.

JARI, Z. & BADURA, J. 2013. Distribution and characteristics of loess in Lower Silesia with reference to the Great Odra Valley. *In:* O'HARA-DHAND, K. & MCLAREN, S. (eds.) *INQUALoess2013 Workshop: Loess & Dust: Geography-Geology-Archaeology.* University of Leicester: Print Services, University of Leicester.

JEFFERSON, I., & ROGERS, C.. 2012. Collapsible soils. In: BURLAND, J., CHAPMAN, T., SKINNER, H., & BROWN, M. (eds.) ICE Manual of Geotechnical Engineering. Institute of Civil Engineers, London.

JEFFERSON, I., TYE, C., NORTHMORE, K.J. 2001. Behaviour of silt: the engineering characteristics of loess in the UK. *In.* Jefferson, I., Murray, E.J., Faragher, E., and Fleming. P.R. (eds.) *Problematic Soils*, Thomas Telford.

JEFFERSON, I., JEFFERSON, B. Q., ASSALLAY, A. M., ROGERS, C. D. F. & SMALLEY, I. J. 1997. Crushing of quartz sand to produce silt particles. *Naturwissenschaften,* 84**,** 148-149.

JEFFERSON, I., ROGERS, C., EVSTATIEV, D. & KARASTANEV, D. 2005. Chapter 25 Treatment of metastable loess soils: Lessons from Eastern Europe. *In:* BUDDHIMA, I. & JIAN, C. (eds.) *Elsevier Geo-Engineering Book Series.* Elsevier.

JEFFERSON, I. & SMALLEY, I. 1995. Six definable particle types in engineering soils and their participation in collapse events: proposals and discussions. *In:* E., D., DIJKSTRA, T. A. & SMALLEY, I. (eds.) *Genesis and Properties of Collapsible Soils.*

JEFFERSON, I. F., SMALLEY, I. J. & NORTHMORE, K. G. 2003. Consequences of a modest loess fall over southern Britain. *American Geologist,* 15**,** 199-208.

JEHRING, S. 2007. Engineering Geology problems in loess deposits. *Oberseminar 06-07, Technische universitat bergakademie freiberg.* Freiberg, Germany.

JENNINGS, I. E. 1960. A revised effective stress law for use in the prediction of the behaviour of unsaturated soils. *Pore Pressure and Suction in Soils.* London, Butterworths.

JENNINGS, J. E. B. & BURLAND, J. B. 1962. Limitations to the use of effective stresses in partly saturated Soils. *Geotechnique,* 12 (2)**,** 125-144.

JENNINGS, J.E. and KNIGHT, K. 1975. A guide to construction on or with materials exhibiting additional settlement due to collapse of grain structure. Proceedings of the 6th Regional Conference for Africa on Soil Mechanics and Foundation Engineering, Durban, South Africa, 1, 99-105.

JONES, J. F. P. C., LAMOUNT-BLACK, J., GLENDINNING, S., BERGADO, D., ENG, T., FOURIE, A., LIMING, H., PUGH, C., ROMANTSHUK, M., SIMPANEN, S. & FENG, Z. 2008. Recent research and applications in the use of electro-kinetic geosynthetics. *The Fourth European Geosynthetics Conference.* Edinburgh Conference Centre, Heriot-Watt University, Scotland

JONES, R. & HODGES, C. 2004. Applications of atomic force microscopy to granular materials: inter-particle forces in air. *In:* ANTONY, S. J., HOYLE, W. & DING, Y. (eds.) *Granular materials: fundamentals and applications, pp. 229-254.* Cambridge: Royal Society of Chemistry.

JOSEPH, S. & THRIVIKRAMAJI, K. P. 2005. Rhizolithic calcrete in Teris, southern Tamil Nadu: Origin and paleoenvironmental implications. *Journal of the Geological Society of India,* 65**,** 158-168.

JOTISANKASA, A. 2005. *Collapse behaviour of a compacted silty clay.* Unpublished thesis - Doctor of Philosophy (PhD), Imperial College London.

KARIMI, A., KHADEMI, H., KEHL, M. & JALALIAN, A. 2009. Distribution, lithology and provenance of peridesert Joess deposits in northeastern Iran. *Geoderma,* 148**,** 241-250.

KATO, K. & KITANO, Y. 1968. Solubility and dissolution rate of amorphous silica in distilled and sea water at 20C. *Journal of Oceanographical Society of Japan,* 24**,** 147-152.

KEDRA-KROLIK, K. & GIERYCZ, P. 2010. Simulation of nucleation and growing of CaCO3 nanoparticles obtained in the rotating disk reactor. *Journal of Crystal Growth,* 312**,** 1945-1951.

KHALILI, N., WITT, R., LALOUI, L., VULLIET, L. & KOLIJI, A. 2005. Effective stress in double porous media with two immiscible fluids. *Geophysical Research Letters,* 32 (L15309)**,** 1-5.

KINGSTON, E., CLAYTON, C., PRIEST, J., BEST, A., 2008. Effect of grain characteristics on the behaviour of disseminated methane hydrate bearing sediments. Proceedings of the 6th International Conference on Gas Hydrates. Vancouver, British Columbia, Canada

KLUKANOVA, A. & FRANKOVSKA, J. 1995. The Slovak Carpathians loess sediments, their fabric and properties. *In:* DERBYSHIRE, E., DIJKSTRA, T. & SMALLEY, I. J. (eds.) *Genesis and Properties of Collapsible Soils.* Dordrecht: Kluwer Academic Publ.

KOLHOFF, I. M. & STENGER, V. A. 1933. The adsorption of calcium and copper from Ammoniacal medium by silica gel. *The Journal of Physical Chemistry,* XXXVIII**,** 474-486.

KRAUSKOPE, K. B. 1956. Dissolution and precipitation of silica at low temperatures. *Geochimica et Cosmochimica Acta,* 10**,** 1-26.

KRINSLEY, D. H. & DOORNKAMP, J. C. 1973. *Atlas of quartz sand surface textures,* London, Syndics of the Cambridge University Press.

KRINSLEY, D.H., & SMALLEY, I.J., 1973. Shape and nature of small sedimentary quartz particles. Science 180, 1277-1279.

KUCHARSKI, E., PRICE, G., LI, H. & JOER, H. A. Year. Engineering properties of CIPS-cemented calcareous sand. *In:* 30th geological congress, 1996 Beijing, Brill. Academia, 92-97.

KUMAR, R., JEFFERSON, I. F., O'HARA-DHAND, K. & SMALLEY, I. J. 2006. Controls on quartz silt formation by crystalline defects. *Naturwissenschaften,* 93**,** 185-188.

LAL, R. 2005. Encyclopedia of Soil Science. Taylor & Francis Inc.

LAMB, H. 1994. *Hydrodynamics,* Trinity College, Cambridge, Cambridge University Press.

LAMBE, T. W. & WHITMAN, R. V. 1969. *Soil mechanics (Series in soil engineering),* New York, John Wiley & Sons.

LANDI, A., MERMUT, A. R. & ANDERSON, D. W. 2003. Origin and rate of pedogenic carbonate accumulation in Saskatchewan soils, Canada. *Geoderma,* 117**,** 143-156.

LATTMAN, L. H. 1973. Calcium carbonate cementation of alluvial fans in southern Nevada. *Geological Society of America Bulletin,* 84**,** 3013-3028.

LEE, D., WOODGER, A. & ORTON, C. 1989. Excavations in the Walbrook Valley. *London Archaedogist,* 6**,** 115-119.

LEFEBVRE, G. 1995. Collapse mechanisms and design considerations for some partly saturated and saturated soils. *In:* DERBYSHIRE, E., DIJKSTRA, T. & SMALLEY, I. J. (eds.) *Genesis and Properties of Collapsible Soils.* Dordrecht: Kluwer Academic Publ.

LEIJ, D. J., ALVES, W. J., VAN GENUCHTEN, M. TH., and WILLIAMS, J. R. 1996, The UNSODA – Unsaturated Soil Hydraulic Database – User's Manual Version 1.0. Report EPA/600/R-96/095. National Risk Management Research Laboratory, Office of Research Development, U.S. Environmental Protection Agency, Cincinnati, OH, 45268, 1-103.

LILL, G. O. 1976. *The nature and distribution of loess in Britain.* Unpublished thesis - Doctor of Philosophy (PhD), University of Leeds.

LILL, G. O. & SMALLEY, I. J. 1978. Distribution of loess in Britain. *Proceedings of the Geologists' Association,* 89**,** 57-65.

LITTLE, D. 1995. Stabilisation of pavement subgrades and base courses with lime. Kendall Hunt Publishing Company.

LOURENCO, S. D. N., GALLIPOLI, D., AUGARDE, C. E., TOLL, D. G., FISHER, P. C., and CONGREVE, A. 2012. Formation and evolution of water menisci in unsaturated granular media. Geotechnique. 62 (3), 193-199.

LOWENSTAM, H. A. & WEINER, S. 1989. *On biomineralization,* New York, Oxford University Press.

LU, P., JEFFERSON, I. F., ROSENBAUM, M. S. & SMALLEY, I. J. 2003. Fractal characteristics of loess formation: evidence from laboratory experiments. *Engineering Geology,* 69**,** 287-293.

LU, N., GODT, Q. & WU, D. 2010. A closed-form equation for effective stress in unsaturated soil. *Water Resources Res.* 46 (5), doi:10.1029/2009WR008646.

LUTENEGGER, A.J. and SABER, R.T. 1988. Determination of collapse potential of soils. Geotechnical Testing Journal, American Society for Testing and Materials, ASTM, 11, 173-178

MADHAVARAJU, J., GARCÍA Y BARRAGÁN, J. C., HUSSAIN, S. M. & MOHAN, S. P. 2009. Microtextures on quartz grains in the beach sediments of Puerto Penasco and Bahia Kino, Gulf of California, Sonora, Mexico. *Revista Mexicana de Ciencias Geológicas,* 26**,** 367-379.

MANDELBROT, B. B. 1983. *The fractal geometry of nature,* New York, Freeman.

MANSOUR, Z., CHIK, Z. & TAHA, M. R. Year. On soil collapse potential evaluation *In:* International conference on construction and building technology, 2008 Kuala Lumpur, Malaysia. University Tenaga Nasional, 21-32.

MARASHI, P., KAVIANI, S., POOLAKI, H. & ZOLFAGHARI, A. R. 2005. *Fundamentals and application of electronic microscopes and analysis methods - Nano world investigation tools,* Tehran, Iran University of Science and Technology.

MATYAS, E. L. & RAHAKRISHNA, H. S. 1968. Volume change characteristics of partly saturated soils. *Geotechnique,* 18**,** 432-448.

MCDOWELL, G. R. & BOLTON, M. D. 2001. Micromechanics of elastic soil. *Soils and Foundations,* 41 (6)**,** 147-152.

MCKERVEY, J. A. & KEMP, S. J. 2001. Mineralogical analysis of Brickearth samples from Europe. *Internal Report IR/01/107.* Keyworth, Nottingham: British Geological Survey.

MCMURDO, D. & GOMEZ, P. 2005. Rains, soils vex road crews. *Rahrump Valley Times*.

MEDERO, G., SCHNAID, F., GEHLING, W. & GALLIPOLI, D. 2005. Analysis of the mechanical response of an artificial collapsible soil. *In:* SCHANZ, T. (ed.) *Unsaturated Soils: Experimental Studies.* Springer Berlin Heidelberg.

MEIER, H. A., SCHLEMMER, M., WAGNER, C., KERREN, A., HAGEN, H., KUHL, E. & STEINMANN, P. 2008. Visualization of particle interactions in granular media. *Transactions on Visualization and Computer Graphics,* 14**,** 1110-1125.

MELLORS, T. W. 1995. The influence of the clay component in loess on collapse of the soil structure. *In:* DERBYSHIRE, E., DIJKSTRA, T. & SMALLEY, I. J. (eds.) *Genesis and Properties of Collapsible Soils.* Dordrecht: Kluwer Academic Publ.

MENG, X. 1998. *Loess and Loess Instability in North China.* Unpublished thesis - Doctor of Phylosophy (PhD), Royal Holloway, University of London.

MILLER, H. 2002. *Modelling the collapse of metastable loess soils* Unpublished thesis - Doctor of Philosophy (PhD), The Nottingham Trent University.

MILODOWSKI, A. E., NORTHMORE, K. J., ENTWISLE, D. C., GUNN, D. A., NELDER, L. M., JACKSON, P. D., RAINES, M. R., BOARDMAN, D. I., ZOURMPAKIS, A., C.D.F., R., KARRI, R. S., DIXON, N., JEFFERSON, I. F., ROUAIGUIA, A. & I.J., S. In Press. The mineralogy and fabric of brickearths and their relationship to engineering properties *Bulletin of Engineering Geology*.

MINGBIN, H., FREDLUND, D. G. & FREDLUND, M. D. 2009. Estimation of SWCC from grain size distribution curves for loess soils in china. *62nd Canadian Geotechnical Conference* Halifax, NS, Canada.

MITCHELL, J. K. 1976. *Fundamentals of soil behaviour*, Wiley.

MITCHELL, J. K. & SOGA, K. 2005. *Fundamentals of soil behaviour, 3rd edn.,* New Jersey, Wiley.

MOLENAAR, N. & VENMANS, A. A. M. 1993. Calcium-carbonate cementation of sand - a method for producing artificially cemented samples for geotechnical testing and a comparison with natural cementation processes *Engineering Geology,* 35**,** 103-122.

MOSS, A. J. 1966. Origin, shaping and significance of quartz sand grains. *Journal of Geological Society of Australia,* 13**,** 97-136.

MOSS, A. J. 1973. Fatigue effects in quartz sand grains. *Sedimentary Geology,* 10**,** 239-247.

Moss, A.J., and Green, P. 1975. Sand and silt grains: predetermination of their formation and proper
ties by microfractures in quartz. Journal of Geological Society 22, 475-495.

MULILIS, J. P., CHAN, C. K. & SEED, H. B. 1975. The effects of method of sample preparation on the cyclic stress-strain behavior of sands. *Earthquake Engineering Research Centre, University of California, Berkeley,* Rept No. EERC 75-18.

MUNOZ-CASTELBLANCO, J. A., PEREIRA, J. M., DELAGE, P. & CUI, Y. I. 2012. The water retention properties of a natural unsaturated loess from northern France. *Geotechnique,* 62**,** 95-106.

NASROLLAHI, N. & ASSADI, L. A. 2007. Kharg Island NGL recovery *In:* IRAN INTERNATIONAL ENGINEERING COMPANY IRITEC (ed.) *Utility* Tehran, Iran: Rahvar Consulting Engineers.

NGI. 1978. *1978 - Rissa Historical landslide* [Online]. Oslo: Norwegian Geotechnical Institute. [Accessed].

NOLAN, G. T. & KAVANAGH, P. E. 1992. Computer simulation of random packing of hard spheres. *Powder Technology,* 72**,** 149-155.

NORTHMORE, K. J., BELL, F. G. & CULSHAW, M. G. 1996. The engineering properties and behaviour of the brickearth of south Essex. *Quarterly Journal of Engineering Geology,* 29**,** 147-161.

NORTHMORE, K. J., BELL, F. G. & CULSHAW, M. G. 1999. Some geotechnical properties of the Claygate 'Beds' and Bagshot 'Beds' of south Essex. *Quarterly Journal of Engineering Geology,* 32**,** 215-231.

NORTHMORE, K. J., JEFFERSON, I., JACKSON, P. D., ENTWISLE, D. C., MILODOWSKI, A. E., RAINES, M. R., GUNN, D. A., BOARDMAN, D. I., ZOURMPAKIS, A., NELDER, L. M., ROGERS, C. D. F., DIXON, N. & SMALLEY, I. J. 2008. On-site characterisation of loessic deposits in Kent, UK. *Proceedings of the Institution of Civil Engineers-Geotechnical Engineering,* 161**,** 3-17.

NOUAOURIA, M. S., GUENFOUD, M. & LAFIFI, B. 2008. Engineering properties of loess in Algeria. *Engineering Geology,* 99**,** 85-90.

O'HARA DHAND, K., ASSADI, A., JEFFERSON, I., SMALLEY, I., 2013, the control of loess grain shape in size distribution data, *In:* NIELD, J, & WILSON, R. (*eds.*) *19th Windy Day: UK aeolian research community meeting*, University of Southampton.

OSIPOV, V. I. & SOKOLOV, V. N. 1995. Factors and mechanism of loess collapsibility. *In:* DERBYSHIRE, E., DIJKSTRA, T. & SMALLEY, I. J. (eds.) *Genesis and Properties of Collapsible Soils.* Dordrecht: Kluwer Academic Publ.

OUHADI, V. R. & GOUDARZI, A. R. 2007. Impact of solubility of carbonate or sulphate salts and collapse potential on the formation of sinkholes. *Journal of Engineering, University of Tabriz,* 34**,** 2-10.

PARKS, D. A. & RENDELL, H. M. 1992. TL Geochronology of brickearth from south-east England. *Quaternary Science Reviews,* 11**,** 7-12.

PARSONS, R. L., JOHNSON, R. M., BROWN, D. A., DAPP, S. & BRENNAN, J. J. 2009. Characterization of Loess for Deep Foundations. *DFI Journal,* 3 (2) 11-21.

PECSI, M. 1990. Loess is not just accumulation of airbourne dust. *Quaternary International,* 7/8**,** 1-21.

PENCK, A. 1931. Central Asia (Zentral Asien Zeit). *The Geographical Journal (Ges Erdkunde zu Berlin),* 129 LXXVI.

PEREIRA DA SILVA, W. & PEREIRA DA SILVA, C. 2011. Lab Fit curve fitting software *In:* GRANDE, U. F. D. C. (ed.). Paraíba, Brazil.

PEREIRA, J., & ALONSO, E. 2009. Insights into the links between microstructure and Bishop's χ parameter for unsaturated soils. *In:* BUZZI, O., FITYUS, S., & SHENG, D. (eds.) *Unsaturated Soils - Theoretical and Numerical Advances in Unsaturated Soil Mechanics.* CRC Press, Boca Raton, FL, USA.

PEREIRA, J., COUSSY, O., ALONSO, E., VAUNAT, J. & OLIVELLA, S. 2010. Is the degree of saturation a good candidate for Bishop parameter. *In:* ALONSO, E. & GENS, A. (eds.) *Unsaturated Soils,* 2, 913-920, CRC Press, Boca Raton, FL, USA.

PRIKLONSKI, V.A. 1952. Gruntovedenia-Vtoraid Chast, Gosgeolzdat, Moscow.

POSADAS, A. N. D., GIMÉNEZ, D., BITTELLI, M., VAZ, C. M. P. & FLURY, M. 2001. Multifractal Characterization of Soil Particle-Size DistributionsMultifractal Characterization of Soil Particle-Size Distributions. *Soil Science Society of America Journal,* 65**,** 1361-1367.

POUCLET, A., HORVATH, E., GABRIS, G. & JUVIGNÉ, E. 1999. The Bag Tephra, a widespread tephrochronological marker in Middle Europe: chemical and mineralogical investigations. *Bulletin of Volcanology,* 61**,** 265-272.

PREENE, M. 2011. Methods of groundwater control by pumping Birmingham, UK: Golder Associates.

PRESTWICH, J. 1863. On the loess of the valleys of the south of England and of the Somme and the Seine. *Proceedings of the Royal Society of London,* 12**,** 170-173.

PUSCH, R. & SCHOMBURG, J. 1999. Impact of microstructure on the hydraulic conductivity of undisturbed and artificially prepared smectitic clay. *Engineering Geology,* 54**,** 167-172.

PYE, K. 1987. *Eolian dust and dust deposits,* London, Academic Press.

PYE, K. 1995. The nature, origin and accumulation of loess. *Quaternary Science Reviews,* 14**,** 653-667.

PYE, K. & BLOTT, S. J. 2004. Particle size analysis of sediments, soils and related particulate materials for forensic purposes using laser granulometry. *Forensic Science International,* 144**,** 19-27.

QIANG, M. R., CHEN, F. H., WANG, Z. T., NIU, G. M. & SONG, L. 2010. Aeolian deposits at the southeastern margin of the Tengger Desert (China): Implications for surface wind strength in the Asian dust source area over the past 20,000 years. *Palaeogeography Palaeoclimatology Palaeoecology,* 286**,** 66-80.

RABINOWICZ, E. 1976. Wear. *Materials Science and Engineering,* 25**,** 23-28.

RAGHAVAN, G. S. V. & OHU, J. O. 1985. Prediction of static equivalent pressure of proctor compaction blows. *American Society of Agriculture and Biological Engineering,* 28**,** 1398-1400.

REYNOLDS, P. J., CATT, J. A., WEIR, A. H. & FISHER, G. C. 1996. Stratigraphy and origin of New Forest brickearths, England. *Journal of Quaternary Science,* 11**,** 203-216.

REZNIK, Y.M. 1989. Discussion of "determination of collapse potential of soils" by A.J. Lutenegger and R.T. Saber. Geotechnical Testing Journal, GTJODJ, 12: 248-249.

ROGERS, C. D. F. 1995. Types and distribution of collapsible soils. *In:* DERBYSHIRE, E., DIJKSTRA, T. & SMALLEY, I. J. (eds.) *Genesis and Properties of Collapsible Soils.* Dordrecht: Kluwer Academic Publ.

ROGERS, C. D. F., BARKER, J. E., BOARDMAN, D. I. & PETERSON, J. 2002. Electrokinetic stabilisation of a silty clay soil *In:* 4th International Conference on Ground Improvement Techniques, Kuala Lumpur, Malaysia. 621-628.

ROGERS, C. D. F., DIJKSTRA, T. A. & SMALLEY, I. J. 1994a. Hydroconsolidation and subsidence of loess: Studies from China, Russia, North America and Europe: In memory of Jan Sajgalik. *Engineering Geology,* 37**,** 83-113.

ROGERS, C. D. F., DIJKSTRA, T. A. & SMALLEY, I. J. 1994b. Particle packing from an earth science viewpoint. *Earth-Science Reviews,* 36**,** 59-82.

ROGERS, C. D. F. & SMALLEY, I. 1993. The shape of loess particles. *Naturwissenschaften,* 80**,** 461-462.

ROGERS, J. J. W., KRUEGER, W. C. & KROG, M. 1963. Sizes of naturally abraded materials. *Journal of Sedimentary Petrology,* 33(3)**,** 628-632.

ROOHNAVAZ, C., RUSSELL, E. J. F. & TAYLOR, H. F. 2011. Unsaturated loessial soils: a sustainable solution for earthworks. *Proceedings of the Institution of Civil Engineers-Geotechnical Engineering,* 164**,** 257-276.

ROSE, J., LEE, J. A., KEMP, R. A. & HARDING, P. A. 2000. Palaeoclimate, sedimentation and soil development during the Last Glacial Stage (Devensian), Heathrow Airport, London, UK. *Quaternary Science Reviews,* 19**,** 827-847.

ROTTINGER, M. 1999. *Selected Simulations of Semiconductor Structures.* Unpublished thesis - Doctor of Philosophy (PhD), Technischen Universität Wien, Fakultät für Elektrotechnik

ROYAL, A. C. D., ROGERS, C. D. F., ATKINS, P. R., CHAPMAN, D. N., CURIONI, G., FOO, K. Y., HAO, T., METJE, N., MOGHAREH ABED, T., SHIRGIRI, N., and WAZLAN, S. 2011. Pipeline Engineering in the Ground: the Impact of Ground Conditions on Pipeline Condition and Maintenance Operations. ASCE. 1598-1609.

RUSSELL, R. J. 1944. Lower Mississippi valley loess. *Geological Society of America Bulletin,* 55 (1)**,** 1-40.

RUST, E., HEYMANN, G. & JONES, G. A. 2005. Collapse potential of partly saturated sandy soils from Mozal, Mozambique. *Journal of the South African Institution of Civil Engineering,* 47**,** 8-14.

SAARENKETO, T. 1998. Electrical properties of water in clay and silty soils. *Journal of Applied Geophysics,* 40**,** 73-88.

SAEJIEW, A., GRUNBERGER, O., ARUNIN, S., FAVRE, F., TESSIER, D. & BOIVIN, P. 2004. Critical coagulation concentration of Paddy soil clays in sodium-ferrous iron electrolyte. *Soil Science Society of America Journal, Division S-2 - Soil Chemistry,* 68**,** 789.

SAKR, M., MASHHOUR, M., and HANNA, A. 2008. Egyptian collapsible soils and their improvement. In *Proceedings of GeoCongress*, New Orleans, USA. 654-661.

SANTAMARINA, J. C. 2003. Soil behavior at the microscale: Particle forces. *In:* GERMAINE, J. T., SHEAHAN, T. C. & WHITMAN, R. V. (eds.) *Soil Behavior and Soft Ground Construction.* New York: Amer Soc Civil Engineers.

SCHAETZL, R. J. 2013. Loess deposits in the Midwestern United States: Geography matters. *In:* O'HARA-DHAND, K. & MCLAREN, S. (eds.) *INQUALoess2013 Workshop: Loess & Dust: Geography-Geology-Archaeology.* University of Leicester: Print Services, University of Leicester.

SERRIDGE, C. J. & SYNAC, O. 2006. Application of the Rapid Impact Compaction (RIC) technique for risk mitigation in problematic soils. *In:* CULSHAW, M. G., REEVES, H. J., JEFFERSON I., & SPINK, T. W., Engineering Geology for Tomorrow's Cities, *Engineering Geology Special Publication,* 22, Paper 294, Geological Society of London.

SFRISO, A., SAGUES, P., QUAGLIA, G., QUINTELA, M. & LEDESMA, O. 2008. Small-strain stiffness of the Pampeano Formation. *IV International Symposium of Deformation Characteritics of Geomaterials.* Atlanta.

SHAO, S., LONG, J., & YU. Q. 2008. Stress-strain relationship with soil structural parameters of collapse loess. *Frontiers of Architecture and Civil Engineering in China*. Vol. 2(2), 151-160.

SHARMA, R. S. 1998. *Mechanical behaviour of unsaturated highly expansive clays* Unpublished thesis - Doctor of Philosophy (PhD), University of Oxford, Keble College

SHARP, M. & GOMEZ, B. 1986. Processes of debris comminution in the glacial environment and implications for quartz sand-grain micromorphology. *Sedimentary Geology,* 46**,** 33-47.

SHEPHERD, R. & RANDELL, R. 2010. *Discoveinrg fossils, Introducing the palaeontology of Great Bretain* [Online]. [Accessed].

SHW600 2009. Manual of contract documents for highway works. *Vol 1. Specification for highway works.* United Kingdom.

SIDES, G. & BARDEN, L. 1971. The microstructure of dispersed and flocculated samples of laolinite, illite and montmorillonite. *Canadian Geotechnical Journal,* 8**,** 391-399.

SINGH, B. & GILKES, R. J. 1993. The recognition of amorphous silica in indurated soil profiles *Clay Minerals,* 28**,** 461-474.

SIVAKUMAR, V. 1993. *A critical state framework for unsaturated soil [Soil compression models].* Unpublished thesis - Doctor of Philosophy (PhD), University of Sheffield.

SIVAPULLAIAH, P. V. & MANJU, M. 2006a. Effect of zeolitization on the volume-change behaviour of kaolinitic soils. *Canadian Geotechnical Journal,* 43**,** 969-978.

SKEMPTON, A. W. 1960. Terzaghi's discovery of effective stress. *In:* BJERRUM, L., CASAGRANDE, A., PECK, R. B. & SKEMPTON, A. W. (eds.) *From Theory to Practice in Soil Mechanics.* New York: John Wiley & Sons.

SMALLEY, I. 2013. Loess: then, now, tomorrow, eventually. *In:* O'HARA-DHAND, K. & MCLAREN, S. (eds.) *INQUALoess2013 Workshop: Loess & Dust: Geography-Geology-Archaeology.* University of Leicester: Print Services, University of Leicester.

SMALLEY, I. 1992. The Teton Dam: rhyolite foundation + loess core = disaster. *Geology Today,* 8**,** 19-22.

SMALLEY, I. 1987. Loess Letter. 17, 8-40.

SMALLEY, I. J. 1970. Cohesion of soil particles and intrinsic resistance of simple soil systems to wind erosion *Journal of Soil Science,* 21**,** 154.

SMALLEY, I. 1966. Formation of Quartz Sand. *Nature* 211**,** 476-479.

SMALLEY, I., MARKOVIC, S. B. 2013. Loessification and Hydroconsolidation: There is a connection. CATENA. 117. 94-99.

SMALLEY, I., O'HARA-DHAND, K., WINT, J., MACHALETT, B., JARY, Z. & JEFFERSON, I. 2009. Rivers and loess: The significance of long river transportation in the complex event-sequence approach to loess deposit formation. *Quaternary International,* 198**,** 7-18.

SMALLEY, I. J., JEFFERSON, I. F., O'HARA-DHAND, K. & EVANS, R. D. 2006 a. An approach to the problem of loess deposit formation: Some comments on the 'in situ' or 'soil-eluvial' hypothesis. *Quaternary International,* 152**,** 109-117.

SMALLEY, I. J., MAVLYANOVA, N. G., RAKHMATULLAEV, K. L., SHERMATOV, M. S., MACHALETT, B., DHAND, K. O. & JEFFERSON, I. F. 2006 b. The formation of loess deposits in the Tashkent region and parts of Central Asia; and problems with irrigation, hydrocollapse and soil erosion. *Quaternary International,* 152**,** 59-69.

SMALLEY, I. J., KUMAR, R., O'HARA DHAND, K., JEFFERSON, I. F. & EVANS, R. D. 2005. The formation of silt material for terrestrial sediments: Particularly loess and dust. *Sedimentary Geology,* 179**,** 321-328.

SMALLEY, I., and JARY, Z. 2005. Maps of worldwide loess distribution: from Keilhack to Kringer and beyond. New Zealand Soil News. 53. 45-9 (reprinted in Loess Letter 55)

SMALLEY, I. J., JEFFERSON, I. F., DIJKSTRA, T. A. & DERBYSHIRE, E. 2001. Some major events in the development of the scientific study of loess. *Earth-Science Reviews,* 54**,** 5-18.

SMALLEY, I. J. & DIJKSTRA, T. A. 1991. The Teton Dam (Idaho, U.S.A.) failure: problems with the use of loess material in earth dam structures. *Engineering Geology,* 31**,** 197-203.

SMART, P. & TOVEY, N. K. 1982. *Electron microscopy of soils and sediments: Techniques,* Oxford, Oxford University Press.

SMITH, B. J., WRIGHT, J. S. & WHALLEY, W. B. 1991. Simulated aeolian abrasion of Pannonian sands and its implications for the origins of Hungarian loess *Earth Surface Processes and Landforms,* 16**,** 745-752.

SMITH, B. J., WRIGHT, J. S. & WHALLEY, W. B. 2002. Sources of non-glacial, loess-size quartz silt and the origins of "desert loess". *Earth-Science Reviews,* 59**,** 1-26.

SOKOLOVICH, V. E. 1965. Silicatization of loessic soils. *Soil Mechanics and Foundation Engineering* 2**,** 3-7.

SOKOLOVICH, V. E. 1976. Process of silication of loess soils. *Fundamenty i Mekhanika Gruntov,* 1**,** 39-40.

SOKOLOVICH, V. E. & GUBKIN, V. A. 1970. Gaseous silicatization of loessic ground. *Fundamenty i Mekhanika Gruntov,* 5**,** 26-28.

SOKOLOVICH, V. E. & IBRAGIMOV, M. N. 1971. Experience of strengthening carbonate and humus soils by silicatization involving the use of carbon dioxide. *Fundamenty i Mekhanika Gruntov,* 6**,** 15-16.

SORBY, H. C. 1858. On the microscopical structure of crystals, indicating the origin of rocks and minerals. *Quarterly Journal of Geological Society, London,* 14**,** 453-500.

SOULIE, F., CHERBLANC, F., EL YOUSSOUFI, M. S. & SAIX, C. 2006. Influence of liquid bridges on the mechanical behaviour of polydisperse granular materials. *International Journal for Numerical and Analytical Methods in Geomechanics,* 30**,** 213-228.

SUDHAKAR, M. R. & SRIDHARAN, A. 1984. Mechanism of sulfate adsorption by Kaolinite. *Clays and Clay minerals,* 32**,** 414-418.

TAJUDIN, S. A. A. 2012. *Electrokinetic stabilisation of soft clay.* Unpublished thesis - Doctor of Philosophy (PhD), University of Birmingham.

TAN, K. H. 2005. *Soil sampling, preparation, and analysis*, Taylor & Francis Group, United States of America.

TARANTINO, A. & TOMBOLATO, S. 2005. Coupling of hydraulic and mechanical behaviour in unsaturated compacted clay. *Geotechnique,* 55 (4), 307–317.

TAYLOR, J. F. 1982. *An introduction to Error Analysis, The Study of Uncertainties in Physical Measurments,* Mill Valley, CA, the United States of America, University Science Books.

TERZAGHI, K. 1936. The shear resistance of unsaturated soil. *1st International Conference on Soil Mechanics and Foundation Engineering.*

TOSSELL, J. A. & VAUGHAN, D. J. 1992. *Theoretical geochemistry: Application of quantom mechanics in the earth and mineral sciences,* United States of America, Oxford University Press.

TOVEY, N. K. 1995. Techniques to examine microfabric and particle interaction of collapsible soils. *In:* DERBYSHIRE, E., DIJKSTRA, T. & SMALLEY, I. J. (eds.) *Genesis and Properties of Collapsible Soils.* Dordrecht: Kluwer Academic Publ.

TROFIMOV, V. T. 1990. Some experimental evidence of formation of syngenetic collapsibility of aeolian loess rocks. *Inzhenernaya Geologiya,* 6**,** 11-24.

TU, G. Z. 1986. Treatment of self-subsiding collapsible loess foundation accidents *Xian Institute of Metallurgy and Construction Engineering***,** 328-331.

TURCOTTE, D. L. 1986. Fractals and fragmentation. *Journal of Geophysical Research: Solid Earth,* 91**,** 1921-1926.

ULERY, A. L. & DREES, L. R. 2008. *Methods of soil analysis,* Madison, Wisconsin, USA, Soil Science Society of America Inc.

VALDES, J. R. 2002. *Fines migration and formation damage.* Unpublished thesis - Doctor of Philosophy (PhD), Georgia Institute of Technology.

VAN OLPHEN, H. 1964. Internal mutual flocculation in clay suspensions. *Journal of Colloid Interface Science,* 19**,** 313-322.

VAN OLPHEN, H. 1977. *An introduction to clay colloid chemistry,* New York, John Wiley & Sons.

VAN PAASSEN, L. A. 2009. Ground improvement by microbially induced carbonate precipitation. *In:* MAGNIFICUS, R., VAN LOOSDRECHT, M. C. M., BRUINING, J., BARENDS, F. B. J., VAN BREUGEL, K., HASSANIZADEH, M., SOGA, K. & BOREL, S. (eds.) *Biogrout.* Delft University of Technology.

VLAHINIC, I., JENNINGS, H., ANDRADE, J., & THOMAS, J. (2011). A novel and general form of effective stress in a partially saturated porous material: The influence of microstructure. *Mech. Mater*. 43(1), 25–35.

WANG, D., FU, B., ZHAO, W., HU, H. & WANG, Y. 2008. Multifractal characteristics of soil particle size distribution under different land-use types on the Loess Plateau, China. *CATENA,* 72**,** 29-36.

WAXMAN, M. H. & SMITS, L. J. M. 1968. Electrical conduction in oil-bearing sands. *Society of Petroleum Engineers Journal,* 8**,** 107-122.

WEST, I. & MILLS, S. 2009. *Chilling and Brownwich Cliffs, Southampton water, Geology of the Wessex Coast of Southern England* [Online]. Southampton: School of Ocean and Earth Science, National Oceanography Centre, University of Southampton. [Accessed].

WEST, I., WEST, C., WEST, T. & BENTLEY, J. 2010. *Barton and Highcliffe, Eocene Strata - Geology of the Wessex Coast of Southern England* [Online]. Southampton: School of Ocean and Earth Science, University of Southampton. [Accessed].

WHEELER, S. J., KARUBE, D. 1996. Constitutive modelling. *In:* ALONSO, E. E., DELAGE, P. (ed.) *Unsaturated Soils.* Balkema, Rotterdam

WHEELER, S., SHARMA, R. & BUISSON, S. 2003. Coupling of hydraulic hysteresis and stress-strain behaviour in unsaturated soils. *Geotechnique,* 53 (1), 41-54.

WIECHERS, H. N. S., STURROCK, P. & MARAIS, G. V. R. 1975. Calcium-carbonate crystallization kinetics *Water Research,* 9**,** 835-845.

WRIGHT, J. & SMITH, B. 1993. Fluvial comminution and the production of loess-sized quartz silt - a simulation study. *Geografiska Annaler Series a-Physical Geography,* 75**,** 25-34.

WRIGHT, J., SMITH, B. & WHALLEY, B. 1998. Mechanisms of loess-sized quartz silt production and their relative effectiveness: laboratory simulations. *Geomorphology,* 23**,** 15-34.

WRIGHT, J. S. 1995. Glacial comminution of quartz sand grains and the production of loessic silt: A simulation study. *Quaternary Science Reviews,* 14**,** 669-680.

WRITE, V. P. 1994. Palesols in shallow marine carbonate sequences. *Earth Science Review,* 35**,** 367-395.

WYNNE, A. 2007. Plans to build a vast oil production plant in Kazakhstan have called for investigation of difficult soils in a far-flung location. *New Civil Engineer nce,* October.

XIA, J. & HAN, A. M. 2009. Cyclic variability in microstructure and physio-mechanical properties of the Xianshu Loess-palaeosol sequence in Nanjing, China. *Engineering Geology,* 104**,** 263-268.

YURUGI, T. I., S. NUMATA, Y, SYKES, K. 2001. SEM/EDX integrated analysis system. *Reaout,* 22**,** 14-18.

ZEGHAL, M., ASCE, & MEDINA, A. M. C. 2008. Effective stress of unsaturated granular soils in a pendular state. *In:* ALSHAWABKEH, A. N., REDDY, K. R. & KHIRE, M. V. (eds.) *GeoCongress 2008: Characterization, Monitoring, and Modelling of Geosystems.* New Orleans, Louisiana: American Society of Civil Engineers.

ZHAO, L. N., FENG, J. D. & WANG, Z. C. 2009. In situ synthesis and modification of calcium carbonate nanoparticles via a bobbling method. *Science in China Series B-Chemistry,* 52**,** 924-929.

ZOURMPAKIS, A. 2005. *Factors affecting bonding in loess soils* Unpublished thesis - Doctor of Phylosophy (PhD), University of Birmingham.

ZOURMPAKIS, A., BOARDMAN, D. I. & ROGERS, C. D. F. Year. Creation of artificial loess soils. *In:* Proceeding of International Conference From Experimental Evidence towards Numerical Modelling of Unsaturated Soils, 2003 Weimar, Germany

ZOURMPAKIS, A., BOARDMAN, D. I. & ROGERS, C. D. F. 2005. Creation of artificial loess soils. *In:* SCHANZ, T. (ed.) *Unsaturated Soils: Experimental Studies.* Berlin: Springer-Verlag Berlin.

ZOURMPAKIS, A., BOARDMAN, D. I., ROGERS, C. D. F., JEFFERSON, I., GUNN, D. A., JACKSON, P. D., NORTHMORE, K. J., ENTWISLE, D. C., NELDER, L. M. & DIXON, N. 2006. Case study of a loess collapse field trial in Kent, SE England. *Quarterly Journal of Engineering Geology and Hydrogeology,* 39**,** 131-150.